

**ÉTUDE ELECTRO-OPTIQUE DE L'INTERFACE
n-ALCANETHIOLS GaAs(001): LES PHÉNOMÈNES DE
SURFACE ET LES APPLICATIONS EN BIO-
DÉTECTION À BASE DE PHOTOLUMINESCENCE**

**ELECTRO-OPTIC INVESTIGATION OF THE
n-ALKANETHIOL GaAs(001) INTERFACE: SURFACE
PHENOMENA AND APPLICATIONS TO
PHOTOLUMINESCENCE-BASED BIOSENSING**

**Thèse de doctorat
Spécialité: Génie électrique**

Composition du jury:

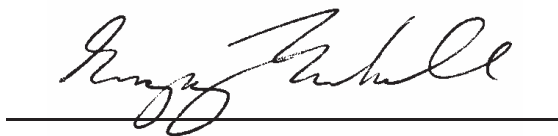
Prof. Jan J. Dubowski, Université de Sherbrooke, directeur

Dr. Farid Bensebaa, National Research Council of Canada, co-superviseur

Prof. Frank Traeger, University of Kassel, expert externe

Dr. Gregory P. Lopinski, National Research Council of Canada, expert externe

Prof. Dominique Drouin, Université de Sherbrooke, rapporteur



© **Gregory M. Marshall**

Université de Sherbrooke
Faculté de génie
Département de génie électrique
et de génie informatique

RÉSUMÉ

Les surfaces de semi-conducteur couplées à des structures moléculaires dérivées de la chimie organique forment la base d'une nouvelle classe émergente de dispositifs à effet de champ. En plus de la recherche dans le domaine d'électronique moléculaire, ces interfaces sont développées pour une variété d'applications de biosenseur en électronique et en optique. Les monocouches auto-assemblées (SAMs) composées de *n*-alcanethiols $[\text{HS}(\text{CH}_2)_n\text{R}]$ qui se couplent à la surface de GaAs(001) par la formation de la liaison covalente S-GaAs sont d'un intérêt pratique. Ces SAMs offrent des fonctionnalités potentielles en termes de chimie requise pour les senseurs et de l'effet de passivation de tel couplage.

Dans cette thèse, l'interface SAM-GaAs est étudiée dans le cadre de biosenseur photonique basé sur la variation de la photoluminescence (PL). Le plan de cette recherche est classé en trois parties : i) l'analyse structurale et compositionnelle de la surface en utilisant la spectroscopie de photoélectrons induits par rayons X (XPS), ii) l'étude des propriétés électroniques à l'interface sous les conditions d'équilibre en utilisant la spectroscopie infrarouge (IR), la méthode de la sonde de Kelvin et XPS et iii) l'analyse de la réponse électro-optique sous l'excitation photonique permanente, en particulier, le photovoltage de surface (SPV) et l'intensité de la PL.

En utilisant un modèle de recouvrement partiel de spectres de la résolution angulaire XPS dans lequel les attributions des composantes sont démontrées être quantitativement valides, le taux du recouvrement de la terminaison méthyle du SAM est démontrée excéder 90%. Parmi les résultats remarquables, c'est l'obtention d'une surface riche en Ga, pauvre en oxyde, et dont l'As élémentaire est présent en quantités sous-monocouches en accord avec la théorie des morphologies surfaciques. L'analyse modale de la transmission des spectres de l'IR montre que l'ordre moléculaire des SAMs est suffisant pour permettre la déduction (selon la loi de Beer-Lambert) des constantes optiques IR, ce qui mène à l'observation d'une augmentation d'absorbance spécifique des SAMs. Par la corrélation de l'absorbance IR avec le potentiel de la couche dipolaire de SAM, le mécanisme de l'augmentation est attribué aux moments vibrationnels ajoutés par la polarisation électronique dans le champ statique des SAMs. Enfin, la position du niveau de Fermi à la surface est déterminée par XPS et est utilisée pour interpréter les résultats de SPV en termes de réduction de la section transversale à la surface pour la capture des porteurs minoritaires, induite par les thiols. L'analyse numérique confirme ce résultat basé sur la théorie de transport de porteur de l'intensité de la PL dans le contexte d'une réduction de la vitesse de recombinaison à la surface.

Mots clés : photonique, biosenseur, GaAs, monocouches auto-assemblées, spectroscopie de photoélectrons induits par rayons X, spectroscopie infrarouge, photoluminescence, niveau de Fermi, photovoltage.

ABSTRACT

Semiconductor surfaces coupled to molecular structures derived from organic chemistry form the basis of an emerging class of field-effect devices. In addition to molecular electronics research, these interfaces are developed for a variety of sensor applications in the electronic and optical domains. Of practical interest are self-assembled monolayers (SAMs) comprised of *n*-alkanethiols $[\text{HS}(\text{CH}_2)_n\text{R}]$, which couple to the GaAs(001) surface through S-GaAs covalent bond formation. These SAMs offer potential functionality in terms of the requisite sensor chemistry and the passivation effect such coupling is known to afford.

In this thesis, the SAM-GaAs interface is investigated in the context of a photonic biosensor based on photoluminescence (PL) variation. The scope of the work is categorized into three parts: i) the structural and compositional analysis of the surface using X-ray photoelectron spectroscopy (XPS), ii) the investigation of electronic properties at the interface under equilibrium conditions using infrared (IR) spectroscopy, the Kelvin probe method, and XPS, and iii) the analysis of the electro-optic response under steady-state photonic excitation, specifically, the surface photovoltage (SPV) and PL intensity.

Using a partial overlay model of angle-resolved XPS spectra in which the component assignments are shown to be quantitatively valid, the coverage fraction of methyl-terminated SAMs is shown to exceed 90%. Notable among the findings are a low-oxide, Ga-rich surface with elemental As present in sub-monolayer quantities consistent with theoretical surface morphologies. Modal analysis of transmission IR spectra show that the SAM molecular order is sufficient to support a Beer-Lambert determination of the IR optical constants, which yields the observation of a SAM-specific absorbance enhancement. By correlation of the IR absorbance with the SAM dipole layer potential, the enhancement mechanism is attributed to the vibrational moments added by the electronic polarizability in the static field of the SAM. Lastly, the surface Fermi level position is determined by XPS and is used to interpret SPV results in terms of a thiol-induced reduction of the surface cross-section for minority carrier-capture. Numerical analysis confirms this result based on the carrier transport theory of PL intensity by means of a reduction of the surface recombination velocity.

Keywords: photonics, biosensor, GaAs, self-assembled monolayers, X-ray photoelectron spectroscopy, IR spectroscopy, photoluminescence, surface Fermi level, surface photovoltage.

SUMMARY of ORIGINAL CONTRIBUTIONS

The content of this thesis is attributed to the author as unpublished work, and as pending or published scientific literature as follows: 1) *Journal of Applied Physics*, “Observation of surface enhanced IR absorption coefficient in alkanethiol based self-assembled monolayers on GaAs(001)” [Marshall *et al.*, 2009a], 2) *Langmuir*, “Surface Dipole Layer Potential Induced IR Absorption Enhancement in *n*-Alkanethiol SAMs on GaAs(001)” [Marshall *et al.*, 2009b], 3) *Applied Surface Science*, “Surface barrier analysis of semi-insulating and n^+ -type GaAs(001) following passivation with *n*-alkanethiol SAMs” [Marshall *et al.*, 2011a], 4) *Nanotechnology*, “Electro-optic investigation of the surface trapping efficiency in *n*-alkanethiol SAM passivated GaAs(001)” [Marshall *et al.*, 2011b], and as contributed in 5) *Journal of Applied Physics*, “Formation dynamics of hexadecanethiol self-assembled monolayers on (001) GaAs observed with photoluminescence and Fourier transform infrared spectroscopies” [Kim *et al.*, 2009], and 6) *Applied Surface Science*, “Molecular self-assembly and passivation of GaAs (001) with alkanethiol monolayers: A view towards bio-functionalization” [Dubowski *et al.*, 2010].

ACKNOWLEDGEMENTS

The author wishes to acknowledge the Université de Sherbrooke and the National Research Council of Canada (NRC), Institute for Chemical Process and Environmental Technology (ICPET) for supporting an extended secondment to ICPET as a Visiting Worker. This opportunity allowed a rich variety of research topics to be pursued and provided access to helpful subject matter expertise. Thanks is also given to the NRC for financial support, including the Graduate Student Scholarship Supplement Program award, and to the Faculté de Génie for accepting graduate course transfer credits from the University of Ottawa.

Appreciation is extended to the director of this work, Prof. Jan J. Dubowski, for financial support, the opportunity to develop the contents of this work to its potential, and for accommodating concurrent obligations to the Canadian Forces Army Reserve. Special thanks are given to Dr. Farid Bensebaa (ICPET), who provided functional supervision, operational support and valuable career mentorship, and to Dr. Gregory P. Lopinski of the NRC Steacie Institute for Molecular Sciences, with whom insightful technical discussions and productive collaborations were the result of much generosity.

The camaraderie, peer learning and technical support offered by several members of Prof. Dubowski's group and members of the ICPET staff are also gratefully acknowledged, especially: Mr. David Kingston, Dr. Ximing Ding, Dr. Oleksandr Voznyy, Dr. Radoslaw Stanowski, Dr. Chan Kyu Kim, Dr. Khalid Moumanis, Dr. Palani Arudra and Dr. Jianfu Ding.

TABLE of CONTENTS

RÉSUMÉ	i
ABSTRACT	ii
SUMMARY of ORIGINAL CONTRIBUTIONS	iii
ACKNOWLEDGEMENTS	iv
TABLE of CONTENTS	v
LIST of FIGURES	viii
LIST of TABLES	xii
ACRONYMS	xiii
CHAPTER 1: INTRODUCTION	1
1.1 Fundamentals of Biosensing	1
1.2 Surface Chemistry and Molecular Self-Assembly	4
1.3 Semiconductor-based Biosensing	8
1.3.1 Channel Conductance Methods	8
1.3.2 Photoluminescence Methods	11
1.4 Motivations and Research Objectives	15
1.4.1 Structural and Chemical Characterization	15
1.4.2 Electronic Properties of the SAM	16
1.4.3 Electro-Optic Response of the GaAs Interface	16
1.5 Structure of the Thesis	17
CHAPTER 2: LITERATURE and THEORY	19
2.1 X-ray Photoelectron Spectroscopy of the SAM-GaAs Interface	19
2.1.1 Surface Composition and Passivation of GaAs	22
2.1.1.1 Inorganic Sulphides	24
2.1.1.2 Organic Thiols	25
2.1.1.3 Oxide Etching	29
2.1.1.4 SAM-GaAs Interface Structure	30
2.1.2 Angle-Resolved XPS Methods	31
2.1.3 Surface Energy Levels	34
2.2 Infrared Spectroscopy and Molecular Ordering in the SAM	37
2.2.1 Quantum Mechanics of the IR Absorption Intensity	39
2.2.2 Polarizability and the Principal Components of the Refractive Index	42
2.2.3 Molecular Structure and Orientation of the SAM	45
2.2.4 Symmetry and the Optical Constants in IR Modeling of the SAM	47
2.3 Surface Energy Levels by the Kelvin Probe Method	49
2.3.1 Work Function Measurements	49
2.3.2 Surface Photovoltage and the Surface Barrier Height	53
2.3.2.1 Excess Carrier Screening of the Space Charge Region	53
2.3.2.2 Surface Charge Modification	55
2.3.2.3 Equilibrium Band-Bending in SPV and PL Models	58
2.4 Photoluminescence of the SAM-GaAs Interface	59
2.4.1 Near-Surface Model of the Photoluminescence	59
2.4.2 Sensor Operation Based on the Dead-Layer	61

2.4.3 Non-Radiative Recombination Theory	63
2.5 Chapter Summary	67
CHAPTER 3: COMPOSITION and STRUCTURAL ANALYSIS by XPS	68
3.1 Experimental Details	68
3.1.1 Sample Preparation	68
3.1.1.1 Wafer Cleaning	68
3.1.1.2 Ethanol Solvent Degassing	69
3.1.1.3 Preparation of Thiol Solution	69
3.1.1.4 Etching and SAM Incubation	70
3.1.2 Recording of XPS Spectra	70
3.1.3 Component Fitting with CasaXPS Software	71
3.2 Spectra and Compositional Stoichiometry	72
3.2.1 GaAs Survey	72
3.2.2 GaAs High-Resolution	75
3.2.3 HDT-SAM Prepared GaAs	80
3.2.4 Compositional Analysis of XPS Data	85
3.3 Angle-Resolved XPS Structural Analysis	87
3.3.1 GaAs Surface Stoichiometry	87
3.3.2 Surface Concentration of Elemental Arsenic	89
3.3.3 Fractional Coverage of the SAM	91
3.4 Chapter Summary	94
CHAPTER 4: INFRARED SPECTROSCOPY of the SAM	95
4.1 Experimental Details	95
4.1.1 SAM Preparation	95
4.1.2 Liquid Thiol for Beer-Lambert Analysis	96
4.1.3 IR Transmission Measurements	96
4.2 Modal Analysis and Observation of SAM Formation Dynamics	97
4.2.1 Modal Analysis of Methyl-Terminated Alkanethiols	97
4.2.2 Formation Dynamics	102
4.3 Beer-Lambert Analysis of the IR Absorption	103
4.3.1 Evaluation of the Absorption Coefficient	103
4.3.2 Absorption Enhancement Effect	106
4.4 Optical Constants of the SAM	107
4.5 Amine-Terminated Alkanethiols	110
4.6 Chapter Summary	113
CHAPTER 5: SURFACE BAND STRUCTURE in EQUILIBRIUM	114
5.1 Experimental Details	114
5.1.1 Kelvin Probe and XPS Work Function Measurements	114
5.1.2 Baseline Thermal Disordering of the SAM	115
5.1.3 Integration of Au Binding Energy Calibrant	116
5.2 Dipole Layer Potential of the SAM	117
5.2.1 Motivations in the Context of IR Enhancement	117
5.2.2 Discussion on Fermi Level Pinning	118
5.2.3 Work Function and the Dipole Layer Potential	120
5.2.3.1 Kelvin Probe Results	120

5.2.3.2 IR Spectroscopy of the Disordered SAM	122
5.2.3.3 XPS Determination of the DLP	123
5.2.4 DLP and the Effective Capacitor Model	125
5.2.5 Correlation with the IR Absorbance and the IR Enhancement Effect	127
5.3 Surface Barrier Analysis following SAM Passivation	134
5.3.1 XPS Results of the Surface Fermi Level	134
5.3.2 Surface Barrier Height and the AUDM	138
5.4 Chapter Summary	141
CHAPTER 6: NEAR-SURFACE ELECTRO-OPTIC PHENOMENA	142
6.1 Experimental Details	143
6.1.1 Sample Preparation	143
6.1.2 Surface Photovoltage Measurements	143
6.1.3 Photoluminescence Measurements	143
6.2 Surface Photovoltage of SAM Passivated GaAs	144
6.2.1 SPV Results	144
6.2.2 SPV Model Parameters	145
6.2.3 Scale Transformation to Photon Irradiance	148
6.2.4 Surface Carrier Capture Coefficients	149
6.2.5 Discussion of SPV Findings	151
6.3 Photoluminescence of SAM Passivated GaAs	153
6.3.1 PL Enhancement in the Flat-Band Regime	153
6.3.2 Transport Model of PL Enhancement	158
6.3.3 Discussion of PL Results	160
6.3.4 Null Enhancement of n^+ GaAs	161
6.4 Significance to the Operation of a Biosensor	162
6.5 Chapter Summary	165
CHAPTER 7: THESIS SUMMARY and CONCLUDING REMARKS	166
7.1 Thesis Summary	166
7.2 Concluding Remarks	169
APPENDIX A	171
APPENDIX B	173
APPENDIX C	176
APPENDIX D	179
APPENDIX E	180
APPENDIX F	182
BIBLIOGRAPHY	183

LIST of FIGURES

Figure 1.1. Generalization of biosensing concept.	2
Figure 1.2. COOH-terminated alkanethiol SAM used for dopamine recognition via electrostatic discrimination on a gold voltammetric electrode.	6
Figure 1.3. OH-terminated and biotinylated polyether thiols form mixed molecule SAMs for streptavidin immobilization.	7
Figure 1.4. HEMT design MOCSEER with porphyrin-based SAM used for the detection of nitric oxide in physiological aqueous solutions.	10
Figure 1.5. Recombination processes in GaAs.	11
Figure 1.6. Near-surface band structure of n-type GaAs in depletion.	13
Figure 2.1. Pictorial descriptions of basic XPS theory.	21
Figure 2.2. Chemical passivation of GaAs surface with a bio-functional alkanethiol SAM.	23
Figure 2.3. As 3d and Ga 3d core level photoelectron spectra of the (NH ₄) ₂ S passivated GaAs(001) surface.	24
Figure 2.4. Regions of the SAM-GaAs interface used for evaluation of the surface sensitivity ratio.	27
Figure 2.5. Ga 3d, As 3d and S 2p core level photoelectron spectra of the ODT passivated GaAs(001) surface.	28
Figure 2.6. SAM matched GaAs(001) reconstruction according to molecular simulations.	31
Figure 2.7. Schematic of ARXPS of an overlayer (L) on substrate (S).	32
Figure 2.8. Energy level diagram of various materials in an XPS experiment.	35
Figure 2.9. Normal vibrational modes of the water molecule.	38
Figure 2.10. Energy well models describing the diatomic potential as a function of internuclear separation.	40
Figure 2.11. Molecular coordinates of the SAM defined by the tilt (θ) of the C-C-C backbone plane, the azimuth with respect to the cubic lattice, and the twist orientation (ψ) about the molecular axis.	45
Figure 2.12. Factors contributing to the work function potential of a semiconductor n-type surface.	50
Figure 2.13. Energy level diagrams illustrating the establishment of the CPD.	51
Figure 2.14. Illustration of the 2D dipole layer potential formed by a self-assembled monolayer on the GaAs(001) surface, after Marshall <i>et al.</i> [Marshall <i>et al.</i> , 2009b].	51
Figure 2.15. CPD as a function of molecular chain length for methyl terminated alkanethiol SAMs on Au, after Lü <i>et al.</i> [Lü <i>et al.</i> , 1999].	52

Figure 2.16. Calculated SPV (solid lines) as a function of the excess carrier density for n-type GaAs under the assumed condition that the surface charge density ($-q N_t$) remains constant.	55
Figure 2.17. Calculated SPV as a function of the excess carrier density for n-type GaAs with a discrete level acceptor state located at E_t and having surface density N_t	57
Figure 2.18. Shockley-Reed-Hall recombination U_{nr} for a trap level E_t located within the band-gap of GaAs for various values of χ	65
Figure 3.1. Low resolution XPS survey spectrum of etched only semi-insulating GaAs(001) at ToA = 0°.	73
Figure 3.2. As per Figure 3.1 showing LMM Auger bands due to Ga and As.	73
Figure 3.3. As per Figure 3.1 showing loss peaks characteristic of the GaAs volume plasmon at +15.6 eV from the parent photoemission line.	74
Figure 3.4. High resolution XPS spectra from the elements identified in Figure 3.1 at ToA = 60°.	77
Figure 3.5. NH ₄ OH etched GaAs following Ar-ion <i>in situ</i> sputtering.	80
Figure 3.6. XPS spectra of unbound molecular thiol, Au bonded thiolate, and the Au film used for Fermi level referenced calibration of the binding energy to Au 4f _{7/2} at 84.00 eV.	81
Figure 3.7. High resolution XPS spectra from semi-insulating GaAs prepared with HDT-SAM. ToA = 60°.	82
Figure 3.8. Comparison of etched only GaAs and as prepared with HDT-SAM in the As 3d region.	84
Figure 3.9. ARXPS data of As:Ga ratio and model analysis according to Equations 3.2 and 3.4 for HDT-SAMs.	88
Figure 3.10. Fractional overlayer model of the corrugated surface.	89
Figure 3.11. Fractional overlayer model of As ⁰ coverage on GaAs prepared with HDT-SAM.	91
Figure 3.12. Fractional overlayer model of HDT-SAM coverage on GaAs.	92
Figure 4.1. Illustration of the technique used to quantify the absorption thickness of a thin layer of liquid thiol pressed between two coverglass slides.	96
Figure 4.2. In transmission mode, SAMs present absorption path length differences (Δl) dictated by the length of their respective molecules.	97
Figure 4.1. Transmission IR spectra of <i>n</i> -alkanethiol [HS(CH ₂) _{<i>n</i>} CH ₃] SAMs on GaAs(001).	98
Figure 4.4. Component analysis of IR spectra.	100
Figure 4.5. CH ₂ asymmetric mode peak frequency vs. modal scale factor; continuous model (line), component fit results (circles), illustrating the correspondence of amplitude and position in the <i>n</i> -scaling model.	101

Figure 4.6. IR peak absorbance (a), and position (b), of the asymmetric C-H stretching mode of alkane CH ₂ in HDT-SAMs.	102
Figure 4.7. CH ₂ asymmetric mode amplitude as a function of the methylene number (circles).	103
Figure 4.8. Liquid phase C-H stretching mode spectra: (a) <i>n</i> 13 / 11 μm, (b) <i>n</i> 9 / 8 μm and (c) <i>n</i> 13 / 4 μm, according to layer thickness.	105
Figure 4.9. Enhancement factor observed for the SAM phase absorption coefficient relative to Beer-Lambert measurements in bulk material.	105
Figure 4.10. Comparison of the principal components of the refractive index determined using Beer-Lambert analysis in the present work (a) and (b) [Marshall <i>et al.</i> , 2009b], with results from IR ellipsometry adapted from Rosu <i>et al.</i> [Rosu <i>et al.</i> , 2009] (c) and (d).	109
Figure 4.11. Comparison of methyl-terminated alkanethiol SAMs HDT and DDT with amine-terminated SAMs of similar length (methylene numbers <i>n</i> = 16 and 11).	111
Figure 4.12. XPS spectra of <i>n</i> 11 ATA-SAMs on GaAs.	112
Figure 5.1(a). Kelvin Probe (KP) CPD (squares) and asymmetric CH ₂ stretching mode peak IR absorbance (circles) vs. chain length for [HS(CH ₂) _{<i>n</i>} CH ₃] SAMs on semi-insulating GaAs(001).	121
Figure 5.1(b). CPD for SAMS as per (a) on heavily Si-doped (<i>n</i> ⁺ -type) GaAs.	121
Figure 5.2. C-H stretching mode IR spectra in transmission of <i>n</i> 15-SAM before and after thermal disordering in 55°C isopropanol (IPA).	122
Figure 5.3. XPS core level As 3d spectra at 0° ToA from etched but untreated GaAs (left) and from GaAs prepared with <i>n</i> 15-SAM (right).	123
Figure 5.4. Generalized band diagram of the XPS measurement in Figure 5.3 showing a reduction of the electron affinity (EA) associated with the surface dipole moments of the SAM (arrows) that result in an increase of the core level (CL) energies.	124
Figure 5.5. XPS core level S 2p / Ga 3s spectra of <i>n</i> 15-SAM before (left) and after thermal disordering (right).	125
5.6. Calculated DLP assuming molecular dipole values in a SAM of non-interacting / surface independent alkanethiols (squares). DLPs evaluated from CPD measurements (circles) for SAMs on semi-insulating GaAs(001).	126
Figure 5.7. Method of calculating the Lorentz local field correction.	131
Figure 5.8. Relative IR absorbance of the asymmetric C-H stretching mode of methylene in <i>n</i> -alkanethiol SAMs on Au (squares) and GaAs(001) (circles) vs. the SAM DLP.	133
Figure 5.9. XPS As 3d core level and valence band regions of semi-insulating GaAs for samples: (circles) passivated with <i>n</i> 15-SAM, and (triangles) etched only with reoxidization.	135

Figure 5.10. XPS spectra: (a) Au 4f peaks labeled with spin-orbit branching, and (b) the O 1s region including spectra following passivation with <i>n</i> 15-SAM (lower series) and from the etched and reoxidized GaAs reference surface (upper series), shifted vertically for clarity.	135
Figure 5.11. Energy level diagram illustrating the XPS binding energy referencing used to determine the surface FL position above the VBE	136
Figure 5.12. (a) Ionized charge centre concentrations for the EL2 donor (solid) and carbon acceptor (dotted) defect levels in undoped semi-insulating GaAs.	139
Figure 6.1. Kelvin Probe SPV measurements on: (a) semi-insulating GaAs; etched only (solid), as prepared with <i>n</i> 15-SAM (dash-dot).	144
Figure 6.2. Schematic comparison of the AUDM-based surface Fermi level (FL) position in Ga-rich n-doped and semi-insulating GaAs.	146
Figure 6.3. Surface FL pinning places an upper boundary on the surface charge density as the energy density of surface states approaches the discrete limit.	147
Figure 6.4. SPV data (circles) and model results (solid lines) for semi-insulating GaAs before and after passivation with <i>n</i> 15-SAM.	149
Figure 6.5. SPV data and model results for n^+ -GaAs before and after passivation with <i>n</i> 15-SAM.	150
Figure 6.6. Schematic of the electric field profiles for: i) the built-in field of the SCR, partially screened under illumination, and ii) the penetrating interfacial dipole layer potential.	152
Figure 6.7. Relative PL efficiency as a function of the excitation power for semi-insulating GaAs before (circles) and after (squares) preparation with <i>n</i> 15-SAM.	154
Figure 6.8. Calculated PL enhancement ratio for semi-insulating GaAs following passivation with <i>n</i> 15-SAMs as a function of the nominal SRV (<i>S</i>).	157
Figure 6.9. Excess minority carrier density depth profile calculated from the transport equation for semi-insulating GaAs in the low-injection regime.	158
Figure 6.10. Calculated PL enhancement ratio for semi-insulating GaAs following passivation with <i>n</i> 15-SAMs as a function of the nominal SRV (<i>S</i>), based on the transport equation.	160
Figure 6.11. Variation of <i>in situ</i> PL as the pH of ethanol solvent is modified from pH 7 for neutral ethanol (pH ₀) to pH 11 by the addition of ammonium hydroxide (pH ⁺) and to pH 4 by the addition of acetic acid (pH ⁻).	163

LIST of TABLES

TABLE 1.1. General classifications of biosensors based on transduction mechanism.	3
TABLE 2.1. Photoemission analysis of GaAs(001) passivated with organic thiols: survey of literature results.	26
TABLE 3.1. Component assignments, specifications and atomic percentages from XPS spectra corresponding to the decompositions in Figure 3.4. Etched only GaAs.	78
TABLE 3.2. Component assignments, specifications and atomic percentages from XPS spectra corresponding to the decompositions in Figure 3.7. HDT-SAM GaAs.	83
TABLE 3.3. Surface sensitivity analysis for HDT-SAM GaAs based on Equation 2.8.	86
TABLE 4.1. Assignment of C-H modal parameters and scaling indicator for the spectral components of $[\text{HS}(\text{CH}_2)_n\text{CH}_3]$ SAMs on GaAs(001).	99
TABLE 5.1. Correspondence of the IR absorbance and DLP in $[\text{HS}(\text{CH}_2)_n\text{CH}_3]$ SAMs on semi-insulating GaAs(001).	128
TABLE 5.2. Evaluation of the VBE referenced surface Fermi level in semi-insulating and n^+ -doped GaAs(001) passivated with $[\text{HS}(\text{CH}_2)_{15}\text{CH}_3]$ SAMs.	137
TABLE 6.1. GaAs parameters for calculation of Equation 6.3.	148
TABLE 6.2. PL enhancement ratio of semi-insulating GaAs(001) following preparation with n15-SAMs.	155

ACRONYMS

a.u.	arbitrary units
aq	aqueous
ARXPS	angle-resolved XPS
ATA	amine-terminated alkanethiol
ATP	adenosine triphosphate
AUDM	advanced unified defect model
C/N	charge neutralizer
CB(E)	conduction band (edge)
CL	core level
COMFE	cooperative molecular field effect
CPD	contact potential difference
cps	counts per second
DDT	dodecanethiol
DIGS	disorder induced gap state
DLP	dipole layer potential
DNA	deoxyribonucleic acid
EA	electron affinity
FL	Fermi level
FRET	fluorescence resonance energy transfer
GIXRD	grazing incidence X-ray diffraction
HDT	hexadecanethiol
HEMT	high electron mobility transistor
HOMO	highest occupied molecular orbital
IMFP	inelastic mean free path
IPA	isopropanol
IR	infrared
ISFET	ion-selective field-effect transistor
KE	kinetic energy
KP	Kelvin probe
L/RHS	left/right hand side
LUMO	lowest unoccupied molecular orbital
MEMS	micro-electrical mechanical systems
MMS	metal-molecular-semiconductor
MOCSER	molecular controlled semiconductor resistor
MOSFET	metal-oxide-semiconductor field-effect transistor
NEXAFS	near edge X-ray absorption fine structure
NIST	National Institute of Standards and Technology
ODT	octadecanethiol
PL	photoluminescence

QCM	quartz crystal micro-balance
RAIRS	reflection absorption infrared spectroscopy
RSF	relative sensitivity factor
SAM	self-assembled monolayer
SCR	space charge region
SEIRA	surface enhanced infrared absorption
SERS	surface enhanced Raman scattering
SPR	surface plasmon resonance
SPV	surface photovoltage
SRV	surface recombination velocity
ToA	take-off angle
ToF-SIMS	time-of-flight secondary ion-mass spectroscopy
UPS	ultra-violet photoelectron spectroscopy
VB(E)	valence band (edge)
VL	vacuum level
XPS	X-ray photoelectron spectroscopy

CHAPTER 1:

INTRODUCTION

The research described in this thesis is focused on the investigation of various electronic and optical phenomena characteristic of the GaAs(001) interface with *n*-alkanethiol self-assembled monolayers (SAMs). Although the results may be considered independently, they complement a broader effort that relates to the development of a photonic biosensor based on intensity modulated photoluminescence (PL) from suitably prepared III-V semiconductor bulk or nanostructured surfaces. It is within this general context the findings of this study are discussed. In addition, conclusions relevant to other semiconductor technologies or that refer to the fundamental material science will be highlighted where appropriate.

In this chapter, the elementary concepts of biosensing and its associated surface chemistry are introduced, which leads to a more specific framework within the context of semiconductor based biosensor designs. A discussion of the research questions to be addressed follows, from which the project objectives are then stated. The chapter concludes with a summary of the original contributions made and a document plan of how the overall paper will be presented.

1.1 Fundamentals of Biosensing

In general terms, the operation of a biosensor device is described by two processes: i) the recognition and immobilization of specific analyte by a biofunctional element, and ii) the detection of characteristic signals by means of a unique transduction mechanism when the device is subsequently probed. Ideally, the signals will relate to the quantity of analyte presented to the sensor and will reflect a high degree of both specificity and sensitivity. Specificity manifests by virtue of the functional nature of the biochemical recognition elements used to immobilize the analyte, i.e., the sensor's ability to distinguish and select for a specific biomolecular species of interest. Sensitivity is a function of the efficacy inherent in the recognition and transduction processes, and is comprised of factors including the signal noise level and the stability or functional integrity of the sensing interface in the environment of operation. In addition, sensor linearity and low response times are practical requirements.

Figure 1.1 is a schematic diagram illustrating the fundamental biosensing concept. Shown are three common examples based on differentiated means of biochemical recognition.

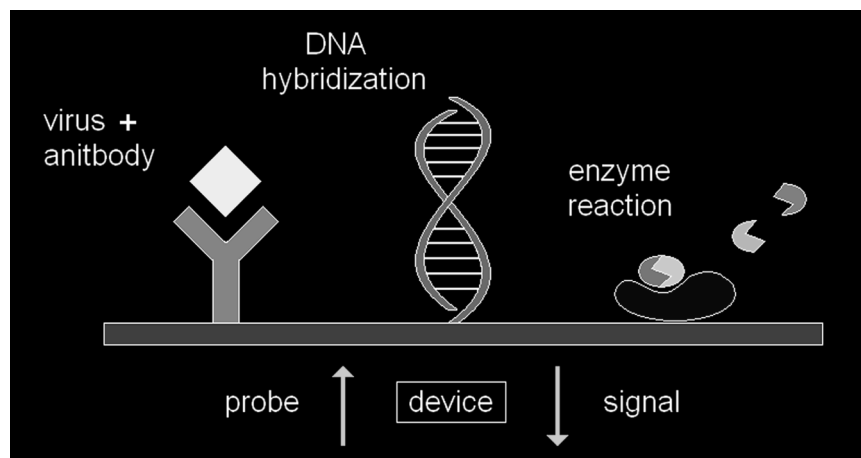


Figure 1.1. Generalization of biosensing concept. The immobilization of specific analyte results in a characteristic signal when the sensing device is subsequently probed. Three common mechanisms of biochemical recognition are shown.

Sensitivity is a critical issue for biosensors, especially those based on antibody-antigen coupling, the reason being that the binding affinity of an antibody is derived in large part from its proteomic structure [Prasad, 2003]. Therefore, if the functional conformation of surface-prepared antibodies becomes compromised, the sensing layer will operate less effectively. Biosensors based on DNA technology are particularly well-suited to illustrate the concept of specificity, which derives from the requirement for base-pair sequence matching between target and probe strands [Zhai *et al.*, 1997]. In order to illustrate the concept of transduction, a useful example is the glucose sensor, which is based on the principle of enzyme reaction. The input components glucose + O₂ are converted to gluconic acid + H₂O₂ by the enzymatic catalyst glucose oxidase. Subsequently, the H₂O₂ product is reduced at the sensor cathode resulting in a measured current, or similarly, the consumption of O₂ is monitored. This transduction mechanism is referred to as amperometric. Amperometric devices based on enzymatic reactions were some of the first biosensors developed, initially reported several decades ago [Clark and Lyons, 1962].

Since then, although many attractive approaches to biosensing have been proposed in the academic and patent literature, commercial success has been daunted by cost and challenged by increases in the effectiveness of high-throughput analytical chemistry [Luong *et al.*, 2008]. Today, the biosensor market remains largely (~ 85%) comprised of glucose sensor variants

[Newman and Turner, 2005]. This level of market dominance is a consequence of the relative maturity of this technology, its perpetual need as a therapeutic diagnostic, and the increasing prevalence of lifestyle associated type 2 diabetes. Developing specialty applications hold the promise of sensing tools for point-of-care medical diagnostics, immunoassay and genomics research, defence and environmental monitoring, and use in the food, drug and agriculture industries. These opportunities have spawned a boom in biosensor research within the past several decades, inviting contributions from several facets of biochemistry, physics, engineering, and more recently, the field of nanoscaled materials.

The classification of biosensors is usually made according to the transduction mechanism through which they operate. Some common examples are categorized in Table 1.1.

TABLE 1.1. General classifications of biosensors based on transduction mechanism.

biosensor classification	transduction mechanism	technology examples
electrochemical	amperometric / voltammetric	<i>in vivo</i> electrode
optical A	spectroscopic	FRET / SERS
optical B	mode dispersion	SPR / waveguide
thermometric	heat of reaction	enzyme calorimetry
stress / mass increase	piezoresistive / piezoelectric	MEMS / QCM
semiconductor A	channel conductance	BioFET
semiconductor B	photoluminescence	near-surface quantum dot

FRET - fluorescence resonance energy transfer; SERS - surface enhanced Raman scattering;
 SPR - surface plasmon resonance; MEMS - micro-electro-mechanical systems;
 QCM - quartz crystal microbalance; BioFET - biosensing field-effect transistor

Although not an exhaustive list, Table 1.1 serves to locate a PL-based biosensing device within the general landscape of sensor technology. Technological examples of the various transduction mechanisms are included in column 3. For instance, electrochemical sensors, in addition to their ubiquitous role in glucose detection, have broad reaching clinical relevance in the areas of *in vivo* blood gas and electrolyte monitoring, despite ongoing biocompatibility issues [Shin and Schoenfisch, 2006]. Optical spectroscopic detection approaches often utilize donor/acceptor energy transfer processes in order to take advantage of proximity modulated fluorescence, made evident, e.g., in the DNA molecular beacon concept [Ortiz *et al.*, 1998]. The intensity of fluorescence labels is also dependent on the local environment, which can be

affected by binding-induced conformational changes in the proteins to which the labels are attached [Watkins and Bright, 1998]. DNA microarray or ‘gene-chip’ technology provides an example of multiplexed spectroscopic analysis that has reached commercial viability. For example, the products offered by Affymetrix Inc. incorporate probe-target DNA hybridization detected by fluorescent labeling, with probes arranged in a two-dimensional (2D) array on a quartz substrate allowing a high degree of parallel analysis. Optical mode dispersive technologies, such as surface plasmon resonance imaging and waveguide arrays, are expected to become competitive once their potential capacity for multiplexed analysis can be leveraged. In a recent example of this type, silicon photonic wire waveguide technology was demonstrated in a cascaded configuration that uses only one optical input to service a multiplexed array of spiral Mach-Zender interferometers, each of which may be functionalized with a different recognition element for *in situ* and parallel processing within a single microfluidic channel [Densmore *et al.*, 2009]. Thermometric sensors are based on calorimetry and are usually developed around an enzyme catalyst. These devices will advance towards miniaturization with the realization of multi-analyte, temperature stabilized microfluidic systems [Ramanathan and Danielsson, 2001]. Sensors that exploit mechanical properties such as differential stress or mass increases utilize the resulting change in substrate conductance or resonant frequency in order to render the detection signal. Cantilevered MEMS [Raiteri *et al.*, 2001], or piezoelectric QCMs [Collings and Caruso, 1997], are common examples of this type.

Discussion of the semiconductor-based varieties will be deferred until Section 1.3. For now it will suffice to categorize them as channel conductance or PL types. To reiterate, the latter approach is the broad topic into which the present work fits. However, since both types substantially depend on the characteristics of the semiconductor interface with molecular sensing architectures, this work bears relevance to the conductance approach as well.

1.2 Surface Chemistry and Molecular Self-Assembly

Common among the biosensor classifications is the need to develop appropriate chemistries that can deliver the required functionality. Surface-based approaches are especially challenging in this regard because of the orientational constraint that is imposed on the molecular order by the semi-infinite plane. Factors like surface coverage, surface

hydrophobicity, non-specific binding, and the presentation of conformationally correct functional sites at the required density are practical considerations that, ultimately, must be addressed. Molecular self-assembly is a ubiquitous and enabling technology that has driven much of the advancement in this critical area [Wink *et al.*, 1997]. Self-assembly processes derive spontaneous molecular order from weak (non-covalent) molecular interactions, such as van der Waals forces or hydrogen bonding; the self-assembled system eventually reaches thermodynamic equilibrium with a structure that is uniquely determined by its size, geometry and number of constituent molecules [Halley and Winkler, 2008]. Note that the equilibrium condition limits the continued aggregation of molecular material. The self-assembly process is also reversible. Two familiar examples of self-assembly found in nature are the phospholipid bilayers that comprise cell membranes and the double-helix arrangement of nucleotides in DNA. In the cell membrane, the hydrophobic effect drives the assembly mechanism, whereas in DNA, the structure is formed by hydrogen bonding. From a practical standpoint, it is the spontaneous nature of self-assembly that makes it attractive for bottom-up approaches to nanotechnology. Self-assembly may even proceed beyond local ordering to incorporate the organization of building blocks into supramolecular assemblies. For example, advanced polyhedral structures, ranging in size from 10 - 40 nm, can be fabricated utilizing hierarchical DNA nanoassembly techniques [He *et al.*, 2008]. A relatively new approach to analyte binding similarly exploits the spontaneous organization of nucleic acid sequences into three-dimensional structures. Known as aptamers, these oligonucleotides, which are developed in an iterative selection and amplification process, have high-affinity for targeted molecules based on their conformation, with binding strength derived from hydrogen bonds or phosphate group associations [McGown *et al.*, 1995]. Immobilized in biosensing applications, for example [Kleijnung *et al.*, 1998], aptamers have the advantage of smaller size and better conformational stability with respect to antibody ligands, factors which, respectively, decrease steric hindrance and improve surface functionality.

For surface-based biosensing applications, an effective approach is to leverage the intermolecular attraction of linear alkanes (*n*-alkanes), the general class of which is described by the formula $[R^i(CH_2)_nR^j]$, where the R^{ij} are individual functional groups. Some common examples of functional alkane terminations are: SH (thiol), NH₂ (amine), OH (hydroxyl), COOH (carboxylic acid), or C-PO(OH)₂ (phosphonic acid). Long-chain *n*-alkanes are

particularly useful for biosensing applications as their intermolecular affinity is strong enough that they spontaneously form two-dimensional pseudo-crystalline monolayers, which satisfies the orientational constraint imposed by the surface. An analogous system for the study of the resulting molecular order is the Langmuir monolayer, which is formed by amphiphilic lipids on liquid surfaces [Kaganer *et al.*, 1999]. If one of the terminal functional groups is suitably reactive, then the monolayer can be covalently attached to the surface forming a SAM. Chemisorption is the term used to differentiate covalently bonded surface adsorption from physisorption, which is based on weaker physical attraction. The chemisorption approach to monolayer self-assembly has been adopted in a number of material systems. The model example is that of $[\text{HS}(\text{CH}_2)_n\text{CH}_3]$ alkanethiol SAMs formed on the Au(111) crystallographic surface. In this case, thiol functional groups react with the Au surface atoms to form covalent S-Au bonds. The resulting organization of the SAM is highly ordered, with an alkane chain tilt orientation of about 25° - 30° from vertical and a surface cell, in Woods notation, of $(\sqrt{3} \times \sqrt{3})R30^\circ$ with respect to the Au(111) lattice [Dubois and Nuzzo, 1992].

When the terminal groups of the SAM are also of the functional type, they can be used to interact directly with specific analyte in a detection scheme, or can be used to anchor higher order recognition elements to the surface. Two illustrative examples of the use of SAMs in biosensor architectures are shown below in Figures 1.2 and 1.3.

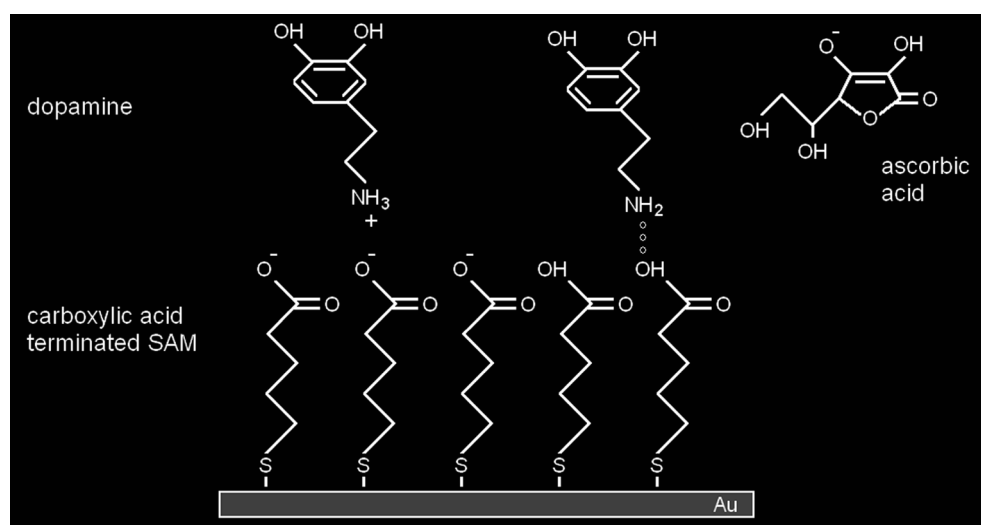


Figure 1.2. COOH-terminated alkanethiol SAM used for dopamine recognition via electrostatic discrimination on a gold voltammetric electrode. Acid dissociation constants determine the charged molar fractions. Hydrogen bonds may also appear.

In Figure 1.2, a carboxylic acid terminated alkanethiol SAM discriminates dopamine, an important neurotransmitter, from ascorbic acid present in the extracellular fluid of the central nervous system [Malem and Mandler, 1993]. Due to their respective acid dissociation constants, the carboxylic acid and ascorbic acid are negatively charged at neutral pH, whereas dopamine carries a positive charge. However, both dopamine and ascorbic acid are electrochemically oxidized at voltammetric electrodes significantly impairing detection specificity. The electrostatic interactions discriminate by selectively presenting the dopamine to the SAM functionalized surface at lower oxidation potentials. In addition, Figure 1.2 depicts that hydrogen bonding between the amine and carboxylic functional groups is a possible second mode of affinity [Chai and Cahen, 2002].

In an example of higher order functionalization, alkanethiol-based SAMs incorporating a biotin functional group are commonly used in order to couple with streptavidin proteins. Subsequently, this protein may be used as a bridge to other biotinylated species, such as a biotinylated antibody or DNA probe strand, given there are four biotin-available binding sites per streptavidin. In practice, a mixed monolayer is often formed using the two molecule types shown in Figure 1.3.

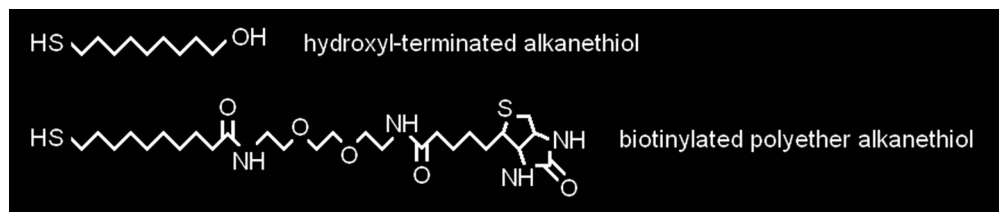


Figure 1.3. OH-terminated and biotinylated polyether thiols form mixed molecule SAMs for streptavidin immobilization. OH-thiols provide spacing and hydrophilic repulsion against the polyether (C-O-C)_n sections resulting in biotin stand-off and reduced steric hindrance.

In this scheme, the shorter (alkane only) molecules act to space out the biotin coupling sites and their hydroxyl termination provides repulsive forces against the hydrophilic polyether part of the longer biotinylated molecule. These properties serve to provide an effective stand-off for the biotin functional group so they may couple to streptavidin with less steric hindrance [Mittler-Neher *et al.*, 1995]. Surface stand-off also helps avoid protein denaturation, i.e., the loss of reactivity stemming from a loss of functional conformation. In the proposed PL biosensor, an alkanethiol-based SAM approach to the functional surface chemistry has been adopted. For example, it was recently demonstrated that influenza A virus could be

specifically immobilized on the GaAs(001) surface using biotinylated polyethylene glycol alkanethiols in a mixed monolayer approach [Duplan *et al.*, 2009].

In addition to the list of practical considerations stated earlier, a primary criterion for effective performance is that the SAMs be compatible with the transduction mechanism. In fact, SAMs have the potential to play an integral role in the transduction mechanism itself. Consequently, it is important to understand their fundamental physical properties. It is only through detailed characterization that such foundational knowledge can be obtained and that new insights may be brought to bear on applications development. This knowledge is required in order to understand the limitations of a particular approach, or to help validate computational models, which ultimately supports more advanced system analysis. In order to develop a specific framework within which the present research may be developed, this investigation focuses on the first order interface, i.e., the physical properties of alkanethiol SAMs and the nature of their coupling to the GaAs(001) surface. Results from more advanced surface chemistry will be discussed only briefly.

Not only do SAMs have relevance within the biosensing context, they have also been adopted for use in the investigation of junction-based molecular electronic applications. In particular, the electronic band alignment and transport characteristics of alkane SAMs are of fundamental importance, which are often studied using metal-molecule-semiconductor (MMS) heterostructures in which the SAMs comprise the insulating barrier. For example, analysis of current-voltage data indicates that tunneling dominates the transport characteristics at high forward biases [Lodha and Janes, 2006; Nesher *et al.*, 2006]. Some general comments on the relevance of the present work to the field of molecular electronics will also be made.

1.3 Semiconductor-based Biosensing

1.3.1 Channel Conductance Methods

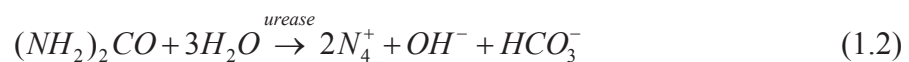
Semiconductor-based sensing devices in the electronic domain are typically designed around the field-effect transistor. Often referred to as BioFETs, or ChemFETs, they derive from the ion-selective FET (ISFET), first developed by Bergveld [Bergveld, 1970]. The operating principle of an ISFET differs little from that of the standard MOSFET, e.g., the gate-insulated, n-channel type, where the gate potential controls the drain current (I_D), i.e., the channel conductance, by varying the charge density in an inversion region below the gate.

Above the threshold voltage (V_{th}) and below saturation, the FET device is ohmic and responds linearly to the gate potential [Streetman and Banerjee, 1999]. In the ISFET, the metal gate is replaced with an electrolytic analyte solution, into which a reference electrode is submerged and is held at some fixed gate potential (V_G) with respect to the semiconductor ground. Protonation of OH-groups on the surface of the gate insulator, typically the semiconductor oxide, changes the surface potential (ψ) at the insulator-electrolyte interface in response to solution pH [Bergveld, 2003a]. The change in surface potential shifts the flat-band voltage, which is the contact potential between the semiconductor and reference electrode in the electrolyte. The ISFET threshold voltage, which depends on the flat-band voltage, is thus directly controlled by the surface potential. Since the gate voltage is held constant, a second means to linearly control the drain current is obtained. The governing ISFET parameters are summarized in the following,

$$I_D \propto [V_G - V_{th}(\psi)] V_D + constant \quad (1.1)$$

where V_D is the applied drain voltage. In practice, a feedback circuit can be used to maintain a constant drain current by modulating the gate voltage, which then serves as the sensor output [Barbaro *et al.*, 1992], and maintains the device within the ohmic regime.

In the BioFET or ChemFET, the surface of the gate insulator is functionalized with a biologically or chemically selective agent, usually imbedded in a semi-permeable membrane. The difference with respect to the ISFET is that the surface potential (i.e., threshold voltage) offset at the gate is now effected by means of pH variation in the sensing layer produced by localized reactions. For illustration purposes, consider the urea sensor, which operates using the following enzymatic reaction mediated by membrane immobilized urease,



producing ammonia, hydroxyl and carboxyl ions. In an ISFET sensor, the relative dissociation of these ionic species determines the pH, and consequently, the charge density at the sensing interface varies [Bergveld, 2003b]. In the actual device, the differential voltage with respect to a reference arm FET can be used in a feedback mechanism to maintain a constant pH through the use of coulombic compensation [van der Schoot and Bergveld, 1987]. The detailed

operational considerations of BioFETs designed for the sensing of charged macro-biomolecules in electrolyte solutions has also been reviewed [Landheer *et al.*, 2005].

Another method of sensing that utilizes FET junctions contrasts with the ion-selective approach in that it is net charge neutral and requires no referencing electrode. Frequently referred to as the Molecular Controlled Semiconductor Resistor (MOCSER), these devices exploit dipole moment variations in a molecular layer prepared on, e.g., the gate insulator [Rudich *et al.*, 2000] or, a back-gated semiconductor channel layer [He *et al.*, 2006]. GaAs-based high electron mobility transistor (HEMT) designs have been also been demonstrated [Wu *et al.*, 2001], as illustrated in Figure 1.4. In these designs, differences in the source-drain current are realized by adsorbate-induced effects on the channel layer potential.

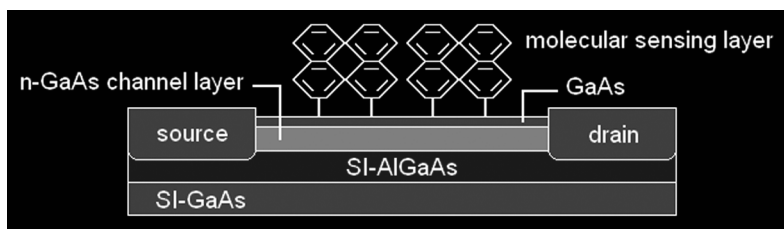


Figure 1.4. HEMT design MOCSER with porphyrin-based SAM used for the detection of nitric oxide in physiological aqueous solutions.

Transduction arises from dipole moment variations of the surface potential, in contrast to the monopole derived field-effect of the ISFET. A MOCSER response can be initiated through the ordered adsorption of polar molecules [He *et al.*, 2006; Song and Lu, 2006], or the induction of dipole moments in polarizable SAMs [Wu *et al.*, 2001]. However, the actual mechanism of transduction has several facets to consider [Natan *et al.*, 2007]. One explanation refers to a Cooperative Molecular Field Effect (COMFE) in which it is suggested that charge transfer can be effected between an ordered 2D molecular layer and its substrate [Cahen *et al.*, 2005]. This charge transfer is thought to result from the establishment of a new surface equilibrium upon the adsorption of specific analyte. Central to the COMFE argument is that the resulting charge transfer minimizes dipole-dipole repulsive forces that act in an ordered 2D molecular array. For example, the COMFE was used to explain current variations through a Si-based MOCSER device, reported in work by Rudich *et al.* [Rudich *et al.*, 2000], where the device was prepared with (methyl-terminated) octadecyl trichlorosilane SAMs and observed under various environmental partial pressures of O₂ and H₂O. The current variations

were opposite in sign, and were suggested by Cahen *et al.* to be linked to a COMFE reversal of dipole moments in the SAM following the physical adsorption of these two species.

Clearly, the surface potential plays an important role in the transduction mechanism of FET-based sensors. This statement generalizes to include the PL-based sensors, as shall become clear in the following section. In this thesis, surface and interface dipoles associated with alkanethiol SAMs have specific implications in terms of the electro-optic response of the GaAs surface. Before proceeding to a more detailed discussion of the research objectives, however, the PL-based approach to sensing must also be given a brief introduction.

1.3.2 Photoluminescence Methods

In practical terms, PL describes the process of radiative recombination in semiconductors following the absorption of supra band-gap energy photons. Optically excited conduction band electrons and valence band holes, once thermalized to their respective band edges, spontaneously transition to the ground state releasing photons characteristic of the band-gap energy. In direct band-gap material, the Bloch wavevector is conserved without phonon-assistance and, therefore, the radiative transition is more efficient. By the same token, the absorption of optical excitation is also made efficient, and consequently, electron-hole pair generation occurs within a thin near-surface layer typically less than a few hundred nanometers thick. Since the optical absorption length is much less than the diffusion length for minority carriers, they reach the surface within their radiative decay lifetime and return to the ground state through trap-assisted non-radiative transitions, as illustrated in Figure 1.5.

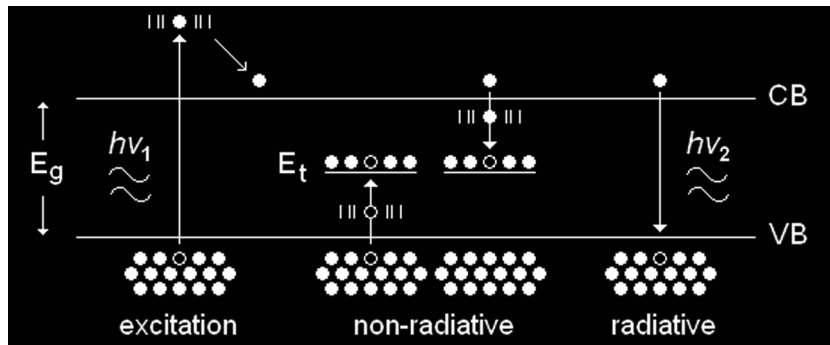


Figure 1.5. Recombination processes in GaAs. Optical excitation generates conduction band (CB) electrons, which relax to the CB-edge by phonon release ($||| \bullet |||$). Subsequent non-radiative relaxations result in carrier pair annihilation at the trap level (E_t) by hole and electron capture. Radiative processes involve direct transitions to the valence band (VB) releasing photons with energy ($h\nu_2 < h\nu_1$) corresponding to the band-gap (E_g).

Consequently, the PL intensity can be highly sensitive to surface conditions that dictate the parameters affecting the rate of surface recombination. Among these parameters list the number density and energy positions of the defect states though which the non-radiative transitions occur. Their type (donor/acceptor) and occupation are also important, as are other surface potential factors that may alter the near-surface band structure. The overall recombination rate is inversely proportional to the minority carrier lifetime (τ), which consists of radiative and non-radiative terms in the reciprocal sum [Yacobi, 2003],

$$\frac{1}{\tau} = \frac{1}{\tau_r} + \frac{1}{\tau_{nr}} \quad (1.3)$$

Two convenient simplifications may be introduced: i) the radiative term is considered an intrinsic bulk quantity, and ii) the non-radiative term is assumed to be dominated by surface conditions. The rates associated with these lifetime terms may be approximated by,

$$r_r = \tau_r^{-1} \approx \beta (n_o + \Delta n) = \beta n \quad (1.4)$$

$$r_{nr} = \tau_{nr}^{-1} = \sigma_p \nu_{th,p} N_t \quad (1.5)$$

for n-doped material specifically. Similar equations for p-doped material may be written directly. In Equation 1.4, n_o is the equilibrium majority carrier (electron) concentration, Δn is the photo-generated excess concentration due to electron-hole pair generation ($\Delta n = \Delta p$), and β is the radiative rate constant for GaAs, applicable under non-degenerate injection [Lambert *et al.*, 1990]. Equation 1.5 is based on Shockley-Reed-Hall recombination theory [Shockley and Read, 1952; Hall, 1952], simplified for the limiting conditions of low level photo-injection and defect energy positions located near mid-gap (i.e., deep levels), where σ_p is the minority carrier capture cross-section, $\nu_{th,p}$ is the minority carrier thermal velocity, and N_t is the trap density (see Chapter 2). The relative yield of PL intensity can be quantified in terms of these rates by defining an internal quantum efficiency (γ_{PL}) [Yacobi, 2003],

$$\gamma_{PL} = \frac{r_r}{r_r + r_{nr}} \quad (1.6)$$

which is, in essence, the governing equation behind the transduction mechanism in an intensity-based PL sensor. Specifically, adsorbate induced changes to either the radiative or non-radiative rate will alter the relative PL yield, which serves as the appropriate metric.

In accordance with the assumption that surface recombination dominates the non-radiative rate, Equation 1.5 may be explicitly defined as a surface quantity referred to as the surface recombination velocity (SRV). Variation of the SRV results in changes to the PL yield. For example, adsorbate-induced reductions of either σ_p or N_t lead to decreases in the non-radiative rate and, consequently, to the enhancement of γ_{PL} . In addition to SRV moderated effects, the depth-integrated radiative emission may be controlled via surface conditions. For example, the near-surface electric field associated with the depletion region typical of n-type surfaces tends to separate photo-generated carriers resulting in a so-called PL ‘dead-layer’ where the radiative rate is significantly decreased [Wittry, 1967]. Consequently, adsorbate-induced modifications of the depletion region directly affect the PL yield when the depth of the dead-layer region is changed. Both the SRV and dead-layer mechanisms are important to the operation of a PL-based sensor designed on the single-crystal wafer. A schematic illustration of the near-surface band-bending typical of most semiconductor surfaces is provided in Figure 1.6 (top), and includes the associated charge densities (bottom) showing the surface trapped charge and space charge that characterize the depletion region.

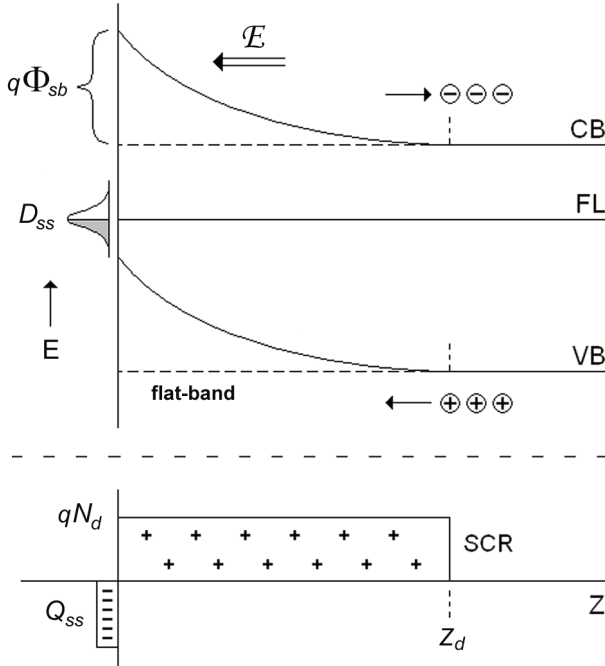


Figure 1.6. Near-surface band structure of n-type GaAs in depletion. Symbols: space charge density (qN_d), space charge region (SCR), depletion depth (z_d), surface trapped charge ($-$), ionized donors ($+$), surface charge density (Q_{ss}), Fermi level energy (FL), conduction/valence band-edges (CBE/VBE), surface barrier height ($q\Phi_{sb}$), built-in electric field (\mathcal{E}) and energy density of surface acceptor states (D_{ss}). Photo-generated excess minority carriers (\oplus) are driven into the SCR by drift and diffusion processes contributing to the non-radiative SRV and a reduction of the radiative recombination rate.

Historically, PL-based sensors have operated using transducer films or direct adsorption, and have been extended to incorporate a wide variety of gas-sensor designs by the group of A.B. Ellis, particularly [Seker *et al.*, 2000]. Transducer films are a general class of analyte sensitive surface treatments designed to affect the necessary surface conditions responsible for PL intensity variation. An early example was based on the PL response of a n-doped Pd-CdS_xSe_{1-x} Schottky diode to adsorbed H₂ [Carpenter *et al.*, 1985]. Hydrogen gas is known to lower the work function of Pd, which, at the n-type junction, establishes a new thermal equilibrium (Fermi level alignment) by decreasing the semiconductor band-bending. By virtue of the dead-layer model, this decrease in the barrier height corresponded to a PL increase. A later example of the transducer type exploited the gas-induced oxidation of a silo-ferrocene functionalized n-GaAs substrate [Van Ryswyk and Ellis, 1986]. Iodine or bromine in a nitrogen gas mixture was used to increase the oxidation state of the ferrocene, resulting in PL quenching, while exposure to hydrazine gas (N₂H₄) reversed the effect, returning the PL to its original intensity. The operation of this sensor was also attributed to the dead-layer model.

In contrast to the transducer film type, direct adsorption sensing refers to the case where analyte adsorbs directly on the semiconductor surface via physical attraction (physisorption), which can be characterized by Langmuir kinetics. In this mode, both PL enhancement and quenching have been attributed to the formation of surface-adsorbate complexes, specifically, those derived from Lewis acid-base chemistry, commonly referred to as adducts. PL enhancement is correlated to the basicity of adduct-forming adsorbates, while acidity correlates with quenching [Luebker *et al.*, 1991]. For example, the lone-pair electron donating potential of Lewis bases, such as the class of gaseous amines, has been suggested to account for PL enhancement in the dead-layer model [Meyer *et al.*, 1988]. In this case, surface trapped electrons are thought to be displaced, resulting in a contraction of the depletion region. However, SRV related phenomena, such as an increase in the minority carrier lifetime, have also been measured depending on the surface preparation [Leung *et al.*, 1990].

In summary, the PL method of semiconductor surface-based sensing relies on analyte-induced variation of the conditions responsible for the overall surface electronic profile. Specifically, variation of the surface potential, including static charge, dipolar or surface complex related effects, can modify the number density, energy distribution, occupation and/or trapping efficiency of surface state defects. A change in these parameters

results in PL yield enhancement or quenching by virtue of the (non-radiative) SRV and (radiative) dead-layer mechanisms. Ideally, designing for the successful operation of a PL biosensor requires a detailed understanding of these mechanisms, the limitations they impose, and how to address them via changes in the surface potential in order to realize a useful dynamic range in a controlled manner. Isolating the effects of these two contributing factors is important to this understanding and factors significantly into the present research.

1.4 Motivations and Research Objectives

In the preceding discussions, the importance of surface chemistry and molecular self-assembly to the operation of biosensors was introduced and the surface potential was highlighted as a critical design parameter in semiconductor-based systems with particular emphasis on the PL sensing method. In this section, questions relevant to the incorporation of molecular self-assembly within the PL approach are defined in order to establish the research objectives. The surface potential and its associated electro-optic effects specific to the alkanethiol SAM interface with the GaAs(001) surface comprise the overall context. This material system represents the prototypical SAM-semiconductor interface and was chosen, in part, in order to leverage the body of literature that reports on it from the perspective of the fundamental material science. Although this system does not incorporate a more sophisticated biosensing architecture, it represents a possible first order molecular architecture in such a design, and further knowledge of it will inform the development process. Consequently, the central hypothesis of this thesis questions how the electro-optic properties of the SAM-GaAs interface derives from its physical structure, and what significance is there for the biosensing mechanisms. Accordingly, this work is categorized into the following three subsections.

1.4.1 Structural and Chemical Characterization

The first category relates to a characterization of the basic structural and chemical parameters. These are important to verify before examining the more detailed electro-optic data. For example, the process of SAM formation requires an etching step in order to remove the native oxide. This promotes coupling of the reactive thiol group to the exposed crystal face through covalent bonding. The resulting GaAs stoichiometry is important to an understanding of the surface state, which has implications with respect to the surface barrier height at the SAM-semiconductor interface. Evidence of physico-chemical signatures

characteristic of thiol chemisorption and molecular ordering of the SAM must also be verified. These speak to the overall structure, coverage and stability of the interface.

1.4.2 Electronic Properties of the SAM

The surface potential introduced to the GaAs interface following SAM formation is a fundamental electronic property with potential implications for the PL intensity via SAM interaction with the GaAs interface states. Therefore, knowledge of the surface potential must first be obtained. Since the SAM is charge neutral and consists of molecules retaining a permanent dipole moment, changes to the external work function are expected, i.e., changes to the vacuum level energy. In addition, the passivation of surface defect states may also be expected, which can, e.g., reduce the surface charge density and associated surface barrier height. This effect is quantified by changes in the surface Fermi level following SAM formation. Moreover, considering the SAM phase as distinct and in view of such theories as the COMFE, it is expected that the electronic properties of the SAM will be altered from that representative of the source material in bulk molecular form. If such a reconfiguration is manifested, it is proposed this will be reflected in changes to the optical constants of the SAM in a manner consistent with its pseudo-crystalline molecular structure.

1.4.3 Electro-Optic Response of the GaAs Interface

Following SAM formation, the passivation of PL quenching surface oxides will be apparent from the stoichiometry of the GaAs surface. Quantification of the surface Fermi level change as a result of SAM formation will be a further step towards understanding the PL response at the SAM-GaAs interface. However, one of the shortcomings of the dead-layer model is that it assumes the photo-injected electron density does not perturb the balance of charge in the equilibrium picture that it implies. As an interfacial layer in the proposed biosensor architecture, how the surface barrier of thiol-passivated GaAs reacts under steady-state photo-injection needs to be investigated. More specifically, an understanding of both the dead-layer and SRV mechanisms is required. It is proposed that thiol-induced effects will influence the near-surface band structure in a manner that is consequential with respect to sensor design. Decoupling of the SRV into its constituent factors, i.e., the capture cross-section and surface trap density, is accomplished using both experimental and modeling approaches in order to provide the necessary insight.

1.5 Structure of the Thesis

In this section, an outline of the overall document plan is presented as follows. Chapter 2 is comprised of the detailed background, in terms of both the relevant literature and theory, which informs the discussion in subsequent chapters and provides the necessary justification of the topics selected. This chapter is divided into the following parts according to the various experimental and numerical methods employed in this work:

- i) X-ray Photoelectron Spectroscopy (XPS), including angle-resolved (ARXPS) techniques, and methods used to obtain the surface Fermi level and work function,
- ii) Infrared (IR) Spectroscopy specific to the molecular ordering, SAM orientation and principal components of the SAM optical constants,
- iii) Kelvin Probe methods including the Surface Photovoltage (SPV) technique, which relate to the work function and the steady-state electronic band structure respectively,
- iv) PL methods and its quantification in terms of the radiative yield enhancement, surface recombination velocity, and power dependence.

Chapter 3 discusses the compositional stoichiometry and structural morphology at the SAM-GaAs interface, as determined by XPS, and largely consists of unpublished results. In addition, details on the method of sample preparation are provided, which are common to the work in the remaining chapters. The ARXPS technique figures prominently with respect to several aspects of the analysis.

Chapter 4 reports on the IR spectroscopy of the SAM revealing evidence for enhanced vibrational properties unique to the SAM phase [Marshall *et al.*, 2009a], from which the optical constants of the SAM are derived [Marshall *et al.*, 2009b]. In addition, *ex situ* IR spectroscopy measurements of the SAM formation dynamics help further the understanding of the self-assembly process [Kim *et al.*, 2009]. Also, a demonstration of second order surface functionalization is briefly described, specifically, the covalent coupling of biotin to amine-terminated alkanethiol SAMs [Dubowski *et al.*, 2010].

The equilibrium energy levels associated with the SAM-GaAs interface are investigated in Chapter 5. For example, the work function change resulting from the SAM's dipole contribution is quantified using XPS and Kelvin Probe methods. Interestingly, the work function change is observed to correlate with the IR absorbance according to the variation in SAM molecular length [Marshall *et al.*, 2009b]. This correlation provides further insight into

the physical basis for the observed vibrational enhancement. Also presented in this chapter are XPS results that specify the equilibrium surface Fermi level position. This allows the surface barrier height to be determined before and after SAM formation [Marshall *et al.*, 2011a], which, as mentioned, is relevant to an understanding of the passivation effect the SAMs impart to the GaAs surface.

Chapter 6 details the conclusions from SPV and PL investigations into the steady-state optical response of SAM passivated GaAs [Marshall *et al.*, 2011b]. This is significant to an understanding of the SAM-GaAs interface in the application of PL-based sensor designs.

Chapter 7 concludes the thesis with a summary of findings and perspectives on future development.

CHAPTER 2:

LITERATURE and THEORY

This chapter discusses the relevant literature and appropriate theoretical background with a view towards a more detailed justification of the research objectives, and provides a foundation for the development of following chapters. In accordance with the outline in Chapter 1, selected topics are reviewed under headings specific to the experimental techniques used to investigate the SAM-GaAs interface. Each section begins with a summary of fundamentals. Within each part, various literature results, methods, and models are described through which opportunities for new understanding are identified. The chapter summary draws these elements together and highlights the specific objectives.

2.1 X-ray Photoelectron Spectroscopy of the SAM-GaAs Interface

XPS is a surface analysis technique that relies on the principle of photoelectric emission. X-ray photons interact with atomic bound electrons, ejecting them with a characteristic kinetic energy (KE). The measured intensity of photoemission is [Vickerman, 1997],

$$I(\theta)_{i,j} = A_o \Phi_x T_{KE} L(Y)_{i,j} \Omega_{i,j} \frac{1}{\cos \theta} \int N_i(z) e^{-z/\Lambda_{KE} \cos \theta} dz \quad (2.1)$$

in units of photoelectron counts per second (cps), and is dependent on the photoelectron emission take-off angle (ToA, θ) relative to the surface normal. The subscripts i, j refer to the particular element and orbital of interest (e.g., O 1s). The prefactors are: the projected analysis area (A_o), the X-ray flux (Φ_x), the spectrometer transmittance (T_{KE}), an orbital asymmetry factor $L(Y)$ and the photoionization cross-section (Ω). The asymmetry factor accounts for the angular distribution of scattering and is dependent on the instrument-defined angle (Y) between the X-ray source and direction of photoelectron collection. The product of $L(Y)$ and Ω is known as the relative sensitivity factor (RSF). The integrand defines the contribution from a volume element of thickness dz at sample depth z having number density $N(z)$. Photoemission intensity is attenuated due to inelastic scattering that follows an

exponential decay law defined by the inelastic scattering mean free path (Λ_{KE}) and the path length ($z / \cos \theta$) through the sample. The value of Λ_{KE} is a material property found in the literature or, e.g., in the NIST database of empirically modeled results [NIST IMFP, 2000].

The kinetic energy of photoelectrons relates to their binding energy (E_B), which is the difference in the initial and final state energies of the parent atom before and after photoemission [Kolasinski, 2002],

$$E_B = E_f - E_i = h\nu - KE \quad (2.2)$$

where $h\nu$ is the excitation source X-ray photon energy. According to Koopmans' Theorem, the binding energy is equal to the negative of the orbital energy calculated in the initial state by the Hartree-Fock method (E_{HF}), such that removal of the electron does not perturb the atomic system [Koopmans, 1934]. In reality, the system is ionized and must return to the ground state, which involves relaxations (∂_R) of both the atom and the surrounding electron configuration in the solid state. Additionally, shifts of the orbital energy occur due to valence charge differences that arise from chemical bonding (∂_V). The total binding energy is,

$$E_B = -(E_{HF} + \partial_V) - \partial_R \quad (2.3)$$

where E_B is referred to the vacuum level. Other energy calibrations are discussed in a following section. When considering changes in E_B , known as chemical shifts (ΔE_B), the relaxation, i.e., a final state effect, may frequently be assumed constant [Kolasinski, 2002],

$$\Delta E_B \approx -\Delta \partial_V \quad (2.4)$$

such that ΔE_B is considered an initial state effect characteristic of the chemical environment in which the atom resides. This is determined by the relative electronegativity between bonding atoms [Brundle *et al.*, 2005], and, e.g., the Madelung potential in a crystal matrix [Kittel, 1986]. Also note that ΔE_B is more readily identified in the higher orbital spectra, since they tend to have narrower line widths, and to a first approximation, all core levels shift by the same energy [Kolasinski, 2002]. See Figure 2.1 for a pictorial description of XPS.

In structurally homogeneous samples, the relative weights of the photoelectron intensities, integrated under their respective peaks, allows one to measure the compositional

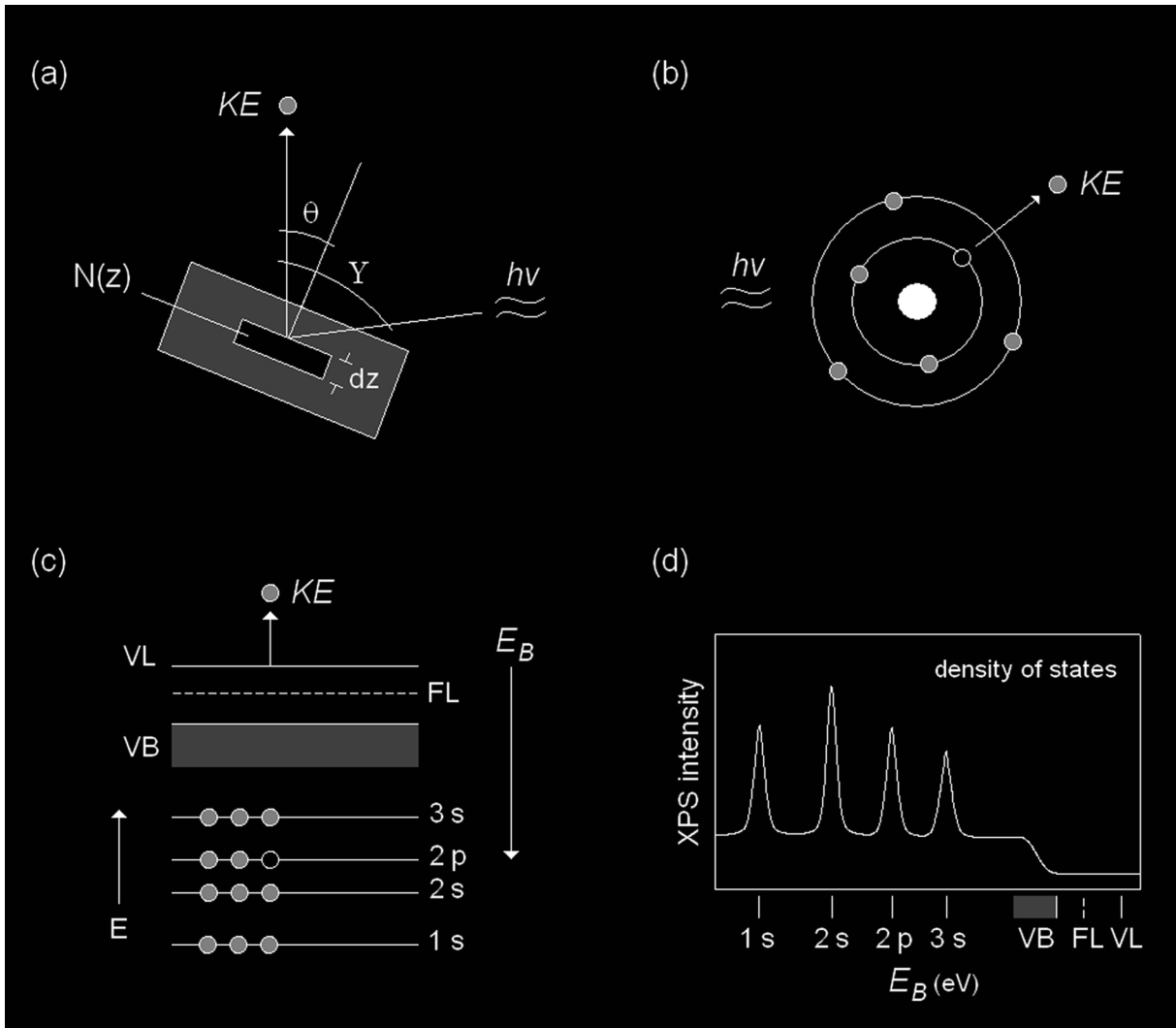


Figure 2.1. Pictorial descriptions of basic XPS theory. (a) Experimental orientations specific to Equation 2.1. (b) The photoelectric effect resulting in ejection of atomic core level electrons. (c) Energy level diagram showing relationships between the core level orbital energies (E), the valance band (VB), the Fermi level (FL), the vacuum level (VL) and the kinetic (KE) and binding energies (E_B). (d) Generic XPS spectrum showing the corresponding photoelectric emission peaks, which reflect both the density of states in the test material and the RSFs of the individual orbitals. The energy scale is referred to the VL as in (c).

stoichiometry of elements given the appropriate RSFs [Brundle *et al.*, 2005]. Integrating Equation 2.1 over depths z from 0 to ∞ and assuming a constant value for $N(z)$ gives,

$$I_{i,j} = A_o \Phi_x T_{KE} \Lambda_{KE} RSF_{i,j} N_i \quad (2.5)$$

Note that the ToA dependence cancels out for this special case. The compositional stoichiometry may now be defined by the atomic percent for the i^{th} element,

$$[A_i] = \frac{N_i}{\sum N_i} = \frac{I_{i,j} / T_{KE} \Lambda_{KE} RSF_{i,j}}{\sum I_{i,j} / T_{KE} \Lambda_{KE} RSF_{i,j}} 100\% \quad (2.6)$$

Since the T_{KE} and Λ_{KE} are KE dependent, they are specific to the E_B of each peak assigned and, therefore, must be accounted for uniquely according to the indices i, j .

The homogeneous sample described above represents an idealized situation. More typically, the region within the XPS sampling depth ($\sim 3\Lambda_{KE}$) has some heterogeneous structure and the approximation $N(z) \approx N$ is no longer valid. An overlayer of surface oxidation is a common example, but other surface chemical states and concentration gradients may arise. In such a case, Equation 2.6 represents only the apparent atomic concentration. Consequently, accurate quantitative analysis in absolute stoichiometric terms cannot be obtained without the ARXPS methods described later.

Lastly, since the sampling depth is determined by Λ_{KE} , which has KE dependence according to $\Lambda_{KE} \propto \sqrt{KE}$ for $KE > 50$ eV [Seah and Dench, 1979], low KE photoelectrons provide the most surface sensitive measurements. By virtue of Equation 2.2, this can be achieved with reduced photon energies or by examining the higher E_B spectra. Inspection of Equation 2.1 indicates a third method is realized by increasing the value of θ .

2.1.1 Surface Composition and Passivation of GaAs with Sulphides and Thiols

In this section, a review of the use of XPS for the qualitative compositional analysis of sulphide and thiol treated GaAs provides a useful segue to the topic of surface passivation. In the context of semiconductor surfaces, the term passivation is meant to convey two distinct but interrelated meanings: i) to protect the surface from reaction with its environment, usually referring to the growth of oxides, by occupation all surface dangling bonds, and ii) to render the surface more bulk-like in its electronic properties, which implies a reduction of the surface

barrier height by a lowering the surface state density. These meanings are interrelated due to the fact that surface oxides, as a dielectric layer, can hold a fixed charge that influences the surface electronic properties. Here, the discussion will be limited to the first meaning, referred to as chemical passivation. Electronic passivation is considered further below.

Chemical passivation may not always be significant on its own without the electronic effects it implies. However, when using the semiconductor surface as a platform for the construction of a biosensing molecular architecture, consideration must be given to the stability of the interface, without which the efficacy of the sensing layer would be impaired. In a biosensing architecture based on the alkanethiol SAM-GaAs interface, it is expected that the SAM will effect a chemical passivation by means of the physical barrier it provides, and by the bonds it forms with the GaAs surface through its sulphur containing thiol endgroup. At the same time, the SAM will accommodate the necessary sensing functionality. This dual purpose approach is evident in the processing schematic illustrated in Figure 2.2.

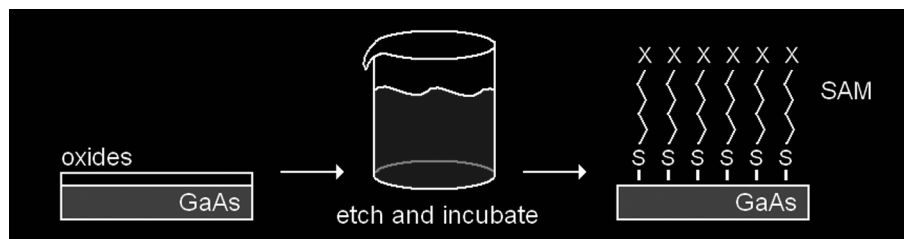


Figure 2.2. Chemical passivation of GaAs surface with a bio-functional alkanethiol SAM. Oxides are removed in solution-based processing and replaced with a functional SAM chemisorbed via covalent S-GaAs bonds. X denotes a generic SAM functionality.

With respect to the use of sulphides or thiols as chemical passivants, three key indicators are: i) oxide reduction following treatment, ii) evidence of surface chemisorption, and iii) the time stability of the interface in the environment of interest. For example, common wet-chemistry processing results in similarly oxide free surfaces, as detailed separately in the paragraphs below. The most relevant indicator is the chemisorption of the sulphide or thiol species, as the case may be. In this regard, XPS can serve to identify the chemical shifts unique to the surface-bonded sulphur atoms, and to their complementary Ga or As surface species. With respect to the latter, it can be difficult to yield accurate results from XPS, since the sampling depth is such that surface species tend to be lost within the intensity generated from the volume contribution. If there is a substantial chemical shift, or if the sampling depth can be reduced, however, then peaks representing the surface bonded species may become resolved.

2.1.1.1 Inorganic Sulphides

Historically, inorganic sulphides have been employed as surface passivants for a variety of junction-based electronic devices, as they are known to form covalent bonds with, e.g., the crystal terminus of clean GaAs(001), resulting in a marked decrease of the surface defect density and, consequently, improved device performance [Malhotra and Wilmsen, 1995]. Solution-based processing methods are conveniently adopted. Examples include: ammonium sulphide $[(\text{NH}_4)_2\text{S} (\text{aq})]$ and sodium sulphide $[\text{Na}_2\text{S} \cdot 9\text{H}_2\text{O} (\text{aq})]$ [Yablonovitch *et al.*, 1987], and carbon tetrachloride solutions of sulphur monochloride $[\text{S}_2\text{Cl}_2:\text{CCl}_4]$ [Li *et al.*, 1994]. In addition, passivation with hydrogen sulphide $[\text{H}_2\text{S}]$ has been performed in the gas phase [Massies *et al.*, 1980], or as a plasma [Herman and Terry, 1992].

The sampling depth limitations of XPS in mind, a definitive result with respect to the identification of S-As and S-Ga chemisorption of inorganic sulphides was reported using synchrotron photon energies of 80-100 eV on the $(\text{NH}_4)_2\text{S}$ passivated GaAs(001) surface [Spindt *et al.*, 1989b]. Reproduced in Figure 2.3 are the component spectra from the As 3d and Ga 3d regions in that report.

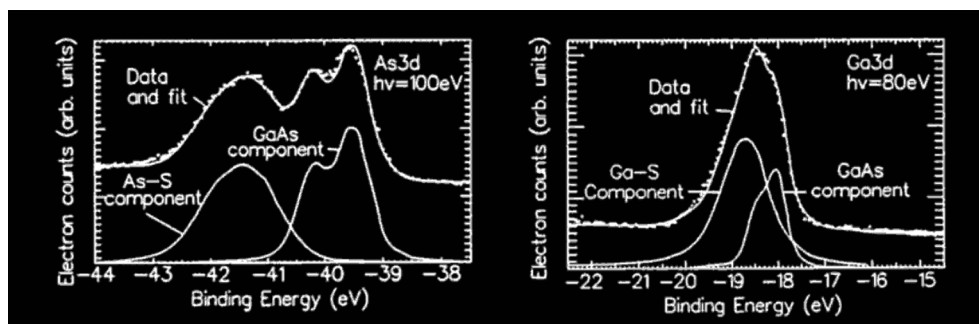


Figure 2.3. As 3d and Ga 3d core level photoelectron spectra of the $(\text{NH}_4)_2\text{S}$ passivated GaAs(001) surface. Energies ($h\nu$) refer to synchrotron source photon excitation. GaAs bulk and S-GaAs species are denoted, after Spindt *et al.* [Spindt *et al.*, 1989b].

Clear evidence of both S-GaAs species is observed. Furthermore, according to the arguments of Spindt *et al.*, S-Ga is the favoured species according to the (bulk sulphide) heats of formation and results in more stable bonds under thermal stress. These results have been corroborated using standard X-ray source energies (monochromatic Al $K\alpha$ 1486.6 eV) in the 2p and 3d regions of As and Ga using $\theta > 65^\circ$ [Lebedev *et al.*, 2003]. Equivalent chemical shifts of up to 2.0 eV were observed for the S-As component in both the 2p and 3d regions, and, similarly, up to 0.6 eV for the S-Ga species. These shifts indicate that sulphide acts as an

oxidizing agent, removing valence charge from the GaAs atoms, which increases their E_B . A more detailed photoemission study of $(\text{NH}_4)_2\text{S}$ passivated GaAs(001), using photon energies similar to that in Spindt *et al.*, and following a series of annealing cycles, proposed that the passivating surface layer consists of an overlayer containing the S-As species and an interlayer consisting of S-Ga bonds and elemental As [Paget *et al.*, 1996]. In these reports, no ΔE_B associated with surface bound sulphur is indicated. The difficulty relates to the fact that the S 2p and S 2s orbitals, which have the two largest photoemission cross-sections for sulphur, have peaks that overlap with Ga 3s core level and As LMM Auger lines respectively, and are therefore challenging to resolve. Secondary sources of interference are the elemental sulphur atoms and sulphur oxides, or the sulphur hydrates typical of $\text{Na}_2\text{S}\cdot 9\text{H}_2\text{O}$ treatment, that remain behind on the GaAs surface after solution-based processing [Spindt *et al.*, 1989b]. Vacuum deposition of sulphur using UV surface photolysis avoids these problems yielding low oxidation chemical states of sulphur near 162 eV, which are characteristic of anionic sulphur species, and are therefore attributed to surface bonding [Zavadil *et al.*, 1994].

2.1.1.2 Organic Thiols

The passivation characteristics achieved using the inorganic sulphides motivated the use of the organic thiols [Lunt *et al.*, 1991], and later, the use of SAM forming long-chain alkanethiols [Nakagawa *et al.*, 1991; Sheen *et al.*, 1992], in efforts to passivate the GaAs(001) surface. In terms of the degree of chemical passivation they afford, results from XPS compositional analysis vary due to the experimental conditions, surface pre-treatments, the adsorbing molecule type and the instrumental parameters employed. Table 2.1 compiles results from several publications where some identifying trends emerge: i) the ΔE_B associated with the Ga 3d peak is not well observed (assignments are usually based on the historical inorganic sulphides data), ii) the ΔE_B of the S-As component in the As 3d (or 2p) region ranges from 1.2 to 1.9 eV, and is better resolved, though is not unambiguous with respect to the residual oxides and the main GaAs peak, and iii) the difference of the S 2p peak measured with respect to the Ga 3s component ranges from 2.0 to 2.6 eV. Note that differences rather than the absolute values of E_B are considered here, since energy scale calibration methods differ among the various publications.

TABLE 2.1. Photoemission analysis of GaAs(001) passivated with organic thiols: survey of literature results.

Molecule	$h\nu$ (eV)	Δ S 2p	Δ As 3d	Δ Ga 3d	Etch	Notes	Reference
HSCH ₂ CH ₂ SH	Al K α	---	---	---	Br ₂ :CH ₃ OH / KOH(aq)	1:1 GaAs	[Lunt <i>et al.</i> , 1991]
HSC ₆ H ₄ Cl	Al K α	---	---	---	+ H ₂ SO ₄ :H ₂ O ₂ :H ₂ O	excess As ^o	"
[CH ₃ (CH ₂) ₁₇] ₂ NCSSNa	Mg K α	---	1.9	---	NH ₄ OH:H ₂ O ₂ :H ₂ O	ECD	[Asai <i>et al.</i> , 1994]
HS(CH ₂) ₃ -Si(OCH ₃) ₃	Al K α	---	1.8	0.55	NH ₄ OH:H ₂ O ₂ :H ₂ O	polymer	[Hou <i>et al.</i> , 1997]
CH ₃ (CH ₂) ₁₇ SH	Al K α	---	1.3 †	---	HCl photoetch	† from As ^o	[Adlkofer and Tanaka, 2001]
biphenyl-4-thiol	130-650	2.5	1.3	---	conc. HCl	excess As ^o	[Shaporenko <i>et al.</i> , 2003]
CH ₃ (CH ₂) ₂ SH	Al K α	2.3	---	---	anneal Ga-rich (4×1)	gas dosing	[Donev <i>et al.</i> , 2005]
CH ₃ (CH ₂) ₁₅ SH	Mg K α	2.0	---	---	NH ₄ OH(aq) / HCl:EtOH	low C etch	[Jun <i>et al.</i> , 2006]
1,8-octanedithiol	Mg K α	2.0	---	---	NH ₄ OH(aq) / HCl:EtOH	S-S bilayer	"
CH ₃ (CH ₂) ₁₇ SH	Al K α	2.2	---	---	NH ₄ OH(aq)	ordered	[McGuiness <i>et al.</i> , 2006]
CH ₃ (CH ₂) ₁₁₋₁₇ SH	Al K α	weak S 2p / As 2p broadening only	---	---	HF(aq) / NH ₄ OH(aq)	MMS	[Nesher <i>et al.</i> , 2006]
CH ₃ (CH ₂) ₁₇ SH	130-580	2.5	1.3	---	NH ₄ OH(aq)	ordered	[McGuiness <i>et al.</i> , 2007a]
1-nonanethiol	Al K α	2.6	1.2 ‡	---	HF(aq) / NH ₄ OH(aq)	‡ As 2p	[Aqua <i>et al.</i> , 2007]
1,9-nonanedithiol	Al K α	2.6	1.5 ‡	---	HF(aq) / NH ₄ OH(aq)	‡ As 2p	"
CH ₃ (CH ₂) ₁₇ SH	Al K α	---	1.2	0.4	HF(aq) and H-clean	gas / liquid	[Budz <i>et al.</i> , 2009]

Al K α - monochromatic 1486.6 eV

Mg K α - anode 1253.6 eV

Δ S 2p is with respect to the Ga 3s peak for the bulk GaAs phase

Δ As and Δ Ga are with respect to the GaAs 3d peaks unless noted

(---) denotes not observed

As^o - elemental As

1:1 GaAs - stoichiometric surface

ECD - electrochemical deposition using ohmic contact to GaAs

polymer - refers to post-formation polymerization of SAM in HCl

† photoetch creates 3 nm excess As^o overlayer : S-As measured from As^o

low C etch - refers to low carbonaceous residual after etching

S-S bilayer - refers to disulphide bridge bond forming SAM bilayer

ordered - fabrication process resulting in highly ordered SAMs

MMS - highly ordered SAM for Hg-molecule-GaAs junction experiments

‡ chemical shift with respect to As 2p of bulk GaAs

gas /liquid - comparative study of gas and solution phase deposition

The S 2p energy positions in Table 2.1 represent a ΔE_b of -1.1 to -1.7 eV from the known chemical state for molecular thiol (R-SH) located at 163.7 eV [NIST XPS, 2003]. This is interpreted as meaning the sulphur is bound as thiolate (R-S⁻) consistent with observed reactions on Au [Castner *et al.*, 1996]. The dissociative adsorption of (propane)thiolate on GaAs was first observed in the gas dosing experiments of Donev *et al.*, where it was proposed that the dissociated hydrogen remains on the surface [Donev *et al.*, 2005]. This was later supported by molecular dynamics calculations, which further revealed that S-H cleavage was subsequent to physisorption from the gas phase [Voznyy and Dubowski, 2008a]. Sulfhydryl recombinative desorption of alkanethiol has been confirmed experimentally, and was shown to be preferential to Ga bonds at temperatures as low as 350 K [Huang *et al.*, 2009]. The S-As bonds can also follow a similar recombinative desorption pathway near room temperature [Dubowski *et al.*, 2010]. These processes require the proximity of adsorbed hydrogen, and their respective activation energies are dependent on the surface reconstruction. Exclusive of these recombinative pathways, the covalency of S-GaAs coupling suggests bond strengths exceeding 40 kcal/mol [Voznyy and Dubowski, 2006; Voznyy and Dubowski, 2008a].

As mentioned earlier, low photon energy photoemission spectroscopy yields enhanced surface sensitivity owing to a decrease in sampling depth. Alternatively, increasing the value of θ provides a similar enhancement factor, as will now be shown. Consider the diagram in Figure 2.4 consisting of the SAM, interface, and bulk GaAs regions.

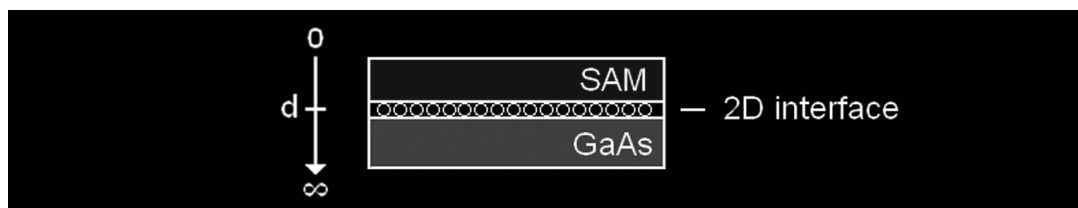


Figure 2.4. Regions of the SAM-GaAs interface used for evaluation of the surface sensitivity ratio. The 2D interface is comprised of surface chemisorbed atoms. The SAM overlayer has thickness d_{SAM} and is comprised of the alkane chain.

The surface sensitivity can be expressed as a ratio of interface to bulk photoemission intensities. For the 2D layer representing the interface region comprised of, e.g., surface thiolate or its complementary GaAs species, the prefactor reduced photoemission intensity (I^*) can be written directly in terms of the 2D surface density (ρ_{surf}) [Carpenter *et al.*, 1989],

$$I_{2D}^* = \rho_{surf} / \cos \theta \quad (2.7)$$

The bulk component is found by integration of Equation 2.1 over depths z from 0 to ∞ , as in Equation 2.5. Dividing this result into Equation 2.7 and canceling common factors associated with attenuation through the overlayer [i.e., $\exp(-d_{SAM}/\Lambda_{SAM} \cos \theta)$] gives,

$$\frac{I_{2D}^*}{I_{bulk}^*} = \frac{\rho_{surf} \sec \theta}{N_{bulk} \Lambda_{bulk}} \quad (2.8)$$

where it is clear that, in addition to decreases in Λ , increasing θ increases the 2D/bulk interface sensitivity ratio. A well-ordered SAM provides a suitable configuration with which to examine thiol-GaAs coupling as the surface density may be predicted and compared to experimental results. McGuinness *et al.* have shown that highly ordered, nearly vertically oriented SAMs of long-chain alkanethiol, such as octadecanethiol (ODT) [$\text{CH}_3(\text{CH}_2)_{17}\text{SH}$] are easily formed on the NH_4OH etched GaAs(001) surface [McGuinness *et al.*, 2006]. Their results using synchrotron photon energies as low as 130 eV have not, however, been able to unambiguously identify either a As-S or Ga-S component in the 3d region. A peak attributed to As-S was assigned within the envelope of the As 3d spectrum, but it is not resolved from the elemental As (As^0), defined in the next section, or from residual oxide components identified as present on the surface [McGuinness *et al.*, 2007a].[†] The Ga 3d, As 3d and S 2p spectra following ODT-SAM formation, as given in Figure 2.5, are adapted from that report.

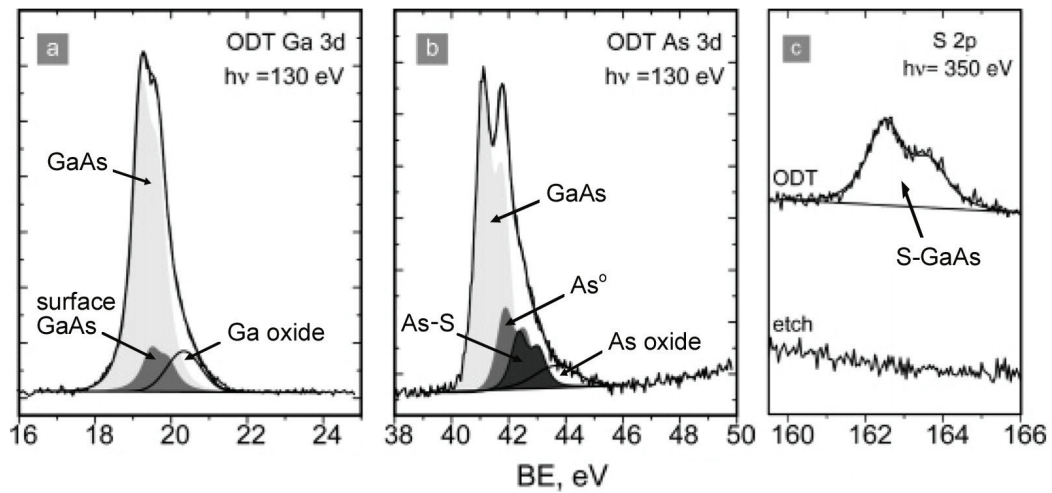


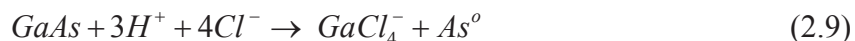
Figure 2.5. Ga 3d, As 3d and S 2p core level photoelectron spectra of the ODT passivated GaAs(001) surface. Energies ($h\nu$) refer to synchrotron source photon excitation. Spectrum components as noted. Adapted from McGuinness *et al.* [McGuinness *et al.*, 2007a].

[†] Oxide species were fitted in the GaAs 3d regions despite that zero emission was observed in the O 1s region.

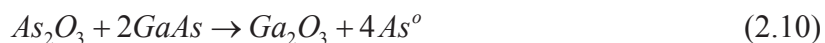
In that same work, Time-of-Flight Secondary Ion Mass Spectrometry (ToF-SIMS) results successfully identified signatures characteristic of both S-GaAs species, but in non-calibrated ratios. Note that in the S 2p region of Figure 2.5 (panel c), photoemission from the Ga 3s component, which should appear around 160 eV, does not appear above the background level. The sampling depth at the energy used is approximately 18 Å, which is about the value of d_{SAM} , or the typical oxide thickness after etching [Moumanis *et al.*, 2006]. Consequently, emission from Ga 3s does not appear to be a complicating factor in the assignment of peaks attributed to chemisorbed thiolate at the low photon energy used.

2.1.1.3 Oxide Etching

The etching reactions listed in Table 2.1 consist of either acid or base solutions, with or without use of an oxidizing agent such as H₂O₂. In general terms, etching proceeds according to the oxidation of the surface, followed by dissolution of the oxide species in an acid, base or a combination of both. If removal of the native oxides (As₂O₃, As₂O₅ and Ga₂O₃) is all that is required, acid or base treatment will suffice. Two common approaches include the use of NH₄OH or HCl. Both result in effective removal of the native oxide [Zavadil *et al.*, 1994]. HCl is also reactive with the GaAs surface and is observed by XPS to increase the surface concentration of As⁰ according to,



which leaves an amorphous layer of As⁰ up to a few angstroms thick and that acts as a chemical stop to further reaction [Alperovich *et al.*, 2004]. Conversely, etching in NH₄OH decreases the concentration of As⁰ relative to HCl treated surfaces [Lu *et al.*, 1989], although As⁰ still remains observable, especially at low synchrotron energies [Lebedev *et al.*, 2004]. The presence of As⁰ on GaAs is usually explained by the reaction [Hollinger *et al.*, 1994],



which is thermodynamically favoured according the larger heat of formation of Ga₂O₃. Moreover, the removal of native GaAs oxides in NH₄OH is based on its dissolution into complex species such as (NH₄)₃AsO₄ and NH₄Ga(OH)₄ [Bryce and Berk, 1996]. Therefore, it is reasonable to conclude that As⁰ is left behind on the surface following the dissolution of the oxide layer and is a result of its lower solubility or its physical attraction to the surface. One

study compared the effectiveness of ethanolic HCl vs. aqueous NH_4OH in terms of the carbonaceous surface contamination left behind after etching and concluded that NH_4OH (aq) was better in this regard [Jun *et al.*, 2006]. Carbonaceous contamination may be left in the form of ethyl chloride resulting from halogenation of the solvent [Alperovich *et al.*, 2004]. Moreover, the reduced surface concentrations of carbonaceous species and of As^0 following NH_4OH etching could be contributing factors to the successful formation of highly ordered SAMs. Indeed, McGuinness *et al.* claim that NH_4OH etching provides the most effective surface preparation in order to achieve the best quality SAMs [McGuinness *et al.*, 2006].

2.1.1.4 SAM-GaAs Interface Structure

The facts concerning the bonding of thiolate, its complementary GaAs surface species, the molecular dynamics involved, and the differences between vacuum reconstructed surfaces and those obtained following wet-etch processing draw a complex picture of the passivation of the GaAs(001) surface with alkanethiol SAMs. Of interest are the results of Adlkofer and Tanaka, which indicate chemical bonding of ODT-SAMs to a 3 nm layer of amorphous As^0 produced after photoetching in HCl [Adlkofer and Tanaka, 2001]. This provides evidence to the effect that the SAM can form on the non-stoichiometric surface and is not required to conform to known GaAs surface configurations. In contrast, GaAs surface reconstructions can be found by simulation that match a nearly ideal, pseudo-orthorhombic pattern of SAM chain packing [Voznyy and Dubowski, 2008b]. Furthermore, it was suggested that the van der Waals forces associated with SAM formation may be strong enough to drive the requisite surface reconstruction. Characteristic of the matching surface type is a trench-ridge structure that leaves half of the dangling bonds exposed and unavailable to thiol coupling, though dissociated hydrogen may help satisfy the electron counting rule. Figure 2.6 illustrates the expected SAM orientation and reconstructed GaAs surface according to Voznyy and Dubowski. One factor not considered in the simulated environment is the presence of As^0 . Thiol bonding with this amorphous species could provide accommodation of dense SAM packing by surface diffusion. However, this is not likely a significant factor, as long-range azimuthal order along the $[1\bar{1}0]$ direction of the GaAs(001) surface has been observed by grazing incidence X-ray diffraction (GIXRD) [McGuinness *et al.*, 2007b], meaning that SAM orientations are dictated by an ordered substrate, in agreement with the direction in Figure 2.6, rather than one that has an amorphous structure.

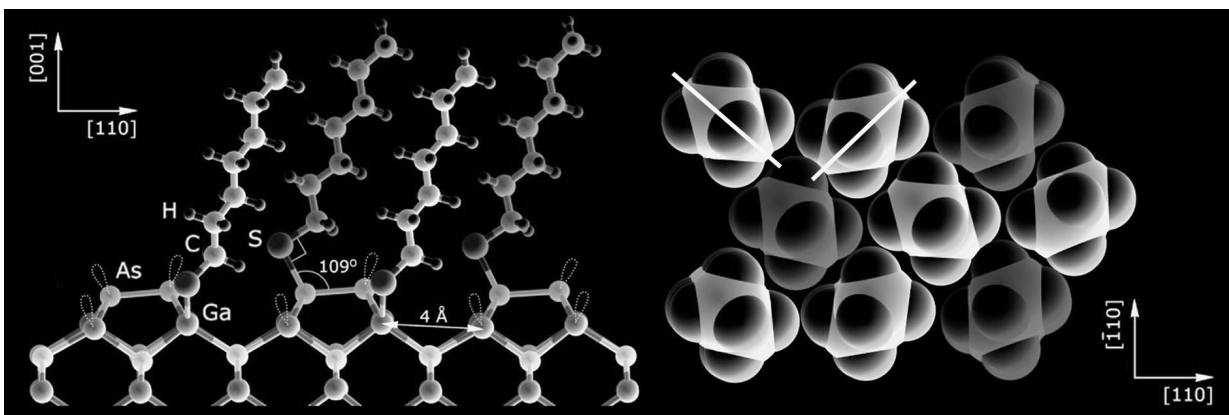


Figure 2.6. SAM matched GaAs(001) reconstruction according to molecular simulations. **Left:** side-view showing S-As and S-Ga bond positions along a trench-ridge structure in the [110] direction. Open loops represent dangling bonds. **Right:** top view of the SAM showing orthorhombic-like packing. Dark/light grey colouring refers to As/Ga bond positions. Black lines indicate alkane C-C-C planes, which are oriented at $\pm 45^\circ$ and tilted 19° from the surface normal. Adapted from Voznyy and Dubowski [Voznyy and Dubowski, 2008b].

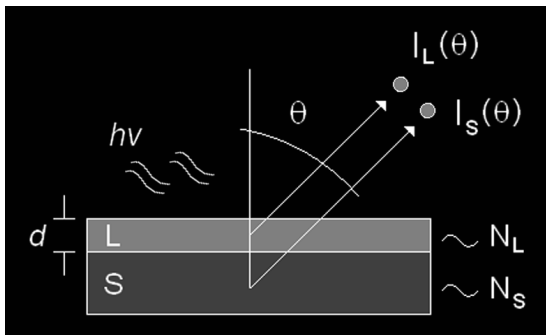
While the various XPS component assignments made in the above cited literature reflect the presence of different surface chemical species by virtue of their binding energies, questions remain that relate to the identification of S-GaAs components in terms of their surface appropriate concentrations. What is the expected sensitivity ratio based on Equation 2.8 and does this reflect what is observed? Does a quantification of bound thiolate agree with its complementary GaAs components? In addition, uncertainty remains concerning the quantification of surface As^0 after SAM formation. Qualitative answers can be obtained by comparing the apparent atomic percentages. However, more detailed quantitative analysis requires the ARXPS methods described in the next section.

2.1.2 Angle-Resolved XPS Methods

In principle, inversion of Equation 2.1 allows one to extract $N(z)$ from an experimentally determined set of angle-resolved data $I(\theta)$. However, as detailed in the review by Cumpson [Cumpson, 1995], Equation 2.1 is the Laplace Transform of the composition depth profile $N(z)$ and its inversion, $N(z) = \mathcal{L}^{-1}[I(\theta), z]$, is highly sensitive to the precision on $I(\theta)$. Cumpson concluded that, for example, provided data typical of XPS, which can have a precision of a few percent at best, due mainly to signal-noise ratio and component fitting limitations, depth resolutions no better than $\Delta z / z \geq 0.8$ may be obtained, even for liberal compositional uncertainties of $\Delta N / N \approx \pm 0.5$. Consequently, most ARXPS methods are

applied to overlayer type models, or other known (*a priori*) structural forms, such that inversion algorithms are not required and higher degrees of precision may be assured. In this section, ARXPS as applied to the analysis of the SAM-GaAs interface is examined. In accordance with the above limitation, standard overlayer models are assumed.

ARXPS methods applied to the investigation of the SAM-GaAs interface have been limited to a quantification of the SAM overlayer thickness. Assuming an *all-trans* conformation of the alkane chain, i.e., a fully extended, C-C-C zig-zag morphology as in Figure 2.6, and assuming the SAM packs densely according to its molecular diameter, an estimate of the average molecular tilt and surface density may be obtained. Results vary depending on the surface preparation and ARXPS method employed. Early reports indicated tilt angles of 56°-60° after HCl etching [Jun *et al.*, 2006; Ye *et al.*, 2003; Zhang *et al.*, 1999]. These results appear mutually reinforcing, however, the ARXPS techniques used leave some doubt as to their accuracy. For example, Jun *et al.* and Ye *et al.* used a simple exponential formulation based on attenuation of GaAs photoemission through the alkane overlayer, but referred the intensity to clean GaAs, which could only be obtained through controlled oxide-free sample preparation they did not use. Zhang *et al.* used a more appropriate self-referenced formulation based on ratioing the thiolate S 2p signal at two emission angles. However, this places high demands on the instrument depth of field and flood area of X-ray illumination, both of which must be large enough to accommodate the projected analysis area without loss at $\theta > 45^\circ$ required to achieve sufficient angular sensitivity. Experimentally, it is more accurate to ratio specific intensities over a number of emission angles [Cumpson, 1995], as is shown in Figure 2.7 and Equation 2.11 for the case of a generic overlayer.



$$d = \Lambda_L \cos \theta \ln \left(1 + \frac{I_L^*(\theta) N_S \Lambda_S}{I_S^*(\theta) N_L \Lambda_L} \right) \quad (2.11)$$

Figure 2.7. Schematic of ARXPS of an overlayer (L) on substrate (S). I_L and I_S are the photoemission intensities from elements having number densities N_L and N_S . Geometric factors cancel in Equation 2.11 yielding accurate values of thickness d .

Apart their shortcomings, the ARXPS reports cited above support the conclusion of a 57° tilt angle specified by ellipsometry in the original works by Nakagawa *et al.* and Sheen *et al.* [Nakagawa *et al.*, 1991; Sheen *et al.*, 1992]. In these reports, however, sample preparation was made from molten alkanethiol at 100°C, a temperature that exceeds the known conformational transition temperature of polycrystalline *n*-alkane (40°C) [Casal *et al.*, 1983], and that of highly ordered alkanethiol SAMs (80°C) [McGuinness *et al.*, 2006]. Therefore, it is unlikely that those analyses were performed on high quality SAMs. As cited earlier, McGuinness *et al.* reported on optimized conditions for highly ordered ODT-SAMs, which were characterized, using near-edge X-ray absorption fine-structure (NEXAFS), as having a tilt angle of 14° [McGuinness *et al.*, 2006]. Clearly, the lower tilt angle yields a greater packing density, and therefore, a higher degree of SAM order. ARXPS analysis on samples prepared using the optimized method have been performed based on the recommended element ratioing method, where SAM thicknesses consistent with tilt angles less than 15° were observed for chain-lengths $n = 11, 13, 15, 17$ [Nesher *et al.*, 2006].

In the present work, ARXPS is used to qualitatively analyze the surface As:Ga ratio, quantify the surface concentration of As⁰, and estimate the SAM coverage. In terms of the methodologies used, the earlier specified shortcomings must be avoided. In addition, consider the validity of using photoemission from the GaAs substrate in the ARXPS analysis of surface species. A primary assumption of Equation 2.1 is that the test sample is amorphous or finely polycrystalline [Cumpson, 1995]. Use of single crystal GaAs can result in errors by electron ‘channeling’ effects that arise from various scattering phenomena, the most familiar of which may be Bragg reflection. The polar anisotropy these effects impose can introduce errors if ARXPS is evaluated at just one emission angle [Alnot *et al.*, 1987]. Consequently, it is important to measure the elemental ratios over several emission angles in order ensure accuracy, where possible, if the GaAs substrate is to be incorporated into the analysis. Another consideration pertains to the unknown relative number density between the SAM and the GaAs substrate. Uncertainty in this regard can be mitigated by the logarithmic separation of variables, as detailed in Chapter 3. Further to this effort, an island-like fractional overlayer model is adopted from Paynter [Paynter, 1999], which will be presented in detail later, but that can be summarized by the following,

$$I = fI'_L + (1-f)I_S + fI'_S \quad (2.12)$$

where f is the fractional coverage of a discontinuous overlayer to be determined, I_s and I_L refer to emissions from the GaAs substrate and overlayer respectively, and the prime notation indicates that attenuation factors associated with the overlayer are applied where required.

2.1.3 Surface Energy Levels

The discussion to this point has been limited to an understanding of XPS and how a qualitative and structurally quantitative picture of the SAM-GaAs interface may be obtained. These are important in terms of an understanding of chemical passivation, but, as mentioned earlier, electronic passivation is a closely related characteristic that has implications for the surface barrier height, which is a fundamental property of the interface and factors significantly into the operation of any junction-based device.

In Chapter 1, an introduction was made of the near-surface band-bending characteristic of semiconductor surfaces, from which the surface barrier height is obtained. The band-bending potential $\Phi(z)$ is formed when electrons/holes from donors/acceptors in the bulk of the material lower their energy to occupy surface defect states that have energy positions located within the band-gap of n/p-type semiconductors. The requirement that the Fermi level be constant throughout the material forces the bending of the conduction and valence band edges resulting in $\Phi(z)$. As illustrated in Figure 1.6, the surface barrier height of n-type material is determined by the positive charge density ($q N_d$) left behind in the space charge region (SCR) following the ionization (depletion) of bulk donors resulting in the occupation of surface acceptor states by electrons. The ionization/occupation of donor/acceptor levels is governed by Fermi-Dirac statistics as detailed later. $\Phi(z)$, the depletion depth z_d , and the space charge density Q_{sc} are determined according to Poisson's equation (see Appendix A),

$$\Phi(z) = \frac{q N_d}{2\epsilon} (z - z_d)^2 \quad (2.13)$$

$$z_d = \sqrt{2\epsilon \Phi_{sb} / q N_d} \quad (2.14)$$

$$Q_{sc} = \sqrt{2\epsilon q N_d \Phi_{sb}} \quad (2.15)$$

where $q \Phi_{sb} = q \Phi(0)$ is the surface barrier height in eV, N_d is the donor number density, and ϵ is the material permittivity. Equation 2.13 describes the quadratic nature of the

band-bending potential. Its derivative describes the build-in field (\mathcal{E}), which is linearly dependent on z and vanishes at z_d . If the position of the surface Fermi level (E_{SF}) can be determined, and N_d is known, then the remaining parameters are obtained. Calculation of the bulk Fermi level requires a solution to the Fermi-Dirac integral of order $1/2$ (see Appendix B),

$$E_F = \xi kT + E_g \quad (2.16)$$

where ξ is a parameter of the integral and E_g is the band-gap energy. For non-degenerate doping, the bulk Fermi level can be approximated by,

$$E_F = E_i + kT \ln(N_d/n_i) \quad (2.17)$$

where E_i is the intrinsic level, kT is the Boltzmann energy, and n_i is the intrinsic carrier concentration. With these definitions, the surface barrier height is,

$$q\Phi_{sb} = E_{SF} - E_F \quad (2.18)$$

In the above, all energy levels (E) are referred to the GaAs valance band-edge (VBE). Equation 2.18 indicates the potential drop across the SCR is negative for n-type surfaces.

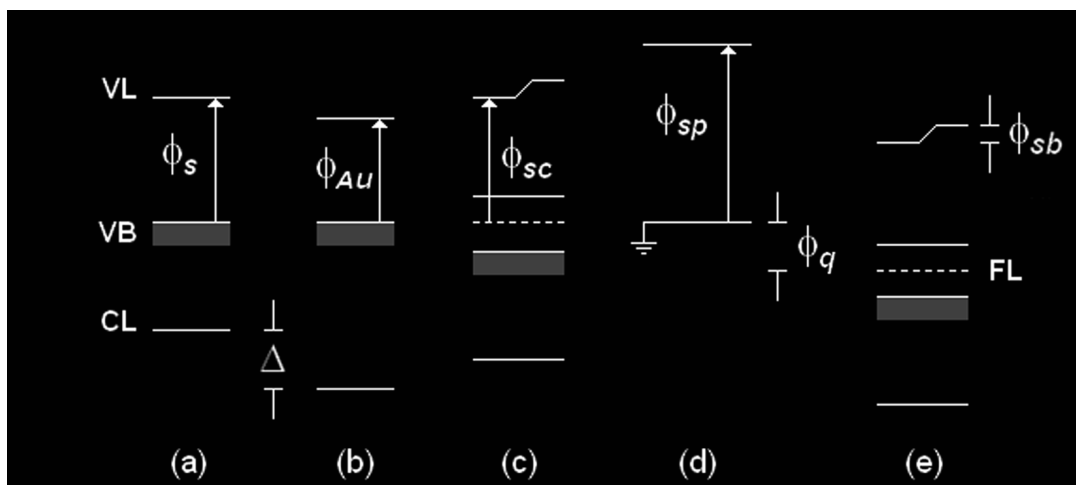


Figure 2.8. Energy level diagram of various materials in an XPS experiment: conducting sample (a), Au calibration (b); semiconductor, grounded (c) or isolated (e), each with respect to the spectrometer ground and associated work function potentials. Abbrev.: VL, vacuum level; VB, valence band; FL, Fermi level; CL, core level. See text for further details.

The position of E_{SF} before and after SAM formation is required in order to interpret the electro-optic response of the interface. XPS is capable of determining this energy if appropriate referencing techniques are used. Note that the Fermi level determined by XPS

represents a good approximation of its value at the surface, since the XPS sampling depth (~ 5 nm) is a small fraction of the depletion depth. Figure 2.8 illustrates the energy levels of various sample types relative to that of the spectrometer (KE analyzer) apparatus. On the far left (a) is a conducting sample that is equipotential with both the spectrometer ground (d) and a separate (external) calibration sample (b). Differences in the sample work function ($q\phi_s$) with respect to the spectrometer ($q\phi_{sp}$) are accounted for by reference to the calibration sample in order to locate the Fermi level energy. The calibration sample is usually a cleaned Au film ($q\phi_{Au}$), and known core level offsets of E_B are applied directly (Δ), or their Fermi edges are made to coincide at the zero of E_B by,

$$q\phi_{sp} = h\nu - KE_{cal} - E_{cal}^* \quad (2.19)$$

$$KE_F = h\nu - q\phi_{sp} \quad (2.20)$$

where KE_{cal} is measured at the calibration point of known binding energy E_{cal}^* , and KE_F is the KE at the Fermi level of the sample. This calibration, which is also available by ultra-violet photoelectron spectroscopy (UPS), is particularly useful if the Fermi edge is not observable, as in the case of semiconductor (c), provided it too is well grounded. In this case, the Fermi level is just the offset of KE_F from the KE at the VBE [Petit *et al.*, 1992]. Note that for the semiconducting samples, i.e., grounded (c) and electrically isolated (e), a generic surface potential barrier ($q\phi_{sb}$) has been applied at the vacuum level that represents the difference with respect to the bulk Fermi level shown. If the sample is electrically isolated, an unknown surface charge potential (ϕ_q) relative to the spectrometer may be established and external calibration is not possible. Sample charging results from the uncompensated holes left behind after photoemission. To circumvent the insulating barrier, use of an internal metal calibrant is required that must obtain the same potential at the surface through the use of sufficient charge compensation [Stephenson and Binkowski, 1975].

Historically, internal Fermi level referencing has been accomplished using post-process metal deposition. Since Au provides a stable Fermi level reference of 84.00 eV relative to the $4f_{7/2}$ core level, it is the primary standard used [NIST XPS, 2003]. In practice, following surface treatment and the recording of XPS spectra, Au would be evaporated or sputtered onto

the sample surface. For example, the surface Fermi level of GaAs was located following various processing steps by reference to the Fermi level of evaporated Au using knowledge of the GaAs core level to VBE binding energy difference [Grant *et al.*, 1981]. For SAMs, three pitfalls of this technique are: i) the potential damage overlayering could impart to the ordered molecular structure of the SAM, ii) the fact that intimate contact with the substrate is not made, and iii) the surface perturbation that may result from excess coverage, i.e., the presence of the calibrant itself can induce a change in the barrier height.

In Chapter 5, a XPS technique is described where the Au calibrant is integrated directly onto the GaAs substrate, prior to SAM formation, as an effective method to achieve Fermi level calibration at the molecular-semiconductor junction, which avoids the pitfalls of the so-called ‘decoration’ method. Moreover, the integration method allows the surface Fermi level to be determined before and after SAM formation, which provides essential information relating to the degree of electronic passivation at the surface. As a result of oxide reduction, removal of surface state density, or the introduction of molecular energy levels at the surface, a repositioning of the surface Fermi level may be effected. Furthermore, the described XPS method provides for a determination of the surface Fermi level under conditions of thermal equilibrium. Note that Raman spectroscopy has been used to probe for a reduction of the depletion depth in this material system, which is characteristic of electronic passivation [Dorsten *et al.*, 1995; McGuinness *et al.*, 2007a], but this method injects carriers into the SCR resulting in a photovoltage, known as the SPV, that screens differences in the equilibrium surface barrier. Under sufficient irradiation, the saturation value of SPV can be equated with the surface barrier if the flat-band condition indicated in Figure 1.6 is reached, and has been used to study alkanethiol SAMs on GaAs [Aqua *et al.*, 2007], but for GaAs particularly, obtaining the flat-band condition is not always assured. The SPV technique will be discussed further in Section 2.3. Using the described XPS technique, an accurate picture of the equilibrium barrier height will be obtained before and after formation of the SAM.

2.2 Infrared Spectroscopy and Optical Constants of the SAM

The IR spectroscopy of materials is based on the resonant absorption of IR radiation at frequencies characteristic of the vibrational motion of molecular bonds. It is defined for the mid-IR spectrum in the region 4000 cm^{-1} - 400 cm^{-1} (wavenumbers), or $2.5\text{ }\mu\text{m}$ - $25\text{ }\mu\text{m}$. In

addition to its usefulness for chemical identification purposes, information related to the molecular structure and physical environment of the material can be obtained. In this section, the application of IR spectroscopy to the analysis of alkanethiol SAMs is reviewed. The objective is to establish a framework in which to discuss the IR absorbance from which the optical constants of the SAM are derived. In Chapter 1, recall that it was proposed, if an electronic configuration unique to the SAM phase is realized, one consequence might be a change to its dielectric properties. The molecular ordering of the SAM factors in significantly to the analysis, as it forms the basis of the anisotropy used to model the IR optical response.

To start, consider the natural molecular vibrations that result in a dynamic change of the internuclear separations and bond angles associated with the constituent atoms. The number of vibrational degrees of freedom depends on the structure of the molecule and the number of atoms N_a . A useful example is the water molecule. The total number of molecular degrees of freedom is $3N_a$. Subtracting the 3 translational and 3 rotational freedoms, the total number of vibrational freedoms is $3N_a - 6$. The resulting 3 vibrational modes of the water molecule, referred to as stretching and bending modes, are illustrated in Figure 2.9. Shown are the dynamic dipole derivatives [Parikh and Allara, 1992], which result from the oscillatory change in molecular polarization along directions referred to as the normal coordinates of vibration (r_q). For any given mode, the molecular partial charges (δ^\pm) vibrate along directions specified by a change of bond length or angle. The normal coordinates are linear combinations of these individual motions (expressed in their molecular coordinates) such that an independent set of normal vibrational modes is formed.

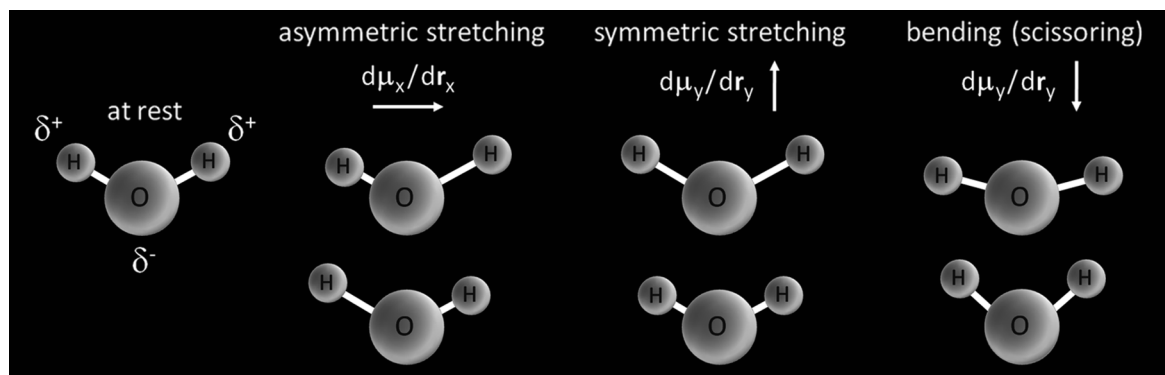


Figure 2.9. Normal vibrational modes of the water molecule. The derivatives indicate the transition dipole moments representing the independent set of molecular polarizations that arise from changes of bond length or angle. Vector directions apply to the top row.

In general, the normal coordinates are found by inspection of the formal molecular symmetries, specifically, the normal modes “form a basis for an irreducible representation of the point group of the molecule” [Harris and Bertolucci, 1989]. For the methylene group (CH₂) C-H vibrations of linear alkane, there are 2 stretching modes (asymmetric, symmetric) and 2 bending modes (rocking, scissoring) [Smith, 1999]. In this work, only the two C-H stretching modes are observable, the asymmetric and symmetric modes similar to the molecular O-H stretching modes in Figure 2.9. The interaction of an IR optical field with the dipole moments associated with these normal mode vibrations results in the resonant absorption of IR radiation at the natural frequencies of these modes as described next.

2.2.1 Quantum Mechanics of the IR Absorption Intensity

Since the restoring force of small bond length displacements is proportional to that displacement ($F = -Kx$), a simple model of the equation of vibrational motion is the quantum harmonic oscillator. Figure 2.10 shows the potential energy curve of a diatomic molecule represented by the Morse potential [Morse, 1929], its harmonic (quadratic) approximation, and the quantized harmonic vibrational levels [Bransden and Joachain, 1989],

$$E_\nu = \frac{h}{2\pi} \sqrt{\frac{K}{m_r}} \left(\nu + \frac{1}{2} \right) = \hbar \omega_o \left(\nu + 1/2 \right) \quad (2.21)$$

where ν is the vibrational quantum number, m_r is the reduced mass ($m_r = m_1 m_2 / (m_1 + m_2)$) of the vibrational system and ω_o is the radial frequency corresponding to the classical oscillator. It is stated without further discussion that the Morse potential is a more appropriate model to use, and results in a first order correction term $[-\hbar \omega_o w_M (\nu + 1/2)^2]$ added to Equation 2.21, where w_M is a constant related to the well depth [Morse, 1929]. With the Morse anharmonicity applied, the energy spacing decreases with increasing ν , and the transition selection rules are extended to $\Delta\nu = \pm 1, \pm 2, \pm 3, \dots$, from which the overtone and combination bands expressed in the near-IR spectral region are obtained [Brugel, 1962]. For the present discussion, use of the quantized simple harmonic oscillator model will suffice.

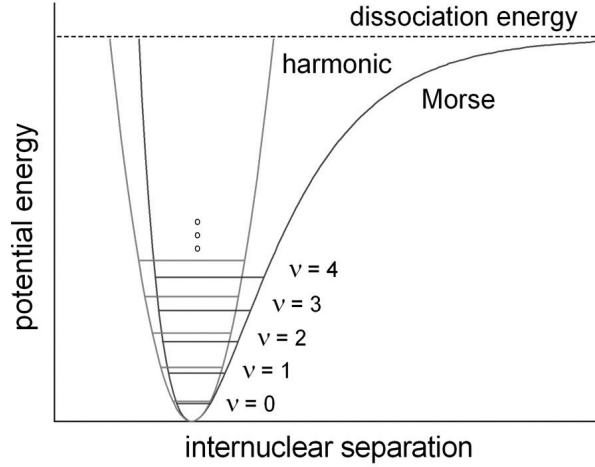


Figure 2.10. Energy well models describing the diatomic potential as a function of internuclear separation. The Morse potential reflects the natural asymmetry and the dissociation energy. The harmonic potential is a convenient approximation for small displacements. The vibrational levels derive from treatment as a quantum oscillator.

The equation of motion can be represented with the time-dependent Schrödinger equation,

$$\left(\frac{-\hbar^2}{2m_r} \frac{\partial^2}{\partial x^2} + \frac{1}{2} Kx^2 + e\mathbf{x} \cdot \mathbf{E}(t) \right) \Psi(x, t) = i\hbar \frac{\partial}{\partial t} \Psi(x, t) \quad (2.22)$$

where \mathbf{x} denotes the displacement along a particular vibrational normal coordinate and e may be considered an effective charge of the mode [Bransden and Joachain, 1989]. The Hamiltonian consists of the kinetic energy term, the harmonic potential, plus a time-dependent perturbation representing the interaction potential of the IR optical field ($\mathbf{E}(t)$) and the dipole operator ($e\mathbf{x}$). Using perturbation theory, the following are defined for isotropic samples (see Appendix C),

$$M_{01} = \langle \psi_1(x) | e\mathbf{x} | \psi_0(x) \rangle = \int_{-\infty}^{\infty} e\mathbf{x} \psi_1^*(x) \psi_0(x) dx \quad (2.23)$$

which is a matrix element referred to as the transition moment for the dipole operator and,

$$W_{01}(t) = \frac{4\pi I_{IR}}{3\hbar^2 c \epsilon_o} M_{01}^2 \quad (2.24)$$

which is the absorption rate for transitions from the ground state $|\psi_0(x)\rangle$ to the excited vibrational state $|\psi_1(x)\rangle$, where the $\psi_\nu(x)$ are eigenfunctions of the time-independent Schrödinger equation, having the eigenvalues E_ν . Equation 2.24 indicates that the absorption

rate is proportional to the incident IR intensity (I_{IR}) times the square of the transition moment. Now consider a redefinition of the dipole operator, expanded about the equilibrium position ($x = a$), such that a permanent molecular dipole (μ_a) may be accounted for,

$$ex = \mu \approx \mu_a + \left(\frac{\partial \mu}{\partial x} \right)_a x \quad (2.25)$$

[Herzberg, 2008]. Substitution of Equation 2.25 in 2.23 gives,

$$M_{01} \approx \mu_a \langle \psi_1(x) | \psi_0(x) \rangle + \left(\frac{\partial \mu}{\partial x} \right)_a \langle \psi_1(x) | x | \psi_0(x) \rangle \quad (2.26)$$

which vanishes in the first term because of eigenfunction orthonormality. The solutions $\psi_v(x)$ to the harmonic oscillator problem are [Bransden and Joachain, 1989],

$$\psi_0(x) = \left(\frac{\zeta}{\pi} \right)^{\frac{1}{4}} \exp(-\zeta x^2/2) \quad (2.27)$$

$$\psi_1(x) = \left(\frac{\zeta}{\pi} \right)^{\frac{1}{4}} \sqrt{2\zeta} x \exp(-\zeta x^2/2) \quad (2.28)$$

where $\zeta = m_r \omega_o / \hbar$. These can be inserted in the second term of Equation 2.26 to give,

$$M_{01} \approx \left(\frac{\partial \mu}{\partial x} \right)_a \sqrt{\frac{2}{\pi}} \zeta \int_{-\infty}^{\infty} x^2 \exp(-\zeta x^2) dx \quad (2.29)$$

The useful integral is,

$$\int_0^{\infty} x^2 \exp(-\zeta x^2) dx = \frac{\Gamma(3/2)}{2\zeta^{3/2}} \quad (2.30)$$

such that Equation 2.29 is [Bishop, 1990],

$$M_{01} \approx \left(\frac{\hbar}{2 m_r \omega_o} \right)^{\frac{1}{2}} \left(\frac{\partial \mu}{\partial x} \right)_a \quad (2.31)$$

Consequently, it is clear from Equations 2.24 and 2.31 that the IR absorption rate is proportional to the square of the dipole moment derivative. This is conveniently expressed as,

$$W_{IR} \propto \left| \mathbf{E}_{IR} \cdot \left(\frac{\partial \boldsymbol{\mu}}{\partial x} \right)_a \right|^2 \quad (2.32)$$

[Parikh and Allara, 1992], since $I_{IR} = c \epsilon_o |\mathbf{E}_{IR}|^2 / 2$, and where the vectorial nature of the interaction has been reintroduced for generality. Equation 2.32 establishes a quantum mechanical basis for the IR selection rule dictating that active modes of vibration must have a changing dipole derivative. A simple example where this clearly manifested is the C-O stretching vibration of carbon dioxide. Since the bonding is linearly symmetric (O-C-O) with 180° bond angles and a zero molecular dipole at rest, only the asymmetric stretching mode is active whereas the symmetric stretching mode is not.

2.2.2 Polarizability and the Principal Components of the Refractive Index

The polarization of material subject to the electric field of an optical wave is the origin of its refractive index (\mathcal{N}). This macroscopic property is derived from the dipole moments ($\boldsymbol{\mu}$) induced at any point in the material (a microscopic effect). Consider that the local field (\mathbf{E}_{loc}) experienced by a given molecule in a dense medium is the superposition of the average electric field of the optical wave (\mathbf{E}) and the field induced by the polarization of the surrounding material (\mathbf{P}). For an isotropic medium, the Lorentz local field correction is,

$$\mathbf{E}_{loc} = \mathbf{E} + \mathbf{P} / 3\epsilon_o \quad (2.33)$$

[Fox, 2010]. Since $\mathbf{P} = \boldsymbol{\mu} N$ or $\mathbf{P} = N \alpha \mathbf{E}_{loc}$, where N is the number density of induced dipoles and α is the molecular polarizability, substitution with Equation 2.33 gives,

$$\mathbf{P} = \frac{N \alpha}{1 - N \alpha / 3\epsilon_o} \mathbf{E} \quad (2.34)$$

Macroscopically, $\mathbf{P} = (\epsilon - \epsilon_o) \mathbf{E}$, where ϵ is the material dielectric constant. Equating the coefficients, dividing through by ϵ_o , and rearranging with $\mathcal{N}^2 = \epsilon / \epsilon_o$ gives,

$$3 \frac{\mathcal{N}^2 - 1}{\mathcal{N}^2 + 2} = N \alpha / \epsilon_o \quad (2.35)$$

known as the Clausius-Mossotti relation [Feynman, 1970]. It is Equation 2.35 that makes the connection between the microscopic domain and the observed macroscopic refraction.

For small oscillations driven by an IR optical field, it is useful to consider the medium as a collection of independent damped harmonic oscillators according to the normal vibrational modes. For simplicity in later modeling, a classical treatment is conveniently adopted in order to find an expression for the polarizability in Equation 2.35. The governing force equation is,

$$m_r \frac{d^2 \mathbf{x}}{dt^2} + m_r \gamma \frac{d \mathbf{x}}{dt} + K \mathbf{x} = e \mathbf{E}_{loc} \quad (2.36)$$

[Fowles, 1989], where γ is a damping constant, which for a harmonic driving force $\mathbf{E}_{loc} = \mathbf{E}_o e^{i\omega t}$ and corresponding dipole displacement $\mathbf{x} = \mathbf{x}_o e^{i\omega t}$ has the solution,

$$\mathbf{x}(t) = \frac{e/m_r}{(\omega_o^2 - \omega^2 + i\gamma\omega)} \mathbf{E}_{loc}(t) \quad (2.37)$$

with $\omega_o = \sqrt{K/m_r}$ defined as the natural resonant frequency specific to the normal mode of interest. Using the definitions $\mathbf{P} = e \mathbf{x} N$ and $\mathbf{P} = N \alpha \mathbf{E}_{loc}$ as before,

$$\alpha(\omega) = \frac{e^2/m_r}{(\omega_o^2 - \omega^2 + i\gamma\omega)} \quad (2.38)$$

which gives the desired dispersion relation. Combining this with Equation 2.35 and generalizing for an ensemble of normal modes making up a spectrum of IR absorption,

$$3 \frac{\mathcal{N}^2 - 1}{\mathcal{N}^2 + 2} = \frac{N e^2}{m_r \epsilon_o} \sum_g \frac{f_g}{(\omega_g^2 - \omega^2 + i\gamma_g \omega)} \quad (2.39)$$

where the f_g are weighting factors known as oscillator strengths, which are normalized such that $\sum_g f_g = 1$, [Hecht and Zajac, 1997].

Note that for IR radiation, the molecular polarizability in Equation 2.35 can be separated into electronic and vibrational contributions. The electronic polarizability (α_e) may be considered frequency independent in the IR region such that,

$$\alpha(\omega) = \alpha_e + \frac{e^2}{m_r} \sum_g \frac{f_g}{(\omega_g^2 - \omega^2 + i\gamma_g \omega)} \quad (2.40)$$

Physically, α_e means that the molecular electronic cloud can be displaced independently of the internuclear separation [Milosevic and Berets, 1993], and, consequently, is the origin of the real part of the refractive index off-resonance from the vibrational modes. At resonance, however, α_e can add a dynamic component to the IR absorption rate under the influence of a static field, the specifics of which will be saved for later discussion in Chapter 5.

Of key importance in relating the IR absorption rate to the optical constants of the SAM is the absorption coefficient defined as $\mathcal{G}(\nu) = 4\pi\kappa\nu$, where ν is the wavenumber frequency of vibration. The absorption coefficients can be determined using Beer-Lambert analysis,

$$\ln(I_{IR}^m/I_{IR}^o) = -\mathcal{G}l \quad (2.41)$$

in terms of the absorption path length (l) through the SAM, where the $I_{IR}^{m,o}$ refer to measured and incident IR intensities. Once the absorption coefficients are determined from the absorbance spectrum, $\text{Re}(\mathcal{N})$ and $\text{Im}(\mathcal{N})$ parts can be found by a suitable means of satisfying the Kramers-Kronig relations [Kittel, 1986].

For an isotropic material the determination of \mathcal{N} from $\mathcal{G}(\nu)$ is a straightforward application of Equation 2.39. For anisotropic media, however, the orientation of the optical axes must first be defined and tensor representation must be used. Using the definitions $\mathbf{P} = (\varepsilon - \varepsilon_o)\mathbf{E}$ and $\varepsilon/\varepsilon_o = 1 + \chi$, the dependence of polarization on the electric field is in general $\mathbf{P} = \varepsilon_o\boldsymbol{\chi}\mathbf{E}$, with $\boldsymbol{\chi}$ being the susceptibility tensor [Fowles, 1989],

$$\boldsymbol{\chi} = \begin{bmatrix} \chi_{1,1} & 0 & 0 \\ 0 & \chi_{2,2} & 0 \\ 0 & 0 & \chi_{3,3} \end{bmatrix} \quad (2.42)$$

which is written in the diagonal form, having found a principal set of coordinate axes, e.g., the molecular coordinates of the SAM, such that the tensor is symmetric. The choice of coordinates for $\boldsymbol{\chi}$ is evident from the description in the following section of the SAM's molecular order and orientation such that uniaxial absorption symmetry ($\chi_{1,1} = \chi_{2,2} \neq \chi_{3,3}$) may be applied. With a material symmetry of this type and by definition $\mathcal{N}^2 = 1 + \chi$, the principal components of the refractive index are obtained as presented in Chapter 4.

2.2.3 Molecular Structure and Orientation of the SAM

In Section 2.1.1.4, a pseudo-orthorhombic packing arrangement of the SAM was identified and an average molecular tilt was defined. The tilt orientation of the SAM was further discussed in Section 2.1.2 in the context of ARXPS analysis. In this section, a closer look at the molecular ordering in the SAM is made for the purpose of establishing the appropriate symmetry for the analysis of the IR optical constants.

Figure 2.11 illustrates the molecular coordinates of the SAM. The molecular tilt (θ) is defined with respect to the substrate normal (lab frame), the azimuth is defined with respect to the GaAs cubic lattice, and a rotational orientation (ψ) of the C-C-C alkane backbone plane (twist) is defined about the molecular axis [Parikh and Allara, 1992]. In addition, the C-H stretching normal mode orientations are indicated with respect to the molecular frame.

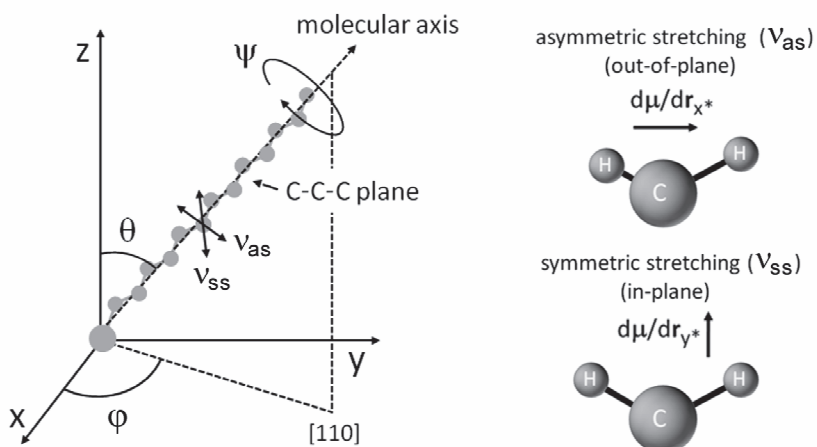


Figure 2.11. Molecular coordinates of the SAM defined by the tilt (θ) of the C-C-C backbone plane, the azimuth with respect to the cubic lattice, and the twist orientation (ψ) about the molecular axis. The C-H stretching normal mode orientations are indicated with respect to the C-C-C plane in the molecular coordinates (asterisk notation).

The twist orientation is $\pm 45^\circ$, meaning that a two-chain surface cell exists with each chain oriented such that the C-C-C planes are separated by 90° [Voznyy and Dubowski, 2008b]. Note that a 43° twist orientation has been observed by NEXAFS [McGuinness *et al.*, 2006], and a $43^\circ/133^\circ$ splitting of the twist orientation has been used to model the IR spectra of a

series of alkanethiol SAMs [McGuiness *et al.*, 2007b]. As made clear by the diagrams on the right of Figure 2.11, the symmetric mode vibrations are coplanar with respect to the C-C-C plane, and the asymmetric mode vibrations are perpendicular. Since the asymmetric and symmetric modes are mutually orthogonal and perpendicular to the molecular axis, and since these modes are equally split in orthogonal directions due to the mixed twist orientation in a two-chain surface cell, only a wavevector directed along the molecular axes would experience the same absorption coefficient for orthogonally polarized waves. This, by definition, describes the optical axis of a crystal with uniaxial absorption symmetry. Consequently, the molecular frame provides a natural set of coordinates with which to describe a diagonalized tensor from which the principal components of the refractive index can be obtained. A simplifying assumption is to consider that, off-resonance, $\text{Re}(\mathcal{N})$ is isotropic.

Since the optical constants are important to an understanding of the SAM as a unique phase with a distinct electronic configuration, the optical constants determined from analysis of the SAM will later be compared to those of bulk alkanethiol material. Liquid and polycrystalline alkanethiol are both considered isotropic phases. In the liquid phase, *gauche* conformations of the bond angles and the lack of molecular order result in random orientations of the dipole transition moments. In the polycrystalline phase, an *all-trans* conformation provides some degree of ordering of the transition moments on the molecular scale, but the micro-crystalline orientations are suitably randomized such that the material may be considered macroscopically isotropic. Prior to the start of this investigation, no direct measurements of the SAM IR optical constants had been published. During the course of the review of *Journal of Applied Physics*, “Observation of surface enhanced IR absorption coefficient in alkanethiol based self-assembled monolayers on GaAs(001)”, an article was released that obtained the SAM dielectric constants using IR ellipsometry [Rosu *et al.*, 2009]. However, no direct comparison with bulk alkanethiol data was reported and, therefore, any SAM specific differences were not addressed. The report of Rosu *et al.* does, however, provide a useful means of corroboration between their IR ellipsometry results and the Beer-Lambert method used in the present work, as will be discussed in Chapter 4.

2.2.4 Symmetry and the Optical Constants in IR Modeling of the SAM

In one application of the use of the optical constants, the absorption coefficient is cast in terms of its molar value and concentration ($\mathcal{G} = \mathcal{G}_{mol} c$), from which an estimation of the surface density can be made ($A/\mathcal{G}_{mol} = cl$) [Li *et al.*, 1993; Zawisza, 2003]. The working assumption in such an approach is the linearity of absorbance with surface coverage, and the correspondence of the absorption coefficient measured from the bulk phase to the conditions at the surface [Flink *et al.*, 2000]. Similarly, the IR optical constants of ODT have been estimated from Beer-Lambert absorption measurements of polycrystalline dispersions of octadecyl disulphide in KBr,[†] which were subsequently adapted for use in the simulation of SAM vibrational spectra [Parikh and Allara, 1992]. Again, any formulation that derives parameters characteristic of the SAM, using input from values measured in the bulk material state, relies for its accuracy on the mutual correspondence of the different phases. For SAMs, this correspondence may not always be direct [Nuzzo *et al.*, 1990], and consequently, it is of fundamental importance to have the optical constants measured directly. In Chapter 4, a Beer-Lambert approach is adopted in order to measure the IR absorption coefficients of the SAM phase, from which the IR optical constants are derived.

The uniaxial nature of the SAM in terms its absorption symmetry, as outlined above, is essential to accurate spectral modeling. In earlier reports, the anisotropic nature of alkane SAMs was handled in the following manner [Allara and Nuzzo, 1985; Nuzzo *et al.*, 1990]. First, IR reflectance spectra (I_{calc}) were obtained from transfer matrix calculations assuming an isotropic layer of bulk material, using \mathcal{N} obtained from solid phase polycrystalline dispersions in KBr, and using the SAM thickness determined from visible spectrum single-wavelength ellipsometry. Next, comparison with the experimentally determined spectra (I_{obs}) was made in order to determine the parameters of the molecular orientation. For example, tilt and twist orientations were obtained by comparison in terms of,

$$I_{obs} = I_{calc} 3 \cos^2 \theta_M \quad (2.43)$$

where θ_M specifies the angle between any given transition moment and the surface normal, which is coincident with the direction of \mathbf{E} for reflection from metallic surfaces, owing to the

[†] KBr is a salt that is transparent in the mid-IR frequently used as a substrate in compressed pellet form.

polarization surface selection rule. The factor 3 derives from spatial averaging of the randomized transition moments in an isotropic reference medium (see Appendix C). Direction cosines were then used to relate the molecular coordinates to the surface coordinate θ_M in order to obtain the tilt and twist values that gave the best solutions to Equation 2.43. However, this formulation assumes all transition moments are similarly aligned, i.e., it does not explicitly account for a two-chain surface cell, or account for the uniaxial nature of the SAM in the evaluation of I_{calc} . Accuracy is obtained because polarization selection artificially creates uniaxial symmetry about the surface normal, i.e., moments in the surface plane are not excited. Consequently, scalar values of \mathcal{N} suffice in Equation 2.43. Later, Parikh and Allara employed a 4×4 transfer matrix formulism that that could accommodate multi-layer anisotropy up to biaxial symmetry [Parikh and Allara, 1992]. For ODT-SAMs on Au, it was found that a two-chain surface cell with $\psi = 50^\circ / -48^\circ$, and uniaxial symmetry about the surface normal, gave the best fit to IR reflectance spectra. As cited above, the spectrum fitting process also relied on the input of \mathcal{N} obtained from polycrystalline material, which was later modified as an iterative variable inside an optimization routine.

Following the method of Parikh and Allara, in simulations of the IR reflectance spectra from alkylsiloxane monolayers on Si, uniaxial symmetry was assigned about the surface normal and vectorized elements of the material dipolar response ($|\mathbf{k}_{x,y,z}| = \kappa_{i,i}$) were written in terms of the bulk isotropic value (\mathbf{k}_{iso}) of the adsorbate [Hoffmann *et al.*, 1995],

$$\mathbf{k}_x = \mathbf{k}_y = \frac{3}{2} \mathbf{k}_{iso} \sin^2 \theta_M \quad (2.44a)$$

$$\mathbf{k}_z = 3 \mathbf{k}_{iso} \cos^2 \theta_M \quad (2.44b)$$

These equations derive from the spherical coordinate projections of the transition moments, with $\varphi_M = 45^\circ$ assumed for uniaxial symmetry, and the fact that $|\mathbf{k}_i| \propto M_i^2$. Note that Equations 2.44 are valid for non-absorbing substrates in the IR region (e.g., semiconductors) where polarization selection does not apply. No twist angle was incorporated into the modeling Hoffmann *et al.* used, other than to recognize that, for vertical chain orientations, uniaxial symmetry implies a random distribution of the methylene C-H stretching transition moments in the surface plane. This interpretation is entirely compatible with the $\psi = \pm 45^\circ$

twist angles as described in the previous section at zero tilt. For the non-zero tilt angles observed, however, the use of $\varphi_M = 45^\circ$ was arbitrarily assigned in order to satisfy the required symmetry, but in fact, there is no uniform azimuthal orientation of the molecular axis that yields true uniaxial symmetry about the surface normal. The assignment is valid because, in reality, the long-range ordering of the SAM is limited to domains that, despite having a uniform azimuthal orientation locally [McGuinness *et al.*, 2007b], may be oriented differently such that, on average, the surface normal remains the axis of symmetry, e.g., domains tilting towards both the $[110]$ and $[\bar{1}10]$ directions, which are crystallographically possible at the surface [Voznyy and Dubowski, 2008b]. In the previously cited work by Rosu *et al.*, a $\varphi_M = 45^\circ$ orientation was similarly adopted in their calculations of the IR ellipsometric response of ODT-SAMs on GaAs(001). Uniaxial symmetry about the surface normal was demonstrated experimentally by sample rotation in this case. Owing to the foregoing considerations, therefore, a uniaxial formulism will also be adopted for use in the Beer-Lambert analysis of the alkanethiol SAM-GaAs system as presented in Chapter 4.

2.3 Surface Energy Levels by the Kelvin Probe Method

2.3.1 Work Function Measurements

In Section 2.13, the surface energy levels were described in terms of XPS core level energies with respect to either the surface Fermi or vacuum level. The difference in these two energies is the surface work function, which quantifies the energy required for an electron to move to a position just beyond the surface. For semiconductors, there are two contributing factors to the work function ($q\phi_{wf} = S + W$) that must be considered. The first factor (S) is an external energy that is a constant function of the semiconductor material and its surface properties, including effects such as the electron affinity ($q\phi_{ea}$) and surface dipole potential (ϕ_d). The internal contribution (W) arises from factors that dictate the position of the bulk Fermi level ($q\phi_F$), e.g., doping concentration, and factors that determine the surface barrier or band-bending potential (Φ_{sb}), i.e., the ionization of surface defects and the space charge. Figure 2.12 illustrates the relationships among the parameters described for an n-type surface, including a surface dipole contribution that is arbitrarily assigned in the manner illustrated, and is meant to represent an adsorbed monolayer of polar molecules.

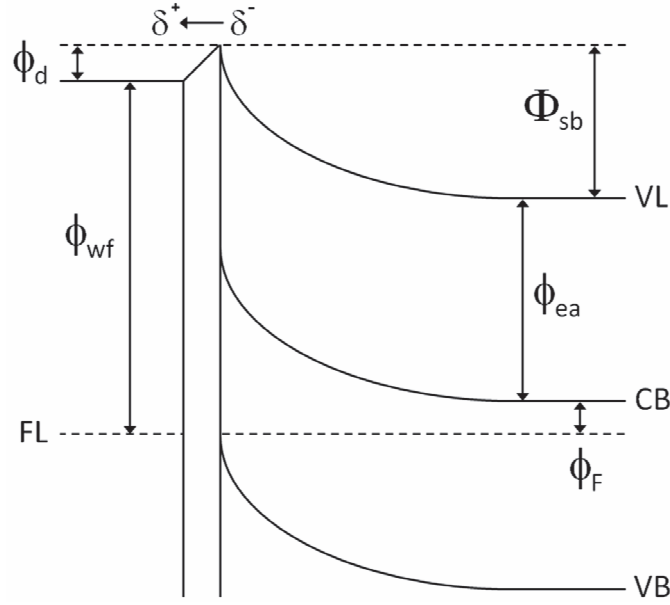


Figure 2.12. Factors contributing to the work function potential of a semiconductor n-type surface. The partial charge elements indicate the ordered adsorption of polar molecules in a monolayer.

For the example illustrated above, the work function is $q\phi_{wf} = q(\phi_F + \phi_{ea} + \Phi_{sb} - \phi_d)$.

Experimentally, the work function of a test sample ($q\phi_t$) can be measured using the Kelvin Probe method. Figure 2.13 illustrates the basic principle on which the method is based, referred to as the contact potential difference (CPD) [Kelvin, 1898; Richardson, 1912]. When two conductors are brought into electrical contact, the requirement for thermal equilibrium nullifies any difference between the two Fermi levels by a finite current (J). Consequently, a potential difference defined as the CPD is established, along with a corresponding electric field (E) extending between the two materials [Meller and Grasser, 2009]. The test sample work function is determined with reference to a calibration standard, usually Au, whose work function is known. In practice, the CPD can be measured with use of a vibrating Au probe brought in close proximity to the test surface in order to take advantage of the resulting change in capacitance [Zisman, 1932]. For a parallel plate geometry of area (A) and separation (d), the capacitance is $C = \epsilon A/d$. With the total charge (Q) held constant, increasing d increases the potential difference (V) between the probe and sample, since $V = Q/C$. Consequently, a complex time-dependent signal is generated in an external circuit whose peak-peak voltage can be represented as $V_{pp} = A_o(CPD - V_b)$, where A_o is an

instrument-dependent constant incorporating the dynamic elements of the capacitance. The backing potential (V_b) is an external circuit potential that just offsets the CPD such that current no longer flows, i.e., the vacuum levels remain aligned as in the initial condition of Figure 2.13. A voltage sweep of V_b produces a linear response of V_{pp} that when extrapolated through zero yields the CPD. This known as the off-null technique [Baikie *et al.*, 1991].

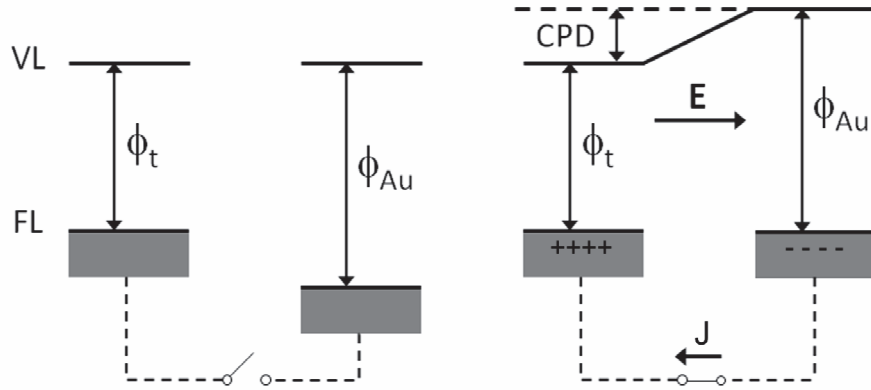


Figure 2.13. Energy level diagrams illustrating the establishment of the CPD. In the initial condition (left) a difference in the work function between test and calibration surfaces results in a Fermi level offset. Following electrical contact (right) an equilibrium is reached resulting in the CPD and corresponding electric field.

For semiconductors, the analogy with Figure 2.13 is direct [Kronik and Shapira, 1999], but for samples with high resistivity, such as semi-insulating GaAs, precautions with respect to contact type, stray capacitance and high noise are required. These will be described in later experimental sections.

Of interest to the present work is the change of work function associated with alkanethiol SAMs of various molecular lengths. As indicated in Figure 2.12, and as further illustrated in Figure 2.14, a monolayer of ordered polar molecules adds a surface dipole contribution ϕ_d to the work function, which will be referred to as the 2D dipole layer potential (DLP). Note that the dipolar orientation indicated in Figures 2.12 and 2.14 decreases the work function.

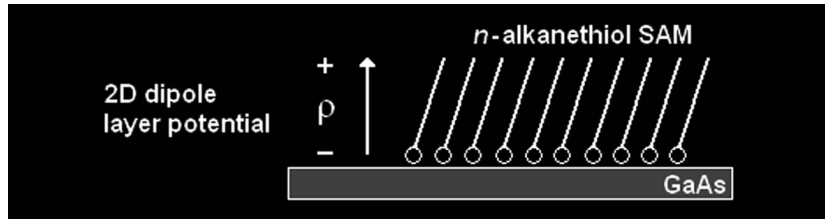


Figure 2.14. Illustration of the 2D dipole layer potential formed by a self-assembled monolayer on the GaAs(001) surface, after Marshall *et al.* [Marshall *et al.*, 2009b].

Since the molecular dipole changes linearly with respect to the number of methylene units, it is expected that the work function contribution of the SAM will also change in a linear manner. Previous results on Au bear this out; e.g., Howell *et al.* reported a work function slope of 20 mV/CH₂ based on results from ODT and dodecanethiol [HS(CH₂)₁₁CH₃] (DDT) SAMs [Howell *et al.*, 2002], and similarly, from the data reproduced in Figure 2.15, Lü *et al.* observed a slope of 14 mV/CH₂ [Lü *et al.*, 1999].

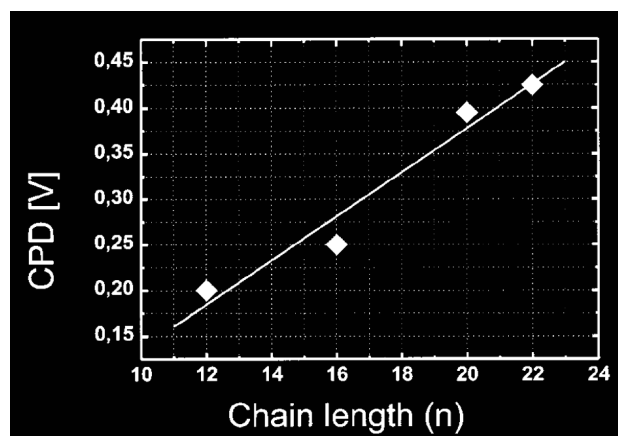


Figure 2.15. CPD as a function of molecular chain length for methyl terminated alkanethiol SAMs on Au (here, n = number of methylene units per molecule + 1), after Lü *et al.* [Lü *et al.*, 1999].

Based on a simple capacitor model of the 2D-DLP that accounted for the molecular dipole and SAM packing density, Howell *et al.* observed that the experimental work function slopes exceeded expectation by up to 2 \times , and noted that the discrepancy could be related to charge transfer between the molecule and substrate. More specifically, charge differences associated with bonding arise since the capacitor model of the SAM was based on the dipole moment of the free thiol molecule, whereas the actual SAM is comprised of bound thiolate. Effects such as the COMFE may also play a role in determining the actual surface dipole potential.

With respect to measurements of the work function of GaAs prepared with alkanethiol SAMs, no results are available that consider the chain length dependence in a similar manner. Therefore, it is meaningful to address this gap experimentally and see what physically insights may be obtained. Measurements and analysis similar to those described above will be conducted on the alkanethiol SAM-GaAs system in Chapter 5. Note that Aqua *et al.* has used the Kelvin Probe method to compare the dipole contributions of monothiol and dithiol ($n = 9$) alkanes on GaAs(001) [Aqua *et al.*, 2007]; however, although these results provide some basis for

comparison, as will discussed in the following section, they were obtained using a SPV saturation technique that does not always guarantee flat-band conditions can be obtained.

2.3.2 Surface Photovoltage and the Surface Barrier Height

In the foregoing discussions, the surface barrier height $q\Phi_{sb}$ was defined (Equation 2.18) and was graphically illustrated (Figures 1.6 and 2.12). However, only the equilibrium condition has been considered up to this point. In view of the present research objectives, an understanding of the steady-state response of the semiconductor to photo-excitation is required. In general terms, when excess carriers are created by optical absorption, both the SCR and surface charge density are modified resulting in recombination dynamics that cannot necessarily be predicted from the equilibrium picture. For example, the dead-layer model is based on a modification of equilibrium band-bending, but is only valid under certain approximations [Seker *et al.*, 2000]. According to what follows, the SCR is screened under sufficient photo-injection and, consequently, the surface barrier is reduced by the SPV the screening creates. The situation can be made more complex by changes in the occupation of surface states that arise as a result of adsorbate-induced differences in the surface trapping rates for excess electrons/holes. This effects the PL through a change of the capture cross-section in the SRV (as detailed in following sections). In terms of a PL-based biosensor platform, it is important to have insight into these processes in order to factor them into ongoing development efforts. Since the focus if this investigation is on the alkanethiol SAM interface with GaAs(001) as a coupling layer in a biosensor platform, the SPV response of thiolated GaAs is highly relevant. In this section, an introduction is given to the theory of SPV in order to support modeling results presented in subsequent chapters. In addition, a discussion of key literature results help place the specific objectives in context.

2.3.2.1 Excess Carrier Screening of the Space Charge Region

The screening effect of excess carriers on the SCR is modeled according to Garrett and Brattain [Garrett and Brattain, 1955], and Johnson [Johnson, 1958], who computed a surface space charge density (Q_{sc}) from Poisson's equation and Gauss's law using the Boltzmann relations for free carriers. In the depletion approximation Q_{sc} is valid to depth z_d ,

$$Q_{sc} = \sqrt{2kT \epsilon n_i F} \quad (2.45)$$

where F is a dimensionless function, which for n-type material can be written as,

$$F = \left[\Psi \left(e^{-\Omega} + \Omega - 1 \right) + \Psi^{-1} \left(e^{\Omega} - \Omega - 1 \right) + \Psi^{-1} \left(e^{\Omega} + e^{-\Omega} - 2 \right) \delta_n \right]^{\frac{1}{2}} \quad (2.46)$$

with doping factor $\Psi = \sqrt{p_o/n_o}$ specified by the equilibrium free carrier concentrations. The dimensionless value $\Omega = q\Phi/kT$ represents the steady-state, non-equilibrium band-bending under photo-excitation when the fractional excess electron density is $\delta_n = \delta n/n_o$. Note that $\delta_p = \Psi^{-2} \delta_n$ with $\delta n = \delta p$ outside the SCR. Note also that Equation 2.45 reduces to Equation 2.15 under equilibrium ($\delta_p = 0$) conditions. The charge screening inherent in Equation 2.45 can be made more explicit by expressing it in terms of the intrinsic Debye length (L),

$$Q_{sc} = 2q n_i L F \quad (2.47)$$

where $L = \sqrt{\varepsilon kT/2q^2 n_i}$. Next, the surface charge density for n-type surfaces can be written,

$$Q_{ss} = -q N_t f_e \quad (2.48)$$

where N_t is the 2D surface trap density, and f_e is the electron occupation factor to be defined shortly. Also note that charge neutrality requires,

$$Q_{ss} + Q_{sc} = 0 \quad (2.49)$$

For illustration purposes, assume a constant value of Q_{ss} ($f_e = 1$) and numerically solve Equation 2.49 for the surface potential $\Phi = \Omega kT/q$ as a function of the fractional excess carrier density in a manner following Aphek *et al.* [Aphek *et al.*, 1998]. Figure 2.16 plots the curves for the given values of N_t , assuming nominal parameters for GaAs and a doping concentration of 10^{17} cm^{-3} . Notice that the SPV saturates above $\delta_n = 1$, and that for larger surface trap densities the saturation SPV is greater. The first observation means that full screening does not come into effect until the excess minority carrier density exceeds the equilibrium majority carrier concentration ($\delta p > n_o$), which can be defined as the high-injection regime. The second observation reflects the fact that the saturation SPV is equal to and opposite in sign of Φ_{sb} . In this case, saturation implies a flat-band condition in the SCR. Saturation SPV methods are often used to determine the equilibrium band-bending,

but for GaAs especially, there are limitations rendering it uncertain that a saturation value can actually be obtained [Aphek *et al.*, 1998].

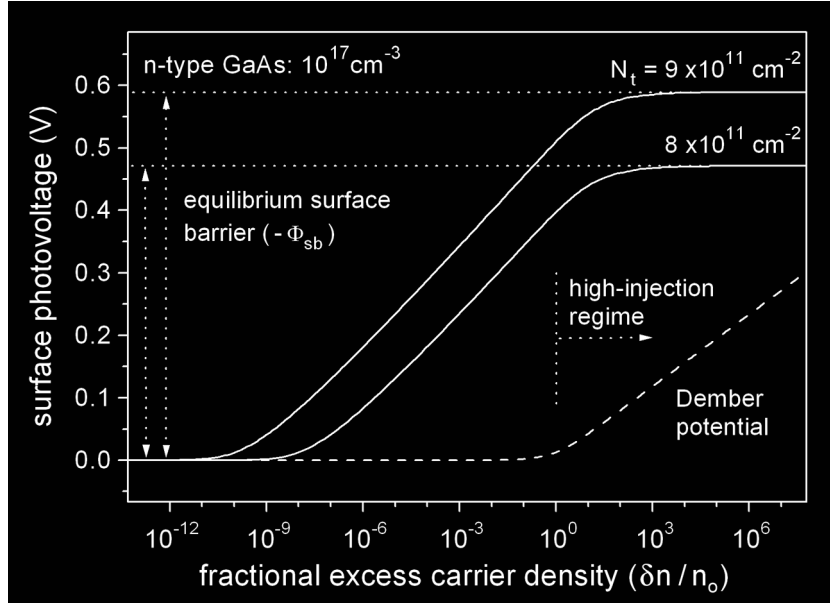


Figure 2.16. Calculated SPV (solid lines) as a function of the excess carrier density for n-type GaAs under the assumed condition that the surface charge density ($-q N_t$) remains constant. The Dember potential (dashed line) is additive with respect to the SPV in the high-injection regime.

One limitation is the Dember potential, and another is the fact that the assumption of a constant surface charge on which the method is based may not be valid. In brief terms, the Dember potential is a voltage induced across the sample bulk that is due to the ambipolar diffusion of excess carriers out of the excitation region [Kronik and Shapira, 1999]. The difference in electron/hole carrier mobility, which is about 20× for GaAs, results in a static field between carrier pairs and, consequently, is the source of a potential difference. The Dember potential is additive with respect to the SPV in a Kelvin Probe measurement and increases in the high-injection regime, as illustrated in Figure 2.16. This is a major limitation to the observation of SPV saturation for GaAs. Surface charge modification, and the limitations it imposes on SPV saturation are discussed in the following section.

2.3.2.2 Surface Charge Modification

In the last section, the example discussed assumed a constant surface charge density. Physically, this can be related to fixed surface trapped charge having a slow exchange rate with the bulk material, e.g., those trapped within a surface oxide layer. [Johnson, 1958]. In

addition, the surface charge varies according to the changing population of surface states, i.e., by virtue of additional fast trap states that have occupation statistics (f_n) corresponding to Shockley-Read-Hall surface recombination (Section 2.4.3), and that are ionized based on their energy level (E_t) within the band-gap and the relative position of the surface Fermi level, which varies according to the degree of photo-induced band-flattening. The surface electron and hole capture coefficients, determined by their respective capture cross-sections and thermal velocities ($C_{n,p} = \sigma_{n,p} v_{th\,n,p}$), also factor into the Shockley-Read-Hall process and contribute to the overall occupation of surface states.

The analytical treatment used for surface state modeling has been presented in papers by Johnson, Apek *et al.*, and Kronik and Shapira, as cited above. Expressions for the occupation factor are given in terms of the fractional carrier density, doping factor, and surface potential as already defined. In addition, the ratio of hole/electron capture coefficients is introduced ($\chi^2 = C_p/C_n$). For acceptor states the occupancy factor (f_n) is written in the following terms,

$$f_n = \left[1 + e^{-(\Phi - \ln \Psi + \nu)} \left(\frac{1 + \Gamma(1 + \delta_n)(1 + \Psi^{-2}\delta_n)}{(1 + \Gamma)(1 + \delta_n)} \right) \right]^{-1} \quad (2.50a)$$

$$\Gamma = \frac{\chi e^{2\nu} e^{-(\Phi - \ln \Psi + \nu)}}{1 + \delta_n} \quad (2.50b)$$

$$\nu = (E_g / 2 - E_t) kT^{-1} \quad (2.50c)$$

Note that for donor states $f_p = 1 - f_n$. With Equations 2.47 and 2.48, both screening and surface charge modification effects can be accounted for. In the approach to modeling, a numerical solution to Equation 2.49 is obtained, as in the example of Figure 2.16. As a second example, Figure 2.17 illustrates the effect of a change in the ratio of carrier capture coefficients assuming a single discrete acceptor state defect located at mid-gap. For surface states, the factor χ can vary over several orders of magnitude depending on its local potential [Kronik and Shapira, 1999; Seker *et al.*, 2000]. Note that a decrease in χ for the depleted n-type surface will result in a smaller SPV at a given excess carrier density because of the persistence of negative surface charge. In other words, a relative decrease in minority carrier

trapping favors the occupation of acceptor states resulting in lower SPV values. Similarly, the compensation of surface charge by more efficient minority carrier trapping results in the SPV saturation condition being met at lower injection rates. Limiting values are reached, similar to those described in Aphek *et al.*, that bound the SPV curves between $10^{-5} < \chi < 10^5$, i.e., the extrema illustrated in Figure 2.17 are envelope functions. More complex SPV curves can result from the incorporation of other defect levels into the model, and may result in apparent saturation plateaus that do not correspond to the flat-band condition [Aphek *et al.*, 1998].

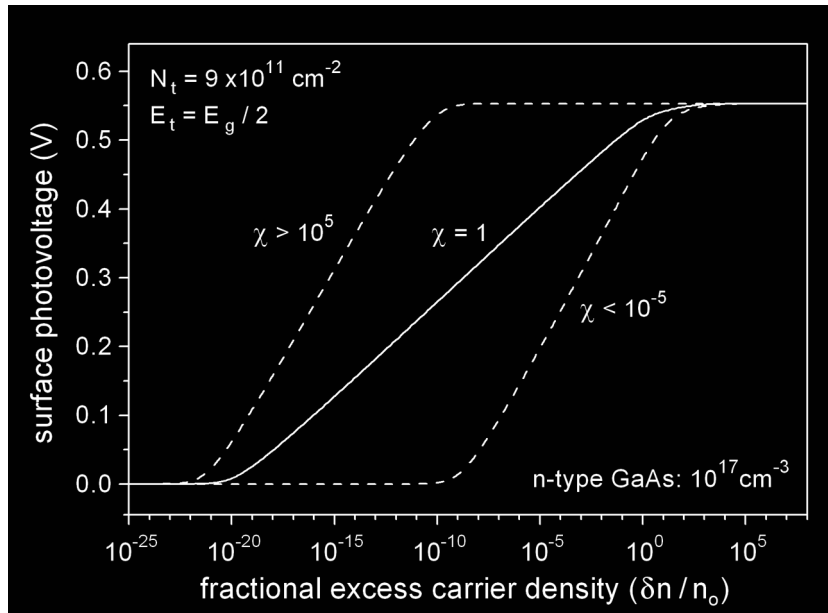


Figure 2.17. Calculated SPV as a function of the excess carrier density for n-type GaAs with a discrete level acceptor state located at E_t and having surface density N_t . In this example, the occupation factor varies under photo-injection according to the ratio of carrier capture coefficients χ .

Though a single discrete acceptor defect was assumed in the example above, a more continuous distribution of surface state energies, or a summation over several discrete defect levels may be considered [Kronik and Shapira, 1999]. In Chapter 6, a single discrete level defect model is adopted for the model analysis of experimental SPV data, the justification for which will derive from the XPS study of the surface Fermi level and its analysis in terms of the Advanced Unified Defect Model (AUDM) owing to Spicer *et al.* [Spicer *et al.*, 1988]. In this case, Equation 2.48 provides an adequate approximation to the surface charge density.

2.3.2.3 Equilibrium Band-Bending in SPV and PL Models

The uncertainty of obtaining the equilibrium band-bending potential by the saturation SPV method for GaAs requires that another method be used. In an earlier section, the use of XPS to determine the surface Fermi level was discussed, and it was noted that with knowledge of the bulk Fermi level position, the equilibrium surface barrier height is easily determined (Equation 2.18). This information provides an important constraint in the SPV model. SPV data observed in the low-injection regime may then be analyzed appropriately; however, no literature data on the SPV of alkanethiol SAMs on GaAs exists. It was mentioned earlier that Aqua *et al.* reported using the SPV saturation method to obtain the equilibrium band-bending potential of monothiol and dithiol alkane SAMs on GaAs in an attempt to estimate the overall change in work function, but only the final result was reported, i.e., the surface dipole contribution attributed to the SAMs. Tomkiewicz *et al.* made intensity-resolved SPV measurements under low-injection conditions and reported that the change in SPV observed following S_2Cl_2 treatment of GaAs was attributed to differences in the initial band-bending, i.e., the degree of electronic passivation [Tomkiewicz *et al.*, 2009]. However, based on the possible change in surface charge under illumination, especially those that are induced by SRV related modifications of χ , as introduced above, the conclusions of Tomkiewicz *et al.* may not be complete. In subsequent chapters, SPV modeling of the SAM-GaAs system will incorporate the equilibrium band-bending determined from XPS.

In view of the effect changes in the capture cross-sections may impart, an important result was obtained by Lunt *et al.* who reported that SRV reduction was a significant factor contributing to PL enhancement in sulphide-treated GaAs, including the organic thiols. This conclusion was based on time-resolved PL under high-injection conditions, where an increase in carrier lifetime implies a decrease in the SRV by reduction of the trap density N_t or carrier capture cross-section $\sigma_{n,p}$ of the relevant surface states [Lunt *et al.*, 1991]. However, distinction between these two factors cannot readily be made without prior knowledge of the initial band-bending, since N_t also relates to the surface charge density at equilibrium. The XPS and SPV analysis presented in this work, along with analysis of the PL response of the interface, enables these distinctions to be made.

2.4 Photoluminescence of the SAM-GaAs Interface

In the following sections, an introduction is made to some the foundational aspects of PL as it relates to conditions at the semiconductor surface, and how modification of these conditions affect the PL intensity. In view of the objectives of this thesis, the intent here is to define the appropriate terms for a semi-quantitative discussion of the manner in which a sensor may operate, but more importantly, to be able to make the necessary distinctions in the analysis of PL data following the passivation of GaAs(001) with alkanethiol SAMs. Such analysis relates to the interpretation of SPV results, as mentioned above, with respect to differentiating the component elements of the SRV.

2.4.1 Near-Surface Model of the Photoluminescence

In n-type material under low-injection conditions, the rate of excess carrier recombination is limited by the time-dependent concentration of holes (minority carriers) defined as,

$$\delta p(t) = \Delta p e^{-t/\tau_p} \quad (2.51)$$

where Δp is the injected hole concentration and τ_p is the minority carrier lifetime defined in Equation 1.3, and as such includes both radiative and non-radiative processes. The appropriate rate equation for minority carrier loss is therefore,

$$\frac{\partial}{\partial t} \delta p^- = -\frac{\delta p}{\tau_p} \quad (2.52)$$

The volume generation rate of excess electron-hole pairs is [Vilms and Spicer, 1965],

$$\frac{\partial}{\partial t} \delta p^+ = I_{rad} (1 - R) \alpha_{ex} e^{-\alpha_{ex} z} \quad (2.53)$$

where I_{rad} is the irradiance of the excitation source, R is the surface reflectance and α_{ex} is the absorption coefficient at the excitation wavelength. The built-in field $\mathcal{E}(z)$ in Equation A.5 and the non-uniform generation specified in the above equation create drift and diffusion currents, respectively, which are expressed, e.g., in the current density for holes,

$$J_p(z) = q \mu_p \delta p(z) \mathcal{E}(z) - q D_p \frac{\partial}{\partial z} \delta p(z) \quad (2.54)$$

where μ_p is the minority carrier mobility and D_p is the diffusion coefficient. Equation 2.54 is substituted in the continuity equation [Streetman and Banerjee, 1999],

$$\frac{\partial}{\partial t} \delta p(z, t) = -\frac{1}{q} \frac{\partial}{\partial z} J_p(z) + \frac{\partial}{\partial t} (\delta p^+ + \delta p^-) \quad (2.55)$$

to obtain the general carrier transport equation [Geisz *et al.*, 1995],

$$\frac{\partial}{\partial t} \delta p(z, t) = D_p \frac{\partial^2}{\partial z^2} \delta p - \mu_p \frac{\partial}{\partial z} [\delta p \mathcal{E}(z)] + I_{rad}(1-R) \alpha_{ex} e^{-\alpha_{ex} z} - \frac{\delta p}{\tau_p} \quad (2.56)$$

Under steady-state conditions the time-derivative is zero; consequently, the spatial distribution of excess holes can be found by solution of Equation 2.56 subject to the following boundary conditions [Mettler, 1977],

$$D_p \frac{\partial}{\partial z} \delta p(z) \Big|_{z=z_d} = S_{eff} \delta p(z_d) \quad (2.57a)$$

$$\delta p(\infty) = 0 \quad (2.57b)$$

where S_{eff} is the effective surface recombination velocity. S_{eff} is defined at the depletion depth z_d and represents the diffusion flux with which minority carriers are swept into the SCR by the built-in field, where they recombine non-radiatively at the surface. Generation and transport in the SCR can be ignored in this model if $z_d \ll 1/\alpha_{ex}$ and $z_d \ll L_p$, where L_p is the diffusion length for holes ($L_p = \sqrt{D_p \tau_p}$) [Kronik and Shapira, 1999]. Consequently, the boundary z_d serves as the effective plane at which to define the SRV in terms of the Shockley-Reed-Hall process [Mettler, 1977], to be discussed in a following section. Note that the above equations also generalize directly to p-type doping.

A solution to Equation 2.56, subject to Equations 2.57, can be obtained numerically as a boundary-value problem [Geisz *et al.*, 1995], or can be solved analytically under the above constraints on z_d [Mettler, 1977]. Note that as result of the use of z_d as a boundary of the problem, the drift component in Equation 2.56 is zero, since $\mathcal{E}(z \geq z_d) = 0$. In addition, it means that recombination may ignored in the SCR, which is in accordance with the principle

of a ‘dead-layer’ [Wittry, 1967]. Once $\delta p(z)$ is determined, the PL can be analyzed in terms of the radiative recombination rate [Vilms and Spicer, 1965],

$$PL \propto \int_{z_d}^{\infty} \frac{\delta p(z)}{\tau_r} dz \quad (2.58)$$

where τ_r is the radiative lifetime as defined in Appendix D. Based on the analytical solution to Equation 2.56 and with Equation 2.58, according to Mettler, the final result is,

$$PL \propto I_{rad} (1 - R) e^{-\alpha_{ex} z_d} \left(\frac{1}{\alpha_{ex} L_p} + \frac{1}{S_{rv}} \right) \quad (2.59)$$

where S_{eff} has been redefined by a reduced value $S_{rv} = S_{eff} \tau_p / L_p$ for convenience. Equation 2.59 makes explicit the separation of the dead-layer and SRV effects. The former is tied into the exponential term by virtue of z_d , and the latter is connected to the term involving S_{eff} .

2.4.2 Sensor Operation Based on the Dead-Layer

Since the dead-layer model figures prominently in the literature on PL-based sensor operation, it is worth the effort to reflect on it to basic level of understanding. Equation 2.59 indicates that if there is a contraction/increase of the depletion depth the PL will increase/decrease. Under the condition that the SRV is constant, a PL ratio can be defined,

$$\frac{PL_2}{PL_1} = \exp[-\alpha_{ex} (z_{d2} - z_{d1})] \quad (2.60)$$

where the numerical subscripts refer to initial and final conditions involving analyte absorption that results in a change of the depletion depth [Seker *et al.*, 2000]. With this expression, a calculation of some basic sensitivities is simple. Rearranging Equation 2.60,

$$\Delta z_d = \frac{1}{\alpha_{ex}} \ln \left(\frac{PL_1}{PL_2} \right) \quad (2.61)$$

and by substitution of Equation 2.14 in 2.15, the difference equation for the surface charge is,

$$\Delta Q_{sc} = q N_d \Delta z_d \quad (2.62)$$

Combining these two and rearranging gives,

$$\frac{PL_2}{PL_1} = \exp\left(-\frac{\alpha_{ex} \Delta Q_{sc}}{q N_d}\right) \quad (2.63)$$

where it becomes apparent that shorter wavelengths (increased α_{ex}) and lower doping concentrations (but lower PL brightness) are more conducive to higher sensitivities. Equation 2.63 clearly shows that if there is a reduction in the surface charge density ($\Delta Q_{sc} < 0$), there is a corresponding increase in PL. As an example, consider a low n-doped sample (10^{16} cm^{-3}) and an excitation wavelength of 532 nm ($\kappa = 0.322$). In this case, the reduction in surface charge density for a modest PL increase of 20% would be approximately $2.5 \times 10^{10} \text{ cm}^{-2}$. This represents about a 25 nm contraction of the SCR. To put this in context, assume a mid-gap surface Fermi level, in which case Equations 2.17 and 2.18 yield a surface barrier height of 620 meV, that when applied to Equation 2.15 gives an initial surface charge density of $3 \times 10^{11} \text{ cm}^{-2}$. In other words, to yield a PL enhancement of 20%, about 1 part in 10 of the existing surface charge has to be displaced. Furthermore, Equation 2.63 indicates that the PL sensitivity increases when the space charge ($q N_d$) is reduced, e.g., if Equation 2.63 is combined with Equations 2.15 and 2.49,

$$\frac{\Delta Q_{ss}}{Q_{ss}} \propto \ln\left(\frac{PL_1}{PL_2}\right) \quad (2.64)$$

Consequently, by virtue of the passivation of surface defect states, which lowers the initial surface barrier, the sensitivity of the device will improve. However, there is an obvious trade-off in dynamic range for designs that exploit dead-layer contractions.

The manner in which the surface charge density gets displaced/augmented in a biosensor relates to the electrostatics of the problem. For example, the addition of fixed charge that adds to the surface charge density, and that may be represented in the same manner as charge trapped in an oxide layer, tends to increase the surface potential and therefore the depth of the SCR resulting in quenched PL. Two examples from the literature that cite this type of interaction are: i) the increase in negative surface charge upon the functionalization of semi-insulating GaAs surfaces with thiol-derivatized aptamer probes for adenosine triphosphate (ATP) detection [Budz *et al.*, 2010], and ii) the presence of halide anions following the gas-induced oxidation of silo-ferrocene functionalized n-doped GaAs surfaces [Van Ryswyk and Ellis, 1986]. Furthermore, Budz *et al.* argued that, based on conformational

changes of the aptamer following complementary base-pair coupling with ATP, the effective (volume) charge density in the sensing layer was reduced resulting in PL enhancement. In this work, the sensing layer was modeled as an ion-permeable membrane immersed in an electrolyte requiring a consistent solution to both the Poisson equation in the semiconductor and the Poisson-Boltzmann equation for solvation effects across the electrolyte-membrane [Landheer *et al.*, 2005]. For *in situ* measurements of this type, the simple fixed charge arguments suggested above do not suffice, but apply in principle. Details related to the interactions of the thiol-GaAs surface complex will be discussed in subsequent chapters.

A final comment in view of Equation 2.64 relates to the conditions that validate the equilibrium picture of the dead-layer model. In terms of the surface barrier height, the conditions that validate this assumption are: i) low-injection, and ii) a high SRV. Looking back at Figures 2.16 and 2.17, some appreciation of this is obtained by recalling that a low SPV implies that SCR screening is reduced. The first condition is obvious in that a low SPV results from low injection. In view of the second condition, if the SRV is high, the excess carrier concentration is reduced, which effectively right-shifts the SPV curve to lower values for a given irradiance. Following this logic, a third condition may be added for n-type surfaces, that being, a value of $\chi \ll 1$. These matters will be given further consideration following the SPV analysis of the SAM-GaAs interface in Chapter 6.

2.4.3 Non-Radiative Recombination Theory

In this section, expressions related to the rate of non-radiative recombination are given, as originally developed by Shockley, Read and Hall [Shockley and Read, 1952; Hall, 1952], in order to formalize terms used in subsequent discussions, particularly as they relate to the SRV. A good review of its formulation is found in Kronik and Shapira.

Consider Figure 1.5 for general bulk processes. Under equilibrium conditions, the process of electron/hole capture is balanced with thermal emission back to the conduction/valance band. Since the emission rate of the trap level at E_t is proportional to its occupancy and density ($n_t = f_n N_t$), the emission rate for electrons is,

$$r_{ne} = e_n n_t \quad (2.65)$$

where e_n is a proportionality constant. For electron capture, the rate is proportional to both the available states ($p_t = f_p N_t$) and the occupation of electrons in the conduction band,

$$r_{nc} = C_n n p_t \quad (2.66)$$

where C_n is the previously defined capture coefficient for electrons (Section 2.3.2.2). Equations 2.65 and 2.66 are equal under equilibrium conditions, therefore,

$$e_n = C_n n p_t / n_t \quad (2.67)$$

From Fermi-Dirac statistics, the occupancy factor at equilibrium is,

$$f_n = \frac{1}{1 + \exp\left[\left(E_t - E_f\right)/kT\right]} \quad (2.68)$$

Since $f_p = 1 - f_n$, Equation 2.67 reduces to,

$$e_n = C_n n_1 \quad (2.69)$$

with,

$$n_1 = n_t e^{(E_t - E_i)/kT} \quad (2.70)$$

when the Fermi level is coincident with the trap level $E_t = E_F$. Now the rate equations are,

$$r_{ne} = C_n n_1 f_n N_t \quad (2.71)$$

$$r_{nc} = C_n n (1 - f_n) N_t \quad (2.72)$$

and similarly for holes,

$$r_{pe} = C_p p_1 (1 - f_n) N_t \quad (2.73)$$

$$r_{pc} = C_p p f_n N_t \quad (2.74)$$

Under steady-state injection, the rate of recombination of electrons and holes is equal,

$$\frac{dn}{dt} = r_{ne} - r_{nc} = \frac{dp}{dt} = r_{pe} - r_{pc} \quad (2.75)$$

Equations 2.71 to 2.74 are substituted in 2.75, which is then solved for f_n and inserted back into one of the recombination rate equations (LHS or RHS of Equation 2.75) to obtain,

$$U_{nr} = \frac{C_n C_p (np - n_i^2) N_t}{C_n (n + n_1) + C_p (p + p_1)} \quad (2.76)$$

using $n_1 p_1 = n_i^2$ from the law of mass action. Equation 2.76 is a form of the well-known Shockley-Read-Hall expression. Dividing by $C_n N_t$ and using $\chi^2 = C_p / C_n$, Equation 2.76 is plotted in Figure 2.18 as a function of E_t within the band-gap for GaAs.

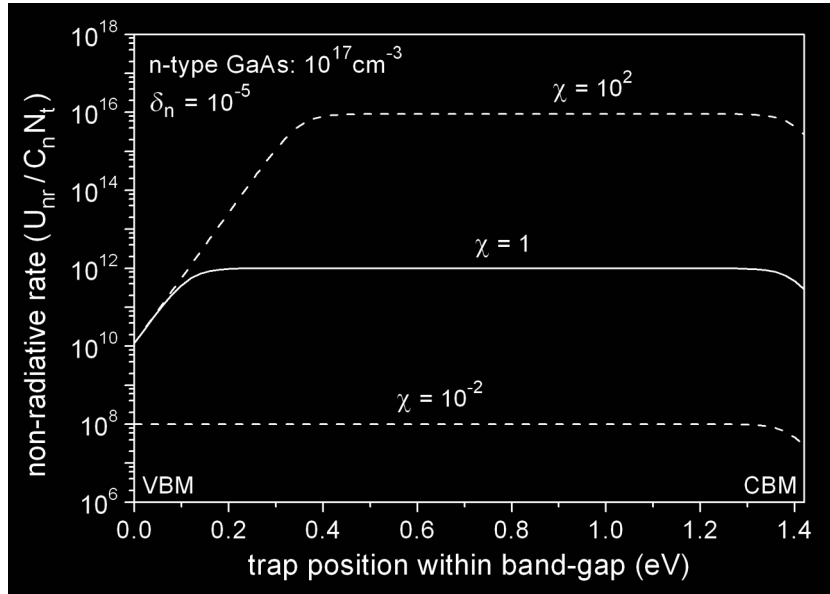


Figure 2.18. Shockley-Reed-Hall recombination U_{nr} for a trap level E_t located within the band-gap of GaAs for various values of χ . The rate has been normalized by the electron capture coefficient C_n and trap density N_t . The fractional excess carrier density δ_n is in the low-injection regime.

For n-type material in the low-injection limit ($n_o \gg p_o$, $\delta p \gg p_o$ and $\delta n \ll n_o$), the figure shows that the rate of recombination rate is maximized over a large middle portion of the band-gap, with scaling that is well approximated by $\chi^2 \delta p$, therefore,

$$U_{nr} = C_p N_t \delta p \quad (2.77)$$

can be considered the dominating expression. Equation 2.77 also demonstrates the dependence of the overall non-radiative rate on minority carrier recombination. In a manner analogous to the expressions developed for the radiative rate in Appendix D, Equation 2.77 gives as the minority carrier non-radiative lifetime,

$$\tau_{nr} = 1 / C_p N_t = 1 / \sigma_p v_{th,p} N_t \quad (2.78)$$

as first introduced in Equation 1.5.

For surface specific recombination, N_t is dimensioned as a surface quantity (cm^{-2}) and Equation 2.78 is then referred to as the surface lifetime, with the quantity $\sigma_p v_{th,p} N_t$ defined as the SRV. In this case, although the surface lifetime is not dimensionally correct, it now has units s/cm, the SRV is used as a fundamental parameter of the surface. To obtain the actual surface lifetime, a convenient estimation will be to multiply by the diffusion length L_p . The SRV is technically described with respect to recombination processes at the surface boundary, but as specified above, it can effectively be defined at the boundary z_d where drift processes dominate minority carrier transport to the surface.

As a final note to this section, consider the PL intensity described by Equation 2.59. Recall that screening in the SCR will occur at sufficient excitation power densities where the surface potential falls to zero in the flat-band condition. In this case, the PL yield will maximize since there will be no drift current contribution to the SRV, i.e., the dead-layer will have been effectively screened out. This was the reason Lunt *et al.* performed their time-resolved studies under high-injection conditions; they wanted to isolate for SRV effects in their experiments. In the analysis of the PL that is to follow, yield saturation under steady-state conditions provides useful insight into the SRV in a similar manner.

2.5 Chapter Summary

The chapter began with a discussion of the chemical passivation of GaAs(001) by sulphides and thiols within the context of the XPS technique. Emphasis was placed on the composition of the interface with respect to chemisorbed thiolate and its complementary GaAs surface species. Identified as requiring further analysis were: i) component assignments with respect to surface appropriate concentrations, including the As⁰ species, and ii) the fractional coverage of the SAM by ARXPS.

Although the chemical passivation of the SAM-GaAs interface has been well-studied, relatively little has been concluded in terms of its electronic passivation. The need to quantify the equilibrium surface barrier height by XPS was established and the means by which this could be obtained was introduced in terms of the relevant surface energy levels.

Next, the foundations of IR spectroscopy were introduced, as they relate to the analysis of alkane materials, with a view to establishing the IR optical constants of the SAM and the possible identification of unique dielectric properties. The molecular ordering of the SAM was considered carefully, as it forms the basis of the uniaxial symmetry used to model the IR optical response.

The Kelvin Probe method of measuring the surface work function was discussed as a way to obtain the surface dipole contribution of the SAM, and the SPV was identified as a dynamic property of the surface under photo-excitation where both screening and surface charge modification processes are relevant. Possible failure of the SPV saturation method for GaAs requires that other methods be imported to support SPV modeling and it was proposed that the surface barrier height determined from XPS could be used.

Lastly, the PL was described in terms of two physical effects applicable under low level excitation: i) a non-emissive layer that is related to the surface barrier, and ii) minority carrier transport and recombination mechanisms that are quantified by an effective SRV. The role these play in PL-based analyte sensing was also discussed. The effect thiol-GaAs coupling has on the steady-state PL is already known to be significant with respect to SRV reduction. However, by incorporating knowledge of the dynamic effects of the initial surface barrier and its steady-state response, decoupling of the dead-layer effect from the SRV, and of the SRV into its constituent factors is possible.

CHAPTER 3:

COMPOSITION and STRUCTURAL ANALYSIS by XPS

The experimental results and physical analysis presented in this chapter are specific to the stoichiometric composition and structural morphology of alkanethiol SAMs fabricated on the GaAs(001) surface. Following a description of the experimental techniques, including the methods of sample preparation, representative spectra and the atomic percentages of etched-only and SAM-passivated samples are provided. Emphasis will be placed on the composition of the interface with respect to chemisorbed thiolate, its complementary GaAs surface species, and to the degree of surface oxidation. Analysis of the component assignments will be performed and compared to expected results based on models introduced in Chapter 2. More detailed structural analysis using ARXPS follows, which will focus on the SAM fractional coverage and the surface concentration of As⁰ following SAM preparation.

3.1 Experimental Details

3.1.1 Sample Preparation

The method of sample preparation used throughout this work follows those prescribed in McGuiness *et al.* [McGuiness *et al.*, 2006] for highly ordered, CH₃ terminated *n*-alkanethiol SAMs on GaAs(001). The required elements adapted from this procedure are: i) the use of degassed ethanol solvent, ii) the use of 28% NH₄OH/H₂O (ammonium hydroxide) for oxide etching, iii) the use of a nitrogen-purged glovebox for SAM processing, and iv) a SAM “incubation” period of at least 20 hours, as described in the following.

3.1.1.1 Wafer Cleaning

GaAs(001) wafers were cleaved into squares along <110> directions with a minimum dimension of 4 mm per side. About 15 ml each of OpticlearTM, acetone and isopropanol were measured into separate 40 ml beakers. The wafers were then cycled through the fluids sequentially, inserting each beaker into a sonic bath for 5 minutes. Excess liquid was removed from the samples with a dry N₂ stream upon transferring from one cleaning solution to the

next. In order to avoid having the samples overlap in the sonic bath, the beakers were tilted such that the wafer pieces were aligned about the beaker's bottom edge. Samples were stored in isopropanol until they were ready to proceed to the etching stage.

3.1.1.2 Ethanol Solvent Degassing

Approximately 300 ml of anhydrous ethanol was measured into a 500 ml Erlenmeyer flask. A sintered glass frit bubbling tube was inserted and the neck was sealed with paraffin film. The flask was positioned with a retort stand into a sonic bath such that the bath and liquid levels in the beaker were approximately equal. During sonication, small adjustments to the position of the flask in the bath were made in order to achieve the resonance that resulted in the maximum cavitation bubble rate in the ethanol. A dry N₂ line was then attached to the bubbling tube. Selecting a gas flow rate low enough to avoid splashing, minimizing the evaporation of ethanol consequently, N₂ was flowed through the solution for at least 3 hours.

3.1.1.3 Preparation of Thiol Solution

Depending on the molar mass of thiol used, the required volume of ethanol solvent was calculated to achieve a 2-3 mM solution. For example, hexadecanethiol (HDT) [CH₃(CH₂)₁₅SH] has a molar mass of 258.5 g mol⁻¹; if the measured quantity of thiol is x_m milligrams, then the volume of solvent required is $V_{sol} = x_m / 2 \text{ mM} \times 258.5 \text{ g mol}^{-1}$ milliliters. It is convenient to use 15-20 ml of solution in 40 ml beakers, therefore the mass of HDT should be approximately 9 mg. One drop of 28% NH₄OH/H₂O (~ 0.05 ml) was added to the ethanol solvent, which equates to a molarity of about 100 mM. This drives the solution to a pH of 10, as measured by an electrode pH meter. Since the acid dissociation constant (pK_a) of alkanethiols exceeds a value of 11 [Danehy and Parameswaran, 1968], it is not likely the addition of the ammonium hydroxide promotes significant dissociation of thiol into thiolate in solution. This can be easily calculated by the dissociation fraction,

$$D(pH) = \frac{1}{1 + 10^{(pK_a - pH)}} \quad (3.1)$$

Consequently, the use of NH₄OH/H₂O in the protocol of McGuiness *et al.* likely adds only a marginal benefit in terms of maintaining an oxide free GaAs surface throughout the SAM incubation process following the etching stage as described next. In order to fully dissolve the

bulk thiol, the beakers were sealed with paraffin film and sonicated for about 30 seconds, or until the liquid was clear.

3.1.1.4 Etching and SAM Incubation

The following procedure was performed in a N₂-purged glovebox. The cleaned GaAs wafers were removed from the isopropanol and dried with a N₂ stream. An amount of ammonium hydroxide was dispensed into a Petri dish in sufficient volume to make a depth of at least 3 mm. Using Teflon tweezers, the wafers were submerged into the dish for a period of 2 minutes. Recalling the discussion of Section 2.1.1.3, treatment with NH₄OH removes the GaAs native oxides by dissolution without attacking the underlying substrate. The samples were then removed from the etchant, immediately flushed with degassed ethanol, and transferred wet (maintaining a surface bead of ethanol) directly into beakers containing the prepared thiol solutions. The beakers were then resealed with paraffin film and stored in a N₂ environment for period of at least 20 hours to allow the SAM to form. Reference wafers were similarly processed and immersed in degassed ethanol, without thiol, as control samples.

After the incubation period, the samples were rinsed vigorously with isopropanol and dried with a N₂ stream. Rinsing was repeated to ensure a mirror-like finish was attained. An important factor to consider in the preparation and measurement analysis of the SAMs is the time stability of the interface. It is understood these surfaces are limited by the extent to which the SAM provides a physico-chemical barrier to the reoxidation of the GaAs interface. For example, McGuinness *et al.* reported that ODT-SAMs remained oxide free beyond 2 weeks as determined by XPS [McGuinness *et al.*, 2006], while Nesher *et al.* reported that the integrity of shorter-chain DDT-SAMs was limited to less than 3 days [Nesher *et al.*, 2006]. Consequently, all samples were measured immediately, or were kept under N₂ conditions until required, in order that the data reflected the best possible initial condition of the samples.

3.1.2 Recording of XPS Spectra

XPS spectra were recorded using a Kratos Analytical Ltd. Axis Ultra DLD instrument. Following preparation, the wafers were immediately loaded into the sample transfer chamber, which was subsequently evacuated to match the ultra-high vacuum conditions in the analysis chamber ($< 10^{-8}$ Torr). A projected analysis area (700 μ m x 300 μ m) was defined by selection of a slot aperture in the transfer lens column. The monochromatic Al K α (1486.6 eV) source

and an analyzer pass energy of 20 eV were selected. In combination with a pre-selected slit width, the pass energy determines the response function of the analyzer. The overall spectral resolution is determined by convolution of the natural lineshape of the photoelectron emission with the instrument response function. For high-resolution spectra, a trade-off is made with the photoelectron count rate requiring increased signal averaging. Typically, 3 acquisition sweeps using a 800-1500 μ s dwell times at 100 meV step sizes were sufficient for working at photoelectron take-off angles greater than 40°. Non-zero take-off angles were obtained by sample stage rotation in the plane of minimum numerical aperture, for which the angular resolution of photoelectron collection was $\pm 5^\circ$.

As a result of the photoelectron emission process, a positive charge is left behind on the sample. The XPS instrument utilizes a magnetic pole-piece lens design that allows for a significant charge neutralization current to be established via the return of low energy photoemission. The samples were mounted using conductive carbon tape. If required, additional charge neutralization can be achieved with the use of injected thermionic electrons. This has the effect of shifting the energy scale closer to the spectrometer Fermi level, and reduces the charge broadening of peaks that results from non-uniform surface potentials that may arise. However, since the binding energy scale requires post-process calibration anyway, and no significant line width reduction was observed with the charge neutralizer, this feature was explicitly needed only where described in later chapters.

3.1.3 Component Fitting with CasaXPS Software

The CasaXPS software was developed by Fairley [Fairley, 1999-2005], and is in widespread use for the quantitative analysis of XPS spectra. Its main features list: i) the model fitting of component peaks from a variety of synthetic lineshapes, ii) model fitting for subtraction of the photoelectron inelastic scattering background, iii) a least-squares optimization algorithm with user input constraints for the fitting of assigned peaks within a defined spectral envelope, and iv) the calculation of apparent atomic percentages, according to Equation 2.6, based on the instrument transmission function and library values for the RSFs.

Ideally, the fitting of synthetic lineshapes to XPS peaks should be based on some knowledge of the underlying physical principles. For example, if the natural lineshape can be represented by a Lorentzian function, the observed spectrum profile will be a convolution of the Lorentzian with the spectrometer function, which can be modeled as a Gaussian function

[Sprenger and Anderson, 1991], the result of which is called a Voigt profile and is represented by closed-form approximations in the software. Physically, the Lorentzian reflects the lifetime broadening of the core-hole filling process [Kolasinski, 2002], which involves the release of Auger electrons or fluorescence. The situation becomes complex if there are mechanisms that leave the sample in an excited state after photoemission; according to Equation 2.2, excited final state energies result in binding energy increases. Moreover, relaxation processes lower the binding energy, as stated in Equation 2.3. These and other factors can skew the observed lineshape and must be treated with asymmetric profiles, the specifics of which will be introduced at the time of their use.

The combination of overlapping species defined by their chemical shifts and the possibility of asymmetry in the component lineshapes increases the complexity within the spectral envelope to which the various peaks are assigned. Unfortunately, not all factors will be known *a priori*, so the guiding principles in the approach to peak fitting must be physical insight, simplicity and consistency. Simplicity implies the use of a minimum number of components and degrees of freedom in the least squares fitting routine. Consistency implies the systematic use of lineshapes and their parameters in the component analysis, which are controlled by constraints on the peak positions, FWHM values, area integrated intensities etc.

The above comments are general in nature and apply throughout this work. In this chapter, as elsewhere, details of the component fitting process will be covered on a case-by-case basis.

3.2 XPS Spectra and Compositional Stoichiometry

3.2.1 GaAs Survey

The spectrum in Figure 3.1 is taken from a GaAs reference wafer in low-resolution survey mode in order to obtain a broad view of the elemental components of the sample. The main photoemission lines and the oxygen and carbon KLL Auger lines are identified on top of a mainly featureless background of inelastically scattered photoelectrons. Auger emission is referred to in electron-shell notation, e.g., KLL refers to a K shell core-hole being filled by a L shell valance electron, with the relaxation energy being carried away by another L shell electron. In general, the inelastic background at E^* increases in proportion to the integrated intensity from all peaks at $E < E^*$. Figures 3.2 zooms in on the broad multi-peak spectrum of LMM Auger lines associated with Ga and As [Poirier and Weaver, 1993]. Note that the O 1s

line appears superimposed on the one of the pseudo-periodic features associated with the Ga LMM band emission. Figure 3.3 shows the occurrence of loss peaks, which correspond to the excitation of volume plasmons by the parent photoemission line at the characteristic energy of 15.6 eV for GaAs [Bideux *et al.*, 2004].

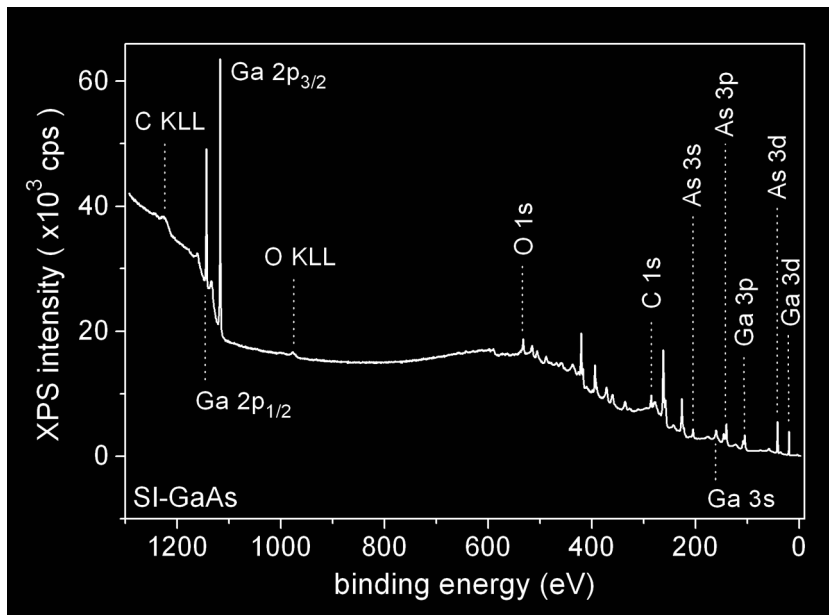


Figure 3.1. Low resolution XPS survey spectrum of etched only semi-insulating GaAs(001) at ToA = 0°.

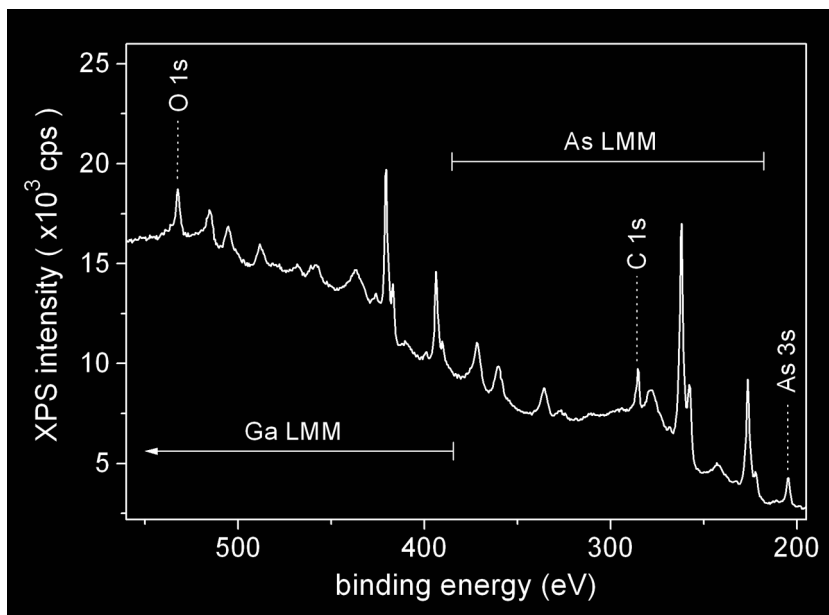


Figure 3.2. As per Figure 3.1 showing LMM Auger bands due to Ga and As. Note the Ga LMM interference with the O 1s photoemission line.

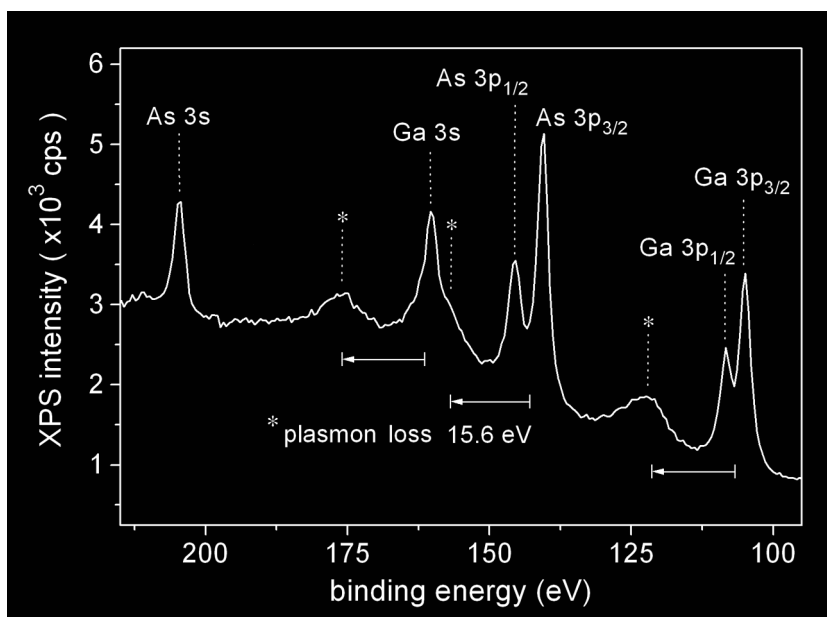


Figure 3.3. As per Figure 3.1 showing loss peaks characteristic of the GaAs volume plasmon at +15.6 eV from the parent photoemission line. Note the overlap of the Ga 3s line with the As 3p plasmon loss.

The Ga 3s peak is superimposed on a plasmon loss peak excited by As 3p, which presents a challenge to the assignment of an appropriate background in this region and to the decomposition of the Ga 3s contribution. Later, these will have a bearing on the analysis of the S 2p line attributed to bound thiol, as the binding energy associated with it overlaps in this spectral region also. Resolved in both Figure 3.1 and 3.3 are the Ga 2p, As 3p and Ga 3p doublets due to spin-orbit coupling.

Spin-orbit coupling arises due to the interaction between the intrinsic spin magnetic moment of an electron and the internal magnetic field created by its orbital angular momentum. The spin magnetic moment has two (quantized) orientations resulting in two potentials with respect to the internal magnetic field. These different potentials are the source of the energy splitting [Briggs, 1998]. Consider the associated quantum numbers. The degeneracy of the orbital angular momentum is $2l+1$, l being the angular momentum quantum number. The spin degeneracy is 2, therefore, there are $2(2l+1)$ states in total. However, the total angular momentum is $j = l \pm s$ and the degeneracy of j is $2j+1$. Since the spin quantum number s is $1/2$, and the number of states is split according to the degeneracy of j , a doublet forms with states numbering $2l+2$ and $2l$. Take the As 3d line as an example, $l = 2$, so the total number of states is 10, which are split into the $j = 5/2$ states

numbering 6 and the $j = 5/2$ states numbering 4. The probability of photoemission is proportional to the number of states, therefore the integrated intensity ratio of the respective peaks should be $l/(l+1) = 2/3$. The spin-orbit coupling ratio is a fundamental constraint used in the component fitting process. Henceforth, labeling of the doublet branches will follow according to the quantum number j .

3.2.2 GaAs High-Resolution

The spectra in Figure 3.4 are from high-resolution scans of an etched semi-insulating GaAs reference wafer at a ToA of 60° . According to Equation 2.8, surface sensitivity increases with increasing ToA θ . Therefore, in order to better resolve the surface species, the sample is measured at high tilt angles. The spectral regions cover the elements observed in Figure 3.1. The GaAs 3d orbitals were selected since they, being in the highest observable orbital, have the narrowest line broadening and, therefore, offer the best resolution. The Ga 3s region was selected in order to baseline the spectrum in advance of its superposition with the S 2p emission associated with thiol, as presented shortly. Quantification data is listed in Table 3.1.

In this chapter, knowledge of the Fermi level position is not required. Therefore, it was sufficient to apply a shift of the binding energy scale to position the spectra to nominal values. The calibration point selected was the C 1s binding energy of adventitious saturated hydrocarbon C-C bonds at 285.0 eV [Briggs and Beamson, 1992], on an etched, but untreated, GaAs reference wafer. This particular sample was allowed to reoxidize in the ambient briefly (~ 3 min) in order to allow for a rendering of the oxide species with high contrast. As a consequence, it became contaminated to a greater degree than would occur if isolation in a N_2 purged environment was maintained. In the latter case, a reduction in adventitious carbon of nearly $10\times$ has been observed on etched-only GaAs. The calibration to C 1s positioned the As 3d_{5/2} peak at 41.37 eV, which was subsequently applied to the remaining samples. This positioned the Fermi level near mid-gap in accordance with its intrinsic value, as a nominal calibration only.

The O 1s spectrum is comprised of the oxide species associated with the reoxidation of the etched-only GaAs surface. No effort was made to decompose this spectrum into its possible constituents (Ga_2O_3 , As_2O_3 , As_2O_5), therefore, only a single component profile was used to capture the total integrated intensity. In this case, a Voigt function/exponential blend

lineshape was used in order to fit the shape of the spectrum envelope. The baseline used for subtraction of the inelastic background was the Shirley function [Shirley, 1972]. This function is widely used and is based on the principle that the background increases in proportion to the integrated intensity, and, therefore, is suitable where a step-edge in the background is observed, i.e., increasing background intensity on the high binding energy side.

In the absence of observable peaks attributable to C-O or C=O oxidation states of carbon, which occur at +1.5 eV and +3.0 eV from the position of C-C bonds, the profile of the C 1s region was fit with a single component Voigt/exponential blend. In contrast to the O 1s region, there is a physical basis for the choice of this asymmetric profile. It is beyond the present scope to investigate this to any depth, except to say that XPS photoemission lines can be asymmetrically broadened due to vibrational fine structure [Gelius, 1974]. Recall that the binding energy is proportional to the final state energy. Following photoemission, if the atom relaxes into a vibrational energy level, rather than to the ground state, the binding energy will increase accordingly. In the language of Equation 2.21, the energy difference will be $E_\nu - E_o$, $\nu = 0, 1, 2, \dots$, with decreasing probability in proportion to the probability of occupation [Briggs, 1998]. For example, consider the C-H stretching modes; they have vibrational energies corresponding to about 2920 cm^{-1} or 0.36 eV. So, there can be fine structure components at $250.0 \text{ eV} + \nu \times 0.36 \text{ eV}$, i.e., near the harmonics of the fundamental vibration. Since the fine structure can be significant with respect to the photoemission linewidth, it manifests as an asymmetry to the high binding energy side.

The fitting of the Ga 3s region was completed next. Though a step-edge in the background about the Ga 3s line region is apparent, as particularly evident in Figure 3.3, the Shirley background was rejected due to the fact that it would be misrepresented by the inclusion of the As 3p plasmon loss peak, i.e., it would not be in proportion to the photoemission, and could introduce error. Instead a linear background type was selected, and the following calibration steps were taken in order to provide a best estimate of the decomposition of this complex region. First, the expected intensity values of the Ga 3s region GaAs and Ga₂O₃ species were obtained based on their values in the Ga 3d region, as discussed below, taking into account the RSF differences between the two orbitals, and the chemical shift of the oxide peak. These were used as constraints of the fitting. Next, a peak was assigned to the As 3p plasmon loss. No constraints were added to this component, as its parameters were unknown.

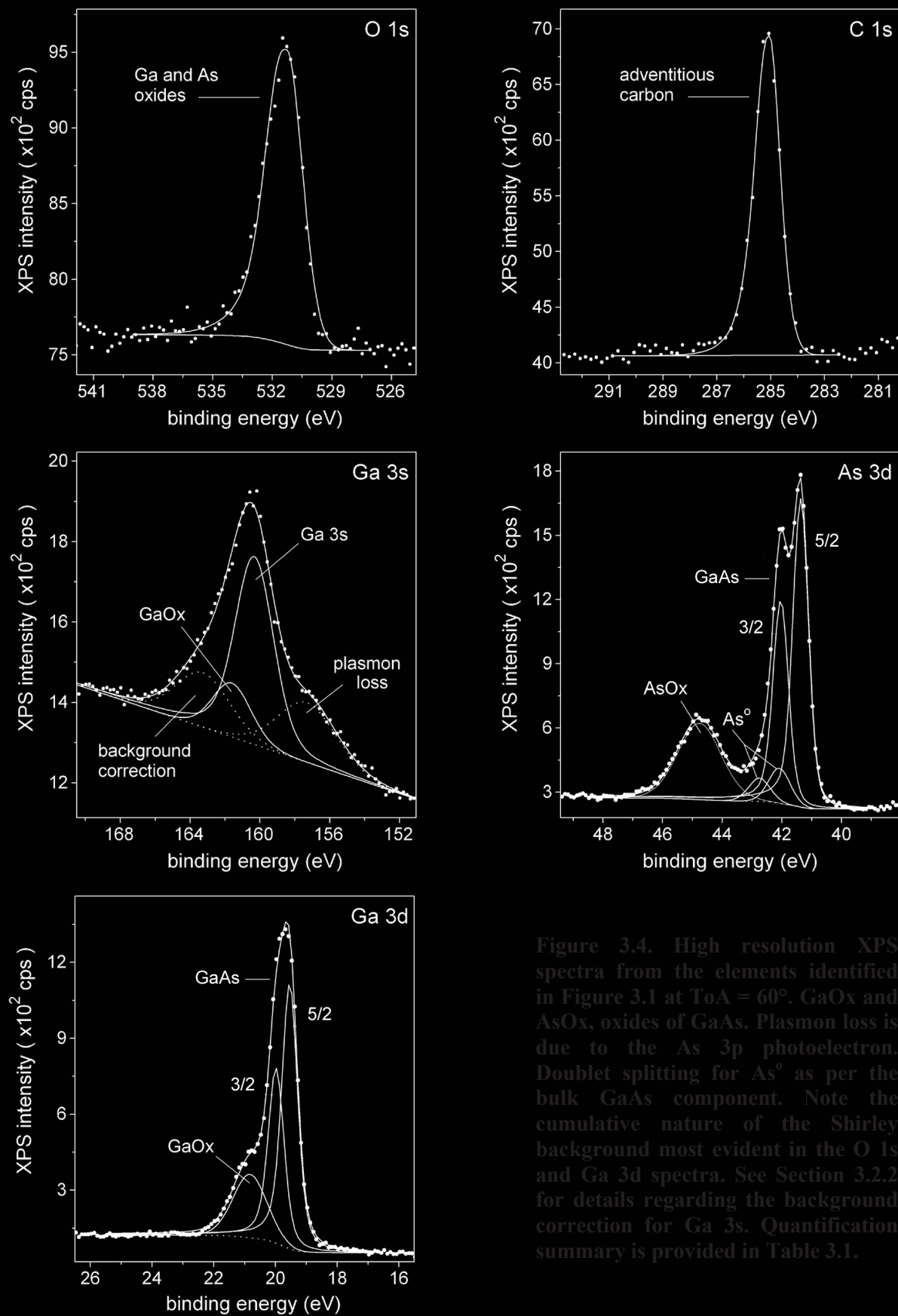


Figure 3.4. High resolution XPS spectra from the elements identified in Figure 3.1 at $\text{ToA} = 60^\circ$. GaOx and AsOx, oxides of GaAs. Plasmon loss is due to the As 3p photoelectron. Doublet splitting for As^0 as per the bulk GaAs component. Note the cumulative nature of the Shirley background most evident in the O 1s and Ga 3d spectra. See Section 3.2.2 for details regarding the background correction for Ga 3s. Quantification summary is provided in Table 3.1.

TABLE 3.1. Component assignments, specifications and atomic percentages from XPS spectra corresponding to the decompositions in Figure 3.4. Etched only GaAs.

Region ^a	Type	Position (eV)	FWHM (eV)	Area (cps)	Total RSF ^b	Atomic (%) ^c
O 1s	GaOx + AsOx	531.3	1.91	4908	2.67	14.3
C 1s	adventitious	285.0	0.95	3692	0.85	33.6
background	correction	163.3	3.67	539	-	-
Ga 3s	GaOx	161.6	2.61	379	0.91	3.2
Ga 3s	Ga(As)	160.3	2.61	1580	0.91	13.5
As 3p	plasmon loss	157.3	3.99	640	-	-
As 3d	AsOx	44.8	1.71	661	1.32	3.9
As 3d (3/2)	As ⁰	42.8	0.85	101	1.31	0.6
As 3d (5/2)	As ⁰	42.1	0.85	153	1.31	0.9
As 3d (3/2)	As(Ga)	42.0	0.61	784	1.31	4.6
As 3d (5/2) ^d	As(Ga)	41.4	0.61	1188	1.31	7.0
Ga 3d	GaOx	20.8	1.29	352	0.77	3.5
Ga 3d (3/2)	Ga(As)	20.0	0.61	585	0.77	5.9
Ga 3d (5/2)	Ga(As)	19.5	0.61	886	0.77	8.9

^a Fractions refer to spin-orbit coupling (total angular momentum).

^b Relative sensitivity factor: product of the photoionization cross-section, orbital asymmetry factor and the instrument transmission function.

^c Evaluated at photoelectron take-off 60° from normal.

^d Approx. intrinsic Fermi level used as a nominal binding energy reference.

Finally, a component was assigned in an *ad hoc* manner to make up the difference with respect to the spectrum envelope, which together with the plasmon loss peak, substitutes for the lack of an accurate background function. It is stressed that this is a best estimate effort only, and is based on an attempt to reconcile the results of the Ga 3s region fitting with what can be obtained in the better resolved Ga 3d region.

The components of the As 3d and Ga 3d regions of GaAs were fitted according to known peak assignments [Poirier and Weaver, 1993], a 2/3 spin-orbit branching ratio, and the energy splitting of the doublets [Moulder *et al.*, 1993; NIST XPS, 2003]. According to the discussion in Section 2.1.1.3, the presence of As⁰ is also expected. This component was fitted with the same doublet parameters used for GaAs phase As, and a chemical shift in agreement with the synchrotron-based results of Shaporenko *et al.* [Shaporenko *et al.*, 2003]. The oxide species were fitted with single component Voigt shapes only. For Ga oxides, this may interpreted as a

representation of Ga_2O_3 . For the As oxides, there is an unresolved mixture of As_2O_3 and As_2O_5 . Spectra have been observed bearing a more intense oxide peak, such as that from the native (cleaned only) wafer, which is weighted towards higher E_B and, therefore, reflects a greater proportion of the higher oxidation state. For reference surfaces measured immediately following etching, transferred under N_2 for example, the oxide peak intensity is smaller and is positioned at a lower E_B . This suggests the fact that the regrowth of oxides proceeds following a progression of oxidation states, such that what is observed is best represented by $\text{Ga}_x/\text{As}_y\text{O}_z$, with $x, y \geq 0$, which explains its broad and featureless profile. The term sub-oxides will be used to refer to oxidation states having $x < 2, y < 3$.

The synthetic lineshape used to fit the GaAs phase 3d (and Ga 3s) components was based on the Doniach-Sunjic profile [Doniach and Sunjic, 1970]. This profile is based on many-body interactions that relate to core-hole screening by conduction band electrons, which generate a peak asymmetry skewed towards the high E_B side. Core-hole screening is a final state effect that lowers the E_B in general [Park and Lagally, 1985]. However, in the Doniach-Sunjic process, screening interactions result in the excitation of low energy electron-hole pairs, and, as such, is a loss process. The cross-section for this effect decreases with the energy of the exciton and, consequently, results in a high E_B shoulder. The applicable criterion for the Doniach-Sunjic profile is a sufficient density of available states near the Fermi level [Lynch and Olson, 1999]. For semiconductors, the bandgap should mitigate the possibility of low energy excitation [Babu *et al.*, 2007]. Despite this fact, the Doniach-Sunjic profile has been successfully used for modeling Si at the SiO_2 interface [Winter and Burgdörfer, 2007], and for modeling In 3d on (oxide free) NH_4OH etched InGaAs [Hinkle *et al.*, 2009]. As was pointed out by Hinkle *et al.*, the correct fitting of an asymmetric profile circumvents the error of assigning sub-oxide components on the high energy tail where none may exist (see footnote to Figure 2.5). To investigate this further, an etched-only GaAs reference sample was cleaned by the application of a scanned Ar-ion beam used for *in situ* sputter depth profiling. Following a 10 min exposure at 10 keV, no O 1s component and a negligible intensity from C 1s were observed. Figure 3.5 shows the As 3d and Ga 3d GaAs phase spectra, each fitted with the Doniach-Sunjic profile, with the small As^0 component fitted with a Voigt profile. The inset shows that no oxides remained on the surface

after sputtering. Although some broadening of the linewidth was observed relative to the spectra in Figure 3.4 ($< 25\%$), due to kinetic disruption of the surface layer under the sputtering beam, the asymmetry of the lineshape remained clear. The GaAs phase Doniach-Sunjic parameters determined from the sputter-cleaned sample in Figure 3.5 were subsequently applied to the spectra in Figures 3.4, and Figure 3.7 as described in the next section, and a good fit was obtained. In accordance with the earlier discussion, the required GaAs asymmetry parameters were lower than those normally required for fitting metals.

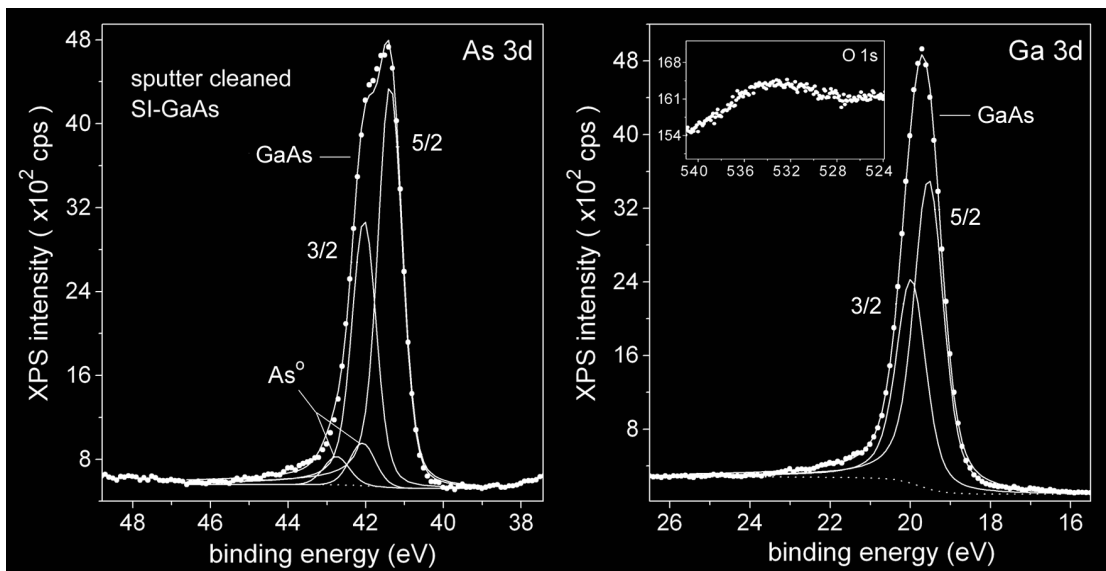


Figure 3.5. NH_4OH etched GaAs following Ar-ion *in situ* sputtering. GaAs phase components were fitted with the Doniach-Sunjic profile, the parameters of which were applied to the fitting of other samples in this work. The inset shows that surface oxides were removed; the shape of the O 1s background is owing to Ga LMM Auger features.

3.2.3 HDT-SAM Prepared GaAs

In this section, the spectral decomposition of a HDT-SAM prepared GaAs surface is presented. The fitting techniques applied in the previous section were employed in general, with specific details as discussed below. In order to provide a baseline for comparison, XPS spectra were recorded from a sample of bulk alkanethiol deposited on a thick Au epilayer/Si substrate. Reference to the Fermi level was made by calibration to the Au $4f_{7/2}$ line at $E_B = 84.00$ eV. The thiol material used was amine-terminated alkanethiol (ATA) $[\text{NH}_3(\text{CH}_2)_{12}\text{SH}]$. For the purposes of this discussion, interest lies in the chemical state associated with the thiol functional group. In its bulk state, ATA is a hydrochloride salt ($\text{R-NH}_2 \cdot \text{HCl}$), which easily forms a saturated solution in ethanol. When left to evaporate

from drops deposited on the Au epilayer, the solution leaves behind a polycrystalline film. Repeated applications built up a film of molecular thiol suitable for XPS analysis. The spectra in Figure 3.6 show two chemical states in the S 2p region and the Fermi level calibration point at the Au 4f_{7/2} branch. The main peak in the S 2p region represents the unbound thiol group at 163.7 eV [NIST XPS, 2003], and the smaller peak is attributed to Au-thiolate bonding at 162.0 eV [Castner *et al.*, 1996], both of which were modeled with known doublet splitting energies [Moulder *et al.*, 1993]. The S 2p profile used was a Voigt/exponential blend for no specific reason other than goodness of fit. The fitting parameters of this calibration sample were subsequently applied to the analysis of the SAM-GaAs interface in the Ga 3s region.

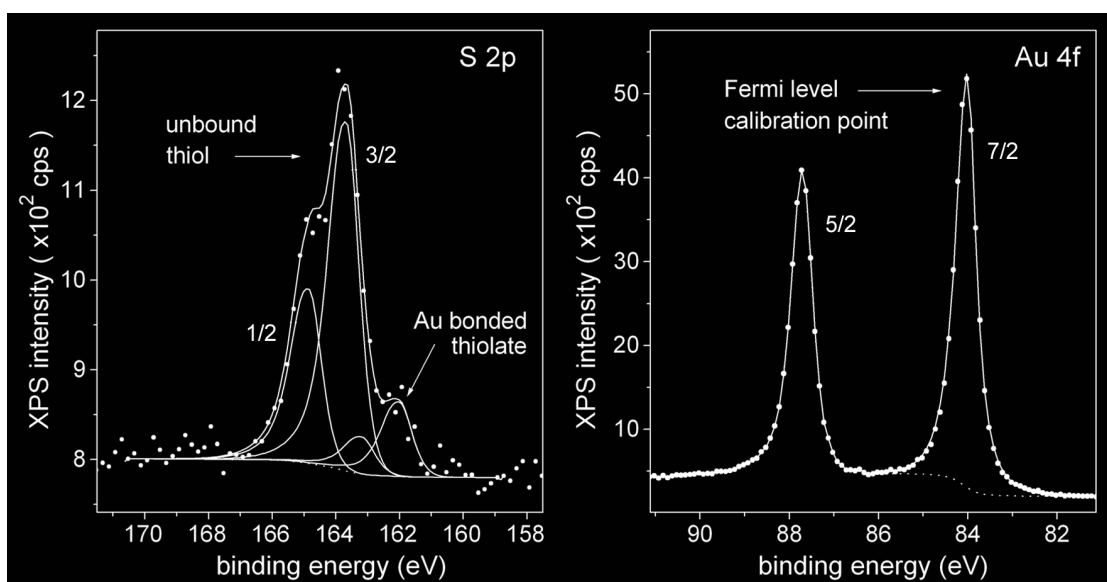


Figure 3.6. XPS spectra of unbound molecular thiol, Au bonded thiolate, and the Au film used for Fermi level referenced calibration of the binding energy to Au 4f_{7/2} at 84.00 eV. Referring to the 3/2 angular momentum, S 2p peak positions are located at: unbound thiol, 163.7 eV; Au bonded thiolate, 162.0 eV.

In Figure 3.7 and Table 3.2, the XPS spectra and quantification summary of a HDT-SAM prepared GaAs surface are provided. In the O 1s region, the Ga LMM feature introduced in Figure 3.2 is clearly observed. A similarly shaped feature has been observed upon *in situ* cleaving [Poirier and Weaver, 1993]. This indicates that the surface oxide concentration has been reduced to below detection limits in this region. The C 1s spectrum is assigned to linear alkane of the SAM. Although efforts were made to isolate this sample in a N₂ purged environment, which has been shown to reduce the presence of adventitious carbon as already mentioned, it remains an uncontrolled variable and its presence cannot be entirely discounted.

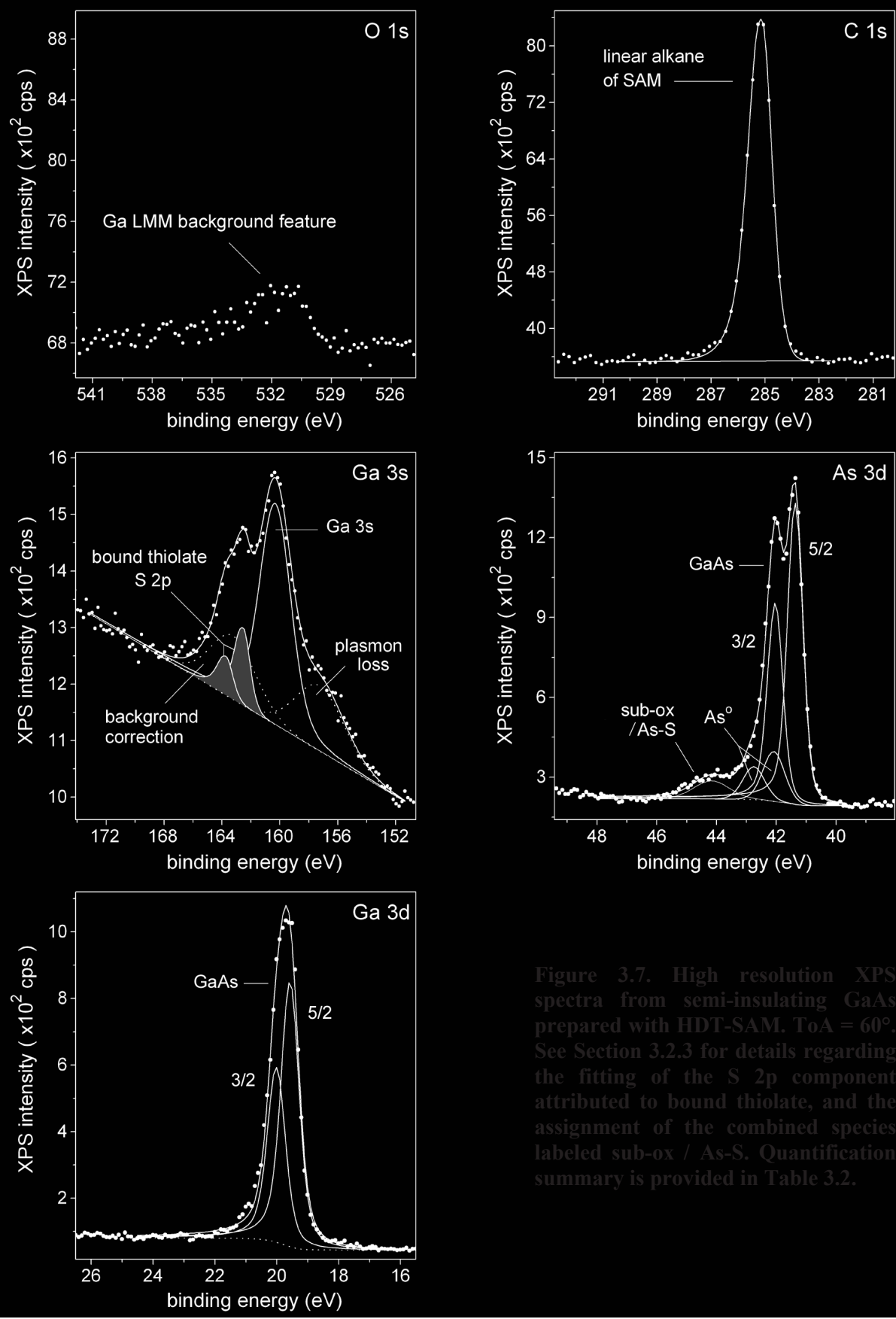


Figure 3.7. High resolution XPS spectra from semi-insulating GaAs prepared with HDT-SAM. ToA = 60°. See Section 3.2.3 for details regarding the fitting of the S 2p component attributed to bound thiolate, and the assignment of the combined species labeled sub-ox / As-S. Quantification summary is provided in Table 3.2.

TABLE 3.2. Component assignments, specifications and atomic percentages from XPS spectra corresponding to the decompositions in Figure 3.7. HDT-SAM GaAs.

Region	Type	Position (eV)	FWHM (eV)	Area (cps)	Total RSF	Atomic (%)
O 1s	nill ^a	-	-	-	-	-
C 1s	linear alkane ^b	285.1	0.89	5882	0.85	59.0
background	Correction	163.2	3.70	451	-	-
S 2p (1/2)	S-GaAs	163.7	1.09	106	1.35	0.7
S 2p (3/2)	S-GaAs	162.5	1.09	213	1.35	1.3
Ga 3s	Ga(As)	160.3	2.55	1293	0.91	12.2
As 3p	plasmon loss	157.2	4.00	502	-	-
As 3d	sub-ox /As-S ^c	44.2	1.40	103	1.32	0.7
As 3d (3/2)	As ^o	42.8	0.85	115	1.31	0.7
As 3d (5/2)	As ^o	42.1	0.85	174	1.31	1.1
As 3d (3/2)	As(Ga)	42.0	0.61	609	1.31	4.0
As 3d (5/2) ^d	As(Ga)	41.4	0.61	923	1.31	6.0
Ga 3d (3/2)	Ga(As)	20.0	0.69	513	0.77	5.7
Ga 3d (5/2)	Ga(As)	19.6	0.69	778	0.77	8.6

^a No determinable quantity of oxide was present above the background Auger features.

^b Some of the intensity attributed to linear alkane may be due to adventitious carbon.

^c This component is attributed to the As-S chemical state and sub-oxides of As.

The S 2p component in the Ga 3s region is assigned to bound thiolate. In order to fit this doublet the following procedure was adopted. First, the plasmon loss and background correction peaks were constrained, in terms of their integrated intensities, peak widths and positions relative to the Ga 3s peak attributed to the GaAs substrate. These constraints were established based on the parameters determined from the reference GaAs sample. No oxide component was applied. Next, this group of three peaks was attenuated to fit the spectrum envelope of the HDT-SAM prepared surface manually; the relative scattering losses incurred are unknown, since the relative thickness difference between the oxide overlayer and SAM was not established. The difference under the spectrum envelope was then filled with the S 2p doublet. A comparison of the Ga 3s atomic percent with that of the Ga 3d line showed that they were in agreement within 15%. The Ga 3s intensity was the lower of the two, 6% of which can be accounted for by the difference in the kinetic energy dependent inelastic scattering mean free path (defined in Equation 2.1), a level of precision that was not

incorporated into the original calibration of Ga 3s. To reiterate, this method is meant to yield a best estimate only.

The component fitted to the As 3d spectrum that was labeled sub-ox / As-S in Figure 3.7 was generalized to a single peak owing to the uncertainty of decomposition in the high energy tail. According to the chemical shift with respect to the As 3d_{5/2} branch (2.8 eV), the oxidation state of this peak is too large, when compared to the literature values in column 4 of Table 2.1 (≤ 1.9 eV), for it to be attributed to As-S alone. Despite the lack of observable intensity in the O 1s region, and the lack of a resolvable Ga oxide, which is thermodynamically favoured according to Equation 2.10, a component of AsOx appears to remain.

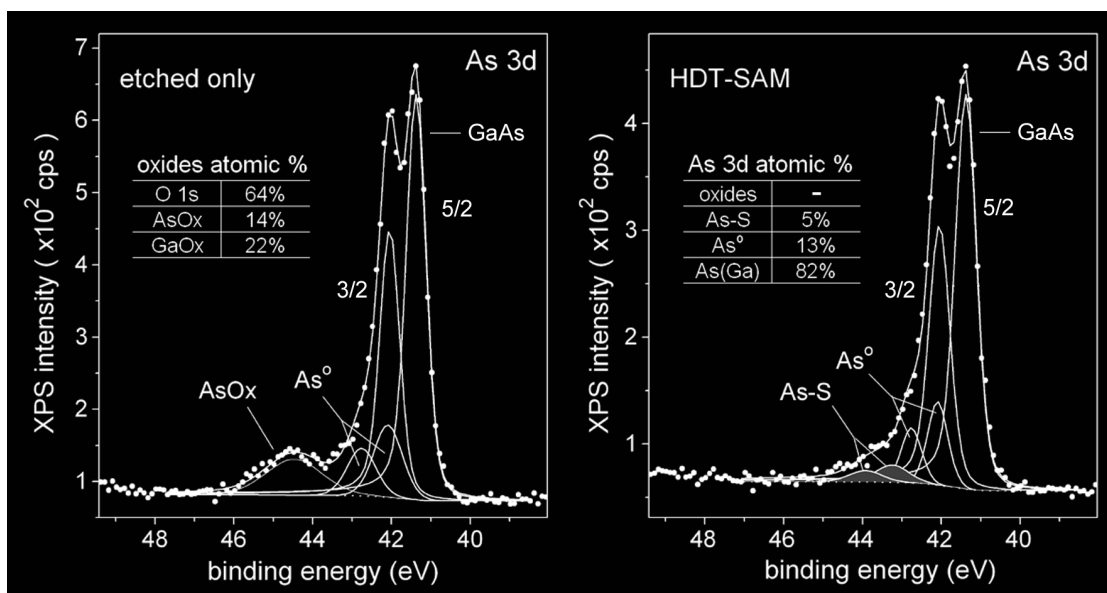


Figure 3.8. Comparison of etched only GaAs and as prepared with HDT-SAM in the As 3d region. Sample processing minimized ambient exposure in order to help resolve the identification of As-S species. Oxides in the etched only sample were consistent with a 2:3 stoichiometry in the low oxidation state of As. The As-S doublet position agrees with literature reports of thiol-GaAs coupling.

In order to examine this problem in more detail, a comparative Ref / HDT-SAM GaAs sample set was prepared where the reference wafer was not allowed to reoxidize, and was exposed to oxygen only through the momentary sample transfer process.[†] In Figure 3.8, the As 3d spectra and relevant quantification values are compared. The reference sample was fitted with a single peak in the oxide region, whereas a As-S doublet was fitted to the sample prepared with HDT-SAM. Inspection of the oxide atomic percentages in the left panel shows

[†] In this case, samples were loaded on the XPS sample bar under N₂ to further minimize O₂ exposure.

good agreement with a 2/3 stoichiometric ratio as per the oxidation states As_2O_3 and Ga_2O_3 . The binding energy of the AsOx peak in Figure 3.8 is 0.3 eV greater than the sub-ox /As-S peak identified in Figure 3.7 indicating that the oxide component in the latter case is indeed a sub-oxide as previously defined. The right panel indicates that no oxidation was observable among the spectra representing the SAM prepared sample. In this case, however, the doublet assigned to As-S was fitted with a chemical shift of 1.8 eV in good agreement with the values cited in Table 2.1, according to Asai *et al.*, Hou et al, and Adlkofer and Tanaka. The point is this; background limitations in the O 1s region of can make it difficult to outright reject the presence of oxides. Without an otherwise observable Ga-S species, this places a premium on the binding energy position of the component fitting in the As 3d tail. Consequently, strict anaerobic measures are required in order to observe GaAs-S coupling in the As 3d region at the appropriate energy. Without this control, sub-oxidation states of As begin to form immediately and interfere with a precise determination of the As-S component.

3.2.4 Compositional Analysis of XPS Data

Evidence for a S 2p chemical shift attributed to GaAs bonded thiolate was observed. Relative to measurements of molecular thiol in Figure 3.6, the binding energy was reduced by 1.2 eV upon formation of S-GaAs bonds. This is less than the 1.7 eV reduction observed for S-Au coupling, but is in good agreement with the summary of observations in column 3, Table 2.1. In that summary, the S-GaAs component is referred to the Ga 3s position for convenient comparison where the values range over 2.0-2.6 eV; a S 2p offset of 2.2 eV from the Ga 3s line is indicated for HDT-SAM prepared GaAs in Table 3.2. The lower chemical shift of S-GaAs coupling relative to that observed for S-Au is due to the core-hole screening effect projected by the metal substrate, which results in an apparent binding energy reduction. Other factors significant to the binding energy of S-GaAs will be discussed in a later chapter.

Analysis of the sensitivity ratio as defined in Equation 2.8 proceeds as follows in order to examine the quantification data in terms of their agreement with surface appropriate concentrations. Table 3.3 lists the numerical values used in Equation 2.8, the calculated results, and the experimental ratios obtained from the data above. The experimental ratio I_{S2p}^*/I_{Ga3s}^* was taken from Table 3.2, whereas I_{AsS}^*/I_{As3d}^* was taken from the values listed in

the right panel of Figure 3.8. The surface density ρ_{surf} was adopted from GIXRD and IR spectroscopy based reports of ODT-SAMs on GaAs [McGuiness *et al.*, 2007b].

TABLE 3.3. Surface sensitivity analysis for HDT-SAM GaAs based on Equation 2.8.

I_{surf}^* / I_{bulk}^*	$N_{bulk} / \text{cm}^{-3}$	$\Lambda_{bulk} / \text{nm}$	$\rho_{surf} / \text{cm}^{-2}$	θ	Calc.	Data
I_{S2p}^* / I_{Ga3s}^*	2.3×10^{22} ^a	2.02	4.7×10^{14}	60°	0.21	0.17
I_{AsS}^* / I_{As3d}^*	2.3×10^{22}	2.16	2.4×10^{14} ^b	60°	0.10	0.06
$I_{AsS+As^0}^* / I_{As3d}^*$	2.3×10^{22}	2.16	5.4×10^{14} ^c	60°	0.22	0.22

^a Bulk density of As and Ga is based on half the nominal atom density for GaAs.

^b Surface density for As-S component is assumed based on a 1:1 ratio with Ga-S species.

^c Compare to, e.g., the planar density of the [001] oriented GaAs lattice $6.3 \times 10^{14} \text{ cm}^{-2}$.

Comparison of the calculated and experimental values in the first row of Table 3.3 indicates that the quantification of S 2p attributed to S-GaAs thiolate is underestimated with respect to the ideal SAM by about 20%. Calibration excludes that the Ga 3s intensity is overestimated in the component fitting, therefore, the lower ratio evident in the data is due to: i) the fractional coverage of the SAM, ii) the difficulty in obtaining a quantitatively correct measurement of the S 2p peak, or iii) polar anisotropies possible in the Ga emission at 60° [Alnot *et al.*, 1987]. In the second row, comparison of the calculated and experimental ratios suggests that the actual ratio of As-S and Ga-S bonded species is less than 1:1, i.e., that the As-S bond fraction is 30-50%. A preference for S-Ga bonding has been suggested based on the affinity of molecular thiol to surface Ga sites through weak sharing of the lone-pair electrons on sulphur atoms with the empty dangling bonds of surface Ga. This affinity results in physisorbed precursors at Ga sites prior to H cleavage of molecular thiol and the formation of a S-Ga bond, which results in a bias of the surface kinetics and preferential bonding to Ga consequently [Dubowski *et al.*, 2010]. In the third row, inclusion of the As⁰ species in the surface layer yields agreement with the predicted ratio assuming a reasonable number for the total surface density, valued as just larger than the ideal SAM density but just less than the planar density of the [100] oriented GaAs lattice. This discussion is continued in the next section following ARXPS analysis of the surface concentration of As⁰.

Another factor that may have some bearing in the apparent bias towards S-Ga bonding is the Ga-rich stoichiometry after NH_4OH etching. Accounting for the GaAs phase components only, the As:Ga ratio is found to be in the range 0.7-0.8. A similar ratio has been observed elsewhere [Aqua *et al.*, 2007]. What this presents in terms of the structural morphology requires the analysis of angle-resolved data as discussed in the next section.

As a final point, note that a Ga-rich surface is consistent with the observation of As^0 , only if it appears as the result of surface reconstruction, and not exclusively as a residual of the oxidation process, as suggested in Section 2.1.1.3, in which case a 1:1 ratio may be expected. In addition, the observation of a Ga-rich surface will figure prominently later, in Chapter 5, when XPS measurements of the surface Fermi level are interpreted.

3.3 Angle-Resolved XPS Structural Analysis

In this section, ARXPS methods are employed in order to: i) examine the As:Ga surface ratio in more depth, ii) estimate the surface concentration of As^0 , and iii) to quantify the SAM coverage using a fractional overlayer model.

3.3.1 GaAs Surface Stoichiometry

In the data presented above, a compositional As:Ga ratio of 0.7-0.8 was observed. As discussed in Section 2.1.2, in order to apply ARXPS methods to precision limited data, the structural form must be known (or assumed) before any quantitative analysis can proceed. In terms of the depth dependence of the As:Ga stoichiometry, no physically justifiable model comes to mind. Therefore, a selection of assumed forms will be modeled in order to bracket the data with the view to a qualitative analysis only. One model of the As:Ga ratio of atomic percentages can be made by assuming a Ga-rich/Ga-terminated surface. Casting the XPS intensity integral into a discrete form indexed over GaAs planes in the [001] direction gives,

$$\frac{I_{As}^*(\theta)}{I_{Ga}^*(\theta)} = \frac{\sum_{m=1}^{\infty} \exp[-a(2m-1)/4\Lambda_{GaAs} \cos \theta]}{\sum_{m=1}^{\infty} \exp[-a(2m)/4\Lambda_{GaAs} \cos \theta] + X_{Ga}} \quad (3.2)$$

where a is the lattice constant for bulk GaAs, and X_{Ga} is a surface density weighting fraction for Ga relative to the planar density in bulk GaAs. For example, at a ToA of 60° and with

$X_{Ga}=1$, the As:Ga ratio is 0.88. As the surface becomes more Ga-rich, e.g., $X_{Ga}=2$, the ratio is 0.71. For $X_{Ga}=0$, the ratio is 1.14 indicating an As-terminated surface. This example illustrates that stoichiometric differences in the terminal plane can have a significant effect on the observed ratio of XPS intensity, even though the surface layer is only a fraction of the overall sampling depth. A second model assumes an exponential form of the As:Ga ratio,

$$R(z) = 1 + (R_o - 1) e^{-z/\beta} \quad (3.3)$$

where R_o is the surface ratio of GaAs and β is a depth constant such that a As:Ga ratio of 1:1 is obtained deep in the material. With this formulation, integration of Equation 2.1 yields,

$$\frac{I_{As}^*(\theta)}{I_{Ga}^*(\theta)} = 1 - \frac{(1 - R_o) \beta}{\beta + \Lambda_{GaAs} \cos \theta} \quad (3.4)$$

Equations 3.2 and 3.4 are plotted in Figure 3.9 along with data from two ARXPS data sets of the As:Ga ratio. The model parameter X_{Ga} was selected in order to coincide the curve with measurements at 60° . The model parameters R_o and β were manually fitted to the data.

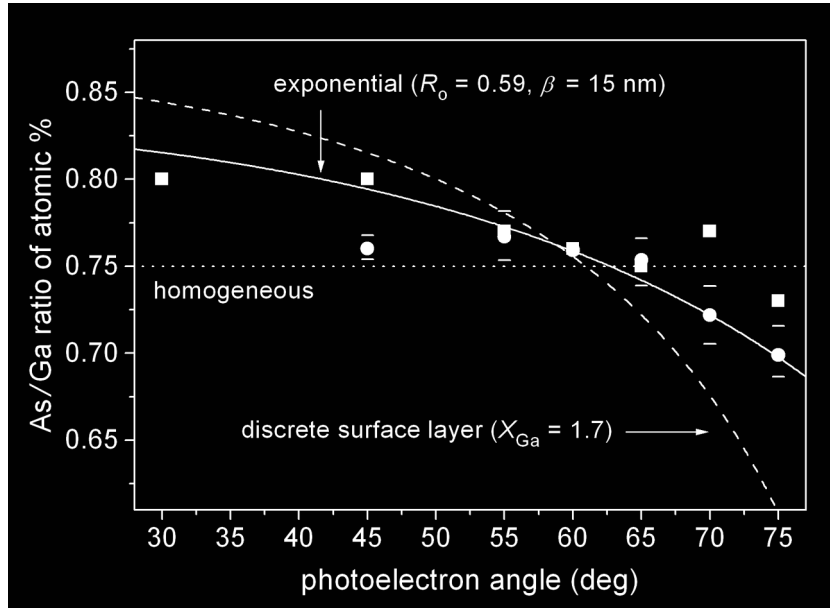


Figure 3.9. ARXPS data of As:Ga ratio and model analysis according to Equations 3.2 and 3.4 for HDT-SAMs. Circles/squares represent independent tests. The bars indicate max/min values over a three spot average (circles).

By inspection of the fitting relative to the data, the discrete surface layer model can be rejected in favour of a more slowly varying depth profile. The exponential profile yields an

acceptable fit, however, without a justifiable reason for this profile to be assumed, and the fact that the ARXPS method is a so-called “ill-conditioned problem”, referring to the issue of inversion of the Laplace Transform [Cumpson, 1995], the precision of the data is insufficient to rule out other model hypotheses. Consequently, the best conclusion that can be made is qualitative to the effect that the surface is Ga-rich, and that the As:Ga ratio remains less than 1 over a significant fraction of the XPS sampling depth.

3.3.2 Surface Concentration of Elemental Arsenic

As previously mentioned, surface As^0 exists as a residual product of oxidation, or results from the reconstruction of an oxide free surface after etching. In Table 3.3, Equation 2.8 was applied to the sum of surface species, i.e., the As^0 and As-S components, and agreement with experimental ratios was achieved at 60° , assuming a reasonable surface density value as previously explained. This observation and the physical reasoning above provides the necessary justification to apply an ARXPS model based on fractional surface coverage in order to quantify the surface concentration of As^0 .

The fractional overlayer model has been described by Paynter [Paynter, 1999]. The left portion of Figure 3.10 illustrates the basic morphology in which a substrate is covered by a surface species with some areal fraction f . The photoemission from volumes not covered by

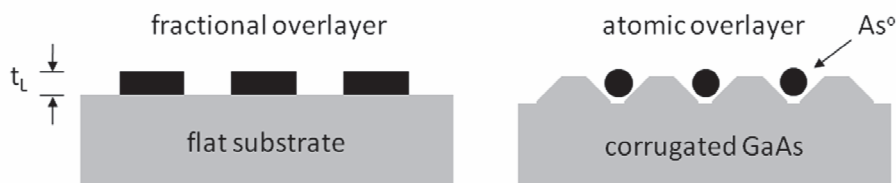


Figure 3.10. Fractional overlayer model of the corrugated surface.

the surface species $(1-f)$ will not be attenuated through the fractional overlayer, whereas emission from volumes under the overlayer will be. In general, the fractional overlayer has some thickness t_L whose emission will carry a self-attenuation term of the form $1 - e^{-t_L/\Lambda_{KE} \cos \theta}$. In contrast, an atomic or elemental surface layer, as in the right portion of Figure 3.10, can be assumed not to self-attenuate; only the substrate photoelectrons passing through it will experience scattering. In this view, surface species intensities according to Equation 2.7 can be divided by the volumetric intensity from the substrate in a ratio of atomic

percentages [Carpenter *et al.*, 1989], as was formulated in Equation 2.8. For sub-monolayers, the method of Carpenter *et al.* should be modified by incorporating a fractional overlayer viz.,

$$\frac{I_{As^0}^*(\theta)}{I_{As}^*(\theta)} = \frac{f_{As^0} \rho_{max} a \sec \theta}{2 \langle R_{AsGa} \rangle \rho_{GaAs} \Lambda_{GaAs}} \left[1 - f_{As^0} + f_{As^0} e^{-d_{As^0}/\Lambda_{As^0} \cos \theta} \right]^{-1} \quad (3.5)$$

Sensitivity to the exponential factor is low for values of d on the order of the van der Waals diameter when $f < 1$, therefore, it was equated to 1 for simplicity in the application of Equation 2.8. In the present application, it is used to improve the precision of fitting to multi-ToA data. In Equation 3.5, ρ_{max} is the maximum surface density of As^0 based on hexagonal close-packing of the van der Waals radius ($d_{As^0}/2$), ρ_{GaAs} is the planar density of GaAs in the [001] direction, and $\langle R_{AsGa} \rangle$ is the θ averaged value of As:Ga, which was assigned a nominal value of 0.75 based on the data above. Equation 3.5 accurately describes the morphology illustrated in the right portion of Figure 3.10, which is based on a trench-ridge like corrugation of the surface, where As^0 partially fills the trenches according to f_{As^0} . Trench-ridge corrugation has been used by Voznyy and Dubowski to describe a GaAs(001) surface construction that is ideally matched to the maximally-packed alkanethiol SAM, as cited in Figure 2.6. This type of morphology is also consistent with the work of Paget *et al.* who described As^0 as being located in an interlayer coincident with Ga-S bonds, but below the height of As-S bonds on the $(NH_4)_2S$ passivated GaAs(001) surface [Paget *et al.*, 1996].

In Figure 3.11, Equation 3.5 is fitted to two ARXPS datasets of the experimental ratio $I_{As^0}^*/I_{As}^*$ taken from HDT-SAM prepared surfaces. Error bars were assigned based on the typical dispersion of As^0 component fitting results. The values of f_{As^0} bracketing this data were 0.3 and 0.4 indicating an As^0 surface density of up to $3.4 \times 10^{14} \text{ cm}^{-2}$. This value is reasonable, since the proposed ridge-filling morphology would exclude greater than 50% coverage. Moreover, a value of $0.4 \rho_{max}$ ($3.4 \times 10^{14} \text{ cm}^{-2}$), when added to the estimated range of As-S coverage ρ_{AsS} ($1.4 - 2.4 \times 10^{14} \text{ cm}^{-2}$) in the second row of Table 3.3, yields a value that agrees with the total As surface density ($4.8 - 5.7 \times 10^{14} \text{ cm}^{-2}$) satisfying the calculations in the third row. The self-consistency of these results supports the following conclusions: i) As^0 exists in sub-monolayer quantities of approximately 30-40% of maximum coverage,

possibly residing in the troughs of a trench-ridge-like corrugation, and ii) that the As-S bond fraction is in the range of 30-50% relative to the total number of GaAs-S bonds. Furthermore, it is interesting to note that the As-S bond fraction is consistent with estimates of the GaAs surface ratio ($R_o = 0.59$) as predicted from the exponential depth profile model in Figure 3.9.

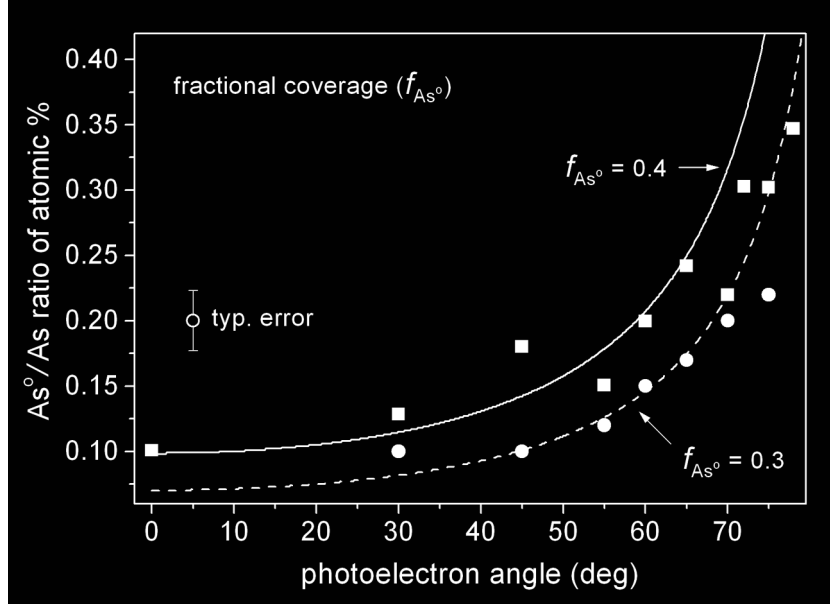


Figure 3.11. Fractional overlayer model of As^0 coverage on GaAs prepared with HDT-SAM. The coverage fraction (f_{As^0}) computes to a surface density of $2.5\text{-}3.4 \times 10^{14} \text{ cm}^{-2}$. Data points are the As^0 / As ratios of atomic percent in the As 3d region.

3.3.3 Fractional Coverage of the SAM

In Figure 3.10 the illustration on the right corresponds to atomic dimensions at the surface. In the left portion, the scale is larger and represents the fractional coverage of the SAM, where $t_L = d_{\text{SAM}}$, and where a coverage fraction $f_{\text{SAM}} < 1$ may result from, e.g., film defects or the formation of domains. Recall that domain formation was discussed in Section 2.2.4 in relation to the uniaxial asymmetry of the optical constants. In this section, a fractional coverage model and data is presented in order to quantify the parameter f_{SAM} .

First consider the C 1s emission intensity from the SAM. Integrating Equation 2.1 over the SAM thickness z from 0 to d_{SAM} gives,

$$I_{\text{C1s}}^*(\theta) = N_{\text{SAM}} \Lambda_{\text{KE}} \left[1 - e^{-d_{\text{SAM}} / \Lambda_{\text{SAM}} \cos \theta} \right] \quad (3.6)$$

which carries the self-attenuation term mentioned in relation to Figure 3.10. Dividing by the intensity from the substrate using the As 3d line, and applying the fractional model gives,

$$\frac{I_{C1s}^*(\theta)}{I_{As3d}^*(\theta)} = \ln \left[\frac{f_{SAM} \left(1 - e^{-d_{SAM}/\Lambda_{C1s} \cos \theta} \right)}{f_{SAM} e^{-d_{SAM}/\Lambda_{As3d} \cos \theta} + (1 - f_{SAM})} \right] + \Delta \quad (3.7a)$$

$$\Delta = \ln \frac{N_{SAM} \Lambda_{C1s}}{\langle R_{AsGa} \rangle N_{As} \Lambda_{As3d}} \quad (3.7b)$$

The logarithm was applied to separate out the term Δ to be used as a constant of the data fitting below. A value for d_{SAM} was adopted based on the molecular length of HDT (2.1 nm) and a molecular tilt of 14° , as reported for ODT in the literature [McGuinness *et al.*, 2006]. For SAMs, since the molecular tilt angle is low and is dependent on $\cos \theta_{SAM}$, Equation 3.7a has weak sensitivity to values of $\theta_{SAM} < 20^\circ$. A tilt angle of 19° was specified in the model results of Voznyy and Dubowski, as cited in Figure 2.6, and was also reported by Rosu *et al.* using IR ellipsometry. The reported value of 14° was measured using NEXFAS, which is a technique highly sensitive to bond orientation, so this value was assumed for the calculations. Data and the model results of Equation 3.7a are plotted in Figure 3.12.

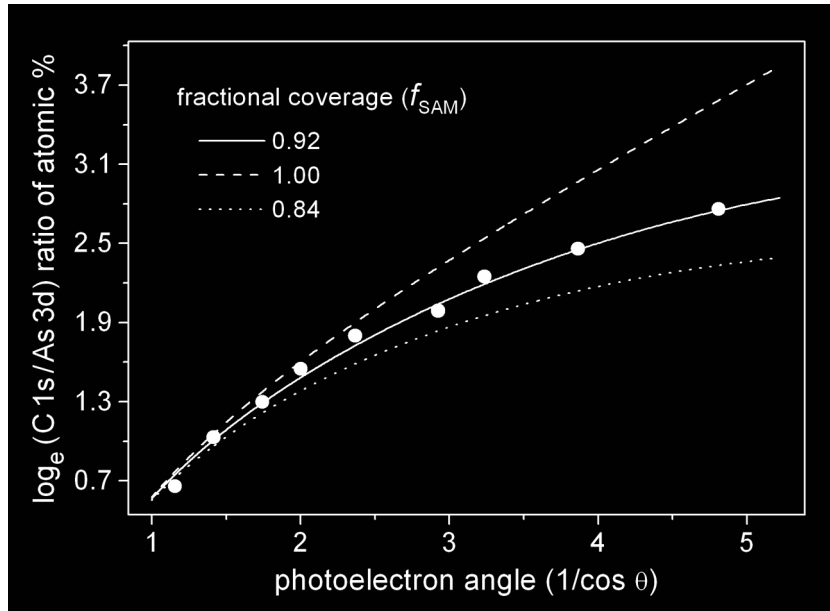


Figure 3.12. Fractional overlayer model of HDT-SAM coverage on GaAs. Data points are the C 1s / As 3d ratios of atomic percent. Dashed and dotted curves illustrate the sensitivity of the model to coverage fraction.

The curves in Figure 3.12 were fitted by varying f_{SAM} and by choosing the offset Δ such that the models coincided at low angle for convenient comparison of their relative sensitivity of curvature. The data indicates a good fit within a few percent of the coverage fraction 92%. Note that in this model, $f_{SAM} < 1$ does not necessarily indicate a bare GaAs surface. Owing to the exponential nature of the attenuation of photoemission through scattering, the areas represented by $1 - f_{SAM}$ in the model could be interpreted as areas that have not yet conformed into the *all trans*, vertically oriented structure. Later, the dynamics of SAM formation will be discussed using IR spectroscopy where it will be made clear that progression into a well-ordered SAM proceeds according to a saturation time profile. A second data set similar to that in Figure 3.12 returned a coverage value of 80%, although that surface retained some evidence of oxidation, whereas the sample in Figure 3.12 was oxide free according to the specifications in Section 3.2.3. Purity of the thiol material used is likely another factor that contributes to coverage losses. For example, stock thiol material is usually specified to a 95% level of purity.

Also note, an offset value Δ of 0.82 was used to fit the 92% curve in Figure 3.12. This represents a number density ratio of about 1.9 in Equation 3.7b. The ideal ratio should be more like 1.5. The difference may be related to the presence of adventitious carbon, the effect of which cancels as a common attenuation factor in the numerator and denominator of Equation 3.7a, the signal from which cannot be separately accounted for in the C 1s region.

The high fractional coverage of the SAM indicates that a significant fraction of the available alkane packing has been achieved. This agrees with the observation that a substantial degree of chemical passivation has been realized. However, as noted earlier, the SAM may not fill all the dangling bonds, depending on the surface construction. Since the fraction of As^0 agrees, in principle, with the trench-ridge surface morphology predicted theoretically, the beneficial effect of thiol coupling in terms the electronic passivation it affords, which remains to be determined, may be limited.

3.4 Chapter Summary

The compositional stoichiometry and structural morphology of alkanethiol SAM passivated surfaces was investigated using XPS. Survey data illustrated the complex nature of the GaAs XPS spectrum and highlighted two regions of interference that had a significant bearing on spectrum analyses at higher resolution: i) the O 1s region was identified as having a background limited by interference with Ga LMM Auger band emissions that ultimately restricted its use in terms of the verification of null oxide surfaces, and ii) background features in the Ga 3s region, particularly as they related to the presence of a As 3p plasmon loss peak, required an *ad hoc* method of background subtraction in order to obtain a quantitatively correct estimate of the Ga 3s photoemission intensity.

In order to decompose high resolution spectra in the Ga 3d and As 3d regions, analysis of Ar-ion beam sputtered GaAs allowed a fitting of the GaAs phase species to be determined using low-asymmetry Doniach-Sunjić lineshape profiles. Though no Ga-S component could be identified in HDT-SAM prepared samples, the As-S species was located at 1.8 eV from the As 3d_{5/2} branch in good agreement with data determined following GaAs treatment with inorganic sulphides, and was estimated to have a bond fraction of 30-50% relative to the total number of GaAs-S bonds. The S-GaAs component fitted in the Ga 3s region exhibited a chemical shift of 1.2 eV, and carried a quantification error of an undetermined nature measuring about 20% relative to the ideal SAM.

The structural morphology of the SAM-GaAs interface was examined using ARXPS techniques. Following NH₄OH etching the surface is Ga-rich. Although the precision of the data did not allow a specific depth profile to be extracted, the Ga-rich stoichiometry was evident over a significant fraction of the XPS sampling depth.

The presence of As⁰ was observed after SAM formation and efforts to quantify it were made using fractional overlayer modeling. A surface density of $2.4-3.4 \times 10^{14} \text{ cm}^{-2}$ was computed, which represents a coverage fraction of 30-40% that can be interpreted in terms of trench-filling of a surface corrugated landscape.

Finally, the fractional coverage of a SAM on oxide free GaAs was evaluated to be 92%. Coverages less than ideal can be expected based on domain formation or other defects that result in the incomplete formation of an ideally-ordered SAM.

CHAPTER 4:

INFRARED SPECTROSCOPY of the SAM

The IR spectroscopy results presented in this chapter refer to absorption characteristics in the C-H stretching mode band from which information related to the molecular structure and physical environment of the SAM are derived. These results are primarily as reported in *Journal of Applied Physics*, “Observation of surface enhanced IR absorption coefficient in alkanethiol based self-assembled monolayers on GaAs(001)” [Marshall et al., 2009a], and includes portions from *Langmuir*, “Surface Dipole Layer Potential Induced IR Absorption Enhancement in *n*-Alkanethiol SAMs on GaAs(001)” [Marshall et al., 2009b] and contributions to *Journal of Applied Physics*, “Formation dynamics of hexadecanethiol self-assembled monolayers on (001) GaAs observed with photoluminescence and Fourier transform infrared spectroscopies” [Kim et al., 2009]. Specifically, modal analysis of the C-H band envelope, coupled with *ex situ* time series data of the formation dynamics, validates the realization of a highly-ordered series of SAMs, which vary by molecular length making them suitable for Beer-Lambert analysis of the absorption coefficient. Based on this coefficient, the optical constants are quantified and compared to measurements made in the bulk liquid thiol phase. This reveals evidence for an electronic configuration unique to the SAM.

4.1 Experimental Details

4.1.1 SAM Preparation

The method of sample preparation follows the directions outlined in Chapter 3. Specifically, alkanethiol solutions in degassed ethanol were prepared at 2-3 mM concentration from each of the following: octadecanethiol (*n*17), hexadecanethiol (*n*15), tetradecanethiol (*n*13), dodecanethiol (*n*11) and decanethiol (*n*9), where the decade prefix refers to *n* + 1 carbon atoms per molecule, accounting for the terminal CH₃ group. From these solutions, a homologous series of *n*-alkanethiol [HS(CH₂)_{*n*}CH₃] SAMs on double-side polished semi-insulating GaAs(001) was formed over a 20 hour period. In addition, a time series of

*n*15-SAMs was made for investigation of the formation dynamics by limiting the incubation period in varying time increments up to the 20 hour specification and beyond.

4.1.2 Liquid Thiol Preparation for Beer-Lambert Analysis

In order to assess the IR characteristics of liquid thiol, samples of *n*9, *n*11 and *n*13 were prepared by wetting neat liquid between two thin (150 μm) coverglass slides. Alkanethiols *n*15 (solid/liquid) and *n*17 (solid) could not be measured in the liquid phase at room temperature. The thickness of the resulting liquid sandwich layer was measured ($\pm 1 \mu\text{m}$) by through-focus 200 \times optical microscopy (Leica DM-RXE), making use of small area voids around the layer, such that the interior surface features of the respective coverglass slides were resolved. The corresponding z-position readings were recorded from a digital translation stage and subtracted. Sample preparation ensured that a suitable void-free area was available for IR transmission measurements. Figure 4.1 illustrates this process in more detail.

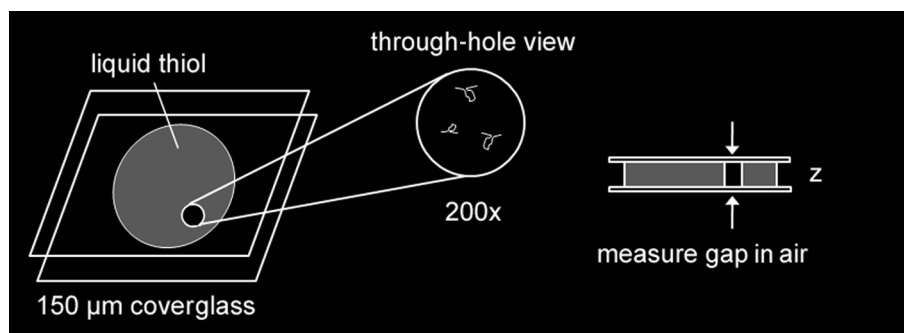


Figure 4.1. Illustration of the technique used to quantify the absorption thickness of a thin layer of liquid thiol pressed between two coverglass slides. Optical microscopy was used to obtain the mechanical thickness through the air gap in small voids by focusing on the slides' interior and tracking the change in z-stage translation.

4.1.3 IR Transmission Measurements of the SAM

IR spectra were recorded in transmission mode using a Bruker Optics Hyperion 2000 Fourier Transform IR-microscope coupled to a Bruker Optics Tensor 27 spectrometer. The probing spot size was approximately 2 mm in diameter, the spectral resolution was set to 4 cm^{-1} , and continuous nitrogen purging of the sample glovebox was used. Spectra were recorded for freshly prepared samples, baselined through an etched GaAs reference wafer (processed in ethanol without thiol as the control) such that the resulting absorbance spectrum $A_{SAM}(\nu)$ revealed features specific to the SAM only, defined as,

$$A_{SAM}(\nu) = -\log_{10} \left(I_{IR}^*(\nu) / I_{IR}^t(\nu) \right) \quad (4.1)$$

where the superscripts t and t^* refer to IR intensities transmitted through etched-only GaAs and GaAs prepared with a SAM respectively. At least 1 min of scanning time was required to achieve a good signal-noise ratio. Semi-insulating GaAs substrates were used as they are well-suited for transmission IR measurements of the SAM phase; because of their high extinction, doped semiconductor or metal substrates can only support grazing-angle reflection IR measurements, making evaluation of the absorption length more difficult. In this context, the present results have relevance in the generalized domain of alkyl-SAMs prepared on a variety of substrates. Specific to a Beer-Lambert analysis of the SAM, Figure 4.2 illustrates the absorption path length difference between SAMs comprised of molecules having two different molecular lengths.

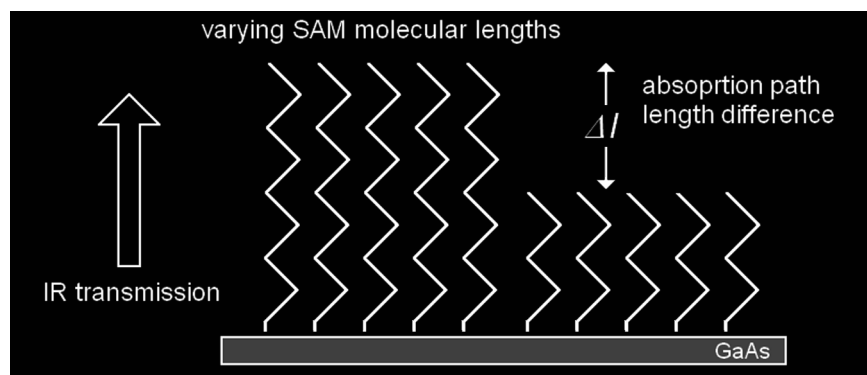


Figure 4.2. In transmission mode, SAMs present absorption path length differences (Δl) dictated by the length of their respective molecules.

4.2 Modal Analysis and Observation of SAM Formation Dynamics

4.2.1 Modal Analysis of Methyl-Terminated Alkanethiols

Absorption spectra for $n17$, $n15$, $n13$, $n11$ and $n9$ SAMs are provided in Figure 4.3. Linear baseline subtractions and vertical spectrum shifts have been applied for clarity. Identifying characteristics are the C-H stretching mode peaks, which are located in the following ranges: (a) $2917\text{-}2921\text{ cm}^{-1}$ (asymmetric mode), (b) $2850\text{-}2851\text{ cm}^{-1}$ (symmetric mode), and (c) two orthogonal stretching modes at (c) associated with the terminal methyl group near 2959 cm^{-1} . Before proceeding to an analysis of the absorbance magnitude, consider the peak position frequencies. In general terms, the peak frequencies are expected to shift to higher energy values (larger wavenumbers) corresponding to an increasing fraction of *gauche* defects

indicating a loss of order in the monolayer [Dubois and Nuzzo, 1992]. Note that an asymmetric mode peak frequency near 2917 cm^{-1} has been measured in the polycrystalline state of various long-chain *n*-alkanes [Nuzzo *et al.*, 1990; Parikh and Allara, 1992], and is often cited as a benchmark indicator of the *all-trans* conformation in the well-ordered SAM [Lodha and Janes, 2006; McGuinness *et al.*, 2007b]. Peak widths will also increase to reflect an increased distribution of conformational states [Dubois and Nuzzo, 1992]. More specifically,

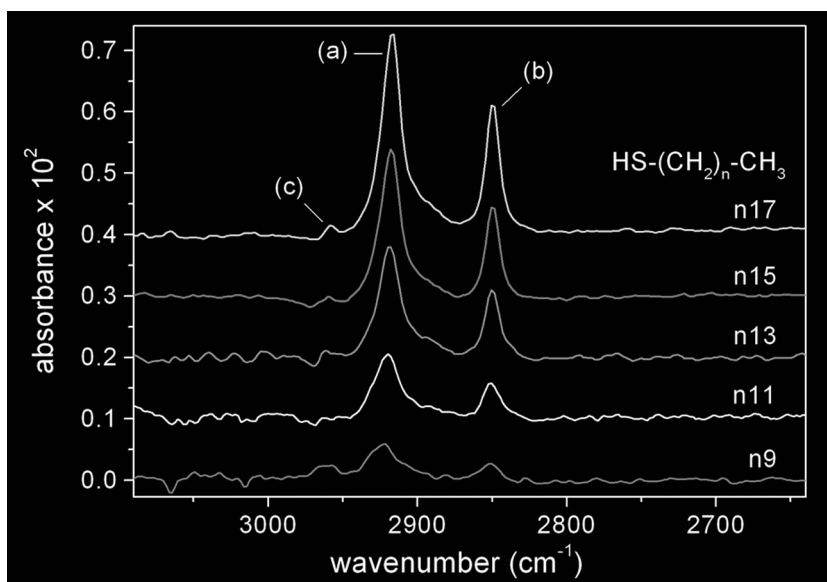


Figure 4.1. Transmission IR spectra of *n*-alkanethiol $[\text{HS}(\text{CH}_2)_n\text{CH}_3]$ SAMs on GaAs(001). C-H stretching modes: asymmetric CH_2 (a), symmetric CH_2 (b), and orthogonal CH_3 stretching modes (c). After Marshall *et al.* [Marshall *et al.*, 2009a].

one must consider that the spectrum envelope consists of several modal contributions, the amplitudes of which for some are not directly related to the number of backbone methylene groups. For example, there are Fermi resonance modes and various modes associated with next-to-endgroup vibrations [Nuzzo *et al.*, 1990; Parikh and Allara, 1992]. Fermi resonance is a band-splitting phenomenon arising from vibrational state mixing when a two modes are energy coincident, usually a fundamental and an overtone, which results in a shift of the fundamental to higher energies. For example, in alkanethiols, Fermi resonances occur between the CH_2 symmetric mode and a lower frequency CH_3 deformation mode near $1370\text{--}1380\text{ cm}^{-1}$ [Nuzzo *et al.*, 1990; Parikh and Allara, 1992]. An example of a next-to-endgroup vibration is located near 2924 cm^{-1} and corresponds to the asymmetric CH_2 vibration adjacent to sulphur [Truong and Rowntree, 1996]. The distribution of these modes,

and their relative weighting, contributes to the apparent position of normal mode peak frequencies. For lower n -values, this effect is more significant since the contribution from the alkane backbone is necessarily less. Consequently, the asymmetric mode peak amplitude will be considered as a generalized feature of the SAM independent of its precise frequency, with the implicit understanding that the spectral envelope contains within it various constant factors independent of n .

In order to justify this assertion, the correspondence of modal distribution with the spectrum envelope peak position and amplitude was studied in detail. Using similar peak assignments and a 60/40 Gaussian-Lorentzian line shape mixing ratio as adopted by Parikh and Allara for the polycrystalline alkyl $C_{19}H_{39}CO_2Na$, an analytical representation of the CH_2 band was developed and fitted to the spectrum of $n17$ -SAM in a manner similar to that described in their report [Parikh and Allara, 1992]. The component assignments are listed in Table 4.1 and the resulting fit is illustrated in Figure 4.4 (top left panel). The model was then set to scale with an arbitrary factor (s) according to the intensity of n -dependent components, leaving the end-group associated elements fixed in amplitude (s/f designations in Table 4.2).

TABLE 4.1. Assignment of C-H modal parameters and scaling indicator for the spectral components of $[HS(CH_2)_nCH_3]$ SAMs on GaAs(001).

Mode description ^{a,b}	position (cm^{-1})	FWHM (cm^{-1})	scaling ^c
CH_3 , asym str (ip)	2959	6	f
CH_3 , asym str (op)	2955	6	f
CH_3 , sym str (FR)	2932	22	s
CH_2 , asym str (α)	2924	13	f
CH_2 , asym str	2917	12	s
CH_2 , sym str (FR)	2902	25	s
CH_2 , sym str (FR)	2889	16	s
CH_3 , sym str	2876	10	f
CH_2 , sym str (α)	2862	12	f
CH_2 , sym str (β)	2854	9	f
CH_2 , sym str	2850	10	s

^a Adapted from References [Parikh and Allara, 1992; Truong and Rowntree, 1996].

^b Abbreviations: ip - in plane (C-C-C), op - out of plane (C-C-C), FR - Fermi Resonance, asym - asymmetric, sym - symmetric, str - stretching, α - CH_2 group adjacent to sulphur, β - CH_2 group adjacent to α .

^c Refers to fixed (f) or n -dependent (s) amplitude in the scaling model.

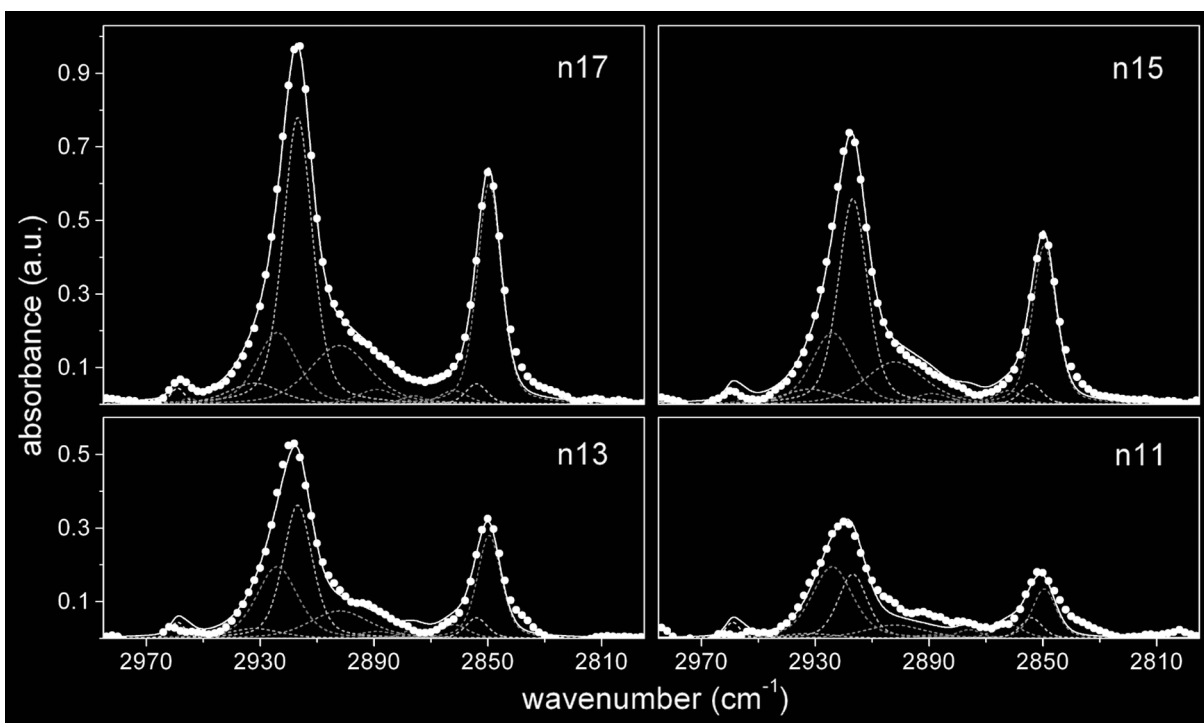


Figure 4.4. Component analysis of IR spectra. Data (circles) and component fit (lines) using fixed and n -dependent C-H stretching mode assignments (dotted lines) referenced by peak position. See Table 4.1 for details. Adapted from Marshall *et al.* [Marshall *et al.*, 2009a].

Under this first-order assumption, the remaining spectral envelopes were fitted by varying the s -factor, the exception being the $n9$ spectrum, owing to a loss of fidelity. Results from the analysis of the $n15$, $n13$ and $n11$ spectra are shown in the remaining panels of Figure 4.4. Agreement is good for the CH_2 asymmetric and symmetric modes, but for example, the intensity of the CH_3 modes near 2959 cm^{-1} does not conform well to the applied model, especially as the value of n decreases, because of the initialization of conformational defects that first tend to form at the chain-ends [Dubois and Nuzzo, 1992; Hautman and Klein, 1990].

The spectrum model may now be used to evaluate the wavenumber position of the generalized asymmetric peak as a function of the scale factor s . This calculation is shown in Figure 4.5, along with the data points corresponding to the real asymmetric peak positions at their respective s -values from the component fit. Note that in the limit of large s , the peak position is asymptotic with 2917 cm^{-1} , i.e., the position associated with the CH_2 asymmetric stretching mode in polycrystalline samples. For small s -values, the peak position approaches the value of 2924 cm^{-1} associated with the fixed amplitude component at that position. Deviation of the data points above the analytical curve is observed to increase as the

chain-length shortens corresponding to the onset of chain-end gauche defects as previously cited. The position of n_9 is estimated, but is expected to correspond to the frequency limit determined by the dominant 2924 cm^{-1} mode for small s -values, and is undifferentiated with respect to the asymmetric mode peak position in disordered thiol, e.g., in liquid thiol as will be shown below. Note that the actual defect fraction responsible for frequency deviations $\sim 1\text{ cm}^{-1}$ is less than a few percent [Dubois and Nuzzo, 1992; Hautman and Klein, 1990]. Therefore, Figure 4.5 indicates that the spectral data and its analytical representation are reasonably self-consistent in terms of amplitude and peak position, and validate the component assignments with respect to a near-crystalline SAM model for values $n \geq 11$.

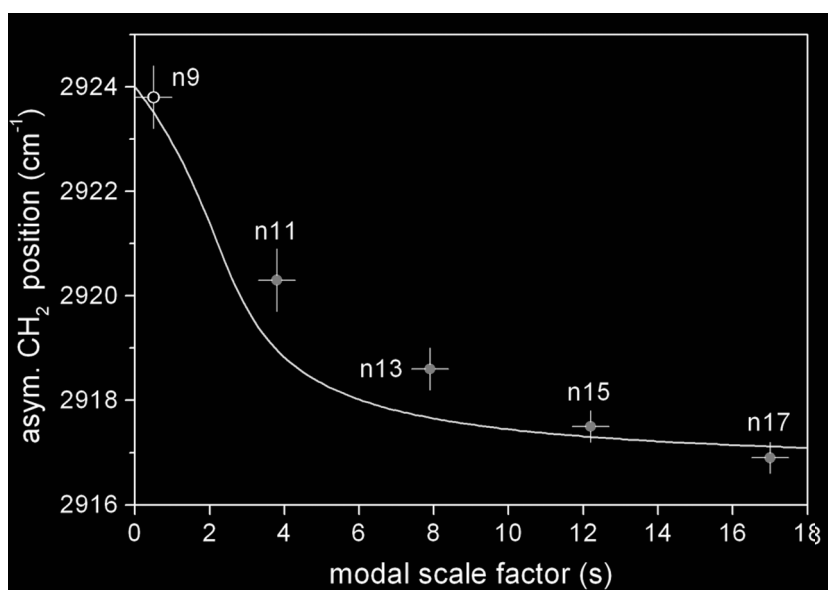


Figure 4.5. CH₂ asymmetric mode peak frequency vs. modal scale factor; continuous model (line), component fit results (circles), illustrating the correspondence of amplitude and position in the n -scaling model. Fitting of the n_9 spectrum was not possible and its position is estimated. After Marshall *et al.* [Marshall et al., 2009a].

Two important conclusions fall out from the above discussion. The first is that the validity of n -dependent component scaling supports the physical model upon which the absorption coefficient is based, i.e., that of a uniformly dense SAM changing by molecular length. The second is that generalized comments about the quality of the SAM, in terms of the fraction of conformational defects, should not hinge upon the asymmetric peak position in its entirety, at least not for comparison between SAMs of two different molecular lengths.

As an aside, it should be clarified that since the SAMs will form on both the front and back of double-side polished wafers, the absorbance magnitudes scale by a factor of 2 when

measured in transmission, increasing the signal to noise ratio. The absorbance doubling effect was confirmed by an experiment where only one side of a wafer was etched before incubating in n 17. The resulting peak amplitude was reduced by a factor of 2 as expected, since the SAM will not form on the oxidized surface.

4.2.2 Formation Dynamics

The conclusion that an increasing asymmetric peak position does not necessarily indicate SAM disorder was based on an analysis of modal weighting as a function of SAM molecular length. Consequently, it was recommended that comparison of peak positions between SAMs of different molecular length be done with caution. In this section, tracking the time evolution of SAM formation into a well-ordered monolayer proceeds on the basis of *ex situ* measurements of peak position, but is carried out for samples prepared from one length type.

Figure 4.6 shows the peak absorption intensities (a) and vibrational energies (b) of the generalized asymmetric C-H stretching mode. Both figures indicate a clear trend towards saturation levels; the peak intensity increases to saturation and the peak frequency decreases. The two parameters demonstrate the time evolution of SAM formation according to previously reported mechanisms [McGuiness *et al.*, 2006]. These include a rapid adsorption phase, followed by a slow reaction phase where the surface density continues to increase and the conformational disorder of the alkane is reduced. In addition, the effects of various intrinsic and extrinsic factors act to increase the IR absorbance, as discussed below.

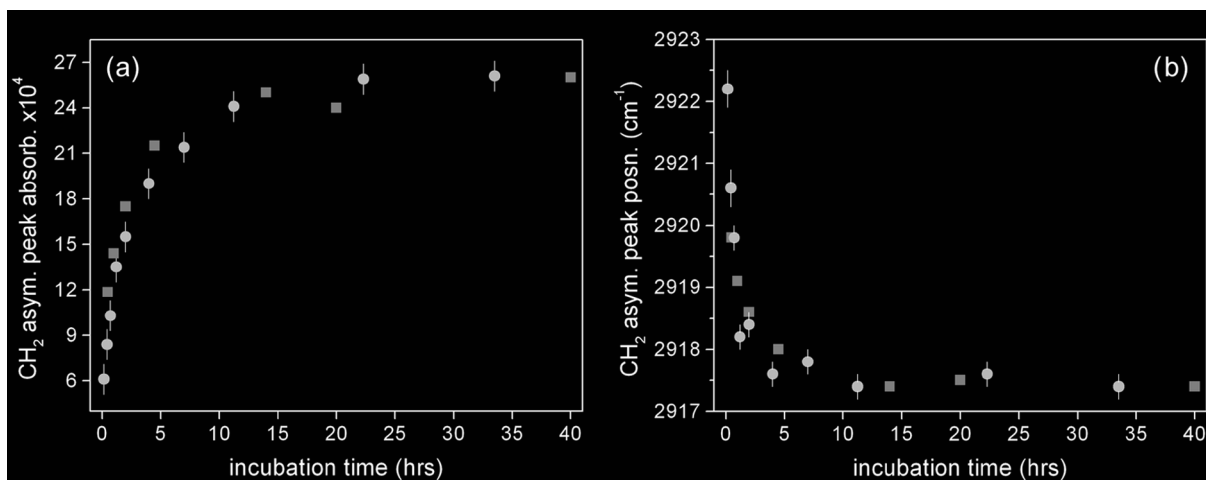


Figure 4.6. IR peak absorbance (a), and position (b), of the asymmetric C-H stretching mode of alkane CH₂ in HDT-SAMs. Circles/squares represent independent data series. Error bars are estimated from the uncertainty in the baseline absorbance in (a) and the precision of peak location in (b). Adapted from Kim *et al.* [Kim *et al.*, 2009].

The saturation of both parameters in Figure 4.6 indicates a minimum incubation time of 20 hours is required.

4.3 Beer-Lambert Analysis of the IR Absorption

4.3.1 Evaluation of the Absorption Coefficient

The absorbance characteristics of the SAM as a function of the methylene number n is now compared with liquid thiol in the context of a Beer-Lambert evaluation of their respective absorption coefficients. The peak absorbances of the CH_2 asymmetric stretching mode is plotted in Figure 4.7. The linearity of the data is immediately apparent and is consistent with the physical model prefaced in Figure 4.2. Also shown in Figure 4.7 is the amplitude from the n -scaling model, which is parameterized by the scale factor s and plotted against a linear mapping of $n(s)$ between n_{11} and n_{17} . Agreement is excellent, and moreover, extrapolation of the model to $s \sim 0$ (between $n = 9$ and $n = 10$) simulates the loss of SAM integrity and predicts a trend consistent with the position of the n_9 data. Consequently, adoption of the values $n > 9$ defining a structural regime of well-ordered assembly is justified.

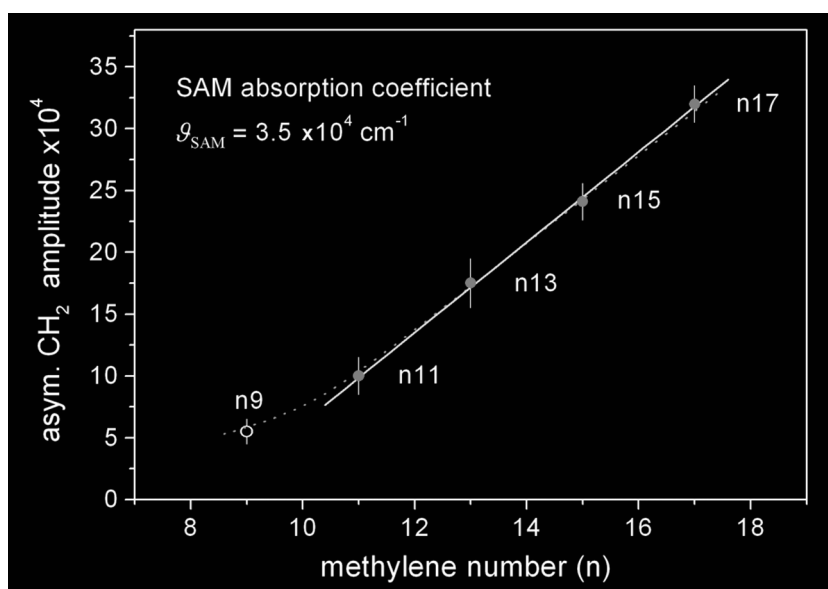


Figure 4.7. CH_2 asymmetric mode amplitude as a function of the methylene number (circles). Slope used to derive the absorption coefficient (line). Amplitude scaling model is parameterized by the scale factor s to a linear mapping of $n(s)$ (dotted line). Adapted from Marshall *et al.* [Marshall et al., 2009a].

Having validated the physical model, the linearity of absorbance with SAM molecular length enables the absorption coefficient to be derived. Taking a slope of 3.7×10^{-4} per unit n from Figure 4.7, dividing by $1.54 \sin 55^\circ \text{ \AA}$, which is the C-C bond length (CH_2 unit) projection along the molecular axis, multiplying by $1/\cos(14^\circ)$ to account for the assumed molecular axis tilt, and considering the aforementioned $2\times$ multiplier, the coefficient value thus obtained is $\mathcal{G}_{\text{SAM}} = 3.5 \times 10^4 \text{ cm}^{-1}$. This value of \mathcal{G}_{SAM} corresponds to the maximum point in the C-H stretching mode region, i.e., at the CH_2 asymmetric mode peak. A frequency spectrum of the absorption coefficient $\mathcal{G}_{\text{SAM}}(\nu)$ could then easily be constructed by normalization of the absorbance spectrum to the \mathcal{G}_{SAM} value.

Note that recent work by McGuinness *et al.* has reported some loss of SAM coverage and organization for values of $n < 15$ in this material system [McGuinness et al., 2007b]. The present results are consistent with their comments in terms of structural organization, having observed a similar increase in *gauche* defects at lower n -values in relation to Figure 4.5. Additionally, the loss of coverage with decreasing n they report (up to 12% for $n11$) may be superimposed on the data presented here, but in a slowly varying manner beyond the sensitivity of the method applied. Owing to the slope error such a case would impart, it is possible that the \mathcal{G}_{SAM} value may be overestimated by up to 5%.

In order to compare \mathcal{G}_{SAM} with its complementary bulk thiol value, liquid phase Beer-Lambert measurements were carried out to determine the respective absorption coefficients for several n -values. Liquid layer thicknesses ranged from $4 \text{ }\mu\text{m}$ to $11 \text{ }\mu\text{m}$ and it was observed that the ratio of absorbances between spectra of a given n -value corresponded to the ratio of their respective thicknesses, as expected by definition in Equation 2.41, and as the example of Figure 4.8 illustrates for $n13$. Next, each absorption coefficient was calculated by referencing the asymmetric peak amplitude and attenuation layer thickness data, the results of which are reported in Figure 4.9 along with the constant value of \mathcal{G}_{SAM} derived from above. Also shown is a data point borrowed from Parikh and Allara, evaluated from the spectrum of κ (imaginary part of the refractive index) in a KBr dispersed IR measurement of polycrystalline $\text{C}_{19}\text{H}_{39}\text{CO}_2\text{Na}$. Figure 4.9 indicates that the SAM phase absorption coefficient carries up to a $6\times$ enhancement factor relative to bulk thiol.

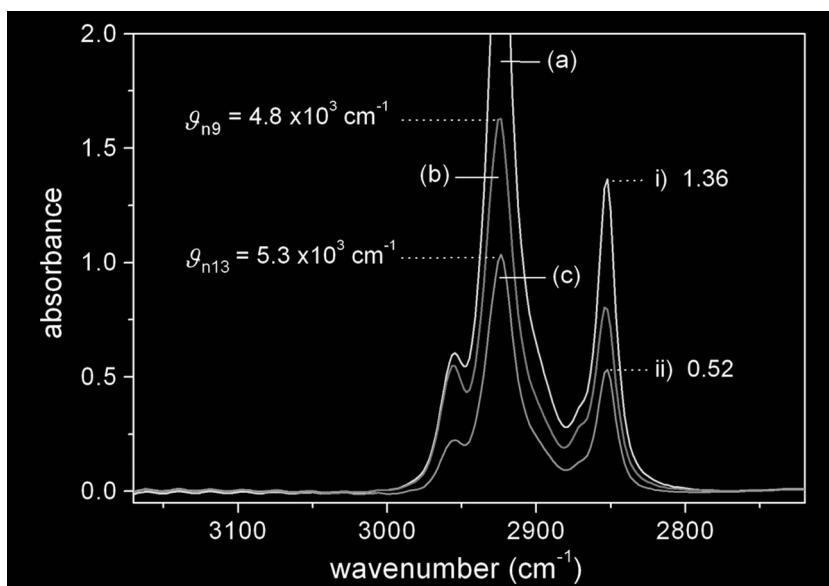


Figure 4.8. Liquid phase C-H stretching mode spectra: (a) n_{13} / 11 μm , (b) n_9 / 8 μm and (c) n_{13} / 4 μm , according to layer thickness. Absorption coefficients g_{n_9} and $g_{n_{13}}$ refer to CH_2 asymmetric mode peak amplitudes. The ratio of points i) and ii) verify the linear dependence of absorbance on layer thickness, in this case for n_{13} . After Marshall *et al.* [Marshall et al., 2009a].

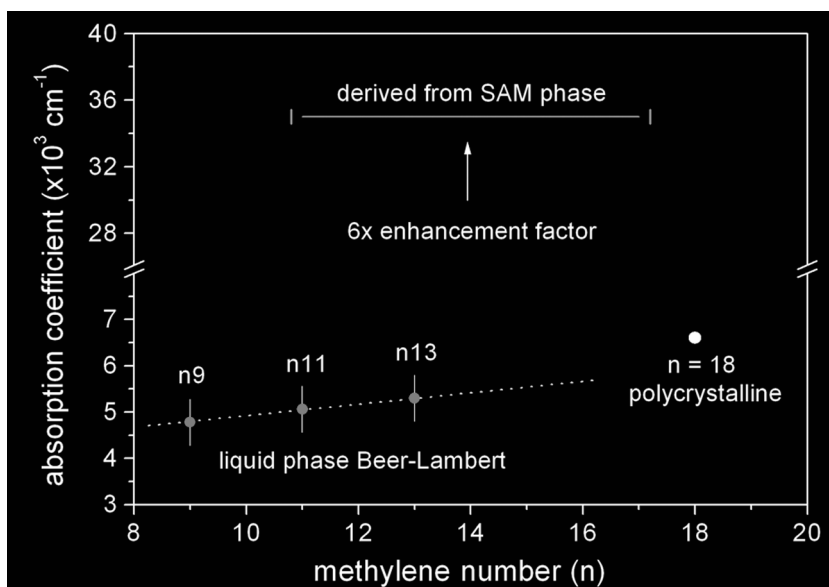


Figure 4.9. Enhancement factor observed for the SAM phase absorption coefficient relative to Beer-Lambert measurements in bulk material. Datum at $n = 18$ evaluated from the spectrum of κ for polycrystalline $\text{C}_{19}\text{H}_{39}\text{CO}_2\text{Na}$ [Parikh and Allara, 1992]. Dotted line for trend visualization only. After Marshall *et al.* [Marshall et al., 2009a].

4.3.2 Absorption Enhancement Effect

The liquid phase trend line in Figure 4.9 suggests that polycrystalline absorption coefficients may be up to 10% higher approximately. However, reported transmission IR measurements of the solid-liquid phase transition in polycrystalline $n\text{-C}_{21}\text{H}_{44}$ thin (2-10 μm) films has demonstrated an intensity reduction of about 30% upon melting [Casal *et al.*, 1983]. Some decrease is expected owing to the lower number density, loss of intermolecular interaction and increased conformational disorder associated with the liquid state. It shall be assumed that the liquid phase absorption coefficients reflect these intrinsic factors by a factor corresponding to the larger estimate, i.e., up to a 40% increase in absorbance upon the crystalline phase transition may be expected. Since the packing density of the pseudo-crystalline SAM is about 25% greater than in the liquid phase, density increases can account for a large fraction of the 40% intensity increase expected upon the SAM transition.

A more significant factor to consider is the spatial orientation of the molecules with respect to the polar orientation of the incident optical wave. According to Equation 2.32, the intensity of the vibrational transition is proportional to $|\mathbf{E}_{IR} \cdot (\partial\boldsymbol{\mu}/\partial\mathbf{x})|^2$. For the case of an isotropic liquid, averaging the \cos^2 term between these two vectors over 4π yields a factor of 1/3 (Appendix C), relative to the maximal case of a fixed molecular orientation of $\boldsymbol{\mu}$ collinear with \mathbf{E}_{IR} . In the SAM, the normal coordinates for both the asymmetric and symmetric vibrations are effectively coplanar with the surface, given that both are directed orthonormal to the molecular axis and that uniaxial asymmetry about the surface normal may be applied. Since the IR spectra were recorded in unpolarized light, averaging in the plane of \mathbf{E}_{IR} for measurements made in transmission is required, which results in an intensity reduction factor of 1/2 for the SAM phase. Note that planar averaging takes care of any further consideration of the SAM's uniaxial nature, in this context, since averaging need only be done once. Therefore, based on orientational considerations, the maximum absorbance scale factor expected for the SAM relative to the liquid phase in the reported measurements is about 1.5 \times .

The combined (intrinsic) effects of phase transition and orientation have accounted for about 2 \times of the 6 \times enhancement factor observed in the data. The remaining 3 \times can be accounted for by considering the possible extrinsic effects of the surface or of intermolecular interactions specific to the SAM phase. These will be considered in more detail in Chapter 5.

4.4 Optical Constants of the SAM

In this section, the principal components of the complex refractive index $\mathcal{N}_{i,i}$, which are based on Equation 2.42 such that $\mathcal{N}_{i,i} = \sqrt{1 + \chi_{i,i}} = \eta_{i,i} + i\kappa_{i,i}$, are now derived from the spectrum of $\mathcal{G}_{\text{SAM}}(\nu) = 4\pi\kappa\nu$ defined in Section 4.3.1. Since the normal coordinates of vibration (r_q) for the symmetric and asymmetric CH_2 stretching modes are mutually orthogonal and perpendicular to the molecular axes, defined by the C-C-C backbone plane, and owing to the discussion regarding the uniaxial absorption symmetry as discussed in Section 2.2.4, the optical axis is defined to be coincident with the surface normal having imaginary components $\kappa_{1,1} = \kappa_{2,2}$ and $\kappa_{3,3}$. More specifically, recall that the equivalency of $\kappa_{1,1}$ and $\kappa_{2,2}$ results from: i) the $\pm 45^\circ$ mixed twist orientation of the C-C-C plane about the molecular axis in a two-chain surface cell, and ii) the possibility of mixed azimuthal orientations that, on average, generates the required symmetry about the surface normal. In order to model the refractive index, equate the coefficients of $\mathbf{P} = \epsilon_o \chi \mathbf{E}$ and Equation 2.34,

$$\epsilon_o \chi = \frac{N \alpha}{1 - N \alpha / 3 \epsilon_o} \quad (4.2)$$

Using $\mathcal{N}^2 = 1 + \chi$, and expanding the polarizability α (in the numerator only) in terms of the electronic and vibrational contributions,

$$\mathcal{N}^2 - 1 = \frac{N \alpha_e / \epsilon_o + N \alpha_v / \epsilon_o}{1 - N \alpha / 3 \epsilon_o} \quad (4.3)$$

or,

$$\mathcal{N}^2 - 1 = \chi_\infty + \frac{N e^2}{m_r \epsilon_o} \sum_g \frac{f'_g}{(\omega_g^2 - \omega^2 + i \gamma_g \omega)} \quad (4.4)$$

where the first term has been reduced to the off-resonance limit of $\chi_{i,i}$, which is assumed equivalent for all i and is valued such that $\eta_\infty = \sqrt{1 + \chi_\infty} = 1.43$, i.e., the real part of the refractive index far from the IR absorption peaks [Parikh and Allara, 1992; Rosu *et al.*, 2009]. In the second term, the vibrational part of Equation 2.40 was substituted such that the normalized oscillator strengths have absorbed the local field correction in the denominator of

Equation 4.3. Generalizing further such that the coefficients of the summation are like-wise accounted for in the normalization, Equation 4.4 can be simplified to,

$$\mathcal{N}(\nu) = \sqrt{1 + \sum_g \left(\frac{f_g''}{\nu_g^2 - \nu^2 + i\gamma_g \nu} \right)}, \quad \eta_\infty = 1.43 \quad (4.5)$$

Consequently, the oscillator strengths f_g'' , and the absorption peak frequencies ω_g and linewidths (damping constants) γ_g of the g^{th} resonant modes become parameters suitable for model fitting to experimental spectra.

Once the parameters of Equation 4.5 are determined, $\eta_{i,i} = \text{Re}(\mathcal{N}_{i,i})$ and $\kappa_{i,i} = \text{Im}(\mathcal{N}_{i,i})$ are immediately known. First, the choice of modal parameters (ω_g and γ_g) were selected from the component assignments in Table 4.1. These were used to reconstruct the spectrum of $\kappa_{x,x} = \kappa_{y,y}$ obtained from an experimental spectrum of HDT-SAM by fitting of the oscillator strengths. The experimental spectrum $\kappa(\nu)$ was normalized to the peak value of \mathcal{G}_{SAM} viz.,

$$\kappa(\nu) = \frac{1}{2} \frac{\mathcal{G}_{\text{SAM}}}{4\pi\nu} \frac{A_{IR}(\nu)}{A_{IR\text{max}}} \quad (4.6)$$

where division by 2 follows from the fact that the observed absorbance $A_{IR}(\nu)$ is the sum of equal and orthogonal components in the surface plane at normal incidence, i.e., by the sum of oscillator strengths for uniaxial symmetry. The components $\eta_{x,x} = \eta_{y,y}$ follow accordingly by numerical transformation. Figure 4.10 shows these results in the upper series (a) and (b).

In the work by Rosu *et al.*, IR ellipsometry was used to determine the dielectric constants specifically for HDT-SAM, expressed similarly using oscillator strength representation. Using their formulation and reported parameters for $\varepsilon = \varepsilon' + i\varepsilon''$, cast in terms of the principal components $\eta_{x,x} = \eta_{y,y}$ and $\kappa_{x,x} = \kappa_{y,y}$ with the relationships,

$$\eta = \left(\frac{\sqrt{\varepsilon'^2 + \varepsilon''^2} + \varepsilon'}{2} \right)^{\frac{1}{2}} \quad \kappa = \left(\frac{\sqrt{\varepsilon'^2 + \varepsilon''^2} - \varepsilon'}{2} \right)^{\frac{1}{2}} \quad (4.7)$$

equivalent components were found. These are plotted in the lower series of Figure 4.10. The correspondence between the ellipsometric (single n -value) and Beer-Lambert determinations

of the optical constants demonstrates their mutual validity. Also, it supports that these constants are invariant with chain-length in the ordered SAM phase since the Beer-Lambert results were obtained from the differential absorption over several values of n . The equivalency of these constants also validates the underlying assumption that the SAMs are sufficiently dense and ordered over these methylene numbers, which suggests the low frequency permittivity ($\epsilon \epsilon_o$) is also n -invariant in the ordered SAM phase. This will factor into the analysis of the SAM 2D-DLP in Chapter 5.

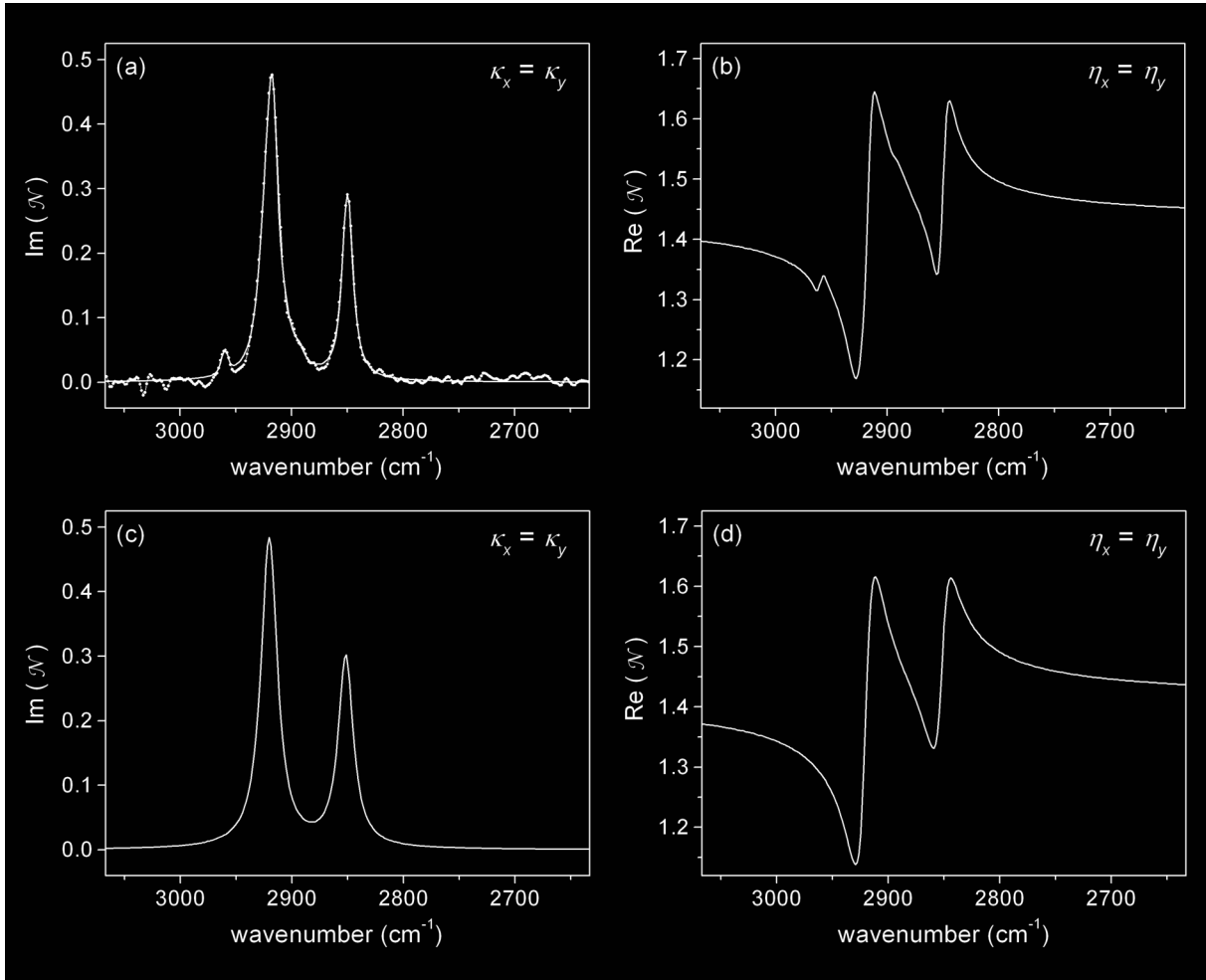


Figure 4.10. Comparison of the principal components of the refractive index determined using Beer-Lambert analysis in the present work (a) and (b) [Marshall et al., 2009b], with results from IR ellipsometry adapted from Rosu *et al.* [Rosu *et al.*, 2009] (c) and (d). The components in the surface plane are shown, which are equal due to uniaxial symmetry. The data in (a) was scaled from absorbance measurements according to the value of ϑ_{SAM} .

Note that under uniaxial symmetry, and for non-zero values of the molecular tilt, $\kappa_{3,3}$ is non-zero. This component is not directly accessed in transmission measurements at normal

incidence and is not shown. It could, however, be readily determined from the following transformation between the molecular coordinates and the surface frame,

$$\begin{pmatrix} M_x \\ M_y \\ M_z \end{pmatrix} = \begin{pmatrix} \cos(\varphi) & -\sin(\varphi) & 0 \\ \sin(\varphi) & \cos(\varphi) & 0 \\ 0 & 0 & 1 \end{pmatrix} \begin{pmatrix} 1 & 0 & 0 \\ 0 & \cos(\theta) & -\sin(\theta) \\ 0 & \sin(\theta) & \cos(\theta) \end{pmatrix} \begin{pmatrix} \cos(\psi) \\ \sin(\psi) \\ 0 \end{pmatrix} \quad (4.8)$$

where M_i are the transition moments in the surface plane, ψ refers to the mixed twist orientation ($\pm 45^\circ$) of the C-C-C backbone plane about the molecular axis, θ refers to the molecular axis tilt assumed (14°) as above, and φ is a rotation about the surface normal such that $M_x = M_y$ according to the required symmetry. Furthermore, in a manner similar to the expressions in Equation 2.44, vectorized elements of the material dipolar response \mathbf{k}_i may be written in terms of $3\mathbf{k}_{iso}$ of the isotropic bulk medium,

$$\mathbf{k}_i = \frac{3}{2} \mathbf{k}_{iso} M_i^2, \quad i = x, y \quad (4.9a)$$

$$\mathbf{k}_z = 3 \mathbf{k}_{iso} M_z^2 \quad (4.9b)$$

The $3\times$ extrinsic factor of IR enhancement referred to in the last section can now be readily understood as an increase in oscillator strength specific to the SAM. In Equation 4.9a, the vectorized response for the SAM is expressed in terms of the effective magnitude k_{iso} , which can be compared to the real isotropic value measured in the liquid phase. Referencing the asymmetric CH_2 peak in Figure 4.10, the value of k_{iso} satisfying Equation 4.9a for the SAM is 0.66. This is $3.1\times$ relative to the value measured from the liquid phase (0.15), accounting for the intrinsic (polycrystalline) conformational and phase related increases previously discussed, which were estimated to be about 40% in the last section.

4.5 Amine-Terminated Alkanethiols

It was mentioned in Chapter 1 that secondary level functionalizations would be discussed briefly. Presented as an independent section, the following is adapted from contributed work in *Applied Surface Science*, “Molecular self-assembly and passivation of GaAs (001) with alkanethiol monolayers: A view towards bio-functionalization” [Dubowski *et al.*, 2010], and

includes some additional material related to SAM ordering. The discussion is appropriate to introduce at this time since it relates to observations using both IR spectroscopy and XPS.

The development of a biosensor platform relies critically on the functionality of the SAM-GaAs interface. Although more complex functionalizations are required for practical applications, the demonstration of covalent bond attachment to the functional groups of a SAM is a relevant first step. To this end, biotin coupling to ATA-SAMs was investigated.[†] Biotin is a protein-ligand typically employed in biochemical assays that can form a covalent bond with the amine termination of ATA-SAMs through its carboxylic acid group. In contrast with SAMs having methyl-terminated thiols of similar length, the IR spectra of SAMs prepared with $\text{HS}(\text{CH}_2)_n\text{NH}_2$ ($n=11,16$) displayed characteristics of a less ordered monolayer, i.e., reduced amplitude and increased vibrational energy. Figure 4.11 shows comparative results for ATA-SAMs prepared in pH neutral ethanol.

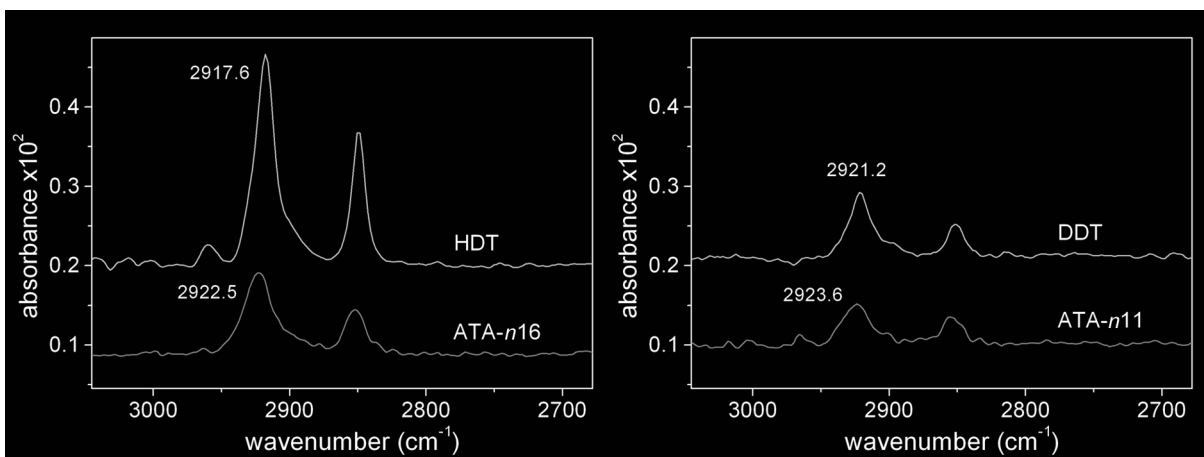


Figure 4.11. Comparison of methyl-terminated alkanethiol SAMs HDT and DDT with amine-terminated SAMs of similar length (methylene numbers $n = 16$ and 11). Numerical values refer to the CH_2 asymmetric stretching mode peak wavenumbers.

Since it is possible that hydrogen bonding between the amine functional groups can promote the formation of a partial bilayer [Wang *et al.*, 2005], the close-packing necessary for a higher degree of SAM order may be sterically hindered. Protonation of the amine groups in solution would also impart a disordering effect resulting from electrostatic repulsion of the head-groups. Anecdotal, however, SAM formation in ethanolic solutions of varying pH did not result in significant differences in the ordering of the SAM. An additional confounding factor to the establishment of a well-ordered SAM in the amine-terminated system may be the

[†] Sample preparation: immersion of $n11$ ATA-SAMs in 2 mg/ml N-hydroxysuccinimidobiotin / dimethyl sulfoxide solvent for 2 hours. Rinsed with isopropanol / deionized water, and dried in N_2 stream.

competition for surface bonding between amine and thiol groups. Both have nucleophilic character, but whereas thiolate presents a charged and therefore more reactive species, amine should form only weak surface bonds. Use of pH neutral ethanol has ruled out significant amine-GaAs bonding in IR and XPS testing, although evidence of surface-bonded R-NH₂ species, e.g., decylamine [CH₃(CH₂)₉NH₂], has been observed at other pH values.

Despite the reduced degree of molecular ordering and the possibility of inverted surface bonding, a S 2p chemical state indicative of thiol chemisorption by HS(CH₂)₁₁NH₂ has been observed as illustrated in Figure 4.12 in the Ga 3s region. Interestingly, a small S-oxide (S_xO_y) component is detected that does not show up in methyl-terminated samples, but is expected if uncoupled thiol is present, e.g., in the inverted or bilayer arrangement. Comparing the N 1s region signal before and after biotin coupling treatment in the right panel of Figure 4.12, a significant increase in nitrogen intensity is observed. Separate tests have ruled out evidence of direct biotin-GaAs coupling. Therefore, given that biotin carries two nitrogen atoms per molecule and that the nitrogen intensity increase is due to covalently bonded biotin, a rough estimate of the degree of amide coupling to the functionalized surface of GaAs(001) is about 40%. This is a reasonable number given the estimated steric limit of 50% in the ideal SAM case. Examples of more sophisticated SAM-based architectures involving biotin include specifically immobilized avidin on biotinylated thiols [Ding *et al.*, 2006], and immobilization of influenza A with biotinylated antibodies interfaced to neutravidin [Duplan *et al.*, 2009].

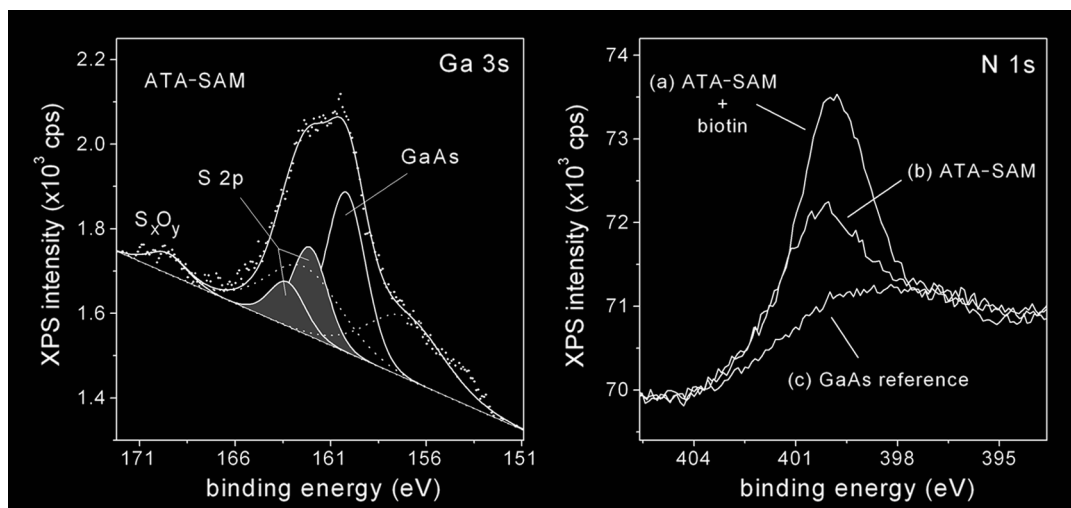


Figure 4.12. XPS spectra of *n*11 ATA-SAMs on GaAs. Left: component assignments in the Ga 3s region according to Chapter 3. S_xO_y component is due to the oxidation of unbound thiol. ToA 55°. Right: N 1s spectra of ATA-SAM after (a) and before (b) biotin coupling, relative to etched-only GaAs background (c). ToA 0°, *hν* - Mg Kα 1253.6 eV.

4.6 Chapter Summary

A homologous series of methyl-terminated n -alkanethiols were fabricated into SAMs and measured in transmission with IR spectroscopy. Modal decomposition of the spectral envelopes into fixed and n -dependent factors showed that a good fitting could be obtained by linear scaling of the n -dependent modes. Both the peak absorbance and wavenumber values were accurately represented in the spectrum model indicating that: i) the series between $n11$ and $n17$ was comprised of uniformly dense SAMs changing by molecular length, and ii) the increasing energies indicated by peak wavenumbers at shorter n -values do not entirely reflect an increase in SAM disorder. *Ex situ* measurements of the SAM formation dynamics in terms of increasing peak absorbance and decreasing peak wavenumbers demonstrated the transformation of the SAM into a highly ordered pseudo-crystalline phase.

Modal decomposition results supported the analysis of the SAM in terms of a Beer-Lambert evaluation of the absorption coefficient. Compared with similar evaluations of the absorption coefficient in the liquid phase, a $6\times$ enhancement factor was evident, $3\times$ of which could be attributed to extrinsic factors unique to the SAM. Casting the absorption coefficient into the principal components of the refractive index demonstrated its equivalence with the dielectric constants as determined by IR ellipsometry, which validated the Beer-Lambert results and the suggestion of a vibrational enhancement. In addition, a transformation from the molecular coordinates to the surface coordinates was specified for the transition moments in terms of the twist and tilt parameters of the SAM, which can be used for obtaining the z -component of the index. Although no functional relationship is yet established for the IR absorption enhancement in the SAM, the observation suggests a direct connection between the physical structure of the SAM and its electro-optic characteristics.

Lastly, amine-terminated alkanethiols were observed to form less-ordered monolayers, as indicated by the reduced absorbance and increased peak wavenumbers evident in their IR spectra. The disordering could be attributed to head-group protonation, or associations with the surface or with each other by nucleophilic or hydrogen-bond attraction. Some evidence for the latter is indicated by the presence of sulphur oxide species in XPS spectra. Despite these facts, S 2p chemical states indicating thiol chemisorption are observed, and functionality of the amine head-group has been demonstrated though biotin coupling as evidenced by an increase in N 1s photoemission intensity.

CHAPTER 5:

SURFACE BAND STRUCTURE in EQUILIBRIUM

The previous two chapters presented results specific to the structural and chemical properties of alkanethiol-SAM passivated GaAs(001). A chemically bonded, high coverage, molecularly ordered monolayer was described, and observations of its unique vibrational characteristics were also made. The discussion now turns to the electronic properties of this interface with a view as to how these interrelate with the observed physical characteristics. The results presented in this chapter are reported in *Langmuir*, “Surface Dipole Layer Potential Induced IR Absorption Enhancement in *n*-Alkanethiol SAMs on GaAs(001)” [Marshall *et al.*, 2009b], and “Surface barrier analysis of semi-insulating and n^+ -type GaAs(001) following passivation with *n*-alkanethiol SAMs” [Marshall *et al.*, 2011a].

Following the experimental details, the first section investigates the work function of the SAM-GaAs interface. Kelvin probe, XPS and IR spectroscopy methods are used to obtain the DLP contribution of the SAM from the CPD, which were defined in Chapter 2. Apart from its fundamental interest in obtaining the band structure, the DLP is investigated in order to help provide insight into the physical mechanisms explaining the IR enhancements reported in Chapter 4. Some relationship with the static field of the DLP is anticipated because of the dependence of \mathcal{N} on the polarization of the medium in Equations 2.34 and 2.35.

In the section following, the surface barrier height is determined based on XPS measurements of the surface Fermi level and calculations of the SCR. These are interpreted in the context of the AUDM and quantify the electronic passivation. Knowledge of this, in addition to the dipole contribution, allows the equilibrium band structure to be determined.

5.1 Experimental Details

5.1.1 Kelvin Probe and XPS Work Function Measurements

Sample preparation followed the method described in Chapter 3 for n_{11} , n_{13} , n_{15} and n_{17} SAMs on undoped semi-insulating and n^+ -type (Si-doped at $1 \times 10^{18} \text{ cm}^{-3}$) GaAs(001). In

order to determine the SAM DLP values, the respective CPDs with respect to a non-contact vibrating Au reference probe was measured using the Kelvin probe (KP Technology Ltd.), as described in Chapter 2. Single point measurements were made in air using a 2 mm probe diameter and front/back surface grounding contact. The dual contact helped stabilize the measurement against surface charge accumulation, and also by counterbalancing the rectifying barrier introduced at the contact interfaces, which is of particular concern for semi-insulating material [Maltby, 1972]. Electronic drift caused by stray capacitance was minimized with the use of a Faraday cage enveloping the Kelvin probe unit that, along with the off-null technique, reduced the CPD noise variation to < 10 mV. Only relative work function measurements were made with respect to the GaAs samples, although comparison of the CPD of cleaned Au and Cu samples against the expected absolute values showed good agreement. Baseline measurements of the GaAs CPD were obtained on etched-only samples and on samples following thermal disordering of the SAM, as described in the next section; the DLP values were then obtained by subtraction of the SAM and baseline CPDs.

In order to verify the DLP values obtained using the Kelvin probe, XPS analysis of the DLP was made. Uncorrected spectra at 0° ToA were measured on semi-insulating GaAs from an etched-only reference surface and from a sample of *n*15-SAM. These spectra were taken in charge neutralization mode with an overcompensating thermionic current used in order to ensure minimal charging differences so that the binding energy could be referred to the vacuum level; more details are to follow. The samples were mounted on conductive carbon tape, but were considered electrically isolated from the spectrometer ground by virtue of the effective barrier introduced by the semi-insulating material, which was verified by the fact that the binding energy could be made to shift by application of the thermionic current.

5.1.2 Baseline Thermal Disordering of the SAM

In order to provide a baseline for quantification of the DLP, a disordered monolayer surface was induced by post-process immersion of *n*15-SAMs in isopropanol (IPA) at 55°C for 1 min, transferred directly from the ethanolic thiol solution without a rinsing/drying step. The added heat provides the necessary conformational energy required to disrupt the molecular order. The disordered SAM removes the dipole contribution to the work function that molecular ordering imparts, therefore, it provides an additional baseline to the GaAs CPD. Consider that in the ideal SAM, disordering without surface desorption may be

counterintuitive. However, local variation from this ideal allows the SAM to disorder in the manner described. For example, it was shown in Chapter 3 that the surface uniformity of the SAM was about 90% or less. Note that at 55° C no significant surface desorption is expected to occur for S-GaAs bond energies reported to be in excess of 40 kcal/mol, which have stability up to 400 K [Voznyy and Dubowski, 2006], although recombinative desorption pathways do exist at lower temperatures as described in Chapter 2. High temperature bond stability may also be inferred from the molecular dynamics simulations of *n*15-SAMs on Au by Hautman and Klein, owing to the fact that surface desorption was not factored into their calculations of the temperature dependent increase in conformational disorder below 400 K [Hautman and Klein, 1989]. Dubois and Nuzzo have provided corresponding IR spectroscopy data that track the molecular dynamic results closely [Dubois and Nuzzo, 1992]. Recalling the results in Chapter 3, the inference to Au is supported by the observation of similar S 2p chemical shifts supporting the covalent nature associated with the thiolate bond. No substantial evidence of surface desorption was observed by XPS as will be demonstrated.

5.1.3 Integration of Au Binding Energy Calibrant

As described in Chapter 2, Fermi level equilibrium with the spectrometer ground is limited by the insulating barrier introduced by high resistivity samples or contacts. In order to circumvent this limitation, Au calibrant was integrated directly onto the GaAs substrates, prior to SAM formation, as an effective method to achieve calibration at the molecule-GaAs junction. Undoped semi-insulating and n^+ -type (Si-doped at $1 \times 10^{18} \text{ cm}^{-3}$) GaAs(001) wafers were used for this part of the study as well. Sample preparation proceeded as follows. Au binding energy reference pads were deposited by evaporation on freshly etched GaAs surfaces using polymethyl methacrylate photoresist and UV photolithography. The pads were about 170 μm in diameter with thicknesses in excess of 50 nm, and were spaced such that one pad resided on each wafer sample once cleaved into approximately 5 mm \times 5 mm sizes. After deposition of *n*15-SAM, the IR spectrum of the monolayer was recorded on one sample to verify that the process of Au pad deposition and subsequent re-etching did not interfere with the formation of a well-ordered SAM. In order to provide a stable contrast for testing, the etched and untreated GaAs-Au hybrid wafers were allowed to reoxidize in air (~ 3 min). The samples prepared with *n*15-SAMs were transferred directly to the XPS chamber from the N_2 environment in which they were prepared, with only a few seconds ambient exposure.

5.2 Dipole Layer Potential of the SAM

5.2.1 Motivations in the Context of IR Enhancement

Since the IR absorbance is dependent on the dipole moment derivative, as evident in Equation 2.32, factors significant to a redistribution of electron density will be significant to the oscillator strength to the extent they effect the molecular polarization. Molecular orbital intermixing and intermolecular Van der Waals forces are possible factors in this regard.

In view of these considerations, two surface mechanisms can be included in the list of extrinsic factors expected to affect a change in the oscillator strength. The first is the dipole moment contribution to the surface potential and the second is the charge transfer associated with chemisorption of the thiol group to the GaAs(001) surface. These factors will contribute to a physico-chemical state modification of the surface environment, possibly resulting in a change of polarization sufficient to account for the observed absorption enhancement.

To further explore these concepts, the IR enhancement effect can be placed in the context of similar observations made in other material systems. In the work described by Dumas *et al.* [Dumas *et al.*, 1986], and Persson and Ryberg [Persson and Ryberg, 1981; Persson and Liebsch, 1981], the adsorption of CO on metals such as Ag and Cu is associated with a reduction in work function, electron donation to the metal from a specific molecular orbital (MO) and a 4× increase in IR absorption intensity. In this case, however, overlap of the MO with the metal Fermi level increases the MO's occupation in what is referred to as backdonation. In this dynamic process, C-O bond stretching modulates the 2π -antibonding MO energy level specifically, which results in charge oscillation between the MO and the metal effecting an enhancement of the vibrational polarizability. In contrast, the lowest unoccupied MO of the SAM-GaAs system is well above the surface Fermi level of the GaAs substrate [Nesher *et al.*, 2006], which rules out this particular effect.

Instead, an explanation in terms of the electronic polarizability is sought. Consider the theoretical electrostatics of *n*-alkanoic monolayers at the air-water interface studied by Taylor and Bayes, which suggest that an increase in local permittivity, and a corresponding reduction in the surface dipole, results from depolarization of the C-H moments in the static field of a 2D molecular array [Taylor and Bayes, 1994]. This work highlights the intimate connection between the surface potential and dielectric constants of an adsorbed monolayer, with potential implications for the IR absorbance.

IR absorption enhancements of the order $10\text{-}10^3$ can also be realized, on rough metal or metal-particle substrates, in what is called Surface Enhanced Infrared Absorption (SEIRA) [Osawa, 2001], and has been observed for ODT molecules adsorbed on Au islands specifically [Enders and Pucci, 2006]. Both electromagnetic (plasma resonance) and chemical mechanisms factor into SEIRA enhancements and research distinguishing the two has been reported [Osawa and Ikeda, 1991; Osawa, 2001] concluding that: 1) scaling of order 10 can be achieved based on the chemical mechanism, and that 2) chemisorption is a required element for this mechanism to manifest. An explanation behind the chemical mechanism related to CO chemisorption on Ag and Cu was just described. The chemical mechanism in SEIRA is less well understood. However, in a review of the SEIRA effect by Osawa, a distinction is made between the electromagnetic and chemical mechanisms in the context of Equation 2.32; the plasma resonance induces an E_{IR} field enhancement, whereas the chemical mechanism is attributed to a change of the molecular derivative $\partial\mu/\partial x$.

Considering the change in physico-chemical environment upon SAM formation, particularly, its dependence on thiol chemisorption and the surface dipole potential, the similarity in the extrinsic enhancement factor ($3\times$) relative to metal-based observations suggests that a related chemical mechanism may exist on the semiconductor surface.

5.2.2 Discussion on Fermi Level Pinning

The CPD measures the relative work function difference between the test semiconductor and probe reference material. In doing so, both the potential associated with the SCR, i.e., the band-bending potential, and the electron affinity are implicit in the data. This is made clear in the band diagram of Figure 2.12. In order to obtain the DLP, which is characteristic of the change in electron affinity, any change in the band-bending potential must be also be accounted for. For example, Lodha and Janes solved the Poisson equation for the equilibrium electrostatic potential of the Au/ODT/ p^+ -GaAs MMS junction using a dipole moment of 0.74 D (debye) per molecule for ODT [Lodha and Janes, 2006]. They found the DLP drop across the ODT layer to be about 380 mV and the band-bending to be only 16 mV. Interestingly, the low surface barrier means that electronic coupling to the metal contact is more easily made from p-GaAs and accounted, in part, for the increased tunneling

conductivity across the MMS junction. The improved coupling is due to the band alignment owing to the outwardly directed sheet dipole layer or DLP as described in Figure 2.14.

On n-type GaAs surfaces and on undoped semi-insulating GaAs, as shall be brought into evidence later, the occupation of surface traps by electrons can lead to a surface Fermi level pinning effect. To illustrate, consider that the surface density of a discrete level defect is high and that the surface Fermi level reflects the energy to which those states are filled, as in Figure 1.6. Consequently, quantities of charge larger than what can be held or exhausted from these discrete levels is required in order to reposition the surface Fermi level. Pinning reflects the limited extent to which the surface can be passivated electronically, since the density of defects states must first be reduced. Electrostatic calculations at semiconductor interfaces assuming a surface charge resulting only from equilibration of the Fermi level will not be accurate. For example, variation of the metal work function in the Schottky contact determines the barrier height ideally. If a high density of surface states exists then the barrier height is fixed by the pinning level instead [Streetman and Banerjee, 1999]. The band diagram across a MOS (or MMS) capacitor will have similar limitations.

Note that changes in the surface Fermi level of GaAs have been observed, e.g., following surface adsorption of metals [Spicer *et al.*, 1975; Grant *et al.*, 1981]. However, reports on the electronic passivation of thiol-GaAs(001) interfaces have indicated that significant surface Fermi level pinning applies. In the pioneering work on sulphides passivation of GaAs by Lunt *et al.* [Lunt *et al.*, 1991], time-resolved PL indicated that under high-injection / flat-band conditions in the SCR, passivation with short-chain thiols led to carrier lifetime increases characteristic of SRV reduction. Rather than a decrease of the dead-layer that repositioning of the surface Fermi level would imply, SRV reduction was attributed to be the more significant with respect to enhancements of the steady-state PL, as discussed in Chapter 2. Lunt *et al.* also made the analogy with pinning effects observed by UPS following passivation with inorganic sulphides [Spindt, 1989a]. Pinning was also observed for ODT-SAMs using Raman scattering [McGuinness *et al.*, 2007a], though the limitations of this technique were already discussed. The pinning effect will be validated using a more precise technique in the section on determination of the surface Fermi level by XPS.

5.2.3 Work Function and the 2D Dipole Layer Potential

5.2.3.1 Kelvin Probe Results

In this section, the n -dependent variation of the CPD is determined, from which the SAM DLPs are later evaluated. Under the pinning condition, the band-bending potential is assumed fixed, which allows the baseline CPD to be obtained from both the etched-only and disordered SAM reference surfaces in order to establish the DLPs by subtraction of the CPD baseline. Independent verification of the DLP for $n15$ -SAM (HDT) is provided by XPS analysis of the relevant binding energy shifts in the section following.

The recorded CPD values (squares) are plotted upon the left axes as a function of the methylene number in Figures 5.1: (a) on semi-insulating GaAs, and (b) on heavily Si-doped (n^+ -type) GaAs. The CPD scale reference is the work function of the Au probe at 0 mV. Shown in (a) are the baseline CPD values of the etched-only GaAs reference (up triangle) and of the thermally disordered $n15$ -SAM (diamond). The (dotted) line forms the baseline CPD value approximating the GaAs work function without the SAM. Implicit in the baseline assumption is that the dipolar contribution from chemisorbed thiolate or oxide layer is approximately the same owing to the similar electronegativities characteristic of both bond types. The solid line of CPD values between $n11$ and $n17$ demonstrates the chain-length correspondence. The CPD changes at a rate 46 ± 3 mV/CH₂ in (a) and 50 ± 4 mV/CH₂ in (b). The IR spectroscopy data (circles) shown along the right axis of (a) represent the peak absorbances of the asymmetric CH₂ stretching mode reproduced from Figure 4.7. Error bars in (a) and (b) were estimated (± 20 mV) based on the repeatability of $n15$ -SAM results.

The slope equivalency between the results in (a) and (b) is in accordance with the pinning effect assumed, i.e., that adsorption of thiols imposes little band-bending change. Absorption of the same molecule type on surfaces having different initial band-bending would be expected to produce different results if there were a band-bending effect. The CPD reaction to molecules of different length may also be expected to be different in this regard. Roughly 500 mV and 750 mV of band-bending is expected for the semi-insulating and n^+ -type material respectively, which equates to an order of magnitude variation in the occupancy of surface states (see in Chapter 6). Therefore, one would expect a more pronounced band-bending change for the semi-insulating type, with slope disparity as a possible consequence.

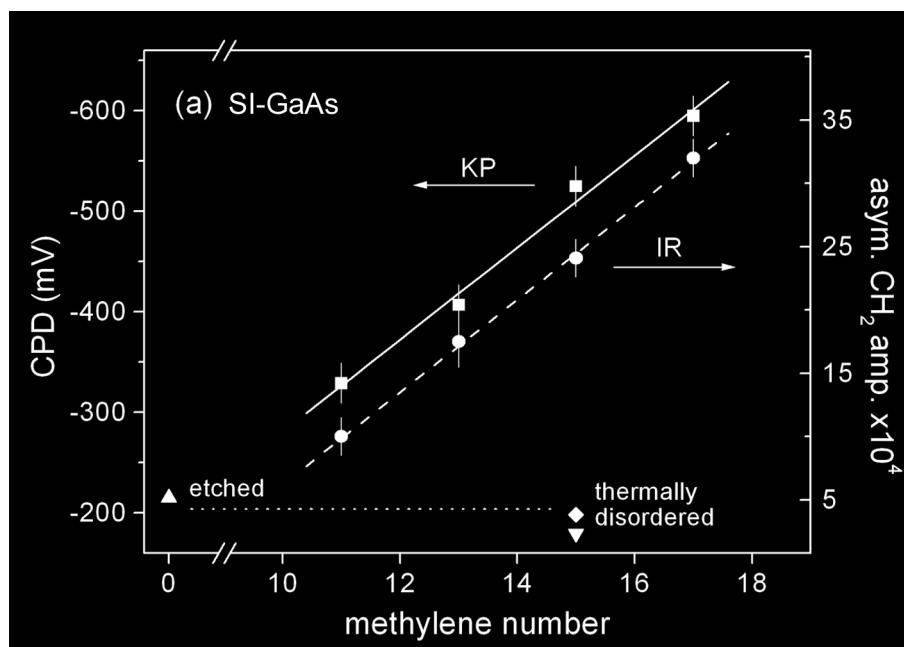


Figure 5.1(a). Kelvin Probe (KP) CPD (squares) and asymmetric CH₂ stretching mode IR absorbance (circles) vs. chain length for [HS(CH₂)_nCH₃] SAMs on semi-insulating GaAs(001). CPD etched only GaAs (up triangle). CPD (diamond) and IR (down triangle) thermally disordered n15-SAM. Baseline CPD (dotted line). Adapted from Marshall *et al.* [Marshall *et al.*, 2009b].

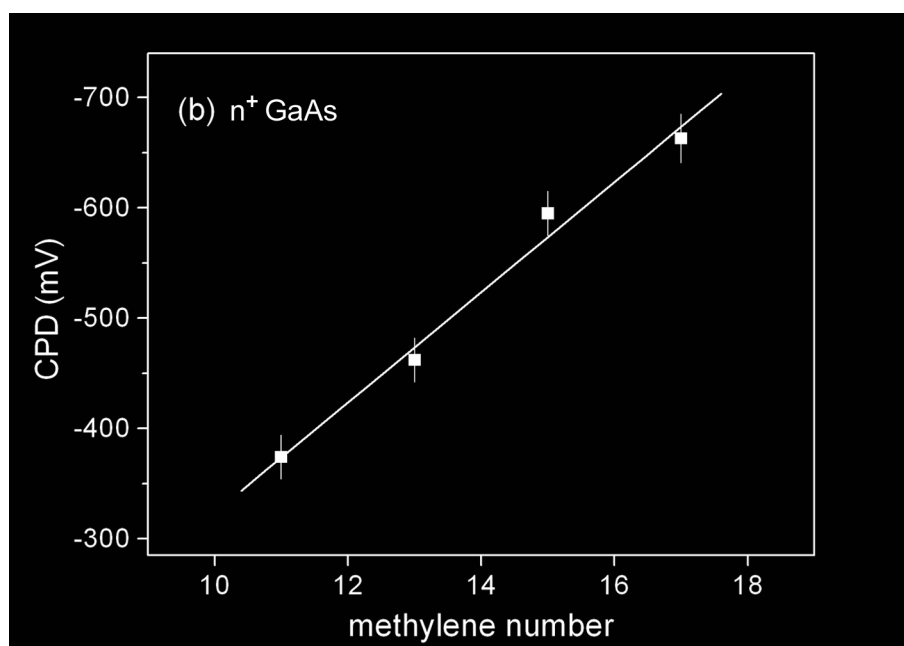


Figure 5.1(b). CPD for SAMS as per (a) on heavily Si-doped (n⁺-type) GaAs. Adapted from the Supporting Information in Marshall *et al.* [Marshall *et al.*, 2009b].

5.2.3.2 IR Spectroscopy of the Disordered SAM

The IR results shown along the right axis of Figure 5.1(a) represent the peak absorbances of the SAM as mentioned. Also shown is the absorbance from a n_{15} -SAM after thermal disordering (down triangle). Representative IR spectra are provided in Figure 5.2. The upper series illustrates the spectrum of C-H stretching modes from a sample of n_{15} -SAM. Identifying characteristics are the: (a) CH_2 asymmetric mode near 2918 cm^{-1} , (b) CH_2 symmetric mode near 2850 cm^{-1} , and (c) the CH_3 mode of the terminal methyl group near 2960 cm^{-1} , as was previously described. The lower series represents the spectrum after thermal disordering. The loss of intensity is significant, at least $6\times$ as expected based on the findings in Chapter 4. Moreover, relative to the purely randomized liquid phase, the molecular orientations after disordering will be more parallel to the surface on average. This effect will increase the relative loss of intensity observed since the orthonormal transition moments will be increasingly perpendicular to the optical field polarization, which is in the surface plane for transmission measurements. However, the reduction of IR signal is not attributed to significant material desorption loss as discussed in the Experimental Details section, and as observed by XPS in the next section.

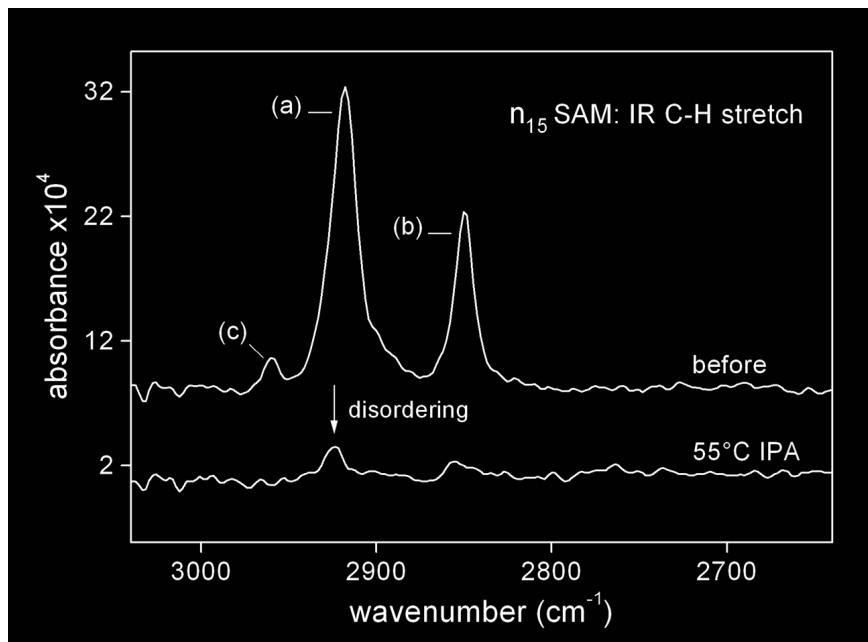


Figure 5.2. C-H stretching mode IR spectra in transmission of n_{15} -SAM before and after thermal disordering in 55°C isopropanol (IPA). Reduction of intensity is due to molecular orientation and the loss of enhancement factors specific to the ordered SAM phase. See text for details. After Marshall *et al.* [Marshall *et al.*, 2009b].

5.2.3.3 XPS Determination of the DLP

Comparative As 3d XPS spectra at 0° ToA are shown in Figure 5.3 from an etched and untreated GaAs reference surface (left) and from a sample of n_{15} -SAM (right). Under the pinning assumption and with the samples electrically isolated, use of an overcompensating charge neutralization current minimizes sample charging differences such that differences in binding energy can be directly equated with a vacuum level referenced increase in the core levels due to the reduction of electron affinity associated with an outwardly directed sheet dipole layer, namely, the 2D DLP. A generalized band diagram of the XPS measurement is provided in Figure 5.4. In Figure 5.3, the difference in the As 3d (uncorrected) binding energy positions associated with the GaAs phase measures 293 meV and reflects a decrease in the surface potential as expected. By comparison with Figure 5.1(a), the observed shift is commensurate with the change in potential one computes for the n_{15} -SAM (303 mV) by subtracting the CPD baseline from the $n = 15$ data point. Mutual agreement of the XPS and Kelvin Probe results supports the use of the CPD baseline to determine the DLP for the other n -values within an assumed tolerance of ± 20 mV.

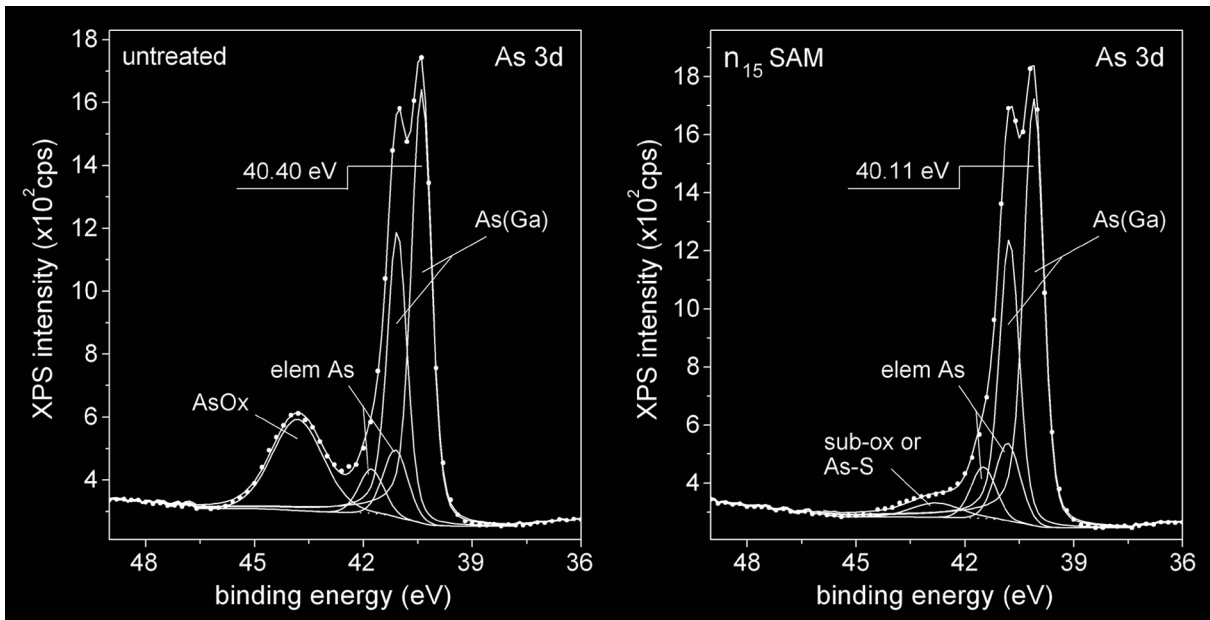


Figure 5.3. XPS core level As 3d spectra at 0° ToA from etched but untreated GaAs (left) and from GaAs prepared with n_{15} -SAM (right). Component peaks: As(Ga), bulk GaAs; elem As, elemental As; AsOx, $\text{As}_2\text{O}_3 + \text{As}_2\text{O}_5$; sub-ox or As-S, residual low oxidation states of As and/or As component of S-GaAs coupling. Doublets represent 5/2 and 3/2 spin-orbit branching. Spectra are charge overcompensated and uncalibrated such that the binding energy reference indicates a change in potential corresponding to the DLP. Adapted from Marshall *et al.* [Marshall *et al.*, 2009b].

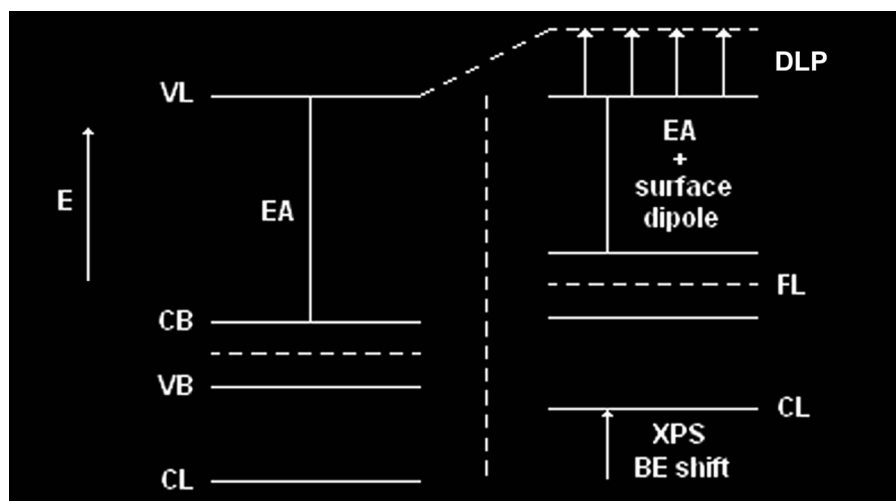


Figure 5.4. Generalized band diagram of the XPS measurement in Figure 5.3 showing a reduction of the electron affinity (EA) associated with the surface dipole moments of the SAM (arrows) that result in an increase of the core level (CL) energies. Adapted from Dubowski *et al.* [Dubowski *et al.*, 2010].

S 2p core level XPS spectra are plotted in Figure 5.5 for thiolate as observed in the ordered *n*15-SAM (left) and after thermal disordering (right). Peak assignments followed according to the fitting procedure in Chapter 3. Three-point box car smoothing was applied (post peak-fitting) in order to render the underlying chemical states more clearly. As prefaced in Section 5.1.2, disordering does not result in substantial surface desorption, which is qualitatively demonstrated by the equivalent S 2p / Ga 3s intensity ratios in Figure 5.5. See Appendix E for a discussion of the use of different ToAs (60° / 75°), which were required in order to render the measurements equally surface sensitive owing to a 2-3× reduction of the attenuating overlayer thickness associated with SAM disordering. Thiol loss amounting to 25 % was also factored into these calculation using a fractional overlayer model, in order to account for the overlayer reduction, though it remains unclear how representative this estimate actually is. The important point is that chemisorbed thiolate is still observed after low-temperature disordering in significant quantity, which is clear from the spectra.

Highlighted in Figure 5.5 is a positive binding energy shift observed for the S 2p core level in the ordered *n*15-SAM configuration. This shift is estimated to be at least + 300 meV with respect to the disordered state near 162.2 eV and demonstrates the change in work function associated with SAM ordering. A similar shift is observed for the C 1s data. The increase in S 2p binding energy in the ordered SAM phase relative to the nominally

referenced Ga 3s line is consistent with an increase in the vacuum level referenced Fermi level position and corroborates the As 3d results in Figure 5.3.

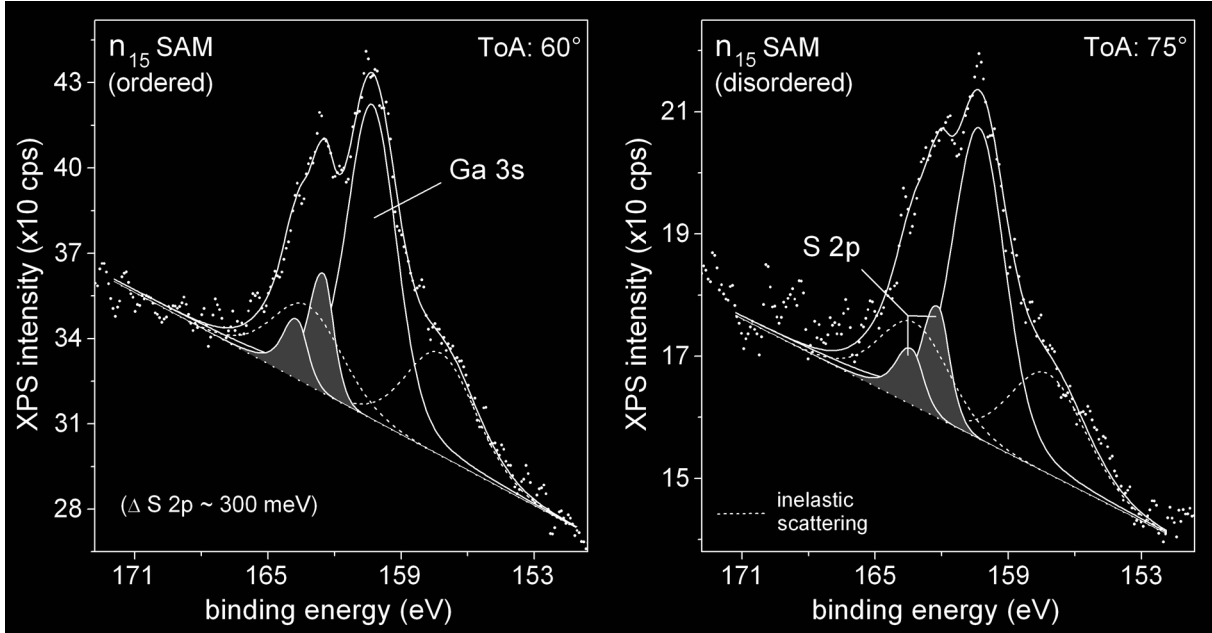


Figure 5.5. XPS core level S 2p / Ga 3s spectra of *n*₁₅-SAM before (left) and after thermal disordering (right). A relative binding energy shift of about 300 meV is observed for the S 2p line in the ordered SAM indicating the change in work function corresponding to the DLP. Spectra are nominally referenced to GaAs (Ga 3s at 160.3 eV) for convenience of comparison. Adapted from Marshall *et al.* [Marshall *et al.*, 2009b].

5.2.4 DLP and the Effective Capacitor Model

Based on the decreasing work functions relative to the baseline identified in Figure 5.1(a), the CPD values indicate that a sheet dipole or 2D DLP may be attributed to the SAM, with moments directed outward and with magnitude proportional to *n*. The net dipole moments are assumed to extend over the length of the molecule [Howell *et al.*, 2002]. The CPD values attributed to the SAMs are subtracted from the baseline CPD identified in Figure 5.1(a) in order to determine the surface potential contribution of each chain-length, i.e., the *n*-dependent DLP values (ΔΦ). These are plotted in Figure 5.6 (circles) and fitted with a linear function. Next, calculated DLPs (ΔΦ_{calc}) are modeled (squares) based on non-interacting and surface-independent gas phase molecules according to,

$$\Delta\Phi_{calc} = \frac{\sigma d}{\epsilon_r \epsilon_o} = \frac{\xi q d}{\epsilon_r \epsilon_o} = \frac{\xi \vec{\rho} \cdot \hat{z}}{\epsilon_r \epsilon_o} \quad (5.1)$$

where σ is the sheet charge density associated with the equivalent capacitor, d is the SAM thickness, ϵ_r and ϵ_0 are the relative and vacuum permittivities, ξ is the molecular surface density ($5.2 \times 10^{14} \text{ cm}^{-2}$) based on 4.24 Å alkane close-packing [Ulman *et al.*, 1989], q is the elementary charge unit, $\vec{\rho}$ is the axial dipole moment per molecule (debye) based on quantum chemistry software results [Howell *et al.*, 2002], and \hat{z} is the unit vector normal to the GaAs surface. Considering the permittivity values for polyethylene and *n*-alkanes, a low frequency limit of $\epsilon_r = 2.2$ is assumed [Weast and Lide, 1990]. Implicit in Equation 5.1 is the molecular length and the tilt angle of the molecular chain-axis with respect to the surface normal. In the present calculations it is assumed that a molecular tilt angle of 14° applies in accordance with the citations and discussion in Section 3.3.3.

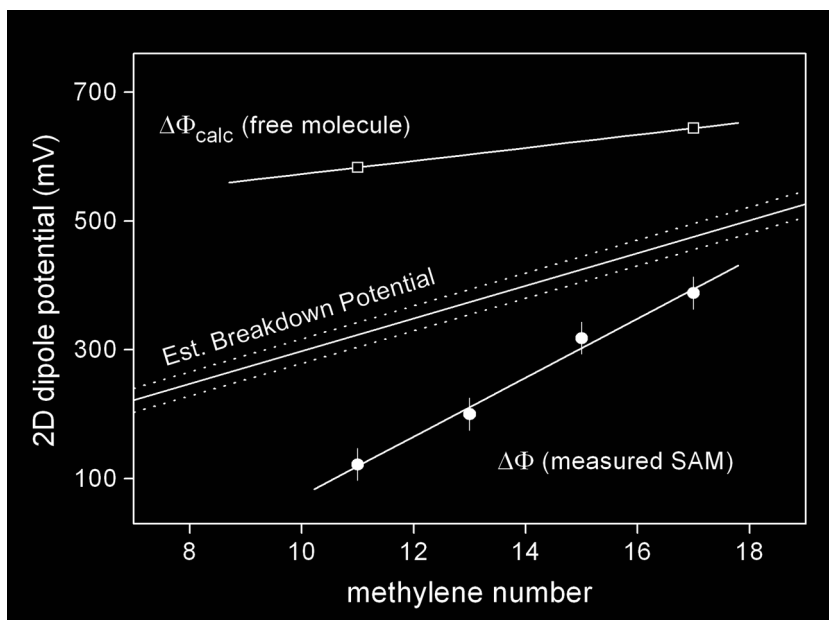


Figure 5.6. Calculated DLP assuming molecular dipole values in a SAM of non-interacting / surface independent alkanethiols (squares). DLPs evaluated from CPD measurements (circles) for SAMs on semi-insulating GaAs(001). The breakdown potential is estimated based on the dielectric strength of polyethylene monolayers and the SAM molecular length. After Marshall *et al.* [Marshall *et al.*, 2009b].

Also shown in Figure 5.6 is the dielectric breakdown potential of the SAM, which is estimated based on the molecular length, and the dielectric strength (200 MV/m) of polyethylene Langmuir-Blodgett monolayers [Sorokin *et al.*, 2002], and polypropylene thin films [Liufu *et al.*, 1998]. Surface-coupled molecular depolarization in dense SAMs of low polarizability (e.g., alkanes) has been referred to in the context of the COMFE as proposed by

Cahen *et al.* [Cahen *et al.*, 2005], and as was introduced in Chapter 1. Contrasted with SAMs of higher polarizability (e.g., systems of π -conjugated molecules), COMFE depolarization refers to the surface-coupled channel through which the SAM reduces the dipole field across itself, a field which can approach the critical limit of dielectric strength. The relations within Figure 5.6 bear this out illustratively and also concur with the findings of Taylor and Bayes in terms of an overall surface dipole reduction [Taylor and Bayes, 1994]. However, for the *n*-alkanoic system they investigated, a saturation of the reduction effect based on methylene moment depolarization was calculated for chain-lengths $n \geq 8$, since this effect was expected to be localized to the region including the first 3-4 methylene groups proximate to the methyl-termination. In our system, we observed a reduction in the absolute surface dipole compared to the model based on non-interacting molecules, but an increase in relative potential in the regime $n11$ to $n17$. This distinction may be owing to the net effects of depolarization, including those related to covalent surface bonding, something that was not a factor in the (non-chemisorbed) Langmuir-Blodgett monolayers featured in the Taylor and Bayes study. For example, proximity of the methyl-termination could increase the polarity of the S-GaAs interface bond reducing the net surface dipole for the shorter chain molecules.

Depolarization mechanisms aside, it is clear that a strong static field is attributed to the SAM. With respect to the critical dielectric limit, Figure 5.6 provides a qualitative view of the substantial static field to which the SAM is exposed. In the next section, this factors into an understanding of the mechanism of IR enhancement.

5.2.5 Correlation with the IR Absorbance and the IR Enhancement Effect

In Figure 5.1(a), the IR and CPD results demonstrate a mutually linear variation, which suggests that the IR absorbance is sensitive to the electrostatic field of the SAM. To support the assertion of this correspondence, comparison of the respective linear functions that were fitted to each of the IR absorbance and DLP values yields the parametric relation,

$$I_{IR}(n) = \beta \Delta\Phi(n) + b \quad (5.2)$$

with $\beta = 40 \times 10^{-4} \text{ V}^{-1}$ and $b = 0.16 \times 10^{-4}$, in terms of volts (V) and dimensionless absorbance units. The intercept (b) is negligible with respect to experimental error, so we may conclude that the IR absorbance is directly proportional to the DLP. This direct proportionality means the two parameters scale at the same rate ($\sim 3\times$), which is evident from the illustrative data

example provided in Table 5.1. Moreover, this scaling is greater than a unitary increase, which may be expected for the IR absorbance particularly, based on the change in absorption path length. Since the variation of IR absorbance is linear in n , as is the DLP in the effective capacitor model of Equation 5.1, it is natural that these two observables will appear linearly correlated when parameterized by n in Equation 5.2. However, it is by virtue of the specific case of direct proportionality (characterized by the zero-intercept) that the scaling of the enhanced IR absorbance is attributed to a functional dependence based on the static field associated with the DLP. Correlation without a physical dependence would be more likely to produce some other (non-equivalent) scaling, characterized by a different intercept. Details relating to the nature of the suggested effect are discussed in the following paragraphs.

TABLE 5.1. Correspondence of the IR absorbance and DLP in [HS-(CH₂) _{n} -CH₃] SAMs on semi-insulating GaAs(001).

Experiment	$n = 11$	$n = 17$	ratio
FTIR CH ₂ asym. str. ^a / $\times 10^{-4}$	9.9	31.8	3.2
$\Delta\Phi$ by Kelvin Probe / mV	119	394	3.3

^a Absorbance at C-H asymmetric stretching mode peak.

In Chapter 4, the IR characteristics observed established that the SAMs are sufficiently uniform, dense and ordered to support that the optical constants are n -invariant in the linear regime investigated. It was stated that this invariance implies the low frequency permittivity ($\epsilon\epsilon_o$) is also n -invariant in the ordered SAM phase. That the permittivity is n -invariant is critically important as it justifies the assertion that the CPD variation in Figures 5.1 (a) and (b) may be represented in the effective capacitor model. Consequently, assurance is given that the surface potential contribution of the SAMs is derived from the dipolar molecular field. Having established this, the correspondence between the IR enhancement and the DLP may now be examined in more detail, and is explored qualitatively in the following.

In Section 5.2.1, it was stated that an explanation for the IR enhancement mechanism was sought in terms of the electronic polarizability. A first order change to this parameter can be written by expansion in terms of the vibrational displacement,

$$\alpha_e = \alpha_o + \frac{\partial \alpha_o}{\partial r_q} \delta r_q \quad (5.3)$$

where α_o is the low-frequency electronic polarizability, and the second term is a change in polarizability due to normal mode vibrational displacement along r_q . Owing to the effective capacitor model, there is an internal field within the SAM,

$$\mathbf{E}_{int} = -\frac{\partial}{\partial z} \Delta \Phi \hat{\mathbf{z}} \quad (5.4)$$

that adds an induced dipole contribution to the permanent molecular dipole μ_a ,

$$\mu = \mu_a + \alpha_e E_r \quad (5.5)$$

or,

$$\mu = \mu_a + \alpha_o E_r + \frac{\partial \alpha_o}{\partial r_q} \delta r_q E_r \quad (5.6)$$

where $E_r = \mathbf{E}_{int} \cdot \hat{\mathbf{r}}_q$, $\alpha_o E_r$ is an induced static moment, and the last term is time-varying due to the vibrational displacement δr_q . The partial derivative of Equation 5.6 along r_q is,

$$\frac{\partial \mu}{\partial r_q} = \frac{\partial \mu_a}{\partial r_q} + 2 \left. \frac{\partial \alpha_o}{\partial r_q} \right|_a E_r \quad (5.7)$$

and is evaluated at the equilibrium point a . The prime notation (μ') combines the permanent dipole with the induced static dipole contribution. The second term represents a dynamic change to the polarizability. Equation 5.7 is substituted into Equation 2.32 in vector form,

$$W_{IR} \propto \left| \mathbf{E}_{IR} \cdot \hat{\mathbf{r}}_q \left(\frac{\partial \mu_a}{\partial r_q} + 2 \left. \frac{\partial \alpha_o}{\partial r_q} \right|_a \mathbf{E}_{int} \cdot \hat{\mathbf{r}}_q \right) \right|^2 \quad (5.8)$$

where it becomes clear that contributions deriving from the internal field and the electronic polarizability add to the IR absorbance. The dependence on the internal field strength of the SAM, coupled with the observation of DLP proportionality, indicate these contributions are significant to an increase of IR absorbance. \mathbf{E}_{int} is a constant function of n according to the effective capacitor model, therefore, Equation 5.8 specifies a fixed enhancement factor.

Note that the dynamic term in Equation 5.8 relies on $\partial\alpha_o/\partial r_q$ being a non-zero value. This polarizability derivative is the fundamental criterion for Raman scattering. In fact, arguments similar to the above have been used to explain field-induced IR bands in centrosymmetric solids, which are normally Raman active only [Burstein and Ganesan, 1965]. Centrosymmetric vibrations are IR inactive, since no dipole derivative exists. An applied field will remove the charge symmetry and excite IR absorption bands by introducing the required dipole derivative. By this logic, the second term of Equation 5.8 relies on the vibrational motions of the SAM being non-centrosymmetric, in which case IR absorption and Raman scattering are not mutually exclusive. Both Raman and IR excitations can be observed for the C-H stretching modes of polymethylene [Abbate *et al.*, 1982]; therefore, by analogy with the alkane backbone of the SAM, it is expected that $\partial\alpha_o/\partial r_q$ applies and the argument is valid.

To explain the contribution of the field-induced static dipole to the IR enhancement, consider that implicit in Equation 5.8 is that $\mu = \mu(r_q)$, with limits about the equilibrium position a such that $\mu(r_q)|_{0,\infty} = 0$, and which has some maximum value $\mu(r_{q\max} \neq a)$ such that the derivative at a is non-zero [Barrow, 1962]. Since molecular vibration is considered a variance about a in accordance with the phase value ωt along this derivative, displacements of a or changes to $\mu(a)$ resulting from perturbations to the electronic structure specific to the SAM phase can result in a new derivative value relative to the isotropic liquid. An increase in the polarization of the oscillator may result in an increase to its polarizability and, consequently, an additional increase to its vibrational amplitude as per Equation 5.8.

An alternative to the static and dynamic factors contributing to a change in the dipole derivative, a third mechanism may act to locally increase the optical field. This mechanism is based on the Lorentz local field correction applied in standard dielectrics [Boyd, 2003], and is illustrated in Figure 5.7. Basically, the field carried by a polarizable material macroscopically (\mathbf{E}_{IR}) can be evaluated by removing a volume of the material (with its polarization charges) and calculating the fields generated by the volume and cavity. By superposition, the average macroscopic field is due to the sum of the volume and cavity fields. Since the relevant field is the one within the cavity (\mathbf{E}_{loc}) where the oscillator under consideration can be placed, it is sufficient to calculate the field due to the polarized spherical volume (\mathbf{E}_{vol}) or,

$$\mathbf{E}_{loc} = \mathbf{E}_{IR} - \mathbf{E}_{vol} \quad (5.9)$$

Since the internal field due to a polarized sphere is $-\mathbf{P}/3\epsilon_o$ [Feynman, 1970], Equation 2.33 follows immediately from Equation 5.9. This treatment applies to isotropic material, e.g., liquid thiol. The factor of 1/3 comes from the spatial averaging of a $\cos^2 \theta$ term, in the manner of Equation C.17, and is explained in several texts [Kittel, 1986; Reitz *et al.*, 1992].

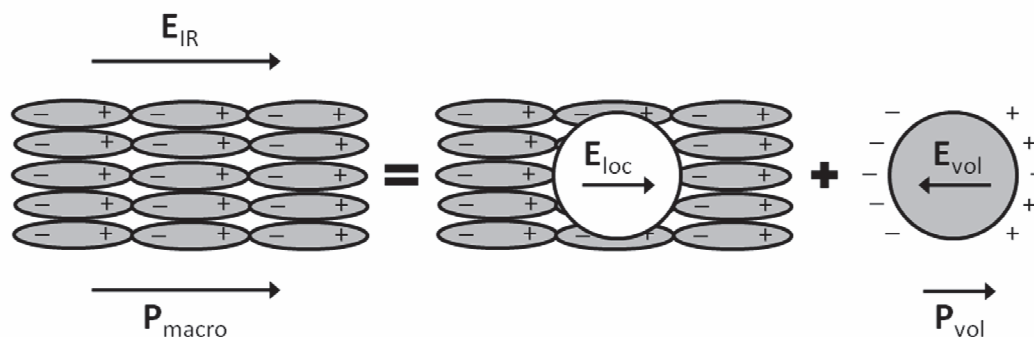


Figure 5.7. Method of calculating the Lorentz local field correction. A spherical volume of material is removed from a polarized medium along with its polarization charges. The local field experienced by a molecule within the cavity is the sum of the optical field carried in the medium macroscopically, plus the field due to the polarized volume. The local field is thus enhanced due to polarization of the surrounding medium.

In the SAM, however, owing to its uniaxial nature, i.e., isotropic in the surface plane with respect to its vibrational polarization, the Lorentz cavity can be reduced to a cylindrical one, in which case the spatial factor becomes 1/2 by averaging in the surface plane,

$$\mathbf{E}_{loc} = \mathbf{E}_{IR} + \frac{\mathbf{P}}{2\pi\epsilon_o} \int_0^{2\pi} \cos^2 \Theta d\Theta = \mathbf{E}_{IR} + \frac{\mathbf{P}}{2\epsilon_o} \quad (5.10)$$

As a check, this result can be referenced to the case of a slot cavity, where the factor is \mathbf{P}/ϵ_o [Feynman, 1970], i.e., the dimensional progression from sphere to slot goes as 1/3, 1/2, 1. Consequently, the contribution to the local field due to polarization induced by the IR optical wave is enhanced by a factor of 1.5× vs. the isotropic case. If the local field is then substituted in Equation 2.32, where its gets squared, the field correction factor could account for a portion of the IR enhancement. Note that this mechanism is independent of the dipole related effects discussed above and, therefore, may exist on its own or in addition to them. To get a sense of the possible contribution of this mechanism, the field correction for both the liquid and SAM phases can be considered quantitatively; this will yield what portion of the IR enhancement

the field correction effect may be responsible for. For the isotropic liquid thiol, substitution of $\mathbf{P} = N \alpha \mathbf{E}_{loc}$ in Equation 2.33 along with the result in Equation 2.35 gives,

$$\mathbf{E}_{loc} = \left(\frac{\mathcal{N}^2 + 2}{3} \right) \mathbf{E}_{IR} \quad (5.11)$$

Similarly, but for the SAM, Equation 5.10 is used in place of Equation 2.33 and gives,

$$\mathbf{E}_{loc}^* = \left(1 - \frac{3}{2} \frac{N_{SAM}(\mathcal{N}^2 - 1)}{N_{iso}(\mathcal{N}^2 + 2)} \right)^{-1} \mathbf{E}_{IR} \quad (5.12)$$

Substitution of the appropriate values of \mathcal{N} , and squaring as per Equation 2.32, results in an estimation of the expected IR enhancement factor based on the local field correction effect when Equation 5.12 is divided by Equation 5.11. For example, evaluating at the wavenumber position of the CH₂ asymmetric stretching mode absorbance maxima, the calculated correction factor about 2. That is, the field correction gives an IR absorption rate that is 2× greater in the SAM than in the liquid thiol, which is significant with respect to the overall scaling of the enhancement. It should be noted, however, that this mechanism is not causal with respect to the observed correlation between the IR absorbance and the DLP. If true, then it would predict the same enhancement factor on other material systems that have a similar structural geometry, i.e., two-chain, hexagonally-packed alkane SAMs.

Consider the case of alkanethiol SAMs on Au, which fit the above criteria and are therefore suitable for comparison. Using Reflection Absorption Infrared Spectroscopy (RAIRS) and CPD data from the literature [Howell *et al.*, 2002; Laibinis *et al.*, 1991], the IR absorbance can be referred to the DLP in the same manner as in Equation 5.2 with the expectation that if the IR / DLP relationship is causal, then the same proportionality will be observed as that on GaAs. Figure 5.8 shows that indeed this is true; the scaling of the IR absorbance with DLP is proportionally the same, though their absolute values are less. Consequently, the Lorentz factor can be rejected as a significant enhancement mechanism. Note that in order to make an equivalent comparison of RAIRS data to IR data in transmittance, the RAIRS absorbance values (n15 to n19) were first linearly extrapolated to the n11-SAM value and then normalized to it in order to factor out absorption path differences. A factor of 1/2 was then applied to the RAIRS data to account for the fact that, on reflection from metal surfaces, the polarization selection rule and image dipole effect result in

a doubling of absorption intensity [Aroca, 2006], which would artificially increase the absorption coefficient if not removed.

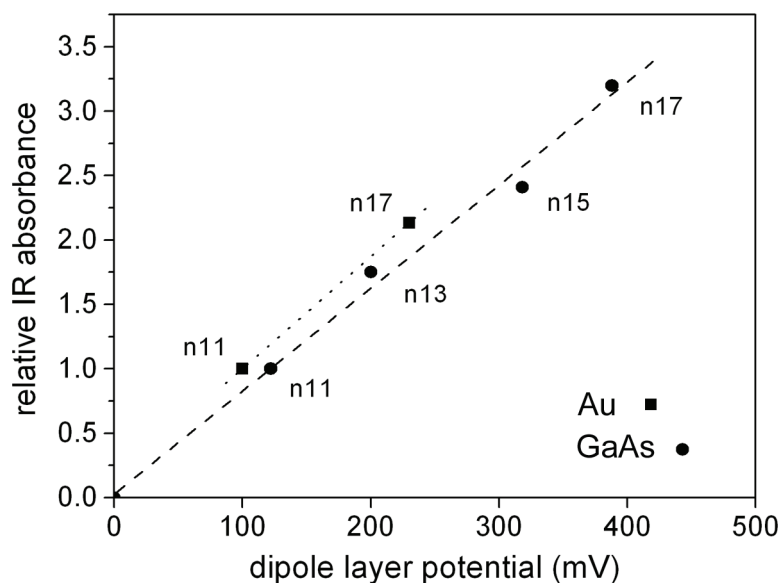


Figure 5.8. Relative IR absorbance of the asymmetric C-H stretching mode of methylene in *n*-alkanethiol SAMs on Au (squares) and GaAs(001) (circles) vs. the SAM DLP. Dashed line indicates directly proportional scaling. Data for Au adapted from Laibinis *et al.* [Laibinis *et al.*, 1991] and Howell *et al.* [Howell *et al.*, 2002].

In summary, the IR enhancement mechanism has been discussed in terms of the additive static and dynamic contributions to the vibrational moment, which are based on the molecular field associated with the DLP and the electronic polarizability of the SAM. The observed correlation of the IR and DLP data can be qualitatively attributed to these mechanisms, and is corroborated by similar results on Au. A possible secondary effect is the Lorentz local field correction applied to the example of uniaxial absorption symmetry as appropriate for the SAM. In this framework, the IR optical field is locally strengthened due to the macroscopic vibrational polarization of the SAM in the plane of uniaxial symmetry. However, IR enhancement by means of this effect cannot satisfactorily explain the IR / DLP correlation and is therefore rejected in favour of a causal relationship specified by Equation 5.8.

5.3 Surface Barrier Analysis following SAM Passivation

Having obtained the DLP contribution to the surface potential, the band-bending is now determined for the n^+ -doped and semi-insulating GaAs substrates in order to complete the band structure in equilibrium. Knowledge of the band-bending requires that the surface Fermi level position with respect to the band-edges be determined precisely. With this, the change in surface Fermi level position before and after passivation can be resolved, which indicates the electronic passivation achieved, i.e., the reduction of surface charge associated with the SCR.

In Chapter 2, the limitations of optical (non-equilibrium) methods and methods that rely on the grounding contact of the sample were discussed. In this section, the integration of Au reference sites onto the GaAs surface, prior to SAM deposition, is shown to be an effective method of XPS binding energy calibration that allows the equilibrium surface Fermi level to be determined. First, the XPS results are shown, and then the method used to determine the Fermi level is explained. Following that, the Fermi level results are discussed in terms of the barrier height with explanations given in the context of physical defect models.

5.3.1 XPS Results of the Surface Fermi Level

The As 3d core level and valence band regions are plotted in Figures 5.9 (a) and (b), for both the n^{15} -SAM prepared, and etched only semi-insulating GaAs surfaces. The As 3d core levels are shown calibrated such that the zero of binding energy corresponds to the VBE, which was estimated by visual extrapolation in the logarithmic domain to a precision of ± 75 meV. Note that the GaAs density of states (XPS intensity) converges to the same zero for both sample types. Therefore, a constant VBE referenced core level energy (As 3d_{VBE}) is validated. Perturbations of the valence band are observed in the spectral region up to 12 eV, which are characteristic of the atomic species in the immediate vicinity of the surface, including the oxides, but since the XPS sampling depth is sufficient to probe to a depth of several lattice constants, the zero of valence band intensity corresponds to the zero of the density of states representing bulk GaAs. On this account, it is expected that As 3d_{VBE} will be the same for both substrates. Application of the As 3d_{VBE} energy for the determination of GaAs surface Fermi levels has been demonstrated [Nesher *et al.*, 2006; Grant *et al.*, 1981]. Specific to the data in Figures 5.9, the well-resolved As 3d_{5/2} spin-orbit branch was referenced by spectral decomposition in CasaXPS and a As 3d_{VBE} value of 40.73 eV was obtained.

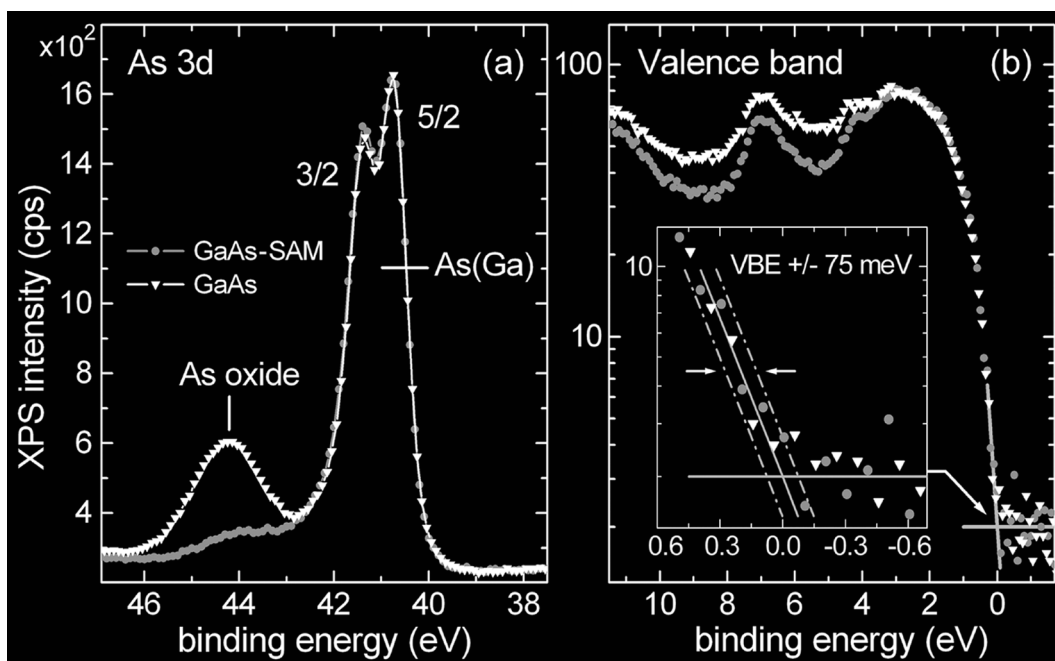


Figure 5.9. XPS As 3d core level and valence band regions of semi-insulating GaAs for samples: (circles) passivated with *n*15-SAM, and (triangles) etched only with reoxidization. Spectra refer to the VBE (solid line intersection), determined by extrapolation in the logarithmic domain. GaAs phase As 3d peaks are labeled with spin-orbit branching; ToA, 0°. After Marshall *et al.* [Marshall *et al.*, 2011a].

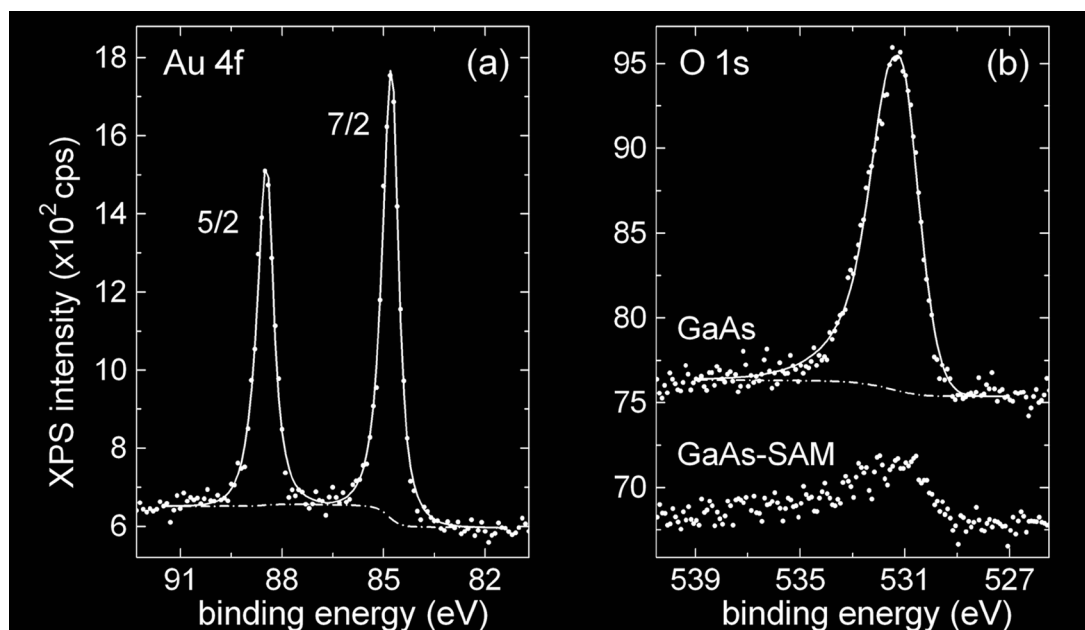


Figure 5.10. XPS spectra: (a) Au 4f peaks labeled with spin-orbit branching, and (b) the O 1s region including spectra following passivation with *n*15-SAM (lower series) and from the etched and reoxidized GaAs reference surface (upper series), shifted vertically for clarity. Spectra are not energy calibrated. ToAs: Au 4f, 0°; O 1s, 60°. After Marshall *et al.* [Marshall *et al.*, 2011a].

XPS spectra were also recorded in the Au 4f region where the Fermi level was referred to the Au 4f_{7/2} line, as indicated in Figure 5.10(a), which provides a stable Fermi level reference at 84.00 eV [NIST XPS, 2003]. Complementary O 1s spectra are plotted in Figure 5.10(b). The O 1s spectra were collected at a 60° photoelectron ToA in order to emphasize surface oxide concentrations in contrast to the 0° ToA used for the other measurements. The O 1s panel shows the oxide intensity of the etched/reoxidized reference sample (upper series) and the null oxide level following SAM passivation (lower series). The shape of the O 1s region background near 532 eV is due to a periodic Ga LMM Auger feature, as discussed in Chapter 3, and thereby demonstrates, within the limit imposed by this background, that the surface oxide concentration is negligible.

When the Au and GaAs materials are equipotential, a measurement of the difference between the Au 4f_{7/2} and As 3d_{5/2} uncalibrated core level energies (Δ_{XPS}) yields the calibrated position of the GaAs surface Fermi level in terms of the energy (E_f) above the VBE as follows, $E_f = 84.00 - \Delta_{XPS} - As\ 3d_{VBE}$, and as graphically represented in Figure 5.11.

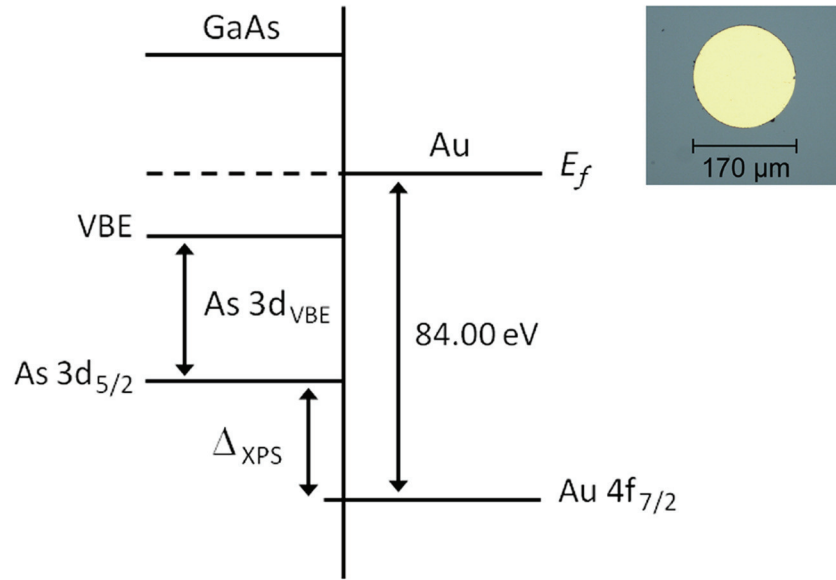


Figure 5.11. Energy level diagram illustrating the XPS binding energy referencing used to determine the surface FL position above the VBE. Core levels refer to the spin-orbit components identified in Figs. 1 and 2. Inset: Optical image showing a Au calibration pad integrated onto the GaAs surface After Marshall *et al.* [Marshall *et al.*, 2011a].

Note that this method is insensitive to work function differences that may arise from oxidation, surface dipoles associated with the SAM, or the effect of any thiol adsorption on the Au pads. These would be reflected in a vacuum level referenced change to the electron affinity, whereas the current method reflects changes to the Fermi level with respect to the core level energies. In order to verify that the two materials were equipotential, biasing applied by a charge neutralization (C/N) current (thermionic emission) shifted the core levels up to 1.1 eV, where it was observed that Δ_{XPS} remained constant within normal peak fitting error (≤ 40 meV). In addition, GaAs spectra were recorded separately from and proximate to the Au pads (relative to the $300 \mu\text{m} \times 700 \mu\text{m}$ XPS field of view), and were found to have equivalent energies.

Table 5.2 (col. 7) lists the Fermi level results for both semi-insulating and n^+ -doped substrate types, based on a calculation of E_f using the uncalibrated energies in cols. 2-5. In col. 6, no significant difference in Δ_{XPS} is observed, with and without C/N biasing applied, confirming the equipotential contact between the GaAs and Au materials. In subsequent tests, E_f repeatability within 60 meV was observed, which accords with the given uncertainties. As a relative measure of error, repeatability within 10 meV specific to the increase in E_f after thiol treatment was obtained. Table 5.2 indicates that the passivating effect of alkanethiol SAMs is limited to a 50 meV reduction in equilibrium band-bending for semi-insulating GaAs and a 20 meV reduction for n^+ -type GaAs, i.e., a strong pinning effect is realized.

TABLE 5.2. Evaluation of the VBE referenced surface Fermi level in semi-insulating and n^+ -doped GaAs(001) passivated with [HS-(CH₂)₁₅-CH₃] SAMs.

sample type	C/N off		C/N on		δ (eV)	E_f (eV)
	As 3d _{5/2}	Au 4f _{7/2}	As 3d _{5/2}	Au 4f _{7/2}		
SI-GaAs (Ref)	41.61 ^a	84.67	40.96	83.99	-0.03 ^b	0.21 ^c
SI-GaAs (SAM)	41.74	84.75	40.62	83.61	-0.02	0.26
n^+ -GaAs (Ref)	41.79	84.37	41.66	84.26	0.02	0.69
n^+ -GaAs (SAM)	41.80	84.35	41.65	84.24	0.04	0.71

^a Columns 2-5, uncalibrated XPS binding energy in eV.

^b Variation of GaAs-Au peak separation (Δ_{XPS}) with up to 1.1 eV bias.

^c Values calculated from columns 2 and 3. Estimated error ± 90 meV.

5.3.2 Surface Barrier Height and the AUDM

In conjunction with known mechanisms of bulk charge balance and the AUDM specified for the GaAs surface [Spicer *et al.*, 1988], the characteristic parameters of the surface barrier are now analyzed in order to verify the accuracy of the Fermi level measurements. In bulk GaAs material, the so-called EL2 defect is attributed to As_{Ga} antisites, which in undoped semi-insulating GaAs is compensated by extrinsic impurities such as carbon, a shallow level acceptor [Martin *et al.*, 1980; Darling, 1993]. As demonstrated later, this mechanism yields the intrinsic-like character in undoped material. In the AUDM, the EL2 is a deep double donor, with levels around 0.75 eV and 0.50 eV above the VBE. These donors, along with shallow level acceptors in the surface region, often attributed to Ga_{As} antisite defects, are required for mid-gap surface Fermi level pinning in n-doped material. Moreover, the AUDM specifies that the surface Fermi level shifts from the mid-gap closer to the VBE by up to 0.5 eV when the surface is Ga-rich [Spicer *et al.*, 1988], a shift more easily accommodated in semi-insulating GaAs without an extrinsic n-type donor. In agreement with the AUDM, Table 5.2 (col. 7) shows that the surface Fermi level exists at E_f values of 0.69 eV for n⁺-type GaAs and 0.21 eV for semi-insulating material, which is observed to be about 15% Ga-rich (XPS atomic percent) after NH₄OH/H₂O etching, as detailed in Chapter 3. The results also concur with evidence of a surface acceptor state at 0.27 eV in undoped semi-insulating GaAs that was found using the method of photothermal radiometric deep-level transient spectroscopy [Mandelis and Budiman, 1999]. As explained in Section 5.2.2, a sufficiently energy dense surface defect can pin the Fermi level as it becomes occupied with charge. Based on its limited repositioning, and its absolute energy, the surface Fermi level of alkanethiol-SAM passivated GaAs(001) is pinned in accordance with the AUDM.

In view of this physical defect model, the surface barrier of semi-insulating GaAs can now be characterized in terms of the ionized charge concentrations (Q_{dd} and Q_{sa}) and the net concentration of free carriers (ΔQ_{fc}) expressed as a function of the Fermi level energy (E_f). These terms are based on typical values for the volume concentration, degeneracy factor and activation energies of the EL2 deep donor (N_{dd}, g_{dd}, E_{dd}) and carbon shallow acceptor (N_{sa}, g_{sa}, E_{sa}) defects [Martin *et al.*, 1980; Darling, 1993].

$$\Delta Q_{fc}(E_f) = 2 q n_i \sinh \frac{(E_i - E_f)}{kT} \quad (5.13)$$

$$Q_{dd}(E_f) = \frac{q N_{dd}}{1 + g_{dd} \exp \left[\frac{(E_f - E_{dd})}{kT} \right]} \quad (5.14)$$

$$Q_{sa}(E_f) = \frac{q N_{sa}}{1 + g_{sa} \exp \left[\frac{(E_{sa} - E_f)}{kT} \right]} \quad (5.15)$$

The degeneracy factor is the ratio $g = g_o/g_1$, where the g_i are the degeneracies of the defect state when occupied by $i = 0, 1$ electrons, q is the elementary charge unit, k is the Boltzmann constant, T is the absolute temperature, and the value n_i is the intrinsic carrier concentration for GaAs. The intrinsic Fermi level energy (E_i) is determined from the ratio of electron/hole effective masses $r_m = m_n^*/m_p^*$ in the expression $2E_i = E_g - 3/2 kT \ln r_m$ (Equation B.18), where E_g is the band-gap energy. Equations 5.13, 5.14, and 5.15 are plotted in Figure 5.12(a).

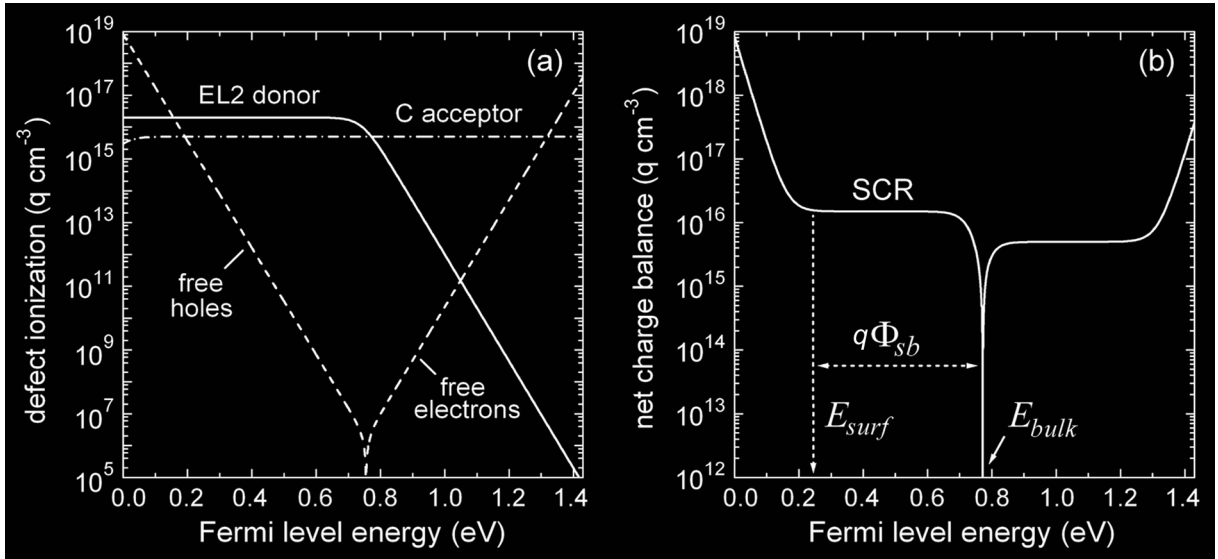


Figure 5.12. (a) Ionized charge centre concentrations for the EL2 donor (solid) and carbon acceptor (dotted) defect levels in undoped semi-insulating GaAs. Free carriers as indicated (dashed). (b) Net charge balance. The zero marks the bulk Fermi level energy (E_{bulk}). The surface Fermi level (E_{surf}) defines the surface potential barrier height ($q\Phi_{sb}$) and limit of ionization in the SCR. After Marshall *et al.* [Marshall *et al.*, 2011a].

The net charge balance for the values assumed is shown in Figure 5.12(b) and is obtained by evaluating the sum,

$$\Sigma Q(E_f) = |\Delta Q_{fc}(E_f) + Q_{dd}(E_f) - Q_{sa}(E_f)| \quad (5.16)$$

yielding an intrinsic-like bulk Fermi level position of 0.77 eV at the charge balance zero, to which the surface barrier is referred. Figure 5.12(b) also indicates that, for semi-insulating GaAs, the excess charge density is $1.5 \times 10^{16} \text{ cm}^{-3}$, which is attributed to a uniform SCR in depletion resulting from ionization of the native defects. We also observe why filling of the surface acceptor states is limited by native defect ionization in semi-insulating GaAs; a charge balance in excess of the ionized defect concentration would imply a further reduction of the surface Fermi level, which is energetically unfavorable, since the surface states would need to fill from the valence band in this case.

Using the surface Fermi level data in Table 5.2, along with: i) the graphical solution in Figure 5.11 for the bulk Fermi level in semi-insulating GaAs, and ii) Equation 2.16 and the details in Appendix B for the bulk Fermi level in n^+ -doped GaAs, including the nominal doping concentration, the surface barrier heights compute to 0.51 eV and 0.76 eV at the SAM passivated interface, respectively, for the two substrate types. In alkanethiol MMS junctions, the large barrier height in n^+ -type GaAs would impose that high forward biases need be applied in order to achieve tunneling current, whereas in p^+ -type it can be obtained at low biases. In contrast, for a photonic biosensor described according to Equation 2.64, the surface barrier height in n -type substrates is relevant to the dynamic range of the device, and may be a desirable characteristic in a sensor based on the dead-layer model, pinning effects aside. However, no improvement in sensitivity is expected without surface state passivation, referring again to Equation 2.64.

One final question to consider is why the SAM does not affect a more substantial degree of electronic passivation. This will become more apparent in the next chapter, when the pinning condition and the actual concentration of occupied surface states is considered quantitatively. A significant factor to be considered in this regard is the lack of site coverage, e.g., as specified by the trench-ridge surface model in Voznyy and Dubowski, which indicates that complete passivation of the available surface sites is sterically hindered by the SAM [Voznyy and Dubowski, 2008b].

5.4 Chapter Summary

The overall purpose of this chapter was to define the band structure of the SAM-GaAs interface in equilibrium, i.e., the band-bending and surface dipole correction to the electronic affinity, while the subtext related to the physical mechanisms that help explain the origins of the IR enhancement and the conditions of electronic passivation following SAM formation.

First, the electronic polarizability of the SAM was identified as a potential factor of the IR enhancement, owing to its relationship with the dielectric constants, which are surface potential sensitive. This created an imperative to measure the DLP associated with the SAM. The n -dependent DLPs were obtained using the Kelvin probe method by analysis of the CPD differential following SAM thermal disordering. The DLP values were then corroborated by analysis of the vacuum level referenced XPS core levels of the GaAs substrate with and without a SAM. A working assumption in these methods was the surface Fermi level pinning effect. Pinning within 50 meV at the alkanethiol-GaAs interface was later verified using a novel approach to XPS binding energy calibration that allowed for a precise determination of the electronic passivation, before and after SAM formation, and from which the band-bending surface barrier height was obtained. Using quantitative analysis, it was shown how the surface Fermi level energy is manifested in the prescriptions of the AUDM.

In the context of an effective capacitor model, the DLP was shown to be a significant fraction of the estimated dielectric breakdown potential of the SAM. This indicated that the SAM supports a strong internal field strength that develops from the molecular dipole. In terms of the IR enhancement mechanism, it was explained how this field strength could generate an increase to the dipole derivatives responsible for the IR absorbance. The explanation was based in the static and dynamic contributions to the vibrational moment that are effected by the SAM internal field and the molecular electronic polarizability. The justification for this explanation lies mainly in the direct proportionality between the IR absorbance and the DLP, which is observed to be equivalent for both SAM-GaAs and SAM-Au systems.

CHAPTER 6:

NEAR-SURFACE ELECTRO-OPTIC PHENOMENA

The passivating effects of alkanethiol SAMs on GaAs(001) were discussed in Chapter 3 in terms of the resulting surface composition and its relative chemical stabilization, and in Chapter 5 in terms of the resulting surface Fermi level changes and surface barrier heights. These relate to the equilibrium condition. However, quantitative understanding of this material system under steady-state optical excitation has been limited to observations of PL enhancement and estimates of the decrease in SRV, which is a fundamental parameter of the surface derived from Shockley-Read-Hall recombination theory, as detailed in Chapter 2.

It was determined from XPS analysis that the passivation of electronically active defect levels was small, i.e., unpinning of the surface FL was limited to less than 50 meV, meaning that only small changes to the surface trapped charge density were realized. This lends further support to the SRV model of PL enhancement by rejecting a dead-layer model explanation. More importantly, it highlights that the surface carrier capture cross-sections $\sigma_{n,p}$ play a significant role in the non-radiative recombination rate since the quantity N_t is not expected to change significantly based on the limited degree of electronic passivation.

With these points in mind, this chapter extends the investigation of the surface electronic state into the non-equilibrium domain by employing SPV and PL measurements, and various numerical analyses in addition, in order to gain further physical insight. The work presented here is published in *Nanotechnology* under the title, “Electro-optic investigation of the surface trapping efficiency in *n*-alkanethiol SAM passivated GaAs(001)” [Marshall *et al.*, 2011b]. The main effort is to distinguish the specific electro-optic effects of a decrease in the hole/electron ratio of carrier capture cross-sections from a reduction of the surface trap density in the SRV. By referencing the initial band-bending previously determined by XPS, SPV modeling is used in order to highlight large scale changes to the cross-section ratio. Observations of the residual band-bending under low-injection conditions are understood in

this context, and are discussed in terms of the effect the interfacial dipole layer formed by thiol-GaAs chemisorption has on the minority carrier dynamics.

A simple SRV model of PL enhancement is then derived that is commensurate with the SPV results and that is supported by more extended modeling based on the transport theory outlined in Chapter 2. In addition, the simplified model accommodates the analysis in the high-injection regime where photo-saturation of the PL efficiency is obtained.

In the final section, conclusions with respect to the various electro-optic phenomena are brought into the context of PL-based sensor operation where their significance is discussed.

6.1 Experimental Details

6.1.1 Sample Preparation

The preparation of *n*-alkanethiol SAMs were detailed in Chapter 3. Semi-insulating GaAs(001) epi-ready wafer was used for this study in addition to heavily doped n^+ -GaAs (Si-doped at $1 \times 10^{18} \text{ cm}^{-3}$) for comparative purposes. Reference samples were prepared following 28% $\text{NH}_4\text{OH}/\text{H}_2\text{O}$ etching by immersion in degassed ethanol solvent without alkanethiol. Samples were prepared under N_2 glovebox conditions and were tested immediately, or where required, were stored under N_2 until tested (SPV < 2 hrs, PL < 6 hrs) and represent the initial condition of the passivated surface immediately following SAM preparation without oxide aging.

6.1.2 Surface Photovoltage Measurements

The Kelvin Probe instrument (KP Technology Ltd.) records the CPD with respect to a non-contact vibrating Au reference probe as detailed in Chapter 5. SPV measurements were obtained by monitoring the change in CPD upon glancing illumination with a cold white light source (fiber-optic illuminator), i.e., the SPV magnitude is quantified as the CPD variation in dark vs. light exposed conditions. A thermopile detector was used to estimate the total optical power emitted from the fiber-optic (175 mW), which projected a transmitted irradiance of about $10^{17} \text{ photons cm}^{-2} \text{ s}^{-1}$, accounting for beam geometric factors and surface reflection.

6.1.3 Photoluminescence Measurements

A stepping stage PL mapper (Philips Electronics Ltd. PLM-150) was used at an excitation wavelength of 532 nm and incident power of 32 mW within an estimated 10 μm Gaussian

mode field diameter (2×10^{23} photons $\text{cm}^{-2} \text{s}^{-1}$). Measurements were stepped in 100-200 μm increments with dwell times on the order of 100 ms. The peak PL intensity was recorded at the emission maximum near 870 nm. A data filter was later used to extract the sampling average and standard deviation from the center 2-4 mm diameter on each wafer so as to exclude sample edge effects. In addition, neutral density filters were used to vary the excitation power in order to derive the PL efficiency from semi-insulating GaAs.

6.2 Surface Photovoltage of SAM Passivated GaAs

6.2.1 SPV Results

In a depleted n-type surface the potential drop across the SCR is negative, and since the SPV represents a reduction in the surface barrier, the SPV is assigned a positive value. The SPV then manifests as a reduction of the work function and a lower CPD with respect to the Au probe. CPD data for semi-insulating and n^+ -type GaAs are shown in Figures 6.1(a) and (b)

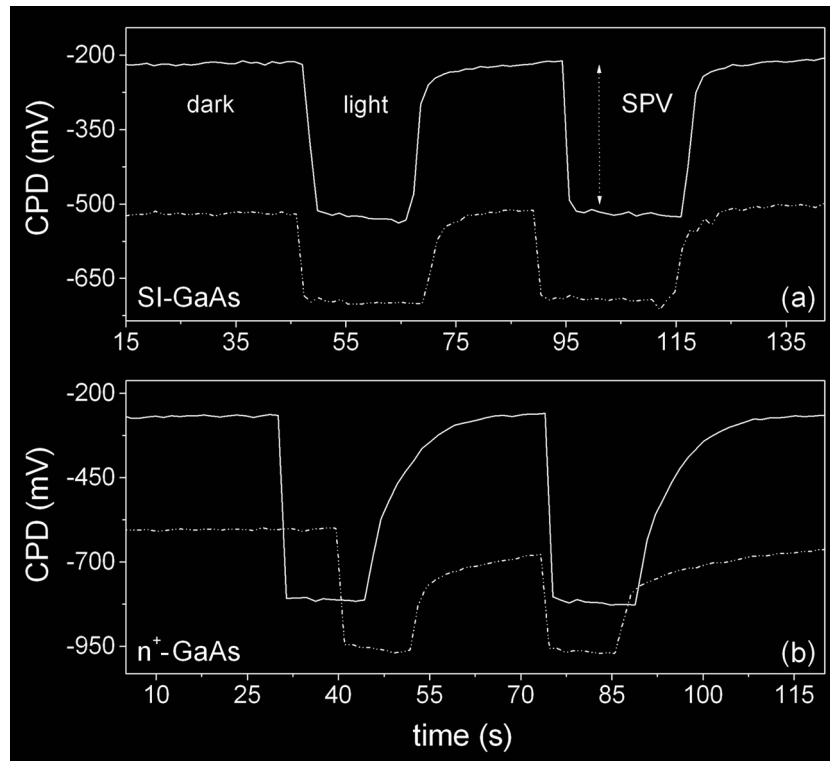


Figure 6.1. Kelvin Probe SPV measurements on: (a) semi-insulating GaAs; etched only (solid), as prepared with n_{15} -SAM (dash-dot). Light conditions refer to cold white light illumination at 10^{17} photons $\text{cm}^{-2} \text{s}^{-1}$. The SPV is quantified as the change in CPD. (b) Similar measurements but on n^+ -GaAs. After Marshall *et al.* [Marshall *et al.*, 2011b].

respectively. In each case, the dark condition work function is approximately 310 - 330 mV lower for the samples prepared with n^{15} -SAMs. The work function reduction is due to the addition of a DLP formed by the SAM having a net dipole moment directed outward [Marshall *et al.*, 2009b]. Evidence of the repopulation of surface states in the transient return to the equilibrium surface potential can also be seen. More importantly, note that the SPV values are reduced for surfaces prepared with n^{15} -SAMs when compared to their respective reference surfaces. The SPV reduction of semi-insulating GaAs measures 134 mV in Figure 6.1(a) and is 187 mV for n^+ -GaAs in 6.1(b). In repeated experiments, SPV reductions for n^{15} -SAMs averaged 148 mV and 185 mV for semi-insulating and n^+ -type surfaces respectively, with a standard error of about ± 30 mV.

To reiterate from the theory in Chapter 2, the SPV is governed, in part, by the screening effect photo-generated excess carriers have on the surface trapped charge, which results in a reduction of the surface barrier. In principle, under sufficiently strong photo-injection, the SCR is completely suppressed leading to SPV saturation and the flat-band condition. However, SPV saturation cannot always be observed in GaAs because of the possible additive contribution of the Demmer potential, the interference from which depends on the ratio of hole and electron capture coefficients at the surface, and which is a strong function of irradiance in the high-injection regime. Therefore, we take the SPV saturation potentials from the equilibrium surface barrier heights ($q\Phi_{sb}$) quoted from the Fermi level XPS results, since they are directly equivalent but opposite in sign. In this case, we observe that Φ_{sb} is at least 200 mV greater than the measured SPV magnitudes and conclude that the SPV results do not reflect photo-saturation levels (i.e., flat bands). Consequently, the observed difference in SPV indicates that the residual non-equilibrium band-bending potential is at least 100 mV greater for the passivated surfaces under the same irradiance conditions.

6.2.2 SPV Model Parameters

Before proceeding to the analysis of the above results in view of Equations 2.45 through 2.50, certain qualifications as applied to a number of model parameters must first be specified. In Equation 2.48, the definition of Q_{ss} is restricted to included only the interface charge associated with Shockley-Read-Hall processes [Johnson, 1958], i.e., no fixed charge is considered. The model parameters E_i are obtained from the equilibrium surface Fermi level

positions of the etched but untreated GaAs surfaces for both semi-insulating and n^+ -doped GaAs and are assigned to surface acceptor states for the purpose of charge modeling. Furthermore, it is assumed that E_t is the dominant surface defect level for both material types in accordance with a Ga-rich stoichiometry and the AUDM. Figure 6.2 provides a graphic comparison of semi-insulating and n^+ -GaAs in the context of the AUDM at equilibrium. For n -type GaAs, surface acceptor states (A^0) are filled from singly ionized dopant levels (D^0) in the SCR near the conduction band edge. Donor levels in the surface region, such as the double donor As_{Ga} antisite associated with the EL2 defect ($D^{0/0}$), raise the FL to a position near mid-gap. In undoped semi-insulating GaAs, the absence of an extrinsic donor means that A^0 can fill from the EL2 levels directly. A Ga-rich surface region implies the concentration inequality $[A^0] > [D^{0/0}]$, which results in FL pinning near the acceptor level.

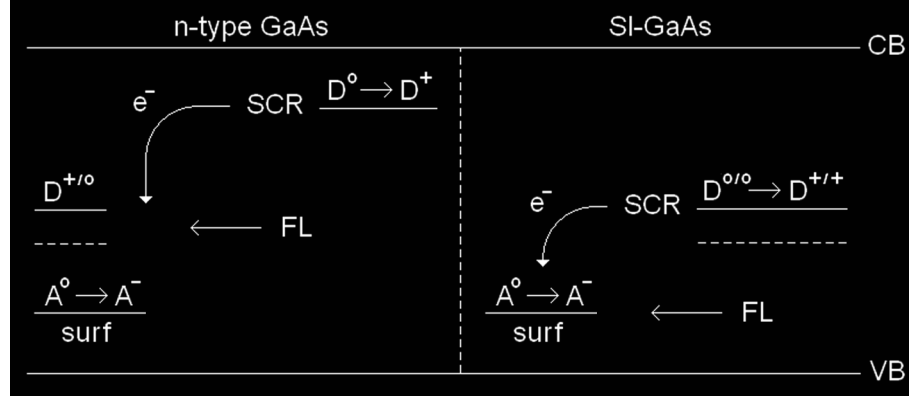


Figure 6.2. Schematic comparison of the AUDM-based surface Fermi level (FL) position in Ga-rich n -doped and semi-insulating GaAs. A^0 ; surface acceptor, D^0 ; extrinsic dopant donor, $D^{0/0}$; intrinsic double donor EL2. The superscript notation refers to neutral or ionized states.

In order to fulfill the parameter requirement for the number density of trap states in Equation 2.48 (N_t), a determination of the equilibrium surface charge density in the discrete state surface Fermi level pinning condition (Q_{ss}^0) is first required. Consider the value of Q_{ss}^0 as the energy density of surface states D_{ss} ($\text{eV}^{-1} \text{cm}^{-2}$) approaches the upper limit,

$$\lim_{D_{ss} \rightarrow \infty} q D_{ss} dE = Q_{ss}^0 \quad (6.1)$$

where dE is the energy bandwidth differential associated with the discrete state. In thermal equilibrium ($\delta_n = 0$), Equation 2.45 may be written as,

$$Q_{sc}^o = \sqrt{2 \varepsilon N_{sc} q \Phi_{sb}} \quad (6.2)$$

Equations 6.1 and 6.2 are then equated based on charge neutrality at equilibrium. Figure 6.3 shows a graphical representation of solutions for the space charge densities (N_{sc}) and equilibrium barrier heights ($q \Phi_{sb}$) corresponding to semi-insulating and n^+ -type GaAs.

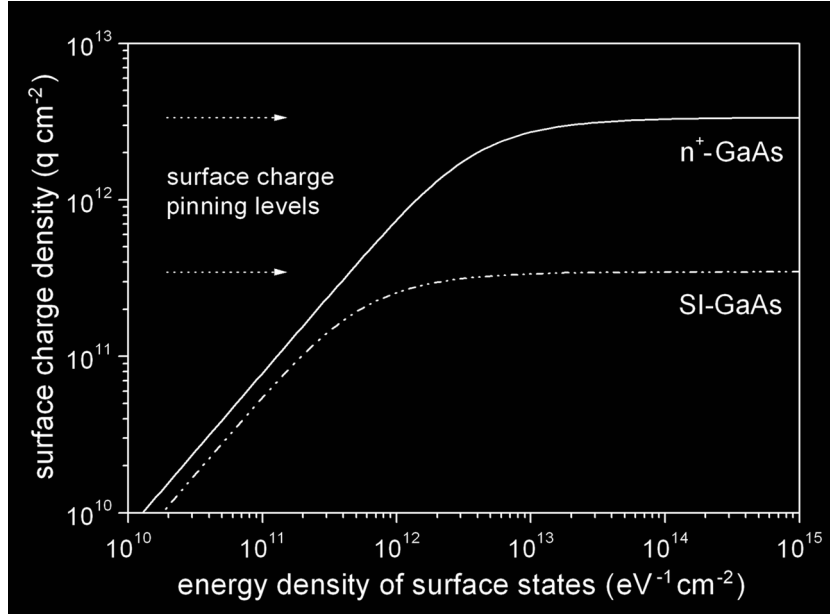


Figure 6.3. Surface FL pinning places an upper boundary on the surface charge density as the energy density of surface states approaches the discrete limit. Pinning is defined such that further increases in the density of surface states does not change the equilibrium band-bending. After Marshall *et al.* [Marshall et al., 2011b].

Surface Fermi level pinning is achieved at about $D_{ss} \approx 6 \times 10^{12} \text{ eV}^{-1} \text{ cm}^{-2}$ in semi-insulating GaAs, and at above an order of magnitude greater in n^+ -type material. The respective estimates of the surface charge density are $Q_{ss}^o = 3.5 \times 10^{11} \text{ q cm}^{-2}$ and $Q_{ss}^o = 3.3 \times 10^{12} \text{ q cm}^{-2}$. Following thiol treatment, small reductions of Q_{ss}^o were necessary in order to redefine the equilibrium barrier height. However, given that the surface Fermi level increases were 50 meV or less, the corresponding reductions of Q_{ss}^o were small ($< 4 \%$). Finally, the associated trap densities were established by dividing the respective values of Q_{ss}^o by their occupation factors (f_n^{SI}, f_n^{n+}) at equilibrium using Equation 2.50, which yielded values of $N_t = 2.1 \times 10^{12} \text{ cm}^{-2}$ for semi-insulating GaAs and $N_t = 3.3 \times 10^{12} \text{ cm}^{-2}$ for n^+ -type GaAs. These results are satisfactory in that they predict near equivalent values, which may be

expected for stoichiometric defects. Note that the surface charge density under pinning is about two orders less than the molecular surface density of thiols for undoped GaAs.

6.2.3 Scale Transformation to Photon Irradiance

In order to relate the SPV model to the measurements above, mapping the incident photon irradiance (I_{rad}) to the excess carrier density ($\delta n = \delta p$) is required. To do so, use is made of the Moss equation, as detailed in the review by Schroder [Schroder, 2001], and as similarly employed by Aphek *et al.* [Aphek *et al.*, 1998]. The Moss equation is written as follows,

$$I_{rad} = \left(\frac{\delta_n n_o}{1-R} \right) \left(S_{eff} + \frac{D_p}{L_p} \right) \left(1 + \frac{1}{\alpha_{ex} L_p} \right) \quad (6.3)$$

and is a function of the fractional excess electron density (δ_n) and the effective SRV (S_{eff}), which was specified in Chapter 2. The constant parameters are: the minority carrier diffusion constant (D_p), the diffusion length (L_p), the optical absorption coefficient (α_{ex}) at the excitation wavelength, and the polarization averaged reflectance (R) specified at glancing incidence ($\sim 75^\circ$ in the experimental setup). Parameter invariance to doping is assumed in the surface region and typical GaAs values are applied as listed in Table 6.1.

TABLE 6.1. GaAs parameters for calculation of Equation 6.3.

hole diffusion constant	D_p	10	$\text{cm}^2 \text{s}^{-1}$
hole diffusion length ^a	L_p	1.3×10^{-4}	cm
absorption coefficient	α_{ex}	7.6×10^4	cm^{-1}
Fresnel reflectance ^b	R	0.29	-

^a adapted from Refs. [Aspnes, 1983] and [Mettler, 1977]

^b polarization averaged, estimated at 75° incidence and 532 nm

Again, the variable S_{eff} is defined at the SCR boundary and accounts for the flux of minority carriers into the SCR where they recombine non-radiatively at the surface. For semi-insulating GaAs, a value of $S_{eff}^{SI} = 1.5 \times 10^5 \text{ cm s}^{-1}$ is assigned, and for n^+ -GaAs a value of $S_{eff}^{n+} = 2 \times 10^6 \text{ cm s}^{-1}$ is used. These values follow the trends in Aspnes [Aspnes, 1983] and Mettler [Mettler, 1977], which correspond to the variation of SRV with doping concentration, or equivalently, the SCR density. Note that by inspection of Equation 6.3, a limiting value of

δ_n can be defined where $S_{eff} \ll D_p/L_p$, i.e., further reductions of S_{eff} will no longer produce higher values of δ_n at a given I_{rad} . This will factor into the analysis in the next section.

6.2.4 Surface Carrier Capture Coefficients

Using the analytical treatment provided in Chapter 2, along with the model parameter and irradiance scaling provided in the previous two sections, the SPV may now be calculated as a function of irradiance and compared to the experimental SPV data. To reiterate, this analysis proceeds under the constraint that the saturation SPV is equated with the surface barrier height as determined by XPS. Figure 6.4 shows the modeling results for semi-insulating GaAs in which the SPV is plotted across a range of χ values.

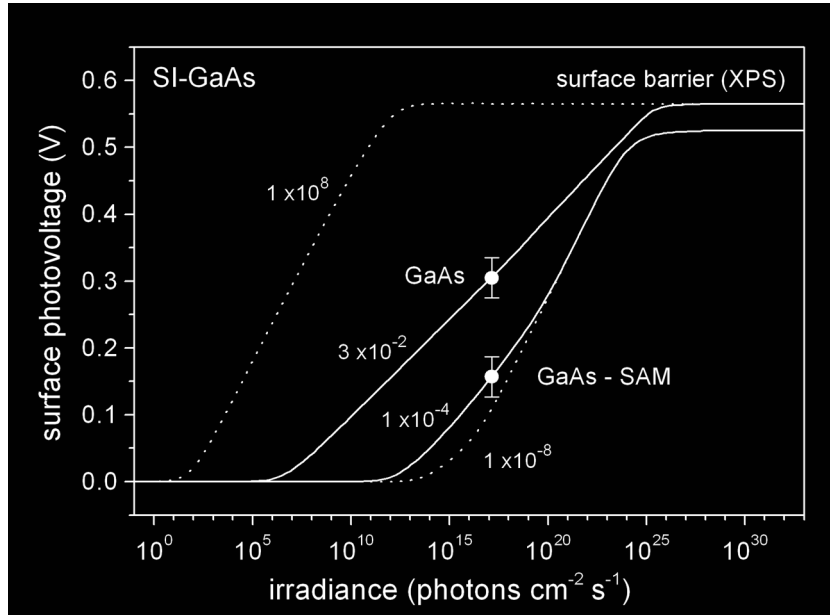


Figure 6.4. SPV data (circles) and model results (solid lines) for semi-insulating GaAs before and after passivation with *n*15-SAM. Numerical values indicate the parameter χ used in the SPV calculations. Limiting envelopes of the SPV function at $\chi = 10^{\pm 8}$ (dotted lines). After Marshall *et al.* [Marshall et al., 2011b].

As specified in Equation 2.50, $\chi^2 = C_p/C_n$ is the hole/electron ratio of surface carrier capture coefficients. The dotted lines represent the SPV envelope functions as discussed in the context of Figure 2.17. In Figure 6.4, χ was selected such that the SPV model approximates the experimental observations for both the GaAs reference surface (at $\chi = 3 \times 10^{-2}$) and the surface prepared with *n*15-SAM (at $\chi = 1 \times 10^{-4}$). In calculating the SPV representing SAM

prepared surfaces, the limiting value of δ_n was assumed and reflects the maximum effect (curve shifting left) a reduction of the SRV can induce following passivation, i.e., $S_{eff} \ll D_p/L_p$, as defined in Section 6.2.3. However, the sensitivity of δ_n to reductions of S_{eff} is small for semi-insulating GaAs, since $S_{eff}^{SI} \approx D_p/L_p$ in Equation 6.3, so, the shifting effect is negligible in this case. More importantly, this low sensitivity highlights the independence of χ in determining the SPV for this material and relaxes the requirement for accurate knowledge of the recombination velocity.

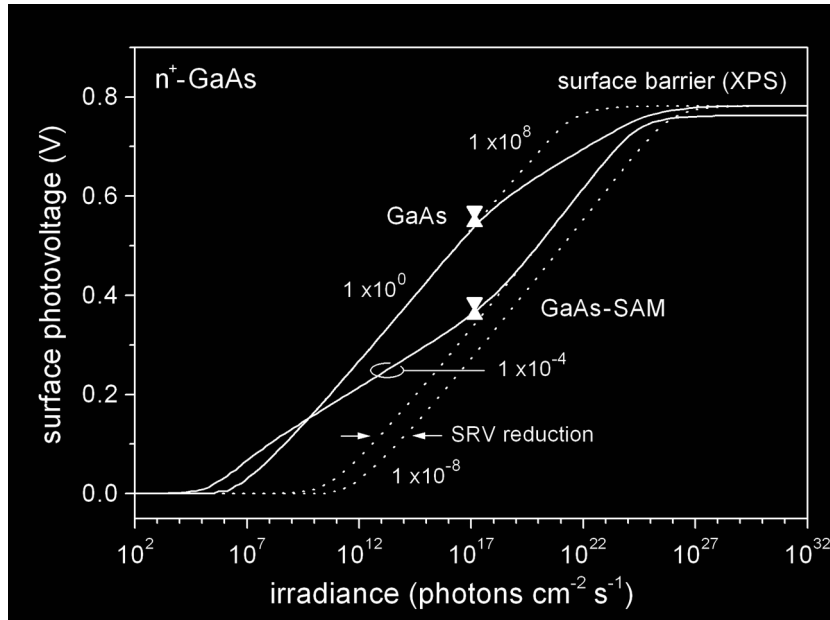


Figure 6.5. SPV data and model results for n^+ -GaAs before and after passivation with $n15$ -SAM. Details as per Figure 6.4. Up/down triangles represent individual test results. The envelope curve shifting left reflects the increase in excess carrier density at a given irradiance due to a reduction of the SRV for the passivated surface. After Marshall *et al.* [Marshall et al., 2011b].

The SPV analysis results on n^+ -GaAs follows in a similar manner to that in Figure 6.5. A value of $\chi \sim 1$ is assigned to the GaAs reference surface, which reflects pinning near mid-gap, and a value of $\chi = 1 \times 10^{-4}$ is assigned to the surface prepared with $n15$ -SAM, assuming again the SRV limited value of δ_n applies following passivation. The SRV induced curve shifting left is more significant for passivated n^+ -GaAs relative to semi-insulating GaAs, as indicated in Figure 6.5 by the opposed arrows. The shifting is greater because $S_{eff}^{n+} > D_p/L_p$ for the reference surface conditions. Despite these specific differences, the data

and model results for n^+ -GaAs reflect the same general characteristics evident in the case of semi-insulating GaAs, namely, a small to negligible change in the equilibrium surface barrier, yet a significant reduction of SPV following thiol treatment under low level photo-injection.

A similar reduction of the SPV (~ 200 mV) has been observed following S_2Cl_2 passivation of n-doped GaAs(001) by Tomkiewicz *et al.* [Tomkiewicz *et al.*, 2009]. The equilibrium surface barrier height was not reported in this study, somewhat limiting their conclusions in that a reduction in equilibrium band-bending was assumed. However, their results do provide a reasonable basis of comparison with the n^+ -GaAs data in Figure 6.5. In addition to the decrease in SPV, the absolute values appear to be accurately reproduced. Their data also show a logarithmic dependence on irradiance in agreement with the modeling presented here. Given that pinning of the surface barrier was not ruled out, the Tomkiewicz results may also be interpreted in terms of a reduction in the χ factor, at least in some part that is not otherwise related to a reduction of surface charge density and increase of the surface Fermi level.

6.2.5 Discussion of SPV Findings

In the foregoing analysis, the change in observed SPV was attributed to a relative increase in the non-equilibrium band-bending following passivation with n -alkanethiol SAMs. This was accounted for in the SPV model by a decrease in the hole/electron ratio of carrier capture coefficients when compared to the untreated surface. How can this be interpreted physically? Consider a change to the minority carrier capture cross-section (σ_p) effected by S-GaAs coupling. In this case, a reduction factor of at least 10^4 is implied in the model fitting of χ to the SPV data for both material types, recalling that $\chi \propto \sqrt{\sigma_p/\sigma_n}$. Moreover, a large scale reduction of σ_p is consistent with the limit $S_{eff} \ll D_p/L_p$ used to scale the irradiance for the passivated surfaces. That a reduction of σ_p is consistent with a reduction of SRV derives from $S_L = \sigma_p \nu_{th,p} N_t$, the expression for Shockley-Read-Hall surface recombination velocity under low level photo-injection, as specified for n-type GaAs in Chapter 2. Note that a large scale reduction of N_t is rejected on the basis of strong Fermi level pinning. Regarding a possible mechanism for a reduction of χ , it is proposed that a significant factor may be electrostatic in nature resulting from the formation of an interfacial dipole layer upon thiol chemisorption as described in the following.

Thiol may be considered an electron pair donor to a complementary GaAs acceptor state resulting in a surface complex of bonding molecular orbitals. The S-GaAs adduct thus formed is characterized by a dipole potential with its moment directed into the surface. The dipole arises from either the electronegativity of sulphur or asymmetry of the molecular orbitals. An interfacial layer of these dipoles will increase the surface work function, as similarly reported by Tomkiewicz *et al.* [Tomkiewicz *et al.*, 2009], who observed, independently of their SPV data, a work function increase of 0.21 eV after passivation of GaAs(001) with S_2Cl_2 . A smaller work function increase at the thiol-GaAs interface is expected because of the lower packing density available to the SAMs and because of the reduced electronegativity of the adsorbing species. Nevertheless, an interfacial dipole layer of the type described may affect the internal potential locally. Specifically, it is proposed that the penetrating field of the S-GaAs dipole layer acts to lower the band levels and invert the band-bending curvature in the near-surface region. A schematic of the respective fields, near-surface band-structure and the effect on minority carrier capture is provided in Figure 6.6.

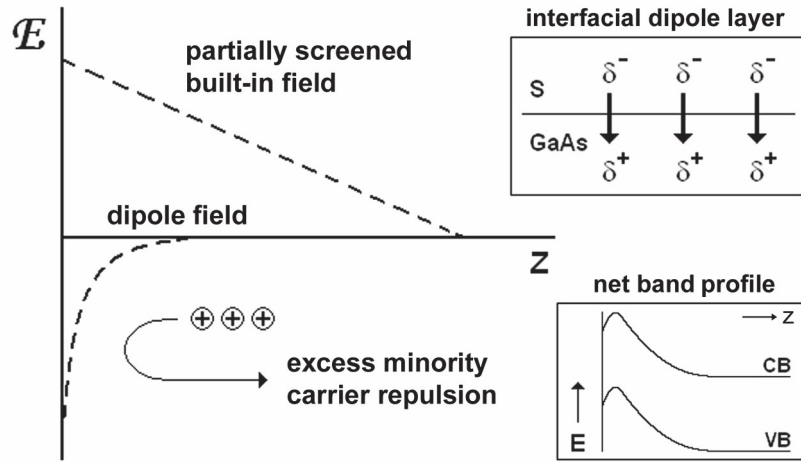


Figure 6.6. Schematic of the electric field profiles for: i) the built-in field of the SCR, partially screened under illumination, and ii) the penetrating interfacial dipole layer potential. Insets: Interfacial dipole layer formed by S-GaAs covalent bonding (top). Net band profile of the thiol-GaAs interface (bottom). After Marshall *et al.* [Marshall *et al.*, 2011b].

The manifestation of such an effect would be determined by: 1) the penetrating field strength relative to the partially screened field of the SCR under photo-injection, and 2) the penetrating field profile, which, as a sum of dipole fields, is dependent on the dipole moment, the inter-dipole distance, and on local domain patterns and disordering defects. As calculated in

the work by Natan *et al.* [Natan *et al.*, 2007], the net result of these effects, for bond polarizations on the order of 1 debye and 2D packing densities typical of adsorbed monolayers, is an exponentially decreasing field strength exceeding 10^4 V/cm at distances up to about 10 nm below the surface. The field strengths associated with the equilibrium surface potentials are also of this magnitude or greater in this region and decrease approximately linearly with SPV in the low-injection regime. This supports that addition of the interfacial dipole and built-in fields creates a local inversion barrier as described, which is sufficient to retard the trapping of excess minority carriers brought to the surface by drift and diffusion processes. Consequently, negative surface charge persists resulting in a relative increase in the residual band-bending as observed. This dipole barrier effectively reduces the surface capture cross-section σ_p , and will increase it for σ_n , which is reflected in the model fitting of $\chi \ll 1$ to the SPV data.

An interesting parallel to the concept of field-dependent cross-sections relates to the findings of Prinz and Rechkunov, who demonstrated a field-enhanced cross-section effect in the depletion region of semi-insulating GaAs Schottky barriers, specific to the EL2 and other defect centers [Prinz and Rechkunov, 1983]. For applied field strengths exceeding 10^4 V/cm, σ_p and σ_n were observed to increase asymmetrically, by up to six orders, with a trend toward $\chi = 1$. Although the details of the Prinz and Rechkunov result do not fit into the framework of the present work directly, at a minimum, they do argue for the field-dependent sensitivity of σ_p and σ_n on the scale discussed and in relation to similar field strengths.

6.3 Photoluminescence of SAM Passivated GaAs

In this section, the PL intensity of alkanethiol passivated GaAs is discussed in the context of a simplified model of the enhancement ratio. The model is also referenced to the transport theory explained in Chapter 2 where agreement is found. In addition, reference will be made to the previous section on SPV in order to reconcile changes to the capture cross-section σ_p within the model results.

6.3.1 PL Enhancement in the Flat-Band Regime

The relative PL efficiency vs. photon irradiance is plotted in Figure 6.7 for semi-insulating GaAs before and after preparation with *n*15-SAM. To obtain the PL efficiencies, the

measured PL intensities were divided by the transmittances of the neutral density filters used to attenuate the laser irradiance in the experimental setup. A PL enhancement factor of about $1.8\times$ is evident for the thiol-treated surface. The enhancement factor, however, depends on the intensity measured from both the passivated surface and the reference surface after etching.

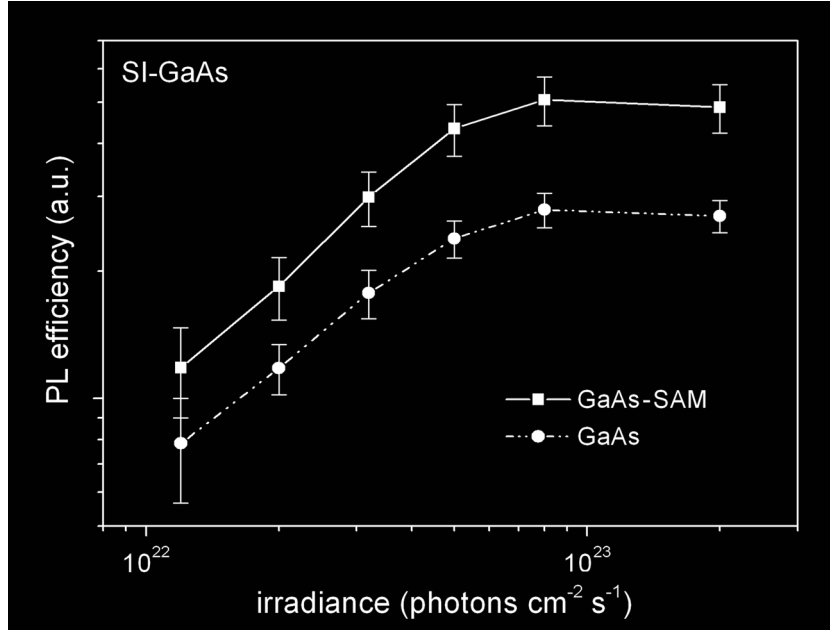


Figure 6.7. Relative PL efficiency as a function of the excitation power for semi-insulating GaAs before (circles) and after (squares) preparation with *n*15-SAM. Yield saturation is evident at irradiances above 10^{23} photons $\text{cm}^{-2} \text{s}^{-1}$ corresponding to the flat-band condition within the SCR. After Marshall *et al.* [Marshall *et al.*, 2011b].

Data recorded within a few hours after sample preparation typically yield enhancement ratios averaging $1.6\times \pm 0.2$ as detailed in Table 6.2. This ratio agrees with results in several literature reports. For example, Lunt *et al.* observed an enhancement of $1.5\times$ using short-chain alkanethiols on n-type GaAs doped at 10^{17} cm^{-3} [Lunt *et al.*, 1991], and Ding *et al.* observed a $1.5\times$ enhancement at 20 K using long-chain alkanethiols on p-type GaAs doped at 10^{17} cm^{-3} [Ding *et al.*, 2006]. Kim *et al.* reported similar enhancements on undoped GaAs/AlGaAs heterostructures [Kim *et al.*, 2009], and Adlkofer *et al.* reported increasing PL enhancement ratios, ranging from $1.9\times$ to $1.5\times$, as the depth of an InAs quantum dot emitting layer was increased below an ODT passivated epitaxial GaAs cap layer [Adlkofer *et al.*, 2002].

An important feature of Figure 6.7 is the saturation of PL yield observed at irradiances above 10^{23} photons $\text{cm}^{-2} \text{s}^{-1}$. Considering the large magnitude of irradiance scale over which the SPV varies, the PL saturation point agrees well with the saturation point predicted by SPV

modeling in Figure 6.4. The two points are expected to coincide. Specifically, the PL yield will saturate when the effective SRV becomes minimized, i.e., when the drift current in the SCR is minimized due to band-flattening.

TABLE 6.2. PL enhancement ratio of semi-insulating GaAs(001) following preparation with n_{15} -SAMs.

PL intensity (a.u.)		ratio
untreated	n_{15} -SAM	
26.7	39.4	1.48
30.2	49.2	1.63
30.5	44.7	1.47
27.0	48.7	1.81
avg		1.6 ± 0.2

The implications of the SPV findings in the context of this PL data will now be examined through a simple model of the PL enhancement ratio, which is based on a reduction of the SRV. As developed in Chapter 2, the low-injection limit of Shockley-Read-Hall surface recombination is $S_L = \sigma_p \nu_{th,p} N_t$. Using Equations 2.76 and 2.77 in the high-injection limit ($\delta_n \gg 1$), the surface recombination velocity can be written,

$$S_H = \frac{C_p C_n}{C_p + C_n} N_t = \frac{C_p}{\chi^2 + 1} N_t \quad (6.4)$$

Inspection of Equation 6.4 shows that $S_H \rightarrow S_L$ as $\chi \rightarrow 0$. Under these conditions, we can use the ratio of effective masses ($r_m = m_n^*/m_p^*$) to place a limiting condition on the approximation $S_H \approx S_L$ that is adopted for the present analysis. Given the definition of thermal velocity $\nu_{th,n,p} = \sqrt{3kT/m_{n,p}^*}$, the ratio of carrier capture coefficients is written $\chi^2 = (\sigma_p/\sigma_n) / (\sqrt{m_n^*/m_p^*})$. The effective mass ratio is $r_m = 0.126$ for GaAs and yields $\chi^2 = 0.36$ when $\sigma_p = \sigma_n$. Using Equation 6.4, $S_L \geq S_H \geq 0.74 S_L$ is obtained subject to $\sigma_p \leq \sigma_n$, which is a limiting condition easily satisfied in the SPV analysis of semi-insulating GaAs, therefore, the use of $S_H \approx S_L$ is justified.

With the high-injection Shockley-Read-Hall surface recombination now simplified in terms of the minority carrier capture cross-section, thermal velocity and the surface trap density, a simple expression for the PL enhancement ratio can be derived. Based on the definition of PL quantum efficiency in Equation 1.6,

$$\gamma_{PL} = \frac{r_r}{r_r + r_{nr}} \quad (6.5)$$

where r_r and r_{nr} are the radiative and non-radiative recombination rates, the PL enhancement ratio is,

$$R_{PL} = \frac{r_r + r_{nr}}{r_r + r'_{nr}} \quad (6.6)$$

with r'_{nr} corresponding to surface conditions after SAM formation. The radiative rate is considered an intrinsic bulk quantity and the non-radiative rate is assumed to be dominated by the surface reaction. Under high-injection non-degenerate excitation, and considering the approximation $S_H \approx S_L$, substitution of Equations 1.4 and 1.5 is appropriate and leads to,

$$R_{PL} = \frac{\beta n L_p^2 + L_p S}{\beta n L_p^2 + L_p S'} \quad (6.7)$$

or,

$$R_{PL} = \frac{D_p + L_p S}{D_p + L_p S'} \quad (6.8)$$

where the surface quantities r_{nr} and r'_{nr} are divided by L_p in order to estimate the actual surface non-radiative recombination rate in units s^{-1} . The last step was made using Equation 1.4 and the approximation $L_p \approx \sqrt{D_p \tau_r}$ made under the assumption $\tau_r \approx \tau_{nr}$, as appropriate for high (but non-degenerate) injection in GaAs where $\beta n \approx S_{eff}/L_p$, in which case $\tau_p \approx \tau_r$.

Equation 6.8 defines the simplified model of PL enhancement, and is plotted in Figure 6.8 as a function of the nominal value of the effective SRV (S) corresponding to the etched and untreated surface. Each curve is calculated assuming a specific reduction factor of $S = S_{eff}$ following passivation with alkanethiol. The solid curve represents a $3\times$ reduction ($S' = S/3$) and the dashed curve represents the limiting value $S' \ll S$. The dash-dotted curve represents

a $2\times$ reduction of S and approximates the lower boundary of R_{PL} subject to the range within which the PL enhancement ratio was observed, which is defined by the boxed area. The curve determined using the limiting value $S' \ll S$ illustrates the upper boundary of R_{PL} as defined by Equation 6.8. The height of the box in Figure 6.8 is determined by the range of PL ratios as provided in Table 6.2, and its width spans the uncertainty in the nominal value of S under high-injection conditions as follows. The right boundary is defined by the value of S_{eff}^{SI} , which includes the drift current contributions associated with the SCR. The left boundary is estimated using Equation 1.5 and represents the SRV limited by thermal kinetics only, i.e., under flat-band conditions, and is calculated using the following values: $N_t = 2.0 \times 10^{12} \text{ cm}^{-2}$ determined from Fermi level pinning, $v_{th} = 1.8 \times 10^7 \text{ cm s}^{-1}$ specified for the hole thermal velocity in GaAs and $\sigma_p = 1.0 \times 10^{-15} \text{ cm}^2$, which is a value based on atomic dimensions for nominal surface conditions [Kronik and Shapira, 1999; Baca and Ashby, 2005].

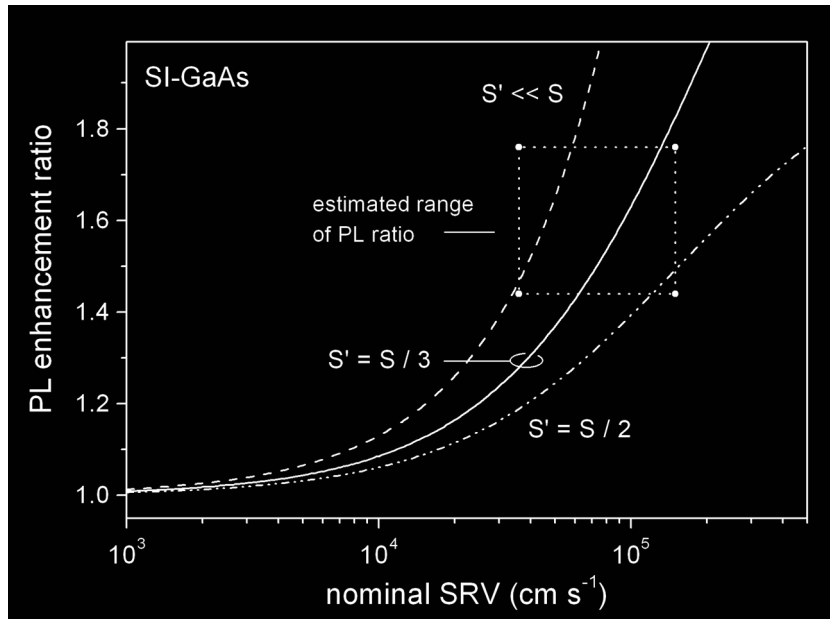


Figure 6.8. Calculated PL enhancement ratio for semi-insulating GaAs following passivation with $n^{+}15$ -SAMs as a function of the nominal SRV (S). Curves are computed for values of $S' < S$ indicating the surface value after passivation. The boxed area demarks the parameter space within which the PL ratio may be found.

The nominal SRV will trend left within this space as the drift current in the SCR is minimized under flat-band conditions, but its actual value remains unknown. Consequently, it will suffice

to simply bracket the values of R_{PL} according to an estimated variation of the governing parameters in the SRV model. The result does, however, reasonably accommodate the PL enhancement ratios observed following thiol treatment.

6.3.2 Transport Model of PL Enhancement

The results in Figure 6.8 were developed for the analysis of PL ratios under high-injection conditions where band-bending in the SCR is minimized due to excess carrier screening. In Chapter 2, the transport theory specific to PL intensity was introduced that included both SRV and dead-layer effects. Under the low-injection conditions for which the theory applies, one can expect that the impact of screening and surface charge modifications characteristic of the SPV will be sufficiently low such that both dead-layer and SRV effects can be realized following surface treatment. However, since it has been shown that strong Fermi level pinning applies and, consequently, that the depletion layer thickness remains approximately the same, the PL ratio under low-injection conditions can be predicted for thiol-passivated GaAs based on SRV reduction using the transport theory, exclusive of dead-layer effects.

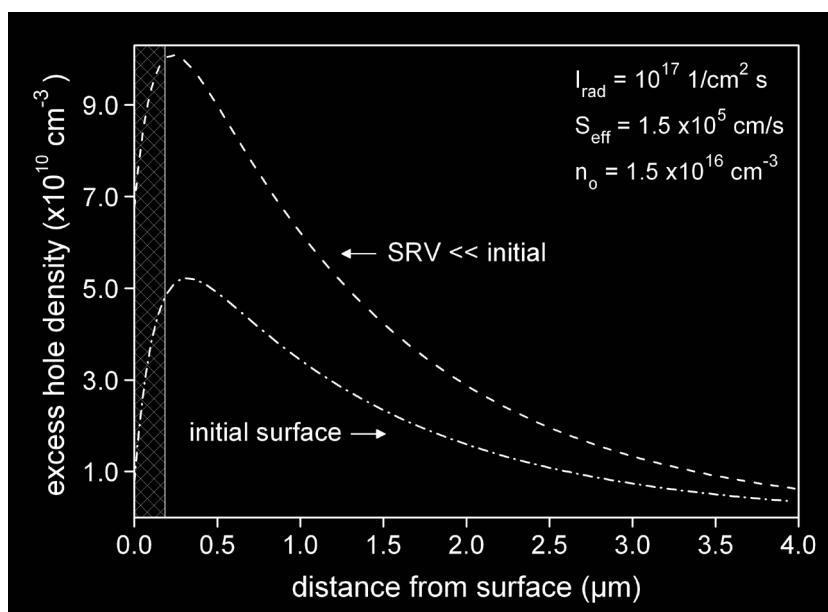


Figure 6.9. Excess minority carrier density depth profile calculated from the transport equation for semi-insulating GaAs in the low-injection regime. The hatched area marks the approximate depth of the depletion region. Other material parameters as per Table 6.1.

First, it is illustrative to plot the depth-dependence of the excess carrier density that results from a solution to Equation 2.56 for the material properties associated with semi-insulating

GaAs (see Table 6.1). This is shown in Figure 6.9 for two cases: i) the initial surface conditions, and ii) the surface for which the ‘reduced’ dimensionless value of SRV ($S_{rv} = S_{eff} \tau_p / L_p$) introduced in Chapter 2 is several orders of magnitude lower. In the evaluation of S_{rv} , the carrier lifetime τ_p is estimated using,

$$\tau_p = (\beta n + S_{eff} / L_p)^{-1} \quad (6.9)$$

which is derived from Equations 1.3 to 1.5, and uses Equation 6.3 in order to obtain the excess carrier density ($\Delta n = n - n_o$). The exponential profiles are due to the diffusion of minority carriers beyond the optical absorption region. The dead-layer, which corresponds to the depletion depth, is marked with hatching. The loss of carrier density evident at depths within the depletion region is due to the drift current contribution in the SCR, which accelerates minority carriers to the surface where they recombine non-radiatively. Using Equation 2.58, the profiles in Figure 6.9 can now be integrated to yield the PL intensity. By forming the appropriate PL intensity ratio, the PL enhancement factor (R_{PL}) can be calculated for a specified reduction of S_{eff} following passivation. For example, R_{PL} approaches a maximum value of 1.8 as S_{eff} approaches zero. This is consistent with the results in Figure 6.8, and is also consistent with the list of literature results provided in Section 6.3.1, which are specific to excitation power densities in the low-injection regime. For illustration, a surface plot of R_{PL} showing the combined effects of dead-layer and SRV reductions is provided in Appendix F, and is based on the material parameters given in Figure 6.9.

Simulation of the high-injection regime can be approximated by allowing the excess carrier density to exceed the donor concentration and forcing the dead-layer to zero. Since $\beta n \approx S_{eff} / L_p$ under steady-state high injection, reduction of S_{eff} / L_p following passivation justifies the simplification that τ_p remains approximately constant. This makes intuitive sense as radiative processes dominate the carrier lifetime under high excitation power densities. In a similar manner described with respect to Figure 6.9, the dimensionless value S_{rv} is determined as a function of S_{eff} , is substituted in the solution to Equation 2.56, and the PL is found by integration of Equation 2.58. Theoretical values of R_{PL} may then be computed and

compared to the experimental ratios, and curves analogous to Figure 6.8 can be constructed. These are shown in Figure 6.10 for comparison, but represent a more complete physical interpretation.

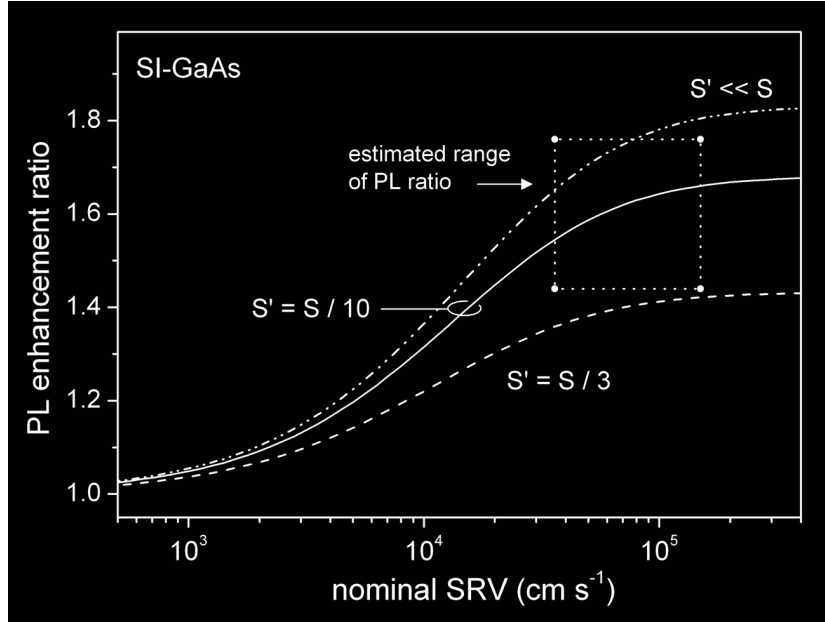


Figure 6.10. Calculated PL enhancement ratio for semi-insulating GaAs following passivation with *n*15-SAMs as a function of the nominal SRV (S), based on the transport equation. Plot details similarly as in Figure 6.8. Calculated for a laser irradiance of 10^{23} photons $\text{cm}^{-2} \text{s}^{-1}$. After Marshall *et al.* [Marshall et al., 2011b].

6.3.3 Discussion of PL Results

Based on the SPV results, a large scale reduction of χ consistent with a significant reduction of the effective SRV was proposed. A significant reduction of the SRV is evident in the PL enhancement modeling above, namely, the $S' \ll S$ result in Figure 6.9 and particularly in Figure 6.10. The conclusions of Lunt *et al.*, which were based on time-resolved PL measurements observed under photo-saturation conditions following a high-injection pulse, reported an SRV reduction measuring just $3\times$ ($S' = S/3$). Their lower value may have resulted from the transient nature of the time-resolved experiment, or may have been due to the lower surface coverage likely realized with the short-chain thiols that were used. Moreover, their technique did not allow for a distinction to be made between a reduction of $\sigma_{n,p}$ or N_t in the SRV. Given that the effect of a large scale decrease of σ_p is supported by both the SPV and PL analysis, and that Fermi level pinning rules out a significant change in

the surface state density, the following conclusion is drawn, i.e., that it is a thiol-induced reduction of σ_p that is most significant to the reduction of SRV responsible for PL increases following passivation with alkanethiol SAMs.

With respect to the Fermi level analysis, note that, in order to account for the $1.6\times$ PL enhancement ratio observed, a dead-layer model explanation would specify a reduction of the equilibrium surface barrier height in excess of 250 meV. This is a substantial degree of electronic passivation that is clearly not supported by the XPS results in Chapter 5. Moreover, consider that if the PL enhancement was due to a dead-layer effect, this would be nullified in the high-injection regime since the bands would be flattened by screening in the SCR.

Furthermore, recall that a discrete energy density distribution of surface defect states was assumed in the context of the AUDM. In the Disorder Induced Gap State (DIGS) model [Hasegawa and Ohno, 1986], a U-shaped energy density distribution of surface defect states is proposed to exist within the band-gap. When reduced to the limit of a discrete level defect the DIGS model predicts a unitary increase of the PL efficiency [Gfroerer, 2000]. Inspection of Figure 6.7 below yield saturation indicates that the efficiency rate is 90% for the thiol-treated surface suggesting that, indeed, a discrete level defect is playing a significant role.

6.3.4 Null Enhancement of n^+ -GaAs

In the above sections, results were reviewed with respect to non-degenerate GaAs only since measurements of the heavily doped n^+ -type material yielded null or indeterminate PL enhancements following thiol treatment. The main reason for this is the fact that the radiative rate becomes large in the degenerate semiconductor. Quite simply, as $r_r \gg r_{nr}$, the PL ratio in Equation 6.6 goes to unity. The validity of extending the carrier transport model into the degenerate regime is questionable, though it does indicate a trend towards null enhancement at the non-degenerate limit. Instead, a qualitative understanding is sufficiently obtained by reflecting on the increasing radiative rate as stated. Moreover, consider that the SRV normally increases proportionally with doping concentration, but for degenerate GaAs, there is a marked reduction from the trend specifying the increase in SRV as the results compiled in Aspnes suggest [Aspnes, 1983]. Consequently, under sufficiently heavy doping, the radiative rate continues to grow but the SRV does not. A limit is reached where $r_r \gg r_{nr}$ and the value of R_{PL} approaches unity, in agreement with the observations on n^+ -GaAs. Note that this result

would apply not only for heavy doping, but also for excess carrier densities sufficient to raise the electron quasi-Fermi level into the conduction band. For GaAs, this will occur for carrier densities above 10^{18} cm^{-3} .

6.4 Significance to the Operation of a Biosensor

The material presented in this chapter is now discussed in the context of the operation of a PL-based biosensor in order to find its practical significance. As a demonstration of preliminary results in this regard, an increase in PL sensitivity to changes in the surface potential following thiol passivation is shown.

The fact that a thiol-treated surface obtains a low degree of electronic passivation works to the advantage of maintaining the dynamic range of the dead-layer if the design is meant to exploit contractions of the SCR. An unfortunate corollary to the lack of passivation is a null improvement in PL sensitivity according to Equations 2.63 and 2.64. However, as will be demonstrated, the use of thiol coupling to anchor functional molecules to the surface is advantageous to sensor operation as it increases the sensitivity to surface potential changes at the semiconductor-electrolyte interface. This effect is believed to be the result of the increase in electron affinity imparted by the S-GaAs interface dipole.

To demonstrate the effect of thiol coupling on PL sensitivity in the context of the dead-layer effect, etched-only and ATA-SAM prepared samples were monitored *in situ* using the PL-mapping apparatus described in Kim *et al.* [Kim *et al.*, 2009]. The samples consisted of an undoped GaAs capped AlGaAs/GaAs heterostructure, also described in Kim *et al.*, and are assumed to have the same band-bending as the undoped semi-insulating bulk samples that have been reported on thus far. Experimentally, the samples were immersed in ethanol and the pH was varied to high and low values by flushing through with ethanol containing a few drops each of either ammonium hydroxide, to obtain a pH of about 11, or acetic acid, to obtain a pH of about 4, as measured by a water referenced electronic pH meter.

According to the well-known Nernst equation, the redox potential of an electrolyte solution is reciprocal with pH. The redox potential characterizes its electron gaining affinity. When the redox potential of the electrolyte is changed by varying the pH, the Fermi level of the semiconductor must reach a new equilibrium resulting in charge flow. For example, if the redox potential is increased, the electrolyte draws charge from donor ionization in the

semiconductor and the dead-layer is increased [Uosaki, 1990]. Conversely, one would expect that increasing the pH would result in a PL intensity increase by dead-layer contraction. Figure 6.11 shows the results from two samples where this is observed: (a) the etched-only surface, and (b) as prepared with ATA-SAM. In the case of Figure 6.11(b), the effect of ATA-SAM formation can also be observed, i.e., an increase in PL due to SRV reduction. When the pH is increased, the PL increases by a factor of 2.2. In (a) the increase is about 1.6 \times .

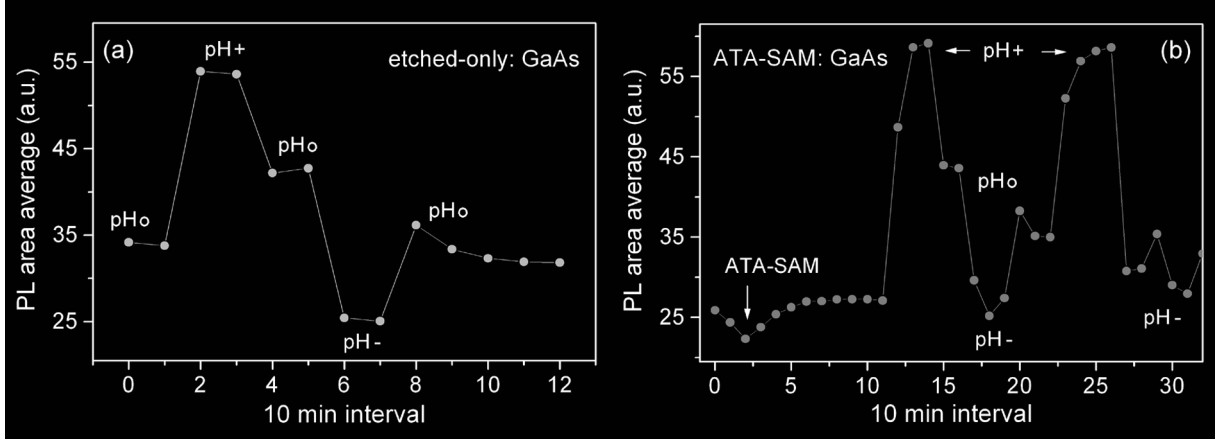


Figure 6.11. Variation of *in situ* PL as the pH of ethanol solvent is modified from pH 7 for neutral ethanol (pH_o) to pH 11 by the addition of ammonium hydroxide (pH⁺) and to pH 4 by the addition of acetic acid (pH⁻): (a) etched-only GaAs, (b) following injection with 3 mM solution of ATA-SAM.

The redox potential can, in effect, be considered as the Fermi level of the electrolyte solution [Zhang, 2001]. The band-bending change can then be understood in the context of the Schottky barrier, in which the band-bending potential is given by the difference ($\Phi_{sb} = \phi_{wf} - \phi_{ea}$) between the work function of the metal and the electron affinity of the semiconductor. A decrease of the vacuum referenced redox potential is analogous to a reduction of the metal work function, thus the surface barrier decreases. How such a decrease is manifested at the surface can be understood by considering the Helmholtz layer that is realized in the solution at the interface. For example, the acid dissociation fraction of X-OH groups that may be attached to the bare GaAs surface approaches 1 in alkaline pH resulting in negatively charged (X-O⁻) surface species [De Vrieze *et al.*, 2001]. Screening by positive ions in the solution results in a potential drop across the layer [Zhang, 2001], which lowers the vacuum level to which the redox potential is referred. In both Figures 6.11 (a) and (b), there appears to be a path dependence in the transition to the baseline PL, i.e., neutral ethanol does not return the PL to its initial intensity. This is as yet unexplained, but may be related to

the re / protonation of the X-OH groups, which would only be complete by about half at neutral pH if the pK_a of X-OH is characteristic of a weak acid.

Referencing the slope of the redox potential's dependence on pH in water, which is about -0.06 mV per pH unit, and assuming it applies similarly to aqueous electrolytes in ethanol, the drop in redox potential at pH 11 will be about 240 meV. This is a substantial fraction of the residual band-bending under the illumination conditions in Figure 6.4, which are roughly the same in this test ($\sim 10^{17}$ photons $\text{cm}^{-2} \text{s}^{-1}$). In addition, the SCR contraction associated with this change in potential, about 57 nm, agrees with the PL increase observed in Figure 6.11(a) as predicted by the dead-layer model for the surface barrier height determined by XPS. Since the potential difference upon pH increase is the same in both (a) and (b), the charge transfer from the substrate in reaching a new equilibrium will also be the same. However, the PL increase for the thiol-treated surface is a factor of 1.3-1.4 greater, which means that the PL sensitivity has increased. The reasons are not entirely clear at this point, however, as mentioned above, the effect could be attributed to the interfacial dipole associated with the S-GaAs polar bond. Its dipole polarity will increase the electron affinity and lower the barrier according to the above expression. Note that the SAM-DLP was ruled out as a contributing factor; the same PL response was observed where methyl-terminated SAMs were used.

6.5 Chapter Summary

The electro-optic characteristics of the semi-insulating and n^+ -type GaAs(001) surfaces passivated with *n*-alkanethiol self-assembled monolayers were investigated using Kelvin probe SPV and PL techniques. Referencing the equilibrium surface barrier height established in Chapter 5, SPV measurements demonstrated a significant (> 100 mV) increase in the non-equilibrium band-bending potential observed under low level photo-injection. Modeling of the SPV accounts for these observations in terms of a large ($> 10^4$) decrease in the hole/electron ratio of surface carrier capture cross-sections, which is suggested to result from the electrostatic potential of the interfacial dipole layer formed upon thiol chemisorption. Specifically, it is argued that the cross-section for minority carrier capture is decreased due to near-surface band modification. Analysis in terms of the SRV in the high-injection regime validated this assertion using a carrier transport model of the PL intensity.

The significance of these findings to PL-based sensor operation were briefly discussed. Thiol-coupling of functional molecules yields the advantage of increased PL brightness by virtue of the effect of a reduced SRV, and does so without compromising the dynamic range of the dead-layer, which is a significant parameter of the transduction mechanism. Thiol-coupling was observed to increase the PL sensitivity to changes in the surface potential at the GaAs-electrolyte interface, which may be attributed to the increase in electron affinity introduced by the S-GaAs interface dipole.

CHAPTER 7:

THESIS SUMMARY and CONCLUDING REMARKS

7.1 Thesis Summary

In Chapter 1, the fundamentals of biosensing were introduced through a variety of examples and molecular self-assembly was discussed as an enabling technology of the required surface chemistry. In this context, the *n*-alkanethiol SAM was introduced as a prototypical coupling interface to more advanced functional molecular architectures. An overview of semiconductor approaches to biosensing was then given and the surface potential was introduced as a fundamental parameter of the various transduction mechanisms. Specifically, two surface potential sensitive mechanisms of the PL-based approach were identified: i) the depletion region dependent PL dead-layer, and ii) the surface state dependent SRV. The scope of the thesis was defined in terms of the electro-optic effects specific to the *n*-alkanethiol SAM interface with GaAs(001) and, in particular, it was questioned how the electro-optic properties of the interface derive from its physical structure, and what significance is there for biosensing mechanisms. Accordingly, the structure of the thesis was broken down into three categories: 1) structural and chemical characterization, 2) electronic properties, and 3) electro-optic response of the SAM-passivated surface.

Chapter 2 provided a foundation of knowledge in theory and literature from which the specific research objectives were identified. These are summarized as: i) the quantitative analysis of assigned surface species by XPS and the fractional uniformity of the SAM as determined by ARXPS methods, ii) the position change of the equilibrium surface Fermi level following SAM formation, iii) a determination of the optical constants of the SAM, iv) the surface dipole contribution of the SAM, and v) analysis of the SRV in terms of the specific contribution of the surface carrier capture cross-sections under steady-state optical excitation. The main body of results were then presented in the ensuing four chapters.

First, a compositional and structural analysis of the SAM-GaAs interface was made and the following conclusions were obtained: i) As-S species characteristic of thiol-GaAs

coupling, identified in XPS spectra following separation of the bulk component by an independently determined asymmetric fitting procedure, were located at a binding energy that agrees with results from the XPS analysis of GaAs(001) passivated with inorganic sulphides, ii) the bond fraction of As-S relative to the total number of GaAs-S bonds was determined to be 30-50%, iii) the S-GaAs component (S 2p) fitted in the Ga 3s region exhibited a chemical shift of 1.2 eV and was found to be quantitatively accurate within 80%, relative to the ideal SAM, considering the limitations of the complex fitting procedure required and the uncertainty with respect to full SAM coverage, iv) the surface was determined to be Ga-rich to a depth significant with respect to the sampling depth of XPS analysis, v) the surface component of As⁰ was determined to have a surface density of $2.4 - 3.4 \times 10^{14} \text{ cm}^{-2}$, which represents a coverage fraction of 30-40% that can be interpreted in terms of a trench-filling morphology and vi) the fractional coverage of a well-ordered SAM was determined to be high, up to 92%, using ARXPS techniques in the logarithmic domain. In general terms, the above conclusions address gaps in the literature with respect to quantitatively consistent XPS component assignments and verify more precisely the premise of a chemically bonded, high coverage SAM.

In Chapter 4, the focus turned to an analysis of the IR optical constants of the SAM and a more detailed look at the modal composition of the C-H stretching modes in terms of what they suggest for the molecular order. It was determined that: i) the homologous series between *n*11 and *n*17 was comprised of uniformly dense SAMs changing by molecular length, and ii) the increasing energies indicated by peak wavenumbers at shorter *n*-values do not entirely reflect an increase in SAM disorder. These conclusions support that transmission IR spectra can be interpreted in terms of a Beer-Lambert evaluation of the absorption coefficient. Using a suitable axis of uniaxial symmetry, the principle components of the refractive index in the IR region were determined and it was observed that the absorbance of the C-H stretching modes of alkanethiol in the SAM phase carries an extrinsic enhancement factor of 3 relative to that in the bulk isotropic liquid phase. The significance here is that, for one, the IR characteristics of well-ordered methyl-terminated SAMs may now be used to provide a quantitative benchmark for comparison with more functional SAMs used for biosensing, which tend to form less well-ordered structures. Secondly, and further pursuant to the thesis objectives, the optical properties of the SAM have been shown to be unique.

How the IR enhancement effect derives from the physical properties of the SAM was a question considered in Chapter 5 following a determination of the SAM's surface dipole contribution. Quantified in terms of a DLP using Kelvin probe and XPS techniques, the dipole contribution indicates a field strength internal to the SAM significant with respect to its dielectric breakdown potential. Furthermore, it was observed that the DLP scales by molecular length in direct proportion to the IR absorbance. Based on this correlation, and the large magnitude of the field, it was proposed that contributions to the vibrational moment were affected by an increase to the static vibrational dipole and a dynamic increase to the electronic polarizability. An alternative explanation was put forward that relates to the Lorentz local field correction, but was rejected on the grounds that it did not accurately predict the enhancement observed for the same SAMs on Au substrates. The same proportionality between the IR absorbance and the DLP was observed in this case, which supports the correlation as causal with respect to the internal field of the SAM.

Having obtained the electron affinity contribution to the surface work function in the form of the SAM-DLP, a determination of the band-bending potential was required in order to establish the overall interface band structure. Utilizing the integrated Au pad approach to Fermi level referencing of the XPS binding energy, it was determined that the electronic passivation effect of the SAM was negligible, i.e., a reduction of the initial band-bending < 10% was obtained, and that the position of the Fermi level corresponded to the prescriptions of the AUDM for a Ga-rich interface. Knowledge of the surface barrier height thus obtained became important in the evaluation of the surface electronic conditions under steady-state optical excitation, especially for semi-insulating GaAs.

In Chapter 6, SPV measurements and numerical analysis, added to knowledge of the surface barrier height from XPS, demonstrated that the decrease in SRV resulting from thiol-GaAs coupling can be attributed to a decrease in the surface cross-section for minority carrier capture. It was proposed that this effect results from the penetrating dipole field of the surface complex formed at the S-GaAs interface. Analysis in the high-injection regime, where surface barrier effects are nullified, helped validate the assertion of a reduction in σ_p utilizing a carrier transport model of PL intensity. In the low-injection regime, *in situ* variation of the redox potential demonstrated the effect of a change in the non-emissive dead-layer region, and it was further shown that the PL sensitivity increases following thiol passivation.

7.2 Concluding Remarks

In addition to explanations relating the physical structure and properties of the SAM-GaAs interface to its electro-optic characteristics, as summarized above, the parallel intent of this work was to inform the development process of a PL-based biosensor employing alkanethiol SAMs as a coupling interface to more advanced molecular chemistry. The following concluding remarks address this objective.

Although methyl-terminated long-chain *n*-alkanethiols form dense and well-ordered molecular films of high surface coverage, SAMs comprised of amine-terminated molecules do not present the same pseudo-crystalline characteristics. Similar results have been observed for other functional terminations, e.g. COOH. However, the nature of the IR enhancement mechanism can belie the true surface coverage when IR spectroscopy is used as a means of comparison, i.e., enhancement means that the IR absorbance is non-linear with coverage. Indeed, as was observed in Chapter 5, a significant reduction of IR absorbance can be observed upon thermal disordering, whereas the XPS signature of chemisorbed thiol remains strong. In terms of the relative passivating effect of a highly-ordered SAM vs. one that is less well-ordered, the chemical passivation will suffer in the *ex situ* environment in the latter case, but the electronic passivation will not suffer to the same degree, as a minimum electronic passivation effect is realized even in the ideal SAM.

The lack of electronic passivation is made clear from consideration of the surface charge density under pinning conditions. In the case of undoped semi-insulating GaAs, more preferable because of its lower surface barrier, pinning requires a charge density of about two orders less than the molecular surface density the SAM can achieve. Since passivation of the available atomic sites is only 50% in the best case, according to the trench-ridge model of surface morphology, electronic passivation will be very limited simply because the molecular density of the SAM cannot match the atomic density of the GaAs. In order to take advantage of the PL sensitivity increase that reducing the surface barrier further would afford, a more effective approach to surface passivation must first be taken before biofunctional elements are immobilized on the surface.

A final point with respect to the transduction mechanism in a PL-based biosensor relates to the separation of SRV and dead-layer effects. Although these mechanism can be separated analytically, it does not mean they can always be independently controlled. Note that a

qualitative general theory of molecule-surface interaction has been proposed by Cohen *et al.* [Cohen *et al.*, 1999], in which the LUMO of the adsorbing molecule interacts with the HOMO of occupied surface states in a surface complex of bonding molecular orbitals. According to this theory, in its manifestation for n-type surfaces, stabilization of the bonding HOMO level implies that some surface states are pushed below the valance band edge (delocalized) effectively reducing the surface state density resulting in a band-bending reduction. At the same time, surface states that are moved closer to the band edges, but are still in the gap, become more “shallow”, which results in a reduced SRV according to the non-radiative Shockley-Read-Hall theory. In the context of the surface complex theory, independence of the SRV and band-bending effects in the present work is valid and can be attributed to the fact that, as an electron-pair donor, sulphur interacts with unoccupied states and, therefore, would not interact with an n-type surface in the manner described. Further to the molecular orbital framework, the large HOMO-LUMO gap (> 3 eV) determined for the alkanethiol-GaAs system [Nesher *et al.*, 2006] suggests a limited overlap of the unoccupied molecular orbitals with the occupied surface state energy levels and, consequently, weak molecular-surface interactions of this type. In general, however, when thinking about the design of a sensor, consideration of the complete set of energy levels and their interactions must be given in order that competing processes do not limit PL sensitivity.

APPENDIX A:

Band Bending Potential, Depletion Depth and Surface Charge Density

In the depletion approximation, the space charge region is comprised of a uniform density, extending from the surface to the point z_d where it becomes zero (see Figure 1.6). As such, a closed-form solution to Poisson's Equation may be found. Poisson's Equation is,

$$\frac{d^2 \Phi(z)}{dz^2} = \frac{\rho}{\epsilon}, \quad 0 < z < z_d \quad (\text{A.1})$$

where $\rho = q N_d$ is the volume space charge density with N_d the doping concentration, or concentration of native ionized defects ($N_d \gg n_o$). Integration of A.1 gives,

$$\frac{d\Phi(z)}{dz} = \frac{q N_d}{\epsilon} z + c_1 \quad (\text{A.2})$$

Applying the appropriate boundary condition at z_d ,

$$\frac{d\Phi(z_d)}{dz} = \frac{q N_d}{\epsilon} z_d + c_1 = 0 \quad (\text{A.3})$$

gives,

$$c_1 = -\frac{q N_d}{\epsilon} z_d \quad (\text{A.4})$$

which is inserted in A.2 yielding the built-in electric field profile,

$$E(z) = \frac{d\Phi(z)}{dz} = \frac{q N_d}{\epsilon} (z - z_d) \quad (\text{A.5})$$

Integration of A.5 gives,

$$\Phi(z) = \frac{q N_d}{\epsilon} \left(\frac{z^2}{2} - z_d z \right) + c_2 \quad (\text{A.6})$$

Applying the appropriate boundary condition at z_d ,

$$\Phi(z_d) = -\frac{q N_d}{\epsilon} \left(\frac{z_d^2}{2} \right) + c_2 = 0 \quad (\text{A.7})$$

gives,

$$c_2 = \frac{q N_d z_d^2}{2 \epsilon} \quad (\text{A.8})$$

which is inserted in A.6 yielding the band-bending potential (Equation 2.13),

$$\Phi(z) = \frac{q N_d}{2\epsilon} (z - z_d)^2 \quad (\text{A.9})$$

With the surface barrier defined as $\Phi(0) = \Phi_{sb}$, A.9 rearranges to,

$$z_d = \sqrt{2\epsilon\Phi_{sb}/q N_d} \quad (\text{A.10})$$

which is the depletion depth (Equation 2.14). Multiplying through by $\rho = q N_d$ gives,

$$Q_{sc} = \sqrt{2\epsilon q N_d \Phi_{sb}} \quad (\text{A.11})$$

(Equation 2.15), defined as the equivalent two-dimensional surface charge density associated with the space charge region, which is equal to, but opposite in sign of the actual surface trapped charge density, in order that charge neutrality is maintained.

References:

[Streetman and Banerjee, 1999]

[Böer, 1992]

APPENDIX B:

Equilibrium Fermi level in the Semiconductor Bulk

The number density of electrons in the conduction band is given by,

$$n_o = \int_{E_c}^{\infty} f(E) N(E) dE \quad (\text{B.1})$$

where $f(E)$ is the Fermi function and $N(E) dE$ is the density of states for a free electron (wavevector \mathbf{k}_n and effective mass m_n^*) in a parabolic potential ($E \propto |\mathbf{k}_n|^2$).

$$f(E) = 1 / 1 + e^{(E-E_F)/kT} \quad (\text{B.2})$$

$$N(E) dE = \frac{\sqrt{2}}{\pi^2} \left(\frac{m_n^*}{\hbar^2} \right)^{\frac{3}{2}} E^{1/2} dE \quad (\text{B.3})$$

Referring the energy to $E_c = 0$, and with β_1 combining terms of the prefactor B.1 becomes,

$$n_o = \beta_1 \int_0^{\infty} \frac{E^{1/2}}{1 + e^{(E-E_F)/kT}} dE \quad (\text{B.4})$$

Using the following change of variables,

$$t = E/kT, \quad \xi = E_F/kT \quad (\text{B.5})$$

B.4 is,

$$n_o = \beta_1 (kT)^{3/2} \int_0^{\infty} \frac{t^{1/2}}{1 + e^{t-\xi}} dt \quad (\text{B.6})$$

which is of the form of the Fermi-Dirac integral,

$$F_j(\xi) = \frac{1}{\Gamma(j+1)} \int_0^{\infty} \frac{t^j}{1 + e^{t-\xi}} dt \quad (\text{B.7})$$

with order $j = 1/2$. Since $\Gamma(3/2) = \sqrt{\pi}/2$, B.6 is now,

$$n_o = \frac{\sqrt{\pi}}{2} \beta_1 (kT)^{3/2} \left[\frac{2}{\sqrt{\pi}} \int_0^{\infty} \frac{t^{1/2}}{1 + e^{t-\xi}} dt \right] \quad (\text{B.8})$$

The prefactor of B.8 rearranges to,

$$N_c = 2 \left(\frac{2\pi m_n^* kT}{h} \right)^{\frac{3}{2}}, \quad N_v = 2 \left(\frac{2\pi m_p^* kT}{h} \right)^{\frac{3}{2}} \quad (\text{B.9})$$

which are called the effective densities of states for the conduction/valence bands. The integral in B.8 can be computed using the Aymerich-Humet approximation for $F_{1/2}(x)$,

$$F_{1/2}(\xi) = \left[\frac{(j+1)2^{j+1}}{\left[b + \xi + \left(|\xi - b|^c + a \right)^{1/c} \right]^{j+1}} + \frac{e^{-\xi}}{\Gamma(j+1)} \right]^{-1}, \quad a = 9.60, b = 2.13, c = 12/5 \quad (\text{B.10})$$

In order to evaluate the Fermi level as function of N_d , let $n_o \approx N_d$, then,

$$F_{1/2}(\xi) = \frac{\sqrt{\pi}}{2} \frac{N_d}{N_c} \quad (\text{B.11})$$

Equating B.10 and B.11, numerically solving for ξ , and using the change of variable B.5,

$$E_F(N_d) = \xi kT + E_g \quad (\text{B.12})$$

(Equation 2.16), where E_g refers the Fermi level back to the valence band maxima.

Equation B.12 is correct for all doping conditions. Under non-degenerate conditions ($E_F < E_c$) specifically, where $E_{c,v}$ are the conduction/valence band minima/maxima, approximation of $f(E_{c,v})$ to the Boltzmann factor can be made, and results in the following for the equilibrium free carrier concentrations,

$$n_o = N_c e^{-(E_c - E_F)/kT} \quad (\text{B.13})$$

$$p_o = N_v e^{-(E_F - E_v)/kT} \quad (\text{B.14})$$

The Fermi level that equates B.13 and B.14 ($n_i = p_i$) is called the intrinsic Fermi level E_i ,

$$\frac{N_c}{N_v} = e^{(E_v + E_c - 2E_i)/kT} \quad (\text{B.15})$$

But from the density of states B.9,

$$\frac{N_c}{N_v} = \left(\frac{m_n^*}{m_p^*} \right)^{\frac{3}{2}} \quad (\text{B.16})$$

so that B.15 is now,

$$kT \ln \left(\frac{m_n^*}{m_p^*} \right)^{\frac{3}{2}} = E_g - 2E_i \quad (\text{B.17})$$

or,

$$E_i = \frac{1}{2} \left(E_g - \frac{3}{2} kT \ln \left(\frac{m_n^*}{m_p^*} \right) \right) \quad (\text{B.18})$$

To get an expression for the Fermi level, write,

$$n_i = N_c e^{-(E_c - E_i)/kT} \quad (\text{B.19})$$

and substitute in B.13,

$$n_o = n_i e^{(E_F - E_i)/kT} \quad (\text{B.20})$$

use $n_o \approx N_d$ and rearrange (Equation 2.17),

$$E_F = E_i + kT \ln(N_d/n_i) \quad (\text{B.21})$$

References:

[Streetman and Banerjee, 1999]

[Aymerich-Humet *et al.*, 1981]

[Sze and Ng, 2007]

APPENDIX C:

Transition Dipole Moment and IR Transition Rate

From Equation 2.21, the one dimensional time-dependent Schrödinger equation is,

$$\left(\frac{-\hbar^2}{2m_r} \frac{\partial^2}{\partial x^2} + \frac{1}{2} K x^2 + e\mathbf{x} \cdot \mathbf{E}(t) \right) \Psi(x, t) = i\hbar \frac{\partial}{\partial t} \Psi(x, t) \quad (\text{C.1})$$

with the time-dependent perturbation energy $e\mathbf{x} \cdot \mathbf{E}(t)$. This has general solutions,

$$\Psi(x, t) = \sum_m c_m(t) \psi_m(x) e^{-iE_m t/\hbar} \quad (\text{C.2})$$

where the $\psi_m(x)$ are the eigenfunctions of the time-independent Schrödinger equation, having eigenvalues E_m . The coefficients give the normalized probability $|c_m(t)|^2$ of state $|\psi_m\rangle$ at time t . Insertion of C.2 in the right-hand side (RHS) of C.1 gives,

$$i\hbar \sum_m \psi_m(x) e^{-iE_m t/\hbar} \frac{\partial}{\partial t} c_m(t) + \sum_m E_m c_m(t) \psi_m(x) e^{-iE_m t/\hbar} \quad (\text{C.3})$$

The LHS of C.1 is just,

$$[H_o + H(t)] \sum_m c_m(t) \psi_m(x) e^{-iE_m t/\hbar} \quad (\text{C.4})$$

where H_o is the time-independent Hamiltonian of the unperturbed system. Since,

$$H_o \psi_m(x) = E_m \psi_m(x) \quad (\text{C.5})$$

the second term of C.3 cancels with the first term of C.4, therefore,

$$i\hbar \sum_m \psi_m(x) e^{-iE_m t/\hbar} \frac{\partial}{\partial t} c_m(t) = e\mathbf{x} \cdot \mathbf{E}(t) \sum_m c_m(t) \psi_m(x) e^{-iE_m t/\hbar} \quad (\text{C.6})$$

With $|\psi_n\rangle$ a state vector of the complete set $\{|\psi_m\rangle\}$, orthonormality implies $\langle\psi_n|\psi_m\rangle = \delta_{nm}$, and then only the terms n survive in the LHS of C.6.

$$i\hbar \frac{\partial}{\partial t} c_n(t) = \sum_m \langle\psi_n(x)|e\mathbf{x} \cdot \mathbf{E}(t)|\psi_m(x)\rangle c_m(t) e^{-i(E_m - E_n)t/\hbar} \quad (\text{C.7})$$

Evaluating at $t = 0$, all terms $c_m(0) = 0$ except $c_0(0) = 1$, i.e., the ground state $|\psi_0\rangle$, at which point the external optical field is applied. Let $c_1(t)$ be the increasing coefficient of the excited state $|\psi_1\rangle$. Along with $\omega_{01} = (E_0 - E_1) / \hbar$, C.7 becomes,

$$i\hbar \frac{\partial}{\partial t} c_1(t) = E(t) \cos \Theta \langle \psi_1(x) | ex | \psi_0(x) \rangle e^{-i\omega_{01}t} \quad (\text{C.8})$$

where Θ is the angle between the optical field and the displacement x . The integral,

$$M_{01} = \langle \psi_1(x) | ex | \psi_0(x) \rangle = \int_{-\infty}^{\infty} ex \psi_1^*(x) \psi_0(x) dx \quad (\text{C.9})$$

is called the transition dipole moment for the vibrational transition from $|\psi_0\rangle$ to $|\psi_1\rangle$ (Equation 2.23). With the time-dependent optical driving function $E(t) = E_o e^{i\omega t}$, integrating C.8 over the transition time gives,

$$c_1(t) = \frac{M_{01} \cos \Theta}{i\hbar} \int_0^t E_o e^{i(\omega - \omega_{01})t'} dt' \quad (\text{C.10})$$

or,

$$c_1(t) = \frac{M_{01} E_o \cos \Theta}{\hbar} \frac{(1 - e^{i(\omega - \omega_{01})t})}{(\omega - \omega_{01})} \quad (\text{C.11})$$

The probability of absorption (per unit frequency) is now,

$$|c_1(t)|^2 = \frac{M_{01}^2 E_o^2 \cos^2 \Theta}{\hbar^2} \frac{4 \sin^2[(\omega - \omega_{01})t / 2]}{(\omega - \omega_{01})^2} \quad (\text{C.12})$$

The actual transition probability is found by integrating over the incident spectral frequencies,

$$P_{01}(t) = \int_{-\infty}^{\infty} |c_1(t)|^2 d\omega = \frac{4M_{01}^2 E_o^2 \cos^2 \Theta}{\hbar^2} \int_{-\infty}^{\infty} \frac{\sin^2[(\omega - \omega_{01})t / 2]}{(\omega - \omega_{01})^2} d\omega \quad (\text{C.13})$$

Using the substitution $y = (\omega - \omega_{01})t / 2$, and $dy = t/2 d\omega$,

$$P_{01}(t) = \frac{4M_{01}^2 E_o^2 \cos^2 \Theta}{\hbar^2} \frac{t^2}{4} \frac{2}{t} \int_{-\infty}^{\infty} \frac{\sin^2 y}{y^2} dy \quad (\text{C.14})$$

or,

$$P_{01}(t) = \frac{2\pi M_{01}^2 E_o^2 \cos^2 \Theta}{\hbar^2} t \quad (\text{C.15})$$

The IR optical irradiance is $I_{IR} = c \varepsilon_o E_o^2 / 2$ and the transition rate is $W_{01} = d P_{01}(t)/dt$, so that C.15 becomes,

$$W_{01}(t) = \frac{4\pi I_{IR} \cos^2 \Theta}{\hbar^2 c \varepsilon_o} M_{01}^2 \quad (C.16)$$

For unpolarized light, or randomly oriented transition dipoles (e.g., liquid phase), the $\cos^2 \Theta$ term can be substituted with its spatially averaged value,

$$\langle \cos^2 \Theta \rangle = \frac{1}{4\pi} \int_0^{2\pi} \int_0^\pi \cos^2 \Theta \sin \Theta d\Theta d\phi = \frac{1}{3} \quad (C.17)$$

so the transition rate of absorption is (Equation 2.24),

$$W_{01}(t) = \frac{4\pi I_{IR}}{3 \hbar^2 c \varepsilon_o} M_{01}^2 \quad (C.18)$$

References:

[Bransden and Joachain, 1989]

[Harris and Bertolucci, 1989]

[Masters and So, 2008]

APPENDIX D:

Radiative Lifetime

The bulk (intrinsic) recombination rate can be written as,

$$U = \beta [np - n_i^2] \quad (\text{D.1})$$

where β is the radiative rate constant for GaAs. Expanding in terms of the excess carriers,

$$U = \beta [n_o p_o + n_o \delta p + p_o \delta n + \delta p \delta n - n_i^2] \quad (\text{D.2})$$

If $n_o \gg p_o$, $\delta p \gg p_o$ and $\delta n \ll n_o$ (low-injection), this reduces to

$$U = \beta [n_o \delta p + \delta p \delta n] \quad (\text{D.3})$$

or,

$$U = \beta n \delta p \quad (\text{D.4})$$

Since the recombination rate is governed by the minority carrier concentration,

$$\frac{d}{dt} \delta p = -\beta n \delta p \quad (\text{D.5})$$

or,

$$\delta p(t) = \Delta p e^{-\beta n t} \quad (\text{D.6})$$

which is the same form as Equation 2.51, therefore, the radiative lifetime is (Equation 1.4),

$$\tau_r = 1/\beta n \quad (\text{D.7})$$

References:

[Dutta, 1993]

APPENDIX E:

XPS Analysis of Surface Desorption on Thermal Disordering

In this section, a characterization of the disordered SAM is made specific to the claim that the surface concentration of thiolate remains high after disordering at 55°C. Although the appearance of equivalent S 2p / Ga 3s ratios in Figure 5.5 is qualitatively correct in terms of this underlying assumption, a more quantitative assessment is required in order to justify the use of different ToAs (60° and 75°). As the calculation below demonstrates, the use of equivalent S 2p / Ga 3s ratios for these angles is justified where a 2-3× reduction in the carbon overlayer thickness is assumed. The analysis here must be qualified as an estimate only, and is an idealization, particularly in view of the non-uniform surface that may result. Nonetheless, an effective 2-3× thickness reduction may be a reasonable value to expect. A thiol loss factor of 25% is applied in the following calculations in order to accommodate the disordering with respect to the ideal SAM using a fractional overlayer model. This factor would result if, e.g., every other molecule along nearest-neighbour directions was desorbed in a square surface cell. In the pseudo-hexagonal surface arrangement, the same criterion would result in a 21% desorption factor, which approaches the limit of fitting tolerance within the complex Ga 3s spectral region.

The ratio of S 2p and Ga 3s normalized XPS photoelectron intensities can be approximated for the ideal SAM as,

$$\frac{I_{S2p}^*}{I_{Ga3s}^*} \approx \frac{1}{\cos 60^\circ} \quad (\text{E.1})$$

and similarly for a fractional layer after disordering,

$$\frac{I_{S2p}^*}{I_{Ga3s}^*} \approx \frac{f e^{-d_{DIS}/\Lambda \cos 75^\circ}}{\cos 75^\circ (1 - f + f e^{-d_{DIS}/\Lambda \cos 75^\circ})} \quad (\text{E.2})$$

where the angles are the respective ToAs, $f = 0.75$ is the fractional coverage after disordering, $d_{DIS} = 0.4 d_{SAM}$ is the effective thickness after disordering (i.e., reduced 2-3x), and Λ is the IMFP through the organic layer. E1 and E2 equate to a value of 2. Therefore, the weighting of S 2p with respect to Ga 3s in the component fittings of Figure 5.5 will be the

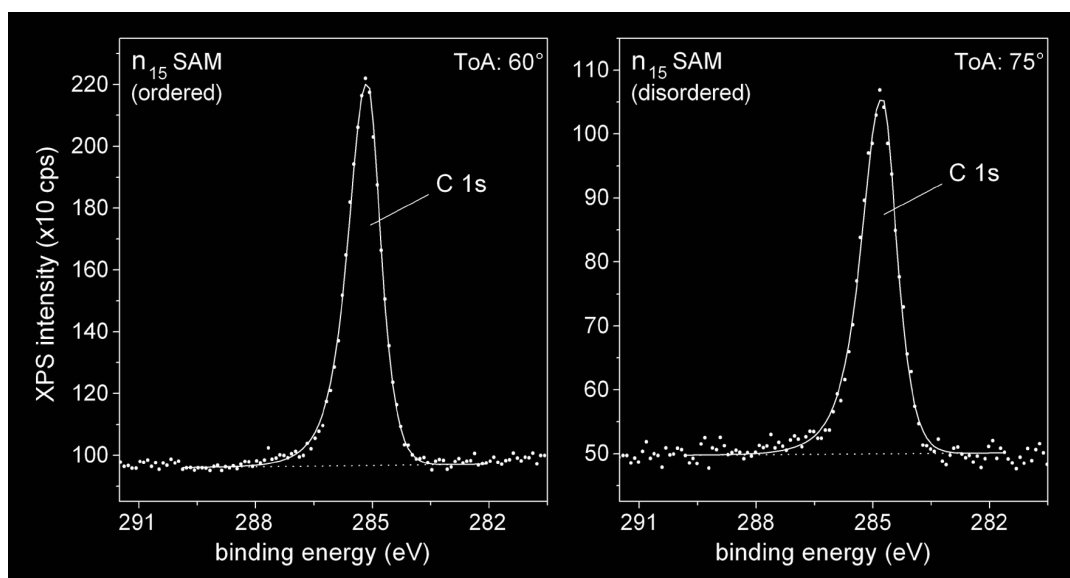
same for 60° and 75° ToAs. The equivalency of E1 and E2 ratios is clear in Table E1.

TABLE E1. Angle-Resolved XPS component data for the ordered (60°) and disordered (75°) SAM in Figures 5.5.

atomic orbital	binding energy ^a (eV)		intensity (cps)	
	60°	75°	60°	75°
C 1s	285.12	284.74	1426.4	712.9
S 2p ^b	162.50	162.16	65.2	31.8
Ga 3s	160.30	160.30	373.6	183.2

^a referencing as described in the Experiment Details.

^b reference the 5/2 spin-orbit branch of S 2p doublet with 1/2 splitting ratio and +1.18 eV separation to 3/2 branch.

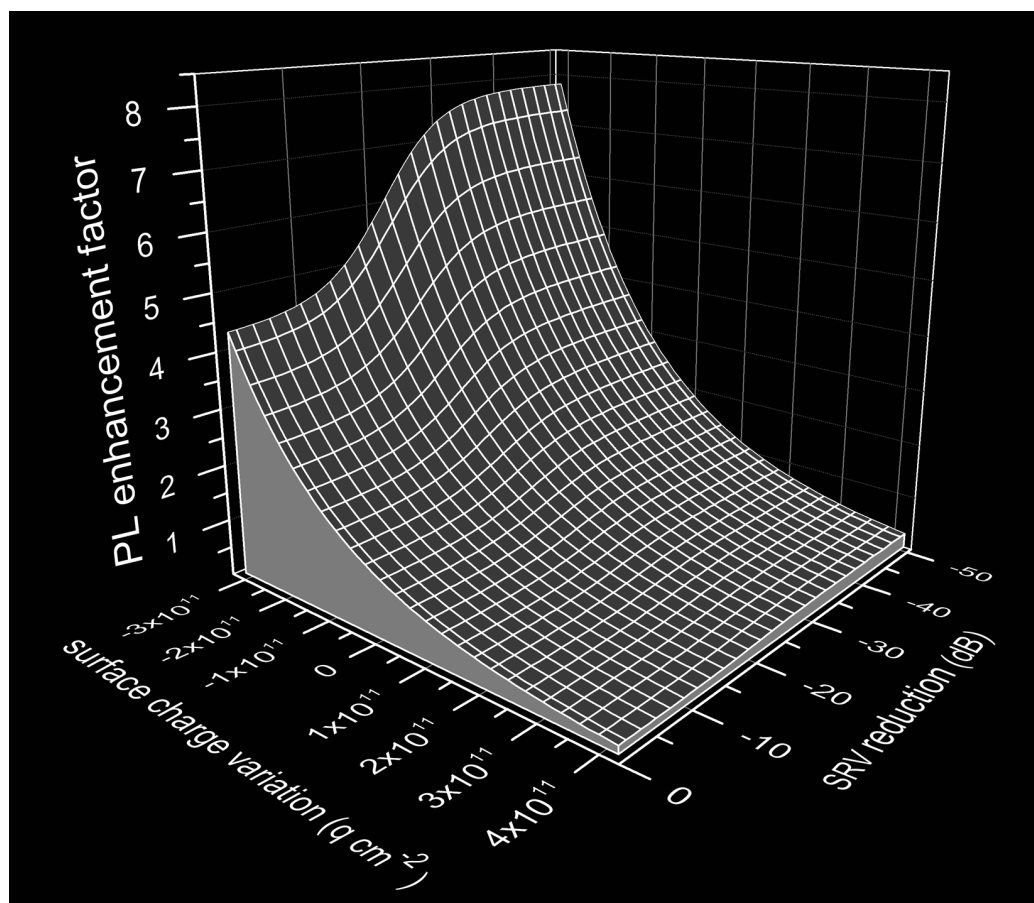


XPS C 1s. Spectra before (60°) and after (75°) thermal disordering of n₁₅-SAM, complementary to S 2p / Ga 3s data in Figures 5.5 and in Table E1.

APPENDIX F:

PL Enhancement Based on Dead-layer and SRV Modifications

The purpose of this appendix is to illustrate an example of PL enhancement where both dead-layer and SRV modifications are effected on the surface simultaneously. The semi-insulating GaAs(001) interface with material parameters, surface barrier height, and low-intensity injection as specified in Figure 6.9 are assumed. The dead-layer modification is cast in terms of the change in surface charge density ($q\text{ cm}^{-2}$) for electrons at a depleted n-type surface, and includes both positive and negative variation. The SRV reduction is based on a dB scale ($10\log X^{-1}$) where X is the fraction of SRV reduction following surface treatment. Considered independently, the exponential dependence of the dead-layer effect produces greater enhancements than is generated by SRV reductions. Maximum contraction of the dead-layer is limited by its initial value, i.e., contraction extends to zero depletion.



Calculated PL Enhancement for SI-GaAs. Model result based on variation with respect to the initial surface condition at PL enhancement factor = 1.

BIBLIOGRAPHY:

- Abbate, S., Zerbi, G., Wunder, S.L. (1982) Fermi resonances and vibrational spectra of crystalline and amorphous polyethylene chains. *The Journal of Physical Chemistry*, vol. 86, no. 16, pp. 3140-3149.
- Adlkofer, K., Duijs, E.F., Findeis, F., Bichler, M., Zrenner, A., Sackmann, E., Abstreiter, G., Tanaka, M. (2002) Enhancement of photoluminescence from near-surface quantum dots by suppression of surface state density. *Physical Chemistry Chemical Physics*, vol. 4, no. 5, pp. 785-790.
- Adlkofer, K., Tanaka, M. (2001) Stable Surface Coating of Gallium Arsenide with Octadecylthiol Monolayers. *Langmuir*, vol. 17, no. 14, pp. 4267-4273.
- Allara, D.L., Nuzzo, R.G. (1985) Spontaneously organized molecular assemblies. 2. Quantitative infrared spectroscopic determination of equilibrium structures of solution-adsorbed *n*-alkanoic acids on an oxidized aluminum surface. *Langmuir*, vol. 1, no. 1, pp. 52-66.
- Alnot, P., Olivier, J., Wyczisk, F., Fadley, C. (1987) Angle-resolved X-Ray photoelectron spectroscopy for the characterization of GaAs(001) surfaces. *Journal of Electron Spectroscopy and Related Phenomena*, vol. 43, no. 3, pp. 263-286.
- Alperovich, V.L., Tereshchenko, O.E., Rudaya, N.S., Sheglov, D.V., Latyshev, A.V., Terekhov, A.S. (2004) Surface passivation and morphology of GaAs(1 0 0) treated in HCl-isopropanol solution. *Applied Surface Science*, vol. 235, no. 3, pp. 249-259.
- Aphek, O.B., Kronik, L., Leibovitch, M., Shapira, Y. (1998) Quantitative assessment of the photosaturation technique. *Surface Science*, vol. 409, no. 3, pp. 485-500.
- Aqua, T., Cohen, H., Vilan, A., Naaman, R. (2007) Long-Range Substrate Effects on the Stability and Reactivity of Thiolated Self-Assembled Monolayers. *The Journal of Physical Chemistry C*, vol. 111, no. 44, pp. 16313-16318.
- Aroca, R. (2006) *Surface Enhanced Vibrational Spectroscopy*, John Wiley & Sons, 261 p.
- Asai, K., Miyashita, T., Ishigure, K., Fukatsu, S. (1994) An application of electrolytic deposition for the electronic passivation of GaAs surfaces through the formation of thin organic films. *Surface Science*, vol. 306, no. 1, pp. 37-41.
- Aspnes, D. (1983) Recombination at semiconductor surfaces and interfaces. *Surface Science*, vol. 132, no. 1-3, pp. 406-421.
- Aymerich-Humet, X., Serra-Mestres, F., Millán, J. (1981) An analytical approximation for the Fermi-Dirac integral. *Solid-State Electronics*, vol. 24, no. 10, pp. 981-982.
- Babu, P.K., Lewera, A., Chung, J.H., Hunger, R., Jaegermann, W., Alonso-Vante, N., Wieckowski, A., Oldfield, E. (2007) Selenium Becomes Metallic in Ru-Se Fuel Cell Catalysts: An EC-NMR and XPS Investigation. *Journal of the American Chemical Society*, vol. 129, no. 49, pp. 15140-15141.
- Baca, A.G., Ashby, C.I.H. (2005) *Fabrication of GaAs Devices*, Institution of Electrical Engineers, 372 p.

- Baikie, I.D., Mackenzie, S., Estrup, P.J.Z., Meyer, J.A. (1991) Noise and the Kelvin method. *Review of Scientific Instruments*, vol. 62, no. 5, pp. 1326-1332.
- Barbaro, A., Colapicchioni, C., Davini, E., Mazzamurro, G., Piotta, A., Porcelli, F. (1992) CHEMFET Devices for biomedical and environmental applications. *Advanced Materials*, vol. 4, no. 6, pp. 402-408.
- Barrow, G.M. (1962) *Introduction to Molecular Spectroscopy*, McGraw-Hill, 350 p.
- Bergveld, P. (1970) Development of an Ion-Sensitive Solid-State Device for Neurophysiological Measurements. *IEEE Transactions on Biomedical Engineering*, vol. BME-17, no. 1, pp. 70-71.
- Bergveld, P. (2003a) Thirty years of ISFETOLOGY: What happened in the past 30 years and what may happen in the next 30 years. *Sensors and Actuators B: Chemical*, vol. 88, no. 1, pp. 1-20.
- Bergveld, P. (2003b) ISFET, theory and practice. Tutorials Program at the 2nd IEEE International Conference on Sensors, October 21, Toronto, Canada, pp. 1-26, Retrieved December 5th 2010, from <http://ewh.ieee.org/tc/sensors/Tutorials/ISFET-Bergveld.pdf>.
- Bideux, L., Baca, D., Gruzza, B., Matolin, V., Robert-Goumet, C. (2004) Surface modification of GaAs during argon ionic cleaning and nitridation: EELS, EPES and XPS studies. *Surface Science*, vol. 566-568, no. 2, pp. 1158-1162.
- Bishop, D.M. (1990) Molecular vibrational and rotational motion in static and dynamic electric fields. *Reviews of Modern Physics*, vol. 62, no. 2, pp. 343-374.
- Böer, K.W. (1992) *Survey of Semiconductor Physics: Barriers, Junctions, Surfaces, and Devices*, Springer, 1496 p.
- Boyd, R.W. (2003) *Nonlinear Optics*, 2nd Edition, Academic Press, 578 p.
- Bransden, B.H., Joachain, C.J. (1989) *Introduction to Quantum Mechanics*, Longman Scientific & Technical, 707 p.
- Briggs, D. (1998) *Surface Analysis of Polymers by XPS and Static SIMS*, Cambridge University Press, 224 p.
- Briggs, D., Beamson, G. (1992) *High Resolution XPS of Organic Polymers: The Scienta ESCA300 Database*, John Wiley & Sons, 306 p.
- Brugel, W. (1962) *An Introduction to Infrared Spectroscopy*, Methuen and Co., 446 p.
- Brundle, C.R., Watts, J.F., Wolstenholme, J. (2005) X-ray Photoelectron and Auger Electron Spectroscopy. In *Ewing's Analytical Instrumentation Handbook*, Cazes J., Ewing, G.W. (eds.), III. Interpretation of Photoelectron and Auger Spectra, CRC Press, pp. 413-419.
- Bryce, C., Berk, D. (1996) Kinetics of GaAs Dissolution in H₂O₂-NH₄OH-H₂O Solutions. *Industrial, Engineering Chemistry Research*, vol. 35, no. 12, pp. 4464-4470.
- Budz, H.A., Ali, M.M., Li, Y., LaPierre, R.R. (2010) Photoluminescence model for a hybrid aptamer-GaAs optical biosensor. *Journal of Applied Physics*, vol. 107, no. 10, pp. 104702-9.

- Budz, H.A., Biesinger, M.C., LaPierre, R.R. (2009) Passivation of GaAs by octadecanethiol self-assembled monolayers deposited from liquid and vapor phases. *Journal of Vacuum Science, Technology B: Microelectronics and Nanometer Structures*, vol. 27, no. 2, pp. 637-648.
- Burstein, E., Ganesan, S. (1965) A method for determining the magnitude of the Raman scattering matrix element for diamond-type crystals. *Journal de Physique*, vol. 26, no. 11, pp. 637-638.
- Cahen, D., Naaman, R., Vager, Z. (2005) The Cooperative Molecular Field Effect. *Advanced Functional Materials*, vol. 15, no. 10, pp. 1571-1578.
- Carpenter, M.K., Van Ryswyk, H., Ellis, A.B. (1985) Photoluminescent response of palladium-cadmium sulfide and palladium-graded cadmium sulfoselenide Schottky diodes to molecular hydrogen. *Langmuir*, vol. 1, no. 5, pp. 605-607.
- Carpenter, M.S., Melloch, M.R., Cowans, B.A., Dardas, Z., Delgass, W.N. (1989) Investigations of ammonium sulfide surface treatments on GaAs. *Proceedings of the 16th Annual Conference on the Physics and Chemistry of Semiconductor Interfaces*, American Vacuum Society, vol. 7, pp. 845-850.
- Casal, H.L., Cameron, D.G., Mantsch, H.H. (1983) Infrared spectra of crystalline *n*-alkanes. Changes observed during the phase I \rightarrow phase II transition. *Canadian Journal of Chemistry*, vol. 61, no. 8, pp. 1736-1742.
- Castner, D.G., Hinds, K., Grainger, D.W. (1996) X-ray Photoelectron Spectroscopy Sulfur 2p Study of Organic Thiol and Disulfide Binding Interactions with Gold Surfaces. *Langmuir*, vol. 12, no. 21, pp. 5083-5086.
- Chai, L., Cahen, D. (2002) Electric signal transfer through nm-thick molecular bilayers. *Materials Science and Engineering: C*, vol. 19, no. 1-2, pp. 339-343.
- Clark, L.C.J., Lyons, C. (1962) Electrode Systems for Continuous Monitoring in Cardiovascular Surgery. *Annals of the New York Academy of Sciences*, vol. 102, Automated and Semi-Automated Systems in Clinical Chemistry, pp. 29-45.
- Cohen, R., Kronik, L., Shanzer, A., Cahen, D., Liu, A., Rosenwaks, Y., Lorenz, J.K., Ellis, A.B. (1999) Molecular Control over Semiconductor Surface Electronic Properties: Dicarboxylic Acids on CdTe, CdSe, GaAs, and InP. *Journal of the American Chemical Society*, vol. 121, no. 45, pp. 10545-10553.
- Collings, A.F., Caruso, F. (1997) Biosensors: recent advances. *Reports on Progress in Physics*, vol. 60, pp. 1397-1445.
- Cumpson, P.J. (1995) Angle-resolved XPS and AES: Depth-resolution limits and a general comparison of properties of depth-profile reconstruction methods. *Journal of Electron Spectroscopy and Related Phenomena*, vol. 73, no. 1, pp. 25-52.
- Danehy, J.P., Parameswaran, K.N. (1968) Acidic dissociation constants of thiols. *Journal of Chemical, Engineering Data*, vol. 13, no. 3, pp. 386-389.
- Darling, R.B. (1993) Electrostatic and current transport properties of n^+ /semi-insulating GaAs junctions. *Journal of Applied Physics*, vol. 74, no. 7, pp. 4571-4589.

- De Vrieze, A., Strubbe, K., Gomes, W.P., Forment, S., Van Meirhaeghe, R.L. (2001) Electrochemical formation and properties of n-GaAs/Au and n-GaAs/Ag Schottky barriers: Influence of surface composition upon the barrier height. *Physical Chemistry Chemical Physics*, vol. 3, no. 23, pp. 5297-5303.
- Densmore, A., Vachon, M., Xu, D., Janz, S., Ma, R., Li, Y., Lopinski, G., Del  ge, A., Lapointe, J., Luebbert, C.C., Liu, Q.Y., Cheben, P., Schmid, J.H. (2009) Silicon photonic wire biosensor array for multiplexed real-time and label-free molecular detection. *Optics Letters*, vol. 34, no. 23, pp. 3598-3600.
- Ding, X., Moumanis, K., Dubowski, J., Frost, E., Escher, E. (2006) Immobilization of avidin on (001) GaAs surface. *Applied Physics A*, vol. 83, no. 3, pp. 357-360.
- Ding, X., Moumanis, K., Dubowski, J.J., Tay, L., Rowell, N.L. (2006) Fourier-transform infrared and photoluminescence spectroscopies of self-assembled monolayers of long-chain thiols on (001) GaAs. *Journal of Applied Physics*, vol. 99, no. 5, pp. 054701-6.
- Donev, S., Brack, N., Paris, N.J., Pigram, P.J., Singh, N.K., Usher, B.F. (2005) Surface Reactions of 1-Propanethiol on GaAs(100). *Langmuir*, vol. 21, no. 5, pp. 1866-1874.
- Doniach, Sunjic (1970) Many-electron singularity in X-ray photoemission and X-ray line spectra from metals. *Journal of Physics C: Solid State Physics*, vol. 3, pp. 285-291.
- Dorsten, J.F., Maslar, J.E., Bohn, P.W. (1995) Near-surface electronic structure in GaAs (100) modified with self-assembled monolayers of octadecylthiol. *Applied Physics Letters*, vol. 66, no. 14, pp. 1755-1757.
- Dubois, L.H., Nuzzo, R.G. (1992) Synthesis, Structure, and Properties of Model Organic Surfaces. *Annual Review of Physical Chemistry*, vol. 43, no. 1, pp. 437-463.
- Dubowski, J., Voznyy, O., Marshall, G. (2010) Molecular self-assembly and passivation of GaAs (0 0 1) with alkanethiol monolayers: A view towards bio-functionalization. *Applied Surface Science*, vol. 256, no. 19, pp. 5714-5721.
- Dumas, P., Tobin, R., Richards, P. (1986) Study of adsorption states and interactions of CO on evaporated noble metal surfaces by infrared absorption spectroscopy: I. Silver. *Surface Science*, vol. 171, no. 3, pp. 555-578.
- Duplan, V., Miron, Y., Frost, E., Grandbois, M., Dubowski, J.J. (2009) Specific immobilization of influenza A virus on GaAs (001) surface. *Journal of Biomedical Optics*, vol. 14, no. 5, pp. 054042-6.
- Dutta, N.K. (1993) *Minority Carriers in III-V Semiconductors: Physics and Applications*, Chapter 1: Radiative Transitions in GaAs and Other III-V Compounds, Semiconductors and Semimetals, vol. 3, Ahrenkiel, R.K., Lundstrom, M.S. (eds.), Academic Press, pp. 1-36.
- Enders, D., Pucci, A. (2006) Surface enhanced infrared absorption of octadecanethiol on wet-chemically prepared Au nanoparticle films. *Applied Physics Letters*, vol. 88, no. 18, pp. 184104-3.
- Fairley, N. (1999-2005) *CasaXPS*    Computer Program, version 2.3.10.
- Feynman, R.P. (1970) *The Feynman Lectures on Physics*, Addison-Wesley, 3 volume set.

- Flink, S., Veggel, F.C.J.M.V., Reinhoudt, D.N. (2000) Sensor Functionalities in Self-Assembled Monolayers. *Advanced Materials*, vol. 12, no. 18, pp. 1315-1328.
- Fowles, G.R. (1989) *Introduction to Modern Optics*, Dover Publications, 328 p.
- Fox, M. (2010) *Optical Properties of Solids*, Oxford University Press, 416 p.
- Garrett, C.G.B., Brattain, W.H. (1955) Physical Theory of Semiconductor Surfaces. *Physical Review*, vol. 99, no. 2, pp. 376-387.
- Geisz, J.F., Kuech, T.F., Ellis, A.B. (1995) Changing photoluminescence intensity from GaAs/Al_{0.3}Ga_{0.7}As heterostructures upon chemisorption of SO₂. *Journal of Applied Physics*, vol. 77, no. 3, pp. 1233-1240.
- Gelius, U. (1974) Recent progress in ESCA studies of gases. *Journal of Electron Spectroscopy and Related Phenomena*, vol. 5, no. 1, pp. 985-1057.
- Gfroerer, T.H. (2000) Photoluminescence in Analysis of Surfaces and Interfaces. In *Encyclopedia of Analytical Chemistry: Applications, Theory, and Instrumentation*, Meyers, R.A. (ed.), John Wiley & Sons, pp. 9209-9231.
- Grant, R.W., Waldrop, J.R., Kowalczyk, S.P., Kraut, E.A. (1981) Correlation of GaAs surface chemistry and interface Fermi-level position: A single defect model interpretation. *Journal of Vacuum Science and Technology*, vol. 19, no. 3, pp. 477-480.
- Hall, R.N. (1952) Electron-Hole Recombination in Germanium. *Physical Review*, vol. 87, no. 2, p. 387.
- Halley, J.D., Winkler, D.A. (2008) Consistent concepts of self-organization and self-assembly. *Complexity*, vol. 14, no. 2, pp. 10-17.
- Harris, D.C., Bertolucci, M.D. (1989) *Symmetry and Spectroscopy: An Introduction to Vibrational and Electronic Spectroscopy*, Dover Publications, 580 p.
- Hasegawa, H., Ohno, H. (1986) Unified disorder induced gap state model for insulator-semiconductor and metal-semiconductor interfaces. *Journal of Vacuum Science, Technology B: Microelectronics and Nanometer Structures*, vol. 4, no. 4, pp. 1130-1138.
- Hautman, J., Klein, M.L. (1989) Simulation of a monolayer of alkyl thiol chains. *The Journal of Chemical Physics*, vol. 91, no. 8, pp. 4994-5001.
- Hautman, J., Klein, M.L. (1990) Molecular dynamics simulation of the effects of temperature on a dense monolayer of long-chain molecules. *The Journal of Chemical Physics*, vol. 93, no. 10, pp. 7483-7492.
- He, T., He, J., Lu, M., Chen, B., Pang, H., Reus, W.F., Nolte, W.M., Nackashi, D.P., Franzon, P.D., Tour, J.M. (2006) Controlled Modulation of Conductance in Silicon Devices by Molecular Monolayers. *Journal of the American Chemical Society*, vol. 128, no. 45, pp. 14537-14541.
- He, Y., Ye, T., Su, M., Zhang, C., Ribbe, A.E., Jiang, W., Mao, C. (2008) Hierarchical self-assembly of DNA into symmetric supramolecular polyhedra. *Nature*, vol. 452, no. 7184, pp. 198-201.
- Hecht, E., Zajac, A. (1997) *Optics*, 3rd Edition, Addison-Wesley, 694 p.

- Herman, J.S., Terry, F.L. (1992) Hydrogen sulfide plasma passivation of gallium arsenide. *Applied Physics Letters*, vol. 60, no. 6, pp. 716-717.
- Herzberg, G. (2008) *Molecular Spectra and Molecular Structure - Vol I*, Read Books, 682 p.
- Hinkle, C.L., Milojevic, M., Vogel, E.M., Wallace, R.M. (2009) The significance of core-level electron binding energies on the proper analysis of InGaAs interfacial bonding. *Applied Physics Letters*, vol. 95, no. 15, pp. 151905-3.
- Hoffmann, H., Mayer, U., Krischanitz, A. (1995) Structure of Alkylsiloxane Monolayers on Silicon Surfaces Investigated by External Reflection Infrared Spectroscopy. *Langmuir*, vol. 11, no. 4, pp. 1304-1312.
- Hollinger, G., Skheyta-Kabbani, R., Gendry, M. (1994) Oxides on GaAs and InAs surfaces: An X-ray-photoelectron-spectroscopy study of reference compounds and thin oxide layers. *Physical Review B*, vol. 49, no. 16, pp. 11159-11167.
- Hou, T., Greenlief, C.M., Keller, S.W., Nelen, L., Kauffman, J.F. (1997) Passivation of GaAs (100) with an Adhesion Promoting Self-Assembled Monolayer. *Chemistry of Materials*, vol. 9, no. 12, pp. 3181-3186.
- Howell, S., Kuila, D., Kasibhatla, B., Kubiak, C.P., Janes, D., Reifengerger, R. (2002) Molecular Electrostatics of Conjugated Self-Assembled Monolayers on Au(111) Using Electrostatic Force Microscopy. *Langmuir*, vol. 18, no. 13, pp. 5120-5125.
- Huang, T., Lin, T., Teng, T., Lai, Y., Hung, W. (2009) Adsorption and thermal reaction of short-chain alkanethiols on GaAs(100). *Surface Science*, vol. 603, no. 9, pp. 1244-1252.
- Johnson, E.O. (1958) Large-Signal Surface Photovoltage Studies with Germanium. *Physical Review*, vol. 111, no. 1, pp. 153-166.
- Jun, Y., Zhu, X., Hsu, J.W.P. (2006) Formation of Alkanethiol and Alkanedithiol Monolayers on GaAs(001). *Langmuir*, vol. 22, no. 8, pp. 3627-3632.
- Kaganer, V.M., Möhwald, H., Dutta, P. (1999) Structure and phase transitions in Langmuir monolayers. *Reviews of Modern Physics*, vol. 71, no. 3, pp. 779-819.
- Kelvin (1898) V. Contact electricity of metals. *Philosophical Magazine Series 5*, vol. 46, no. 278, pp. 82-120.
- Kim, C., Marshall, G.M., Martin, M., Bisson-Viens, M., Wasilewski, Z., Dubowski, J.J. (2009) Formation dynamics of hexadecanethiol self-assembled monolayers on (001) GaAs observed with photoluminescence and Fourier transform infrared spectroscopies. *Journal of Applied Physics*, vol. 106, no. 8, pp. 083518-5.
- Kittel, C. (1986) *Introduction to Solid State Physics*, 6th Edition, John Wiley & Sons, 646 p.
- Klejung, F., Klusmann, S., Erdmann, V.A., Scheller, F.W., Fürste, J.P., Bier, F.F. (1998) High-Affinity RNA as a Recognition Element in a Biosensor. *Analytical Chemistry*, vol. 70, no. 2, pp. 328-331.
- Kolasinski, K.W. (2002) *Surface Science*, John Wiley & Sons, 330 p.
- Koopmans, T. (1934) Über die Zuordnung von Wellenfunktionen und Eigenwerten zu den Einzelnen Elektronen Eines Atoms. *Physica*, vol. 1, no. 1-6, pp. 104-113.

- Kronik, L., Shapira, Y. (1999) Surface photovoltage phenomena: theory, experiment, and applications. *Surface Science Reports*, vol. 37, no. 1-5, pp. 1-206.
- Laibinis, P.E., Whitesides, G.M., Allara, D.L., Tao, Y.T., Parikh, A.N., Nuzzo, R.G. (1991) Comparison of the structures and wetting properties of self-assembled monolayers of *n*-alkanethiols on the coinage metal surfaces, copper, silver, and gold. *Journal of the American Chemical Society*, vol. 113, no. 19, pp. 7152-7167.
- Lambert, B., Sermage, B., Deveaud, B., Clerot, F., Chomette, A., Regreny, A. (1990) Radiative and non-radiative recombination in GaAs-AlGaAs superlattices. *Surface Science*, vol. 228, no. 1-3, pp. 210-212.
- Landheer, D., Aers, G., McKinnon, W.R., Deen, M.J., Ranuarez, J.C. (2005) Model for the field effect from layers of biological macromolecules on the gates of metal-oxide-semiconductor transistors. *Journal of Applied Physics*, vol. 98, no. 4, pp. 044701-15.
- Lebedev, M.V., Ensling, D., Hunger, R., Mayer, T., Jaegermann, W. (2004) Synchrotron photoemission spectroscopy study of ammonium hydroxide etching to prepare well-ordered GaAs(1 0 0) surfaces. *Applied Surface Science*, vol. 229, no. 1-4, pp. 226-232.
- Lebedev, M.V., Mayer, T., Jaegermann, W. (2003) Sulfur adsorption at GaAs(1 0 0) from solution: role of the solvent in surface chemistry. *Surface Science*, vol. 547, no. 1-2, pp. 171-183.
- Leung, L.K., Meyer, G.J., Lisensky, G.C., Ellis, A.B. (1990) Modulation of the time-resolved photoluminescence of cadmium selenide by adduct formation with gaseous amines. *The Journal of Physical Chemistry*, vol. 94, no. 4, pp. 1214-1216.
- Li, D., Swanson, B.I., Robinson, J.M., Hoffbauer, M.A. (1993) Porphyrin based self-assembled monolayer thin films: synthesis and characterization. *Journal of the American Chemical Society*, vol. 115, no. 15, pp. 6975-6980.
- Li, Z.S., Cai, W.Z., Su, R.Z., Dong, G.S., Huang, D.M., Ding, X.M., Hou, X.Y., Wang, X. (1994) S₂Cl₂ treatment: A new sulfur passivation method of GaAs surface. *Applied Physics Letters*, vol. 64, no. 25, pp. 3425-3427.
- Liufu, D., Wang, X.S., Tu, D.M., Kao, K.C. (1998) High-field induced electrical aging in polypropylene films. *Journal of Applied Physics*, vol. 83, no. 4, pp. 2209-2214.
- Lodha, S., Janes, D.B. (2006) Metal/molecule/p-type GaAs heterostructure devices. *Journal of Applied Physics*, vol. 100, no. 2, pp. 024503-8.
- Lü, J., Eng, L., Bennewitz, R., Meyer, E., Güntherodt, H., Delamarche, E., Scandella, L. (1999) Surface potential studies of self-assembling monolayers using Kelvin probe force microscopy. *Surface and Interface Analysis*, vol. 27, no. 5-6, pp. 368-373.
- Lu, Z.H., Lagarde, C., Sacher, E., Currie, J.F., Yelon, A. (1989) A surface analytical study of GaAs(100) cleaning procedures. *Journal of Vacuum Science, Technology A: Vacuum, Surfaces, and Films*, vol. 7, no. 3, pp. 646-650.
- Luebker, E.R.M., Leung, L.K., Murphy, C.J., Lisensky, G.C., Ellis, A.B. (1991) Chemical Sensing Applications of Semiconductor Photoluminescence. In *Biotechnology: Bridging Research and Applications*, Kamely, D., Chakrabarty, A.M., Kornuth, S.E. (eds.), Session IV: Material Biotechnology, Kluwer Academic Publishers, pp. 317-332.

- Lunt, S.R., Ryba, G.N., Santangelo, P.G., Lewis, N.S. (1991) Chemical studies of the passivation of GaAs surface recombination using sulfides and thiols. *Journal of Applied Physics*, vol. 70, no. 12, pp. 7449-7467.
- Luong, J.H., Male, K.B., Glennon, J.D. (2008) Biosensor technology: Technology push versus market pull. *Biotechnology Advances*, vol. 26, no. 5, pp. 492-500.
- Lynch, D.W., Olson, C.G. (1999) *Photoemission Studies of High-Temperature Superconductors*, Cambridge University Press, 450 p.
- Malem, F., Mandler, D. (1993) Self-assembled monolayers in electroanalytical chemistry: application of ω -mercapto carboxylic acid monolayers for the electrochemical detection of dopamine in the presence of a high concentration of ascorbic acid. *Analytical Chemistry*, vol. 65, no. 1, pp. 37-41.
- Malhotra, V., Wilmsen, C.W. (1995) *Handbook of Compound Semiconductors*, Chapter 7: Passivation of GaAs and InP, Holloway, P.H., McGuire, G.E. (eds.), William Andrew Co., pp. 328-369.
- Maltby, J.R., Reed, C.E., Scott, C.G. (1972) An improved apparatus for clean surface studies of high resistivity photoconductors. *Journal of Physics E: Scientific Instruments*, vol. 5, pp. 584-586.
- Mandelis, A., Budiman, R.A. (1999) Evidence of a Surface Acceptor State in Undoped Semi-Insulating GaAs by Photothermal Radiometric Deep Level Transient Spectroscopy. *Journal Superficies y Vacio*, vol. 8, pp. 13-17.
- Marshall, G.M., Bensebaa, F., Dubowski, J.J. (2009a) Observation of surface enhanced IR absorption coefficient in alkanethiol based self-assembled monolayers on GaAs(001). *Journal of Applied Physics*, vol. 105, no. 9, pp. 094310-7.
- Marshall, G.M., Lopinski, G.P., Bensebaa, F., Dubowski, J.J. (2009b) Surface Dipole Layer Potential Induced IR Absorption Enhancement in *n*-Alkanethiol SAMs on GaAs(001). *Langmuir*, vol. 25, no. 23, pp. 13561-13568.
- Marshall, G.M., Bensebaa, F., Dubowski, J.J. (2011a) Surface barrier analysis of semi-insulating and n^+ -type GaAs(001) following passivation with *n*-alkanethiol SAMs. *Applied Surface Science*, vol. 257, no. 9, pp. 4543-4546.
- Marshall, G.M., Lopinski, G.P., Bensebaa, F., Dubowski, J.J. (2011b) Electro-optic investigation of the surface trapping efficiency in *n*-alkanethiol SAM passivated GaAs(001). Manuscript submitted to *Nanotechnology*.
- Martin, G.M., Farges, J.P., Jacob, G., Hallais, J.P., Poiblaud, G. (1980) Compensation mechanisms in GaAs. *Journal of Applied Physics*, vol. 51, no. 5, pp. 2840-2852.
- Massies, J., Dezaly, F., Linh, N.T. (1980) Effects of H₂S adsorption on surface properties of GaAs {100} grown *in situ* by MBE. *Journal of Vacuum Science and Technology*, vol. 17, no. 5, pp. 1134-1140.
- Masters, B.R., So, P.T.C. (2008) *Handbook of Biomedical Nonlinear Optical Microscopy*, Oxford University Press, 896 p.

- McGown, L.B., Joseph, M.J., Pitner, J.B., Vonk, G.P., Linn, C.P. (1995) The nucleic acid ligand. A new tool for molecular recognition. *Analytical Chemistry*, vol. 67, no. 21, pp. 663A-668A.
- McGuiness, C.L., Blasini, D., Masejewski, J.P., Uppili, S., Cabarcos, O.M., Smilgies, D., Allara, D.L. (2007b) Molecular Self-Assembly at Bare Semiconductor Surfaces: Characterization of a Homologous Series of *n*-Alkanethiolate Monolayers on GaAs(001). *ACS Nano*, vol. 1, no. 1, pp. 30-49.
- McGuiness, C.L., Shaporenko, A., Mars, C.K., Uppili, S., Zharnikov, M., Allara, D.L. (2006) Molecular Self-Assembly at Bare Semiconductor Surfaces: Preparation and Characterization of Highly Organized Octadecanethiolate Monolayers on GaAs(001). *Journal of the American Chemical Society*, vol. 128, no. 15, pp. 5231-5243.
- McGuiness, C.L., Shaporenko, A., Zharnikov, M., Walker, A.V., Allara, D.L. (2007a) Molecular Self-Assembly at Bare Semiconductor Surfaces: Investigation of the Chemical and Electronic Properties of the Alkanethiolate-GaAs(001) Interface. *The Journal of Physical Chemistry C*, vol. 111, no. 11, pp. 4226-4234.
- Meller, G., Grasser, T. (2009) *Organic Electronics*, Springer, 338 p.
- Mettler, K. (1977) Photoluminescence as a tool for the study of the electronic surface properties of gallium arsenide. *Applied Physics A: Materials Science, Processing*, vol. 12, no. 1, pp. 75-82.
- Meyer, G.J., Lisensky, G.C., Ellis, A.B. (1988) Evidence for adduct formation at the semiconductor-gas interface. Photoluminescent properties of cadmium selenide in the presence of amines. *Journal of the American Chemical Society*, vol. 110, no. 15, pp. 4914-4918.
- Milosevic, M., Berets, S. (1993) Applications of the Theory of Optical Spectroscopy to Numerical Simulations. *Applied Spectroscopy*, vol. 47, no. 5, pp. 566-574.
- Mittler-Neher, S., Spinke, J., Liley, M., Nelles, G., Weisser, M., Back, R., Wenz, G., Knoll, W. (1995) Spectroscopic and surface-analytical characterization of self-assembled layers on Au. *Biosensors and Bioelectronics*, vol. 10, no. 9-10, pp. 903-916.
- Morse, P.M. (1929) Diatomic Molecules According to the Wave Mechanics. II. Vibrational Levels. *Physical Review*, vol. 34, no. 1, pp. 57-64.
- Moulder, J.F., Stickle, W.F., Sobol, P.E. (1993) *Handbook of X Ray Photoelectron Spectroscopy*, Chastain, J. (ed.), Perkin-Elmer, Physical Electronics Division, 275 p.
- Moumanis, K., Ding, X., Dubowski, J.J., Frost, E.H. (2006) Aging and detergent washing effects of the surface of (001) and (110) GaAs passivated with hexadecanethiol. *Journal of Applied Physics*, vol. 100, no. 3, pp. 034702-5.
- Nakagawa, O.S., Ashok, S., Sheen, C.W., Mårtensson, J., Allara, D.L. (1991) GaAs Interfaces with Octadecyl Thiol Self-Assembled Monolayer: Structural and Electrical Properties. *Japanese Journal of Applied Physics*, vol. 30, no. 12b, pp. 3759-3762.
- Natan, A., Kronik, L., Haick, H., Tung, R. (2007) Electrostatic Properties of Ideal and Non-ideal Polar Organic Monolayers: Implications for Electronic Devices. *Advanced Materials*, vol. 19, no. 23, pp. 4103-4117.

- National Institute of Standards and Technology (NIST), Electron Inelastic-Mean-Free-Path (IMFP) Database version 1.1 (2000) Retrieved May 26th 2010, from <http://www.nist.gov/srd/nist71.htm>.
- National Institute of Standards and Technology (NIST), X-ray Photoelectron Spectroscopy (XPS) Database version 3.5 (2003) Retrieved December 5th 2010, from <http://srdata.nist.gov/xps/Default.aspx>.
- Nesher, G., Vilan, A., Cohen, H., Cahen, D., Amy, F., Chan, C., Hwang, J., Kahn, A. (2006) Energy Level and Band Alignment for GaAs-Alkylthiol Monolayer-Hg Junctions from Electrical Transport and Photoemission Experiments. *The Journal of Physical Chemistry B*, vol. 110, no. 29, pp. 14363-14371.
- Newman, J.D., Turner, A.P. (2005) Home blood glucose biosensors: a commercial perspective. *Biosensors and Bioelectronics*, vol. 20, no. 12, pp. 2435-2453.
- Nuzzo, R.G., Dubois, L.H., Allara, D.L. (1990) Fundamental studies of microscopic wetting on organic surfaces. 1. Formation and structural characterization of a self-consistent series of polyfunctional organic monolayers. *Journal of the American Chemical Society*, vol. 112, no. 2, pp. 558-569.
- Ortiz, E., Estrada, G., Lizardi, P.M. (1998) PNA molecular beacons for rapid detection of PCR amplicons. *Molecular and Cellular Probes*, vol. 12, no. 4, pp. 219-226.
- Osawa, M. (2001) Surface-Enhanced Infrared Absorption. In *Near-Field Optics and Surface Plasmon Polaritons*. Topics in Applied Physics, vol. 81, Springer, pp. 163-187.
- Osawa, M., Ikeda, M. (1991) Surface-enhanced infrared absorption of p-nitrobenzoic acid deposited on silver island films: contributions of electromagnetic and chemical mechanisms. *The Journal of Physical Chemistry*, vol. 95, no. 24, pp. 9914-9919.
- Paget, D., Bonnet, J.E., Berkovits, V.L., Chiaradia, P., Avila, J. (1996) Sulfide-passivated GaAs(001). I. Chemistry analysis by photoemission and reflectance anisotropy spectroscopies. *Physical Review B*, vol. 53, no. 8, pp. 4604-4614.
- Parikh, A.N., Allara, D.L. (1992) Quantitative determination of molecular structure in multilayered thin films of biaxial and lower symmetry from photon spectroscopies. I. Reflection infrared vibrational spectroscopy. *The Journal of Chemical Physics*, vol. 96, no. 2, pp. 927-945.
- Park, R.L., Lagally, M.G. (1985) *Solid State Physics: Surfaces*, Academic Press, 565 p.
- Paynter, R.W. (1999) Angle-resolved X-ray photoelectron spectroscopy studies of the evolution of plasma-treated surfaces with time. *Surface and Interface Analysis*, vol. 27, no. 2, pp. 103-113.
- Persson, B.N.J., Liebsch, A. (1981) Collective vibrational modes of isotopic mixtures of CO on Cu(111) and Cu(001). *Surface Science*, vol. 110, no. 2, pp. 356-368.
- Persson, B.N.J., Ryberg, R. (1981) Vibrational interaction between molecules adsorbed on a metal surface: The dipole-dipole interaction. *Physical Review B*, vol. 24, no. 12, pp. 6954-6970.

- Petit, E.J., Houzay, F., Moison, J.M. (1992) Interaction of atomic hydrogen with native oxides on GaAs(100). *38th National Symposium of the American Vacuum Society*, American Vacuum Society, vol. 10, pp. 2172-2177.
- Poirier, D.M., Weaver, J.H. (1993) GaAs(110) by XPS. *Surface Science Spectra*, vol. 2, no. 3, pp. 201-208.
- Prasad, P.N. (2003) *Introduction to biophotonics*, John Wiley & Sons, 622 p.
- Prinz, V.Y., Rechkunov, S.N. (1983) Influence of a Strong Electric Field on the Carrier Capture by Nonradiative Deep-Level Centers in GaAs. *Physica Status Solidi (b)*, vol. 118, no. 1, pp. 159-166.
- Raiteri, R., Grattarola, M., Butt, H., Skládal, P. (2001) Micromechanical cantilever-based biosensors. *Sensors and Actuators B: Chemical*, vol. 79, no. 2-3, pp. 115-126.
- Ramanathan, K., Danielsson, B. (2001) Principles and applications of thermal biosensors. *Biosensors and Bioelectronics*, vol. 16, no. 6, pp. 417-423.
- Reitz, J.R., Milford, F.J., Christy, R.W. (1992) *Foundations of Electromagnetic Theory*, 4th Edition, Addison Wesley, 630 p.
- Richardson, O.W. (1912) XXIII. The electron theory of contact electromotive force and thermoelectricity. *Philosophical Magazine Series 6*, vol. 23, no. 134, pp. 263-278.
- Rosu, D.M., Jones, J.C., Hsu, J.W.P., Kavanagh, K.L., Tsankov, D., Schade, U., Esser, N., Hinrichs, K. (2009) Molecular Orientation in Octanedithiol and Hexadecanethiol Monolayers on GaAs and Au Measured by Infrared Spectroscopic Ellipsometry. *Langmuir*, vol. 25, no. 2, pp. 919-923.
- Rudich, Y., Benjamin, I., Naaman, R., Thomas, E., Trakhtenberg, S., Ussyshkin, R. (2000) Wetting of Hydrophobic Organic Surfaces and Its Implications to Organic Aerosols in the Atmosphere. *The Journal of Physical Chemistry A*, vol. 104, no. 22, pp. 5238-5245.
- Schroder, D.K. (2001) Surface voltage and surface photovoltage: history, theory and applications. *Measurement Science and Technology*, vol. 12, no. 3, pp. R16-R31.
- Seah, M.P., Dench, W.A. (1979) Quantitative electron spectroscopy of surfaces: A standard data base for electron inelastic mean free paths in solids. *Surface and Interface Analysis*, vol. 1, no. 1, pp. 2-11.
- Seker, F., Meeker, K., Kuech, T.F., Ellis, A.B. (2000) Surface Chemistry of Prototypical Bulk II-VI and III-V Semiconductors and Implications for Chemical Sensing. *Chemical Reviews*, vol. 100, no. 7, pp. 2505-2536.
- Shaporenko, A., Adlkofer, K., Johansson, L.S.O., Tanaka, M., Zharnikov, M. (2003) Functionalization of GaAs Surfaces with Aromatic Self-Assembled Monolayers: A Synchrotron-Based Spectroscopic Study. *Langmuir*, vol. 19, no. 12, pp. 4992-4998.
- Sheen, C.W., Shi, J.X., Märtensson, J., Parikh, A.N., Allara, D.L. (1992) A new class of organized self-assembled monolayers: alkane thiols on GaAs(100). *Journal of the American Chemical Society*, vol. 114, no. 4, pp. 1514-1515.

- Shin, J.H., Schoenfisch, M.H. (2006) Improving the biocompatibility of in vivo sensors via nitric oxide release. *The Analyst*, vol. 131, no. 5, pp. 609-615.
- Shirley, D.A. (1972) High-Resolution X-Ray Photoemission Spectrum of the Valence Bands of Gold. *Physical Review B*, vol. 5, no. 12, pp. 4709-4714.
- Shockley, W., Read, W.T. (1952) Statistics of the Recombinations of Holes and Electrons. *Physical Review*, vol. 87, no. 5, pp. 835-842.
- Smith, B.C. (1999) *Infrared Spectral Interpretation: A Systematic Approach*, CRC Press, 286 p.
- Song, J., Lu, W. (2006) Chemically gated AlGaIn/GaN heterostructure field effect transistors for polar liquid sensing. *Applied Physics Letters*, vol. 89, no. 22, pp. 223503-3.
- Sorokin, A.V., Bai, M., Ducharme, S., Poulsen, M. (2002) Langmuir-Blodgett films of polyethylene. *Journal of Applied Physics*, vol. 92, no. 10, pp. 5977-5981.
- Spicer, W.E., Gregory, P.E., Chye, P.W., Babalola, I.A., Sukegawa, T. (1975) Photoemission study of the formation of Schottky barriers. *Applied Physics Letters*, vol. 27, no. 11, pp. 617-620.
- Spicer, W.E., Liliental-Weber, Z., Weber, E., Newman, N., Kendelewicz, T., Cao, R., McCants, C., Mahowald, P., Miyano, K., Lindau, I. (1988) The advanced unified defect model for Schottky barrier formation. *Journal of Vacuum Science, Technology B: Microelectronics and Nanometer Structures*, vol. 6, no. 4, pp. 1245-1251.
- Spindt, C.J., Besser, R.S., Cao, R., Miyano, K., Helms, C.R., Spicer, W.E. (1989a) Photoemission study of the band bending and chemistry of sodium sulfide on GaAs(100). *Journal of Vacuum Science, Technology A: Vacuum, Surfaces, and Films*, vol. 7, no. 3, pp. 2466-2468.
- Spindt, C.J., Liu, D., Miyano, K., Meissner, P.L., Chiang, T.T., Kendelewicz, T., Lindau, I., Spicer, W.E. (1989b) Vacuum ultraviolet photoelectron spectroscopy of (NH₄)₂S-treated GaAs(100) surfaces. *Applied Physics Letters*, vol. 55, no. 9, pp. 861-863.
- Sprenger, D., Anderson, O. (1991) Deconvolution of XPS spectra. *Fresenius' Journal of Analytical Chemistry*, vol. 341, no. 1-2, pp. 116-120.
- Stephenson, D.A., Binkowski, N.J. (1975) X-ray photoelectron spectroscopy of silica in theory and experiment. *Journal of Non-Crystalline Solids*, vol. 22, no. 2, pp. 399-421.
- Streetman, B., Banerjee, S. (1999) *Solid State Electronic Devices*, 5th Edition, Prentice Hall, 558 p.
- Sze, S.M., Ng, K.K. (2007) *Physics of Semiconductor Devices*, John Wiley & Sons, 827 p.
- Taylor, D.M., Bayes, G.F. (1994) Calculating the surface potential of unionized monolayers. *Physical Review E*, vol. 49, no. 2, pp. 1439-1449.
- Tomkiewicz, P., Arabasz, S., Adamowicz, B., Miczek, M., Mizsei, J., Zahn, D., Hasegawa, H., Szuber, J. (2009) Surface electronic properties of sulfur-treated GaAs determined by surface photovoltage measurement and its computer simulation. *Surface Science*, vol. 603, no. 3, pp. 498-502.

- Truong, K.D., Rowntree, P.A. (1996) Formation of Self-Assembled Butanethiol Monolayers on Au Substrates: Spectroscopic Evidence for Highly Ordered Island Formation in Sub-Monolayer Films. *The Journal of Physical Chemistry*, vol. 100, no. 51, pp. 19917-19926.
- Ulman, A., Eilers, J.E., Tillman, N. (1989) Packing and molecular orientation of alkanethiol monolayers on gold surfaces. *Langmuir*, vol. 5, no. 5, pp. 1147-1152.
- Uosaki, K. (1990) Characterization of semiconductors by photoluminescence and electroluminescence measurements in electrolyte solutions. *Trends in Analytical Chemistry*, vol. 9, no. 3, pp. 98-103.
- van der Schoot, B.H., Bergveld, P. (1987) ISFET based enzyme sensors. *Biosensors*, vol. 3, no. 3, pp. 161-186.
- Van Ryswyk, H., Ellis, A.B. (1986) Optical coupling of surface chemistry. Photoluminescent properties of a derivatized gallium arsenide surface undergoing redox chemistry. *Journal of the American Chemical Society*, vol. 108, no. 9, pp. 2454-2455.
- Vickerman, J.C. (1997) *Surface Analysis - The Principal Techniques*, John Wiley & Sons. 451 p.
- Vilms, J., Spicer, W.E. (1965) Quantum Efficiency and Radiative Lifetime in *p*-Type Gallium Arsenide. *Journal of Applied Physics*, vol. 36, no. 9, pp. 2815-2821.
- Voznyy, O., Dubowski, J.J. (2006) Structure, Bonding Nature, and Binding Energy of Alkanethiolate on As-Rich GaAs (001) Surface: A Density Functional Theory Study. *The Journal of Physical Chemistry B*, vol. 110, no. 47, pp. 23619-23622.
- Voznyy, O., Dubowski, J.J. (2008a) Adsorption Kinetics of Hydrogen Sulfide and Thiols on GaAs (001) Surfaces in a Vacuum. *Journal of Physical Chemistry C*, vol. 112, no. 10, pp. 3726-3733.
- Voznyy, O., Dubowski, J.J. (2008b) Structure of Thiol Self-Assembled Monolayers Commensurate with the GaAs (001) Surface. *Langmuir*, vol. 24, no. 23, pp. 13299-13305.
- Wang, H., Chen, S., Li, L., Jiang, S. (2005) Improved Method for the Preparation of Carboxylic Acid and Amine Terminated Self-Assembled Monolayers of Alkanethiolates. *Langmuir*, vol. 21, no. 7, pp. 2633-2636.
- Watkins, A.N., Bright, F.V. (1998) Effects of Fluorescent Reporter Group Structure on the Dynamics Surrounding Cysteine-26 in Spinach Calmodulin: A Model Biorecognition Element. *Applied Spectroscopy*, vol. 52, no. 11, pp. 1447-1456.
- Weast, R.C., Lide, D.R. (1990) *CRC Handbook of Chemistry and Physics*, 70th Edition, CRC Press.
- Wink, T., Zuilen, S.J.V., Bult, A., Bennekou, W.P.V. (1997) Self-assembled Monolayers for Biosensors. *The Analyst*, vol. 122, no. 4, pp. 43R-50R.
- Winter, H., Burgdörfer, J. (2007) *Slow Heavy-Particle Induced Electron Emission from Solid Surfaces*, Springer, 254 p.

- Wittry, D.B. (1967) Measurement of Diffusion Lengths in Direct-Gap Semiconductors by Electron-Beam Excitation. *Journal of Applied Physics*, vol. 38, no. 1, pp. 375-382.
- Wu, D.G., Cahen, D., Graf, P., Naaman, R., Nitzan, A., Shvarts, D. (2001) Direct Detection of Low-Concentration NO in Physiological Solutions by a New GaAs-Based Sensor. *Chemistry*, vol. 7, no. 8, pp. 1743-1749.
- Yablonovitch, E., Sandroff, C.J., Bhat, R., Gmitter, T. (1987) Nearly ideal electronic properties of sulfide coated GaAs surfaces. *Applied Physics Letters*, vol. 51, no. 6, pp. 439-441.
- Yacobi, B.G. (2003) *Semiconductor Materials: An Introduction to Basic Principles*, Springer, 242 p.
- Ye, S., Li, G., Noda, H., Uosaki, K., Osawa, M. (2003) Characterization of self-assembled monolayers of alkanethiol on GaAs surface by contact angle and angle-resolved XPS measurements. *Surface Science*, vol. 529, no. 1-2, pp. 163-170.
- Zavadil, K.R., Ashby, C.I.H., Howard, A.J., Hammons, B.E. (1994) Ultraviolet photosulfidation of III-V compound semiconductors for electronic passivation. *The 40th National Symposium of the American Vacuum Society*, American Vacuum Society, vol. 12, no. 4, pp. 1045-1049.
- Zawisza, I. (2003) Electrochemical and Photon Polarization Modulation Infrared Reflection Absorption Spectroscopy Study of the Electric Field Driven Transformations of a Phospholipid Bilayer Supported at a Gold Electrode Surface. *Biophysical Journal*, vol. 85, no. 6, pp. 4055-4075.
- Zhai, J., Cui, H., Yang, R. (1997) DNA based biosensors. *Biotechnology Advances*, vol. 15, no. 1, pp. 43-58.
- Zhang, Q., Huang, H., He, H., Chen, H., Shao, H., Liu, Z. (1999) Determination of locations of sulfur, amide-nitrogen and azo-nitrogen in self-assembled monolayers of alkanethiols and azobenzenethiols on Au (111) and GaAs (100) by angle-resolved X-ray photoelectron spectroscopy. *Surface Science*, vol. 440, no. 1-2, pp. 142-150.
- Zhang, X.G. (2001) *Electrochemistry of Silicon and its Oxide*, Springer, 544 p.
- Zisman, W.A. (1932) A New Method of Measuring Contact Potential Differences in Metals. *Review of Scientific Instruments*, vol. 3, no. 7, pp. 367-370.